NATIONAL TECHNICAL UNIVERSITY OF ATHENS
School of Naval Architecture and Marine Engineering
Laboratory of Ship and Marine Hydrodynamics (LSMH)

Hydroelastic analysis and optimization of biomimetic propulsion systems with application to ship energy-saving devices

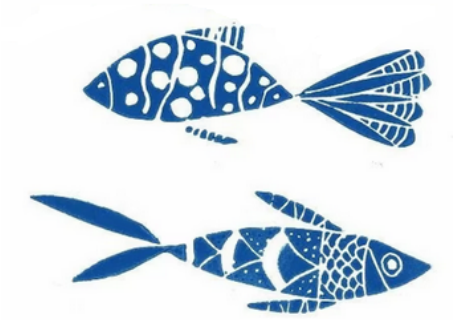

This dissertation is submitted for the degree of
Doctor of Engineering

PhD Thesis

Dimitra Anevlavi

Advisory Committee:
K. Belibassakis, Professor NTUA (Supervisor)
K. Giannakoglou, Professor NTUA
G. Papadakis, Assistant Professor NTUA

Athens, 2024

NATIONAL TECHNICAL UNIVERSITY OF ATHENS
School of Naval Architecture and Marine Engineering
Laboratory of Ship and Marine Hydrodynamics (LSMH)

Hydroelastic analysis and optimization of biomimetic propulsion systems with application to ship energy-saving devices

PhD Thesis

Dimitra Anevlavi

Examination Committee:

1. K. Belibassakis* Professor NTUA (Supervisor)
   School of Naval Architecture and Marine Engineering
2. K. Giannakoglou*, Professor NTUA
   School of Mechanical Engineering
3. G. Papadakis*, Assistant Professor NTUA
   School of Naval Architecture and Marine Engineering
4. G.A. Athanassoulis, Emeritus Professor NTUA
   National Technical University of Athens
5. G.S. Triantafyllou, Emeritus Professor NTUA
   National Technical University of Athens
6. S. Voutsinas, Professor NTUA
   School of Mechanical Engineering
7. V. Riziotis, Associate Professor NTUA
   School of Mechanical Engineering

*Member of Advisory Committee

Athens, 2024

ΕΘΝΙΚΟ ΜΕΤΣΟΒΙΟ ΠΟΛΥΤΕΧΝΕΙΟ
Σχολή Ναυπηγών Μηχανολόγων Μηχανικών (ΣΝΜΜ)
Εργαστήριο Ναυτικής και Θαλάσσιας Υδροδυναμικής

Υδροελαστική ανάλυση και βελτιστοποίηση βιομιμητικών συστημάτων πρόωσης με εφαρμογή σε συσκευές εξοικονόμησης ενέργειας πλοίου

Διδακτορική Διατριβή της

Δήμητρας Ανεβλαβή

Επταμελής Εξεταστική Επιτροπή:

1. Κ. Μπελιμπασσάκης*, Καθηγητής ΕΜΠ (Επιβλέπων)
   Σχολή Ναυπηγών Μηχανολόγων Μηχανικών
2. Κ. Γιαννάκογλου*, Καθηγητής ΕΜΠ
   Σχολή Ναυπηγών Μηχανολόγων Μηχανικών
3. Γ. Παπαδάκης*, Επίκουρος Καθηγητής ΕΜΠ
   Σχολή Ναυπηγών Μηχανολόγων Μηχανικών
4. Γ.Α. Αθανασούλης, Ομότιμος Καθηγητής ΕΜΠ
   Εθνικό Μετσόβιο Πολυτεχνείο
5. Γ.Σ. Τριανταφύλλου, Ομότιμος Καθηγητής ΕΜΠ
   Εθνικό Μετσόβιο Πολυτεχνείο
6. Σ. Βουτσινάς, Καθηγητής ΕΜΠ
   Σχολή Μηχανολόγων Μηχανικών
7. Β. Ριζιώτης, Αναπληρωτής Καθηγητής ΕΜΠ
   Σχολή Μηχανολόγων Μηχανικών

*Μέλος Συμβουλευτικής Επιτροπής

Αθήνα, 2024

Dedicated to my sailing family - you have been a constant inspiration.

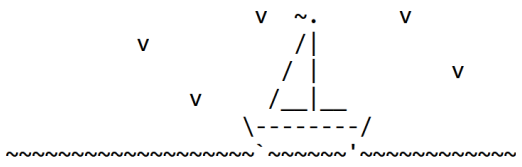

Abstract

Aquatic locomotion has been an active field of research for decades and continues to inspire technological solutions, ranging from small-scale propulsion systems for autonomous underwater vehicles (AUVs) to larger-scale energy-saving devices (ESDs) for ships. In particular, the thrust-producing kinematics emulated by the majority of flapping-foil systems are, in fact, inspired from *thunninform* swimmers. *Thunninform* locomotion is found among marine mammals, sharks, and fish species such as the Bluefin tuna, who can achieve remarkable efficiency over large distance cruising without sacrificing agility. Extensive experimental and numerical research on aquatic locomotion suggests that passively deforming wings with properly tuned material properties can attain greater propulsive efficiency compared to equivalent rigid wings and thus are prime candidates for optimization studies. The present work addresses two relevant engineering problems related to lifting surfaces for hydrodynamic propulsion with direct technological applications. These problems are the hydro-elastic analysis of passively morphing wing thrusters and the prediction of partial cavitation phenomena on hydrofoils operating beneath the free surface.

Related to the former, within the context of this thesis the cost-effective computational tool *FlexWing3D* has been developed to address the fluid-structure interaction problem related to the elastic response and hydrodynamic performance evaluation of passively deforming wings operating as marine thrusters (or thrust augmentation devices) that undergo prescribed flapping motion. The elastic response of wing submerged within the fluid medium is implicitly nonlinear since wing deformation affects the hydrodynamic pressure and vice-versa. To tackle the implicit non-linearity, a strongly coupled partitioned scheme has been developed. The model couples an unsteady boundary element method (3dBEM), that is based on potential theory and treats the hydrodynamic problem of lifting flows around wings, with a finite element method based on Discrete Kirchhoff Triangles (2dFEM) that provides predictions for the response of a thin plate with stiffness variation assuming small strains/rotations. The proposed method is suitable for response predictions on wings of general geometry that operate in largely attached flow conditions. The computational tools are written in C/C++ and have

GPU-acceleration features exploiting the capabilities of tailor-made CUDA-kernel functions for parallel computation on NVIDIA graphics cards. For simplicity, in the present work, thrusters are assumed to be fully submerged within the fluid medium; and interaction with other boundaries, such as the wavy free surface or other bodies, is negligible. Optimization studies for realistic AUV propulsion scenarios are conducted, involving both actively and passively morphing wings, revealing trends that are useful to the design of more efficient bio-mimetic thrusters.

Our motivation behind the latter engineering problem studied here is derived from the findings of several studies concluding that hydrofoils operating near the free surface are highly prone to cavitation phenomena, which can significantly affect their operation and may also result in adverse effects such as induced noise, vibration, structural failure and drop in performance. Particularly, cavitation is defined as the appearance of vapor cavities that are in contact with the hydrofoil surface in an otherwise homogeneous liquid medium. Moreover, advances in computational and experimental research have led to a better understanding of this multi-phase phenomenon, thus enabling researchers to predict and alleviate its adverse effects on hydrofoil performance. However, the number of works found in the literature concerning high-fidelity cavitation models with free surface effects remain limited, mainly due to the complex nature of the physical problem.

Our contribution to this field is a new continuous adjoint BEM-based optimization prediction method for the analysis of partially cavitating hydrofoils operating beneath the free surface. Following an inverse problem formulation, the attached-cavity is parameterized using B-spline interpolation and is modeled as a free-streamline. The design variable vector consists of the control points affecting the attached cavity shape and the cavitation number. Under the fixed cavity length assumption, the design variable vector is determined upon solution of the optimization problem along with the velocity potential. The hydrofoil moves at a constant speed at close proximity to the free surface, and free-surface elevation, following a linearization assumption, is evaluated after the solution has been obtained. The *PCavPreMod* numerical model, written in Matlab, is found to predict well the cavity shape and cavitation number when compared against experimental data and other methods from the literature. A parametric study concerning the effects of Froude number and submergence depth on the cavitation number and cavity shape is included and discussed. The findings suggest that *PCavPreMod* can facilitate the preliminary design of partially cavitating hydrofoils operating beneath the free surface effects in conjunction with higher-fidelity multi-phase flow models. Finally, the present model is formulated so that it can be extended to treat 3-D, unsteady sheet cavitation of biomimetic thrusters operating beneath the wavy free surface; Propeller blade sheet cavitation is also another application that is considered as future extension.

Περίληψη στα Ελληνικά

Ο Διεθνής Ναυτιλιακός Οργανισμός (IMO) τα τελευταία χρόνια φέρνει στο προσκήνιο τις περιβαλλοντικές επιπτώσεις του κλάδου της ναυτιλίας και υιοθετεί μέτρα που επιδρούν στη σχεδίαση και τη λειτουργία πλοίων με στόχο τη μείωση των αερίων ρύπων και την αντιμετώπιση του φαινομένου του θερμοκηπίου [1], [2]. Έμφαση δίνεται κυρίως στη μείωση των εκπομπών διοξειδίου του άνθρακα (CO_2), μεθανίου (CH_4), οξειδίων του αζώτου (NO_x) και φθοριούχων αερίων ($F\text{-}Gases$), με τα τελευταία να σχετίζονται με εφαρμογές ψύξης και κλιματισμού. Τα δύο βασικά μέτρα που έχουν ληφθεί είναι ο σχεδιαστικός δείκτης ενεργειακής απόδοσης ($EEDI$) και το σχέδιο διαχείρισης της ενεργειακής αποδοτικότητας ($SEEMP$). Με τις νέες νομοθετικές ρυθμίσεις, οι πλοιοκτήτριες εταιρείες ενθαρρύνονται να λάβουν σοβαρά υπόψη το ενδεχόμενο υιοθέτησης νέων καινοτόμων τεχνολογικών προϊόντων που καθιστούν δυνατή τόσο την ενεργειακή αναβάθμιση της απόδοσης του υπάρχοντος στόλου αλλά και τη ναυπήγηση ενεργειακά αποδοτικότερων και φιλικότερων προς το περιβάλλον πλοίων [3].

Υπό το πρίσμα αυτό, η συνεισφορά της έρευνας στον τομέα της υδροδυναμικής βελτιστοποίησης σύγχρονων συστημάτων πρόωσης συμβατικών αλλά και μη, καθώς και η ανάπτυξη τεχνολογίας για την αξιοποίηση πληθώρας πηγών ανανεώσιμης ενέργειας (κυματική, αιολική, ηλιακή) είναι επιτακτική. Σε ότι αφορά τα μη συμβατικά συστήματα πρόωσης, ήδη από τις αρχές της δεκαετίας του '90 η μελέτη και η σχεδίαση βιομιμητικών προωθητήρων που είναι εμπνευσμένοι από τους μηχανισμούς ώσης και ελιγμών που απαντώνται στα θαλάσσια θηλαστικά και στα τονοειδή κεντρίζει το ενδιαφέρον της επιστημονικής κοινότητας [4], [5]. Άλλωστε, δεν είναι τυχαίο πως ο αριθμός των δημοσιεύσεων στα πεδία αριθμητικής και πειραματικής προσομοίωσης ροών γύρω από πτέρυγες σε λειτουργία προωθητήρα αλλά και απομάστευσης ενέργειας από κύματα/ρεύματα έχει πληθύνει σημαντικά τα τελευταία χρόνια. Τα αποτελέσματα είναι ιδιαιτέρως ενθαρρυντικά και καταδεικνύουν πως τα βιομιμητικά πτερύγια μπορούν να παράξουν ώση με βαθμό απόδοσης εξίσου υψηλό με τις ναυτικές έλικες, καθιστώντας τα συστήματα αυτά φιλικότερα προς το περιβάλλον. Επιπλέον, η χαμηλόσυχνη λειτουργία τους, στο τυπικό εύρος αριθμών αδιάστατης συχνότητας Strouhal $0.2 - 0.4$ όπου και παρατηρείται η μεγιστοποίηση της απόδοσης [6], δεν επιβαρύνει τον υποθαλλάσιο χώρο με υψηλά επίπεδα υποθαλάσσιου θορύβου σε

αντίθεση με τις ναυτικές έλικες.

Πολλά πρωτότυπα έχουν ήδη κατασκευαστεί σε μικρή κλίμακα, με γνωστότερα παραδείγματα τεχνολογικών εφαρμογών μη συμβατικών συστημάτων πρόωσης αυτά των ρομποτικών ψαριών *RoboTuna* και *SoFi* του MIT, που σχεδιάστηκαν για την εξερεύνηση θαλάσσιου βυθού. Τα υλικά καθώς και οι μηχανισμοί ελέγχου που χρησιμοποιήθηκαν για την κατασκευή αυτών των πρωτοτύπων είναι ικανά να προσδώσουν δυνατότητες ενεργητικής και παθητικής παραμόρφωσης στα πτερύγια πετυχαίνοντας υψηλούς βαθμούς απόδοσης σε συνδυασμό με ικανότητα ελιγμών. Η ανάπτυξη ρομποτικών ψαριών έχει εμπνεύσει πληθώρα άλλων συστημάτων πρόωσης για μη επανδρωμένα αυτόνομα υποθαλάσσια οχήματα (AUV) [7], [8] με διάφορα βιομιμητικά χαρακτηριστικά.

Όσον αφορά τις ναυπηγικές εφαρμογές για πλοία, μη συμβατικές διατάξεις συστημάτων πρόωσης, που βασίζονται σε απαραμόρφωτα δυναμικά πτερύγια έχουν προταθεί κατα καιρούς ως εναλλακτική των ναυτικών ελίκων. Ωστόσο, η τοποθέτηση ταλαντούμενων πτερυγίων σε πρύμνη ήδη διαμορφωμένη για κλασική διάταξη με ναυτική έλικα απαιτεί κοστοβόρες μετασκευές. Δεδομένων των τεχνολογικών δυσκολιών και του υψηλού κόστους σε συνάρτηση πάντοτε με το οικονομικό όφελος της εγκατάστασης αυτής ως επένδυση, η χρήση βιομιμητικών προωθητήρων ως κύριο σύστημα πρόωσης ποντοπόρων πλοίων έχει σχεδόν εγκαταληφθεί, ενώ τη θέση της διαδέχεται η μελέτη τους ως συστήματα υποβοήθησης πρόωσης και εξοικονόμησης ενέργειας [9]. Το δυναμικό πτερύγιο που μελετήθηκε στο πλαίσιο του ευρωπαϊκού ερευνητικού προγράμματος *SeaTech* Horizon20 αποτελεί ένα τέτοιο παράδειγμα. Τοποθετείται στην πλώρη και η λειτουργία του με κατάλληλο νόμο ενεργητικού ελέγχου για τη γωνία πρόσπτωσης οδηγεί σε μείωση της ολικής αντίστασης του πλοίου σε κυματισμούς, απόσβεση της κατακόρυφης ταλάντωσης και του προνευτασμού, ενώ απομαστεύει μικρό ποσό κυματικής ενέργειας παράγοντας επιπλέον ώση, βλ. [10], [11]. Μία επιπρόσθετη καινοτομία αποτελεί η μελέτη της βιομιμητικής συσκευής σε συνέργεια με το ναυτικό κινητήρα με στόχο την αξιοποίηση της παραγώμενης ώσης προς αύξηση της απόδοσης, καταδεικνύοντας πόσο σημαντική είναι η ολιστική μελέτη των συστημάτων πρόωσης και εξοικονόμησης ενέργειας πλοίου.

Το αντικείμενο της παρούσας εργασίας αφορά τη μελέτη βιομιμητικών συστημάτων τύπου ταλαντούμενου πτερυγίου. Πιο συγκεκριμένα επικεντρώνεται στην ανάλυση προβλημάτων συμπεριφοράς και βελτιστοποίησης μέσω αριθμητικών προσομοιώσεων που πραγματοποιούνται με τον κώδικα *FlexWing3D που αναπτύχθηκε για αυτό το σκοπό*. Το υπολογιστικό εργαλείο βασίζεται σε μία πλήρως συζευγμένη μέθοδο συνοριακών και πεπερασμένων στοιχείων που μπορεί να χρησιμοποιηθεί για την πρόλεξη των υδροδυναμικών φορτίσεων αλλά και της απόκρισης παθητικά παραμορφούμενων πτερύγων γενικής γεωμετρίας σε λειτουργία βιομιμητικού προωθητήρα, υπό το πρίσμα μοντελοποίησης του σύνθετου προβλημάτος αλληλεπίδρασης ρευστού και κατασκευής. Η μαθηματική διατύπωση του υδροδυναμικού προβ-

λήματος βασίστηκε στη θεωρία ιδανικού ρευστού, ενώ επεκτάθηκε για αυτό το σκοπό 3-Δ κώδικας συνοριακών στοιχείων (boundary element method, BEM) του εργαστηρίου ΕΝΘΥ [12]. Το εργαλείο αυτό χρησιμοποιήθηκε επίσης σε προβλήματα ανάλυσης και βελτιστοποίησης ενεργητικά παραμορφούμενων πτερύγων. Η πτέρυγα με τη σειρά της ως κατασκευή μοντελοποιείται ως λεπτή πλάκα μεταβαλλόμενου πάχους και για τους αριθμητικούς υπολογισμούς αναπτύχθηκε 2-Δ κώδικας πεπερασμένων στοιχείων (finite element method, FEM) με στοιχεία Discrete Kirchhoff Triangles (DKT). Ο προωθητήρας θεωρήθηκε πλήρως βυθισμένος και τυχόν αλληλεπιδράσεις με άλλα σύνορα, όπως λ.χ. η κυματισμένη ελεύθερη επιφάνεια, ανομοιογένειες του πυθμένα και άλλα σώματα αμελούνται, στα πλαίσια αρχικής ανάπτυξης της παρούσας μεθοδολογίας. Εξετάζονται ενδεικτικά σενάρια βελτιστοποίησης της απόδοσης βιομιμητικών προωθητήρων με κατάλληλη ρύθμιση των παραμέτρων της γεωμετρίας και κινηματικής υπό περιορισμούς, με αποτελέσματα αξιοποιήσιμα στο σχεδιασμό τέτοιων συσκευών. Η επίλυση των προβλημάτων βελτιστοποίησης βασίστηκε σε αλγόριθμο sequential quadratic programming, όπου ο υπολογισμός των παραγώγων ευαισθησίας πραγματοποιείται με σχήμα πεπερασμένων διαφορών και διαδοχικές κλήσεις του συζευγμένου υδρο-ελαστικού υπολογιστικού εργαλείου.

Τέλος, στο πλαίσιο διερεύνησης μεθόδων βελτιστοποίησης, και λαμβάνοντας υπόψη τον αυξημένο κίνδυνο εμφάνισης φαινομένων σπηλαίωσης για υδροτομές που λειτουργούν κοντά στην ελεύθερη επιφάνεια, αναπτύχθηκε το μόνιμο 2-Δ υπολογιστικό εργαλείο *PCavPreMod* για την πρόλεξη φαινομένων μερικής σπηλαίωσης με επιδράσεις ελεύθερης επιφάνειας. Το μαθηματικό μοντέλο βασίστηκε στις υποθέσεις της θεωρίας ιδανικού ρευστού υιοθετώντας διατύπωση 'αντίστροφου' προβλήματος για το σχήμα της προσκολλημένης φυσαλίδας, που μοντελοποιείται ως άγνωστη γραμμή ροής. Για την επίλυση του προβλήματος βελτιστοποίησης που προκύπτει χρησιμοποιήθηκε η συνεχής συζυγής μεθόδος. Η επαλήθευση του μοντέλου πραγματοποιήθηκε μέσω συγκρίσεων με άλλες μεθόδους και πειραματικά δεδομένα από τη βιβλιογραφία, όπου καταδεικνύεται πως η πρόλεξη του σχήματος της φυσαλίδας και του αριθμού σπηλαίωσης είναι αρκετά ικανοποιητικές. Επιπλέον, παρουσιάζονται αποτελέσματα παραμετρικής μελέτης για τη διερεύνηση επιδράσεων αριθμού Froude, γωνίας πρόσπτωσης και βύθισης από την ελεύθερη επιφάνεια σε σπηλαιούμενες υδροτομές. Το μοντέλο *PCavPreMod* μπορεί να αξιοποιηθεί για τη μελέτη και το σχεδιασμό υδροτομών σε συνέργεια με άλλα μοντέλα πρόλεξης φαινομένων σπηλαίωσης, ενώ η επέκταση του σε μη-μόνιμες ροές στις 3-Δ δίνει τη δυνατότητα πρόλεξης σπηλαίωσης φύλλου σε πιο σύνθετες γεωμετρίες όπως οι ναυτικές έλικες.

Η εργασία αποτελείται από τρία διακριτά μέρη. Το Κεφ. 1 που προηγείται περιλαμβάνει συνοπτική βιβλιογραφική ανασκόπηση σε θέματα που αφορούν σύγχρονα συστήματα πρόωσης με έμφαση στη βιομιμητική πρόωση ταλαντούμενου πτερυγίου, σύγχρονες μεθόδους σχεδιασμού με εργαλεία βελτιστοποίησης, ενώ γίνεται αναφορά στη σπηλαίωσης υδροτομών με επίδρασεις ελεύθερης επιφάνειας. Το πρώτο μέρος

περιλαμβάνει τα Κεφ. 2-4 όπου παρουσιάζονται τα υπολογιστικά εργαλεία που αναπτύχθηκαν για την ανάλυση και βελτιστοποίηση βιομιμητικών προωθητήρων που αλλάζουν σχήμα ενεργητικά ή παθητικά με στόχο την αύξηση της απόδοσης τους. Το δεύτερο μέρος περιλαμβάνει το Κεφ. 5 όπου παρουσιάζονται παραδείγματα εφαρμογής της συνεχούς συζυγούς μεθόδου στο πρόβλημα πρόλεξης φαινομένων μερικής σπηλαίωσης υδροτομών που κινούνται με σταθερή ταχύτητα κάτω από την ελεύθερη επιφάνεια. Τέλος, παρουσιάζονται συνοπτικά σε ξεχωριστό Κεφάλαιο τα επιμέρους συμπεράσματα της παρούσας διατριβής, ενώ δεν παραλείπονται προτάσεις και κατευθύνσεις μελλοντικής έρευνας. Το τελευταίο μέρος συνοψίζει τα ευρήματα της εργασίας και προτείνει κατευθύνσεις για μελλοντική έρευνα.

Acknowledgments

The present work was supported by the SeaTech H2020 research and innovation program funded by the European Union's Horizon 2020 under grant agreement No 857840 and the Retrofit55 Horizon Europe research program under grant agreement No 101096068.

Ms. Dimitra Anevlavi is a recipient of the Special Account for Research Funding (E.L.K.E.) Scholarship Program of the National Technical University of Athens for her doctoral studies during 2021-2024.

The author would also like to acknowledge the financial support received from the Hellenic Short-sea Shipowners Association (H.S.S.A.) via the Bureau Veritas Scholarship Program 2020 for Maritime Studies, the Bodossaki Foundation Graduate Scholarship Program 2020-21, and the Society of Naval Architects and Marine Engineers (SNAME) via the Graduate Scholarship Program 2020 and SNAME SOME 2023 Graduate Awards which were valuable to the completion of this work.

Thanks

Completing this work as part of my doctoral studies has been both challenging yet rewarding, and I am grateful for the support of others that made it possible. Firstly, I would like to thank my supervisor, Professor Kostas Belibassakis, for being a mentor and for conveying his enthusiasm for mathematical modeling, hydrodynamics, and bio-mimicry that stands for the concept of emulating systems, models, or elements of nature to solve complex engineering problems.

I would also like to express gratitude to my colleagues, Assistant Prof. Evangelos Filippas at the University of West Attica and Lecturer Angelina Karperaki at Aston University in Birmingham, for motivating me to pursue academic studies and helping me navigate through numerous lines of code during the initial stages of this project. To Senior Lecturer Th. Papathanasiou at Aston University in Birmingham for taking the time to discuss and provide insight into finite element analysis, continuum mechanics and numerical methods.

To Prof. Emeritus G. Athanassoulis for the engaging discussions on mathematics, physics, and philosophy that he led during the selective courses at the National Technical University of Athens. The lectures not only strengthened my background in mathematics but also renewed my interest in numerical modeling. More importantly, they taught me the value of patience and perseverance when studying complex concepts.

To Assistant Prof. G. Papadakis for conveying his enthusiasm for computational fluid dynamics, high-performance computing and coupling methods for fluid-structure interaction simulations. To Professor K. Giannakoglou for introducing me to optimization algorithms, mesh generation techniques and their direct engineering applications. He generously shared relevant literature on the continuous adjoint method that played a crucial role in the development of our partial cavitation prediction model presented in this thesis.

To Professor S. Bal at the Istanbul Technical University and Professor S. Kinnas at the University of Texas at Austin. They have provided valuable insights on potential-based cavitation prediction methods and have given access to the PCPAN software, which allowed the thorough validation of our adjoint-based partial cavitation model for hydrofoils.

Special thanks to Professor S. Voutsinas, who I deeply admire for his perspective on academia and his contribution to aerodynamics, but especially for introducing me to offshore sailing. For a naval architect like myself, familiarization with sailing comprises of several things I am also enthusiastic about studying, such as the aerodynamics of sails, sea-keeping in wavy seas, and many others. During the offshore races, I had the opportunity to experience firsthand what it means to travel as a seafarer, practice hands-on problem-solving, work in a team, communicate with others, and meet truly inspiring people.

I am also extremely grateful for the support and technical advice of all the people in LSMH, but especially my colleagues Spiros Zafeiris and Andreas Alexandris-Galanopoulos for our uplifting conversations that helped me stay motivated. To my classmates and yearlong friends Afroditi Zafeiri, Nikos Manos, Iro Malefaki, and Dr. Panos Sioulas, for their support and encouragement. To my family and to mother for wholeheartedly believing in me, helping me complete numerous lengthy scholarship applications, and voluntarily proofreading this manuscript. And to Kostis Ritsonis for being there for me, and showing me that finishing this journey marks new, exciting beginnings.

Dimitra Anevlavi
May, 2024

Contents

List of Figures

List of Tables

Chapter 1

Introduction

"Only the best is good enough."
Ole Kirk Christiansen, *The Lego Group*

Over the last few years, the International Maritime Organization (IMO) that stands as specialized UN agency, has brought the environmental impact of maritime industry to the forefront by imposing mandatory measures and regulations in order to contribute to the global fight against climate change through decarbonizing shipping by 2050 [1], [2]. Emission-reduction measures target mainly CO_2 (carbon dioxide), CH_4 (methane), NO_x (nitrous oxide), SO_x (sulfur oxide) and fluorinated gases.

Under IMO's amended, as of July 2011, pollution prevention treaty (MARPOL), the Energy Efficiency Design Index (EEDI) and the Ship Energy Efficiency Management Plan (SEEMP) became mandatory measures for all seagoing vessels. IMO forges ahead and develops new short-term regulations for existing vessels, such as the attained and required Energy Efficiency Existing Ship Index (EEXI). As shown schematically in Figure 1.1, the required Energy Efficiency Existing Ship Index (EEXI) is calculated based on a reduction factor and expressed as a percentage relative to the EEDI reference line, based on the efficiency of ships built between 1999 and 2009. Particularly, ships built between 2013-2015 are required to have a design efficiency that is at least equal to the reference line. Ships built between 2015-2020 comply with EEDI requirements only if they attain an index that is at least 10% below the reference line. The same measure for ships built after 2025 requires 30% EEDI reduction for compliance, pushing towards more efficient designs.

On 14 July 2021, the European Commission also adopted a series of legislative proposals to deliver the European Green Deal, the 'Fit for 55' package, setting out how it intends to reduce its net greenhouse gas GHG by at least 55% by 2030,

compared to 1990 levels. These policies pave the way for Europe to become the world's first climate-neutral continent by 2050. In addition, the positive effects of various market-based measures (MBMs) and environmental policies, such as carbon taxes and emission trading systems, are studied, and are expected to boost decarbonization efforts as highlighted in Lagouvardou et al. 2023 [3].

Apart from using alternative fuels as a prominent solution to decarbonize shipping, the industry is currently assessing unconventional energy and technology solutions to attain more drastic reductions in emissions [13], [14]. Shipowner companies are also encouraged to actively invest in retrofit projects that would reduce the environmental impact of their fleet while ensuring that the vessels comply with IMO ambitious regulations.

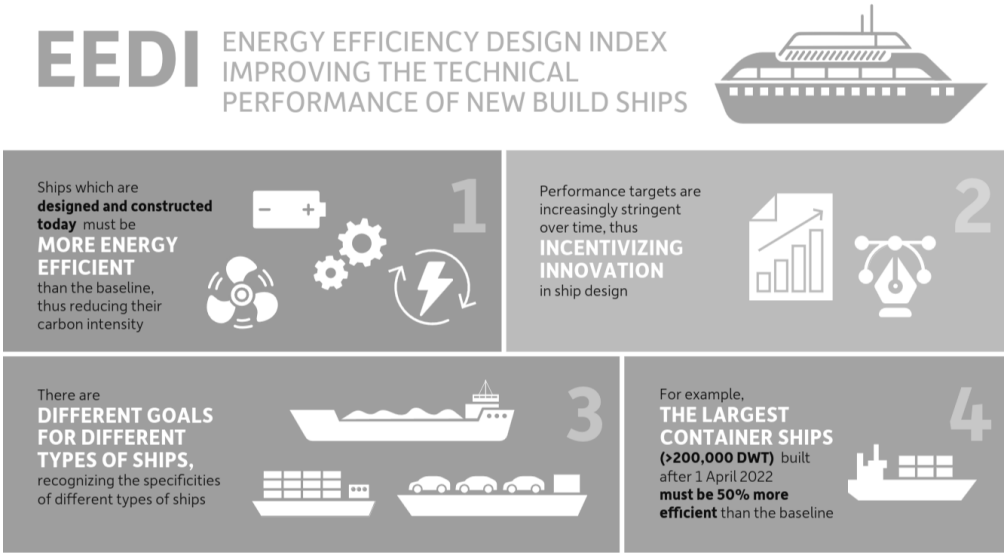

Figure 1.1: Improving the performance of new-build vessels via EEDI [15].

1.1 Energy-saving devices (ESDs) and unconventional ship propulsion systems

In general, the term ship energy-saving devices (ESDs) refers to various retrofit solutions designed for commercial vessels that aim to reduce the rotational or axial energy losses of the propulsion system, most commonly targeting water flow around the propeller [14]. For instance, a vessel equipped with stern energy-saving devices delivers the required thrust at lower engine power, thus operating at lower fuel consumption, which results in emission reduction. Typically ESDs are categorized based on the operation principle as *upstream* and *downstream* devices.

Upstream devices are installed in the upstream of a propeller and by interfering with the inflow they aim to improve propeller efficiency. These include (1) pre-ducts, see e.g. [16]-[17], with the Becker Mewis Duct as one recognizable design and (2) pre-swirl stators and fins, see e.g. the numerical works [18], [19] and [20].

On the other hand, *downstream* devices are mounted in the wake of a propeller and improve the overall efficiency of the system by recovering rotational losses of the wake. Notable devices include (1) rudder fins, see e.g. the computational and experimental results for the thrust-rudder fin design from [21]-[22], and (2) propeller boss-cap fins (PBCF) that mitigate losses from hub vortices as shown in [23].

A useful summary of the reported performance improvement after installation of various types of ESDs can be found in [24]. In their work, it is also highlighted that *downstream* energy-saving devices achieve between 2%–5% efficiency gain, whereas for *upstream* devices these figures can range between 4%-14% based on model tests and sea trials, paving the way for successful future retrofit projects.

State-of-the-art design of ESDs requires an association between optimization frameworks and computational fluid dynamics (CFD). For completeness, simulations performed in the preliminary design phase should address unsteady hydrodynamic load prediction, cavitation behavior, and underwater noise emissions. In the literature, there is a distinction between works that propose a methodology or a framework that can facilitate the design of certain types of energy-saving devices and works that are concerned with the design and assessment of full-scale ESD retrofitting.

Regarding the latter, comparisons between the proposed computational tools and full-scale sea trial results are extremely valuable, yet rather scarce. For instance, the proposed computational framework in [16] was used for the optimal design of a pre-duct for a Japan bulk carrier, and full-scale trials after retrofitting showed a remarkable 10% improvement in propulsive efficiency, which corresponds to higher gains compared to the previous duct design; installed to the same carrier. Suggesting that numerical computations using reliable software (i.e. extensively validated against model-scale experiments, full-scale data or other works from the literature) prove to be extremely valuable to the design of similar projects.

Apart from ESDs, unconventional propeller geometries, such as the contracted tip-loaded (CLT) propellers and the highly skewed KAPPEL designs, have emerged through extensive experimental and numerical studies with an aim to produce blade geometries with enhanced efficiency and improved cavitation performance [25],[26] and [27]. Each concept has its own strengths and limitations, since compliance with design requirements and other aspects including cavitation mitigation, low acoustic noise, maximum efficiency, structural integrity, and various techno-economic factors are often contradictory to one another.

Particularly, CLT designs were motivated by the idea of tip-vortex-free propellers and are quite distinguishable from conventional geometries due to their substantial tip chord length and the large end-plates attached to the tip. End-plates follow the entire tip chord length and point toward the blade's pressure sides. These designs are typically unskewed, they introduce mechanical strength challenges and may be prone to certain types of cavitation, see, e.g. [28]. Traditional design methods may fail to produce CLT designs that outperform conventional blades, and therefore optimization-based methodologies may be more suitable for the preliminary design phase, as discussed in the recent work by Gaggero et al. 2016 [26]. In [26], a CLT propeller geometry is produced via an optimization process and is then studied in terms of open-water propeller performance, unsteady cavitation, and induced pressure pulses to highlight the advantages of CLT designs.

On the other hand, Danish engineer Jens Julius Kappel presented the KAPPEL propeller in the early 2000s after a long development process. It stands out from the CLT design in several ways. The blade tips are lifted and curved gradually towards the suction side of the propeller with a large amount of skew. In that sense, the blades are non-planar lifting surfaces, differing substantially from most conventional propellers. Successful designs of these unconventional propellers are proprietary or patented works, and consequently blade geometry data that is available in the literature for benchmarking is quite limited. However, some works reveal key aspects relating to the performance gains.

Sea trials with the conventional propeller and the KAPPEL propeller have been performed and have proved an efficiency gain of 4% in favor of the new propeller. The efficiency enhancement was attributed to lower propeller-induced pressure fluctuations as shown in [27]. In addition, the recent work by [29] investigates the effects of various tip-rake distributions on the performance of KAPPEL-like propellers in terms of propulsive performance and mitigation of cavitation phenomena, suggesting that a 2.5% performance enhancement is observed from the RANSE-CFD computations. Findings also indicate that an increase in tip-rake magnifies the low-pressure value and area on the suction side blade surface, which together with a phenomenon of the tip-vortex stretching and inhibition of wake vortex contraction, are beneficial to the elevation of propulsion efficiency.

1.2 Biomimetic thrusters

Lighthill's study on the hydro-mechanics of fish locomotion, written in the early 70's [30], is one of the earliest efforts in the field. Fish locomotion remains an active research field and still contains various unknown aspects. The abundance of evolutionary designs nature offers has not ceased to inspire propulsion solutions based on the detailed classification of biomimetic thrusters and appendages used

in autonomous underwater vehicles (AUVs) found in [31].

The combined efforts of experimental biologists and engineers through the years have identified some key aspects related to the performance of artificial propulsion systems, those mimicking fish-locomotion, see [32]. These are presented schematically in Figure 1.9. Key parameters include hydrodynamic shapes and morphology, fish-propulsion kinematics, sensory perception, advanced actuation, active and/or passive morphing, composite materials, and material property distribution. In addition, autonomous operation and adaptability are responsible for the fascinating abilities of aquatic swimmers.

Nowadays, engineering applications that mimic the mechanics of aquatic locomotion often use soft materials in manufacturing, advanced active actuation, and sensing to achieve a glimpse of the versatility and agility found in nature, see, e.g., [7], [8]. Flapping foils are popular for AUVs due to their advantages over rotary propellers,

- low-frequency operation,
- high thrust/power ratios,
- low drag on the switched-off position,
- superior maneuverability,
- acceptable cavitation characteristics,
- versatile operation, i.e., stabilizer and controller modes,

making them a well-suited propulsion system for small autonomous underwater vehicles (AUVs) designed for oceanic exploration, based on reviews the in Rozhdestvensky & Ryzov[4] and Shyy et al. [6].

The applications summarized in the recent review by Xing et al. 2023 [9] include flapping foils as ESD-retrofit solutions for sea-going vessels. *Thunniform* locomotion lies at the core of most flapping-foil system's operating principle; where thrust-producing kinematics are emulated using a superposition of out-of-phase heave and pitch motions.

Notable efforts on thrust-augmentation devices based on flapping foils for ocean going vessels include the experiments conducted by Bøckmann & Steen 2014 [33]. Fixed foils were mounted on the model vessel, shown in Figure 1.2 [left], and results show that wing hydrodynamic forces lead to a reduction of ship resistance by 9-17%, for the examined sea states; by suppressing ship heave and pitch motions in waves. Soon after, this idea led to the development of WAVEFOIL's modular bow-wing retrofit solution, shown in Figure 1.2, with several installations on medium-sized vessels operating in the North Sea.

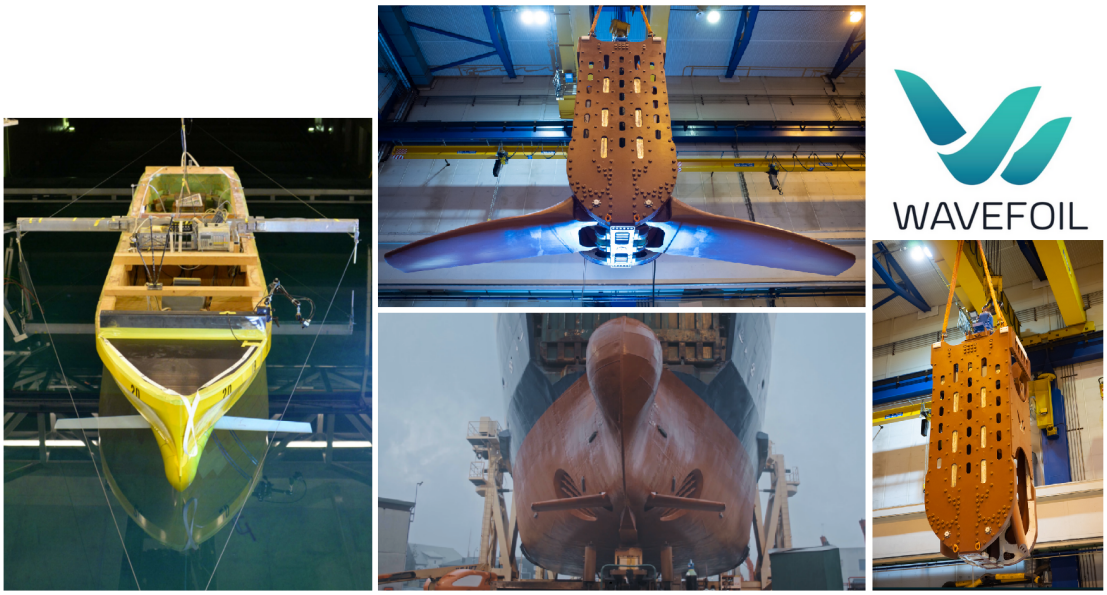

Figure 1.2: The tanker ship model with two fixed foils from the experiments conducted by Bøckmann & Steen 2014 [33] [left] and the modular technology solution developed by WAVEFOIL [right]

.

Recently, the EU-funded SeaTech consortium has developed two symbiotic ship engine and propulsion innovations, 'Next generation short-sea ship dual-fuel engine and propulsion retrofit technologies', that when combined, lead to a great increase of fuel efficiency and radical emission reductions (see also: https://seatech2020.eu/). Emphasis is given on future innovations that will be characterized by high retrofitability and maintainability, offering ship owners attractive return-on-investment due to resulting fuel and operational cost savings.

The proposed renewable-energy-based propulsion innovation consists of a dynamic wing mounted at the ship bow, resembling technologies already deployed as stabilizers, to augment ship propulsion in moderate and higher sea states, capturing wave energy, producing extra thrust, and damping ship motions. Project findings have been published in Belibassakis et al. 2022 [10], Ntouras et al. 2022 [11] and Bowker & Townsend 2022 [34]. Snapshots of the towing tests in calm water with and without the dynamic wing from [10] are shown in Figure 1.5. Figure 1.6 contains material from the experimental work conducted in Southampton model basin [34]. The completion of this EU-funded research project marks the deployment of large-scale dynamic wing devices on an ocean-going vessel to verify the enhancement of such a retrofit on the attained energy indices and the reduction of emissions. Similar works include [35] and [36].

In the context of unconventional propulsion systems, various configurations of flapping-foil thrusters were studied in the early 90s as alternatives for marine propellers, see, e.g., [9], [37]. The comprehensive experimental study conducted in Vermeiden et al. 2012 [38], which focused on the performance assessment of a newly developed flapping-wing propulsion system for seagoing vessels, achieved a remarkable 81% propulsive efficiency for the flapping propulsor at proper loading compared to 63% for the ship's screw-propeller at design point. The efficiency variations were measured at a higher Reynolds number $200,000$ by varying systematically loading, pitching amplitude, chord- length, chordwise flexibility and fin-spacing. Based on their observations, the flapping propulsor sweeps a larger area compared to a conventional propeller (i.e. $5-15\%$). A single-shaft flapping mechanism that was tested in their experiments is shown in Figure 1.7. This mechanisms allows for vertical/pitching oscillations, whereas tandem configurations of the device where found to increase the system's efficiency.

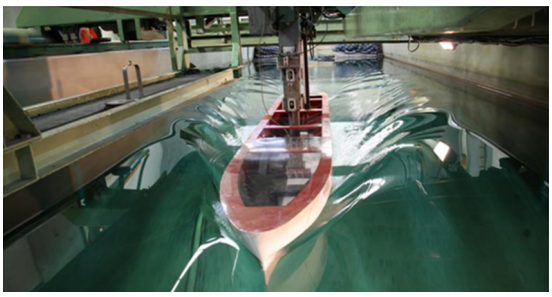

Figure 1.3: (a)

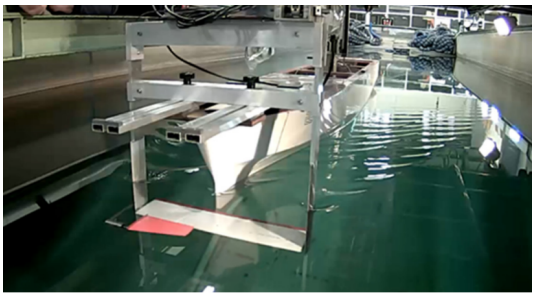

Figure 1.4: (b)

Figure 1.5: Tank tests of the hull model in calm water (a) without and (b) with the dynamic wing from Belibassakis et al. 2021 [39].

Cycloidal drive propulsion that also exploits flapping wing dynamics for thrust generation and maneuvering has reached a technological readiness level (TRL) that allows for larger-scale deployment targeting ocean going vessels. For instance, the innovative ABB Dynafin stand-alone propulsion system, shown in Figure 1.8, is an all electric propulsion concept that combines cycloidal propeller technology with bio-mimicry in terms of design and kinematics, to achieve higher efficiency compared to conventional shaft line configurations, suggesting that there is space in the industry for new propulsion solutions. Wings have leading edges with tubercles mimicking the fin morphology of Humpback whales.

The low-frequency operation of flapping thrusters leads to significantly lower underwater noise emissions, and proper tuning of kinematic, geometric, and structural parameters can yield high propulsion efficiency at low-speed cruising. However, installations of flapping-foil systems require a complete redesign of the hull

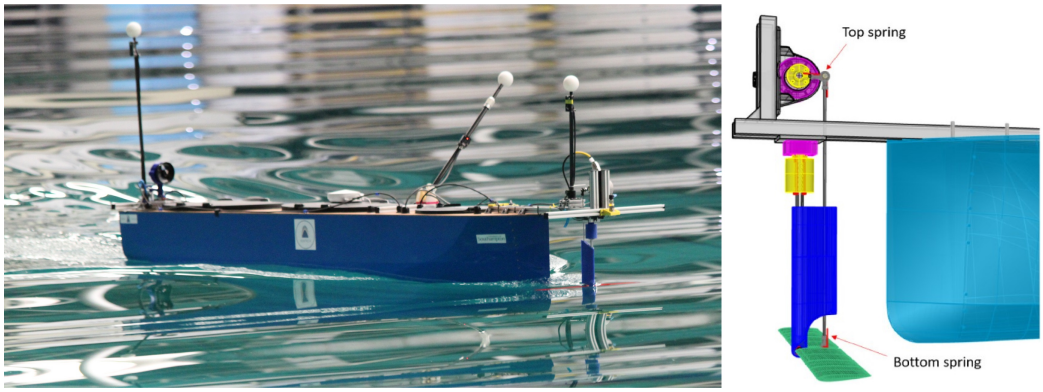

Figure 1.6: Free running generic cargo ship model with bow foil [left] and computer-aided design (CAD) rendering of the foil mechanism [right] from the experimental work in Bowker & Townsend 2022 [34].

lines at the stern and thus have not gained much popularity. Applications of flapping thrusters have been redirected towards their use as thrust-augmentation devices and ESDs with an emphasis on retrofit-ability and re-tractability.

Other applications of flapping foils include energy extraction of wave and tidal renewable resources, especially in coastal areas [40]. The mutual existence of waves with strong following, oblique or opposing currents at various nearshore places, which otherwise is characterized by quite a low wave potential, offers motivations for a comprehensive investigation of such resources and the development of hybrid technological devices, see, e.g., the analysis in [41] for a concept semi-activated oscillating hydrofoil device.

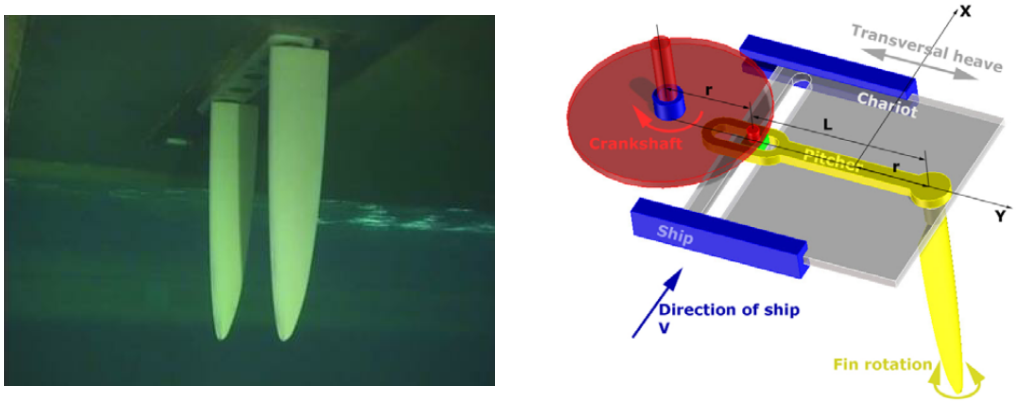

Figure 1.7: Schematic representation of the single-shaft flapping mechanism [right] and twin-foil configuration [left] tested experimentally in Vermeiden et al. 2012 [38] as a stand-alone propulsion system in tandem configurations.

Figure 1.8: ABB's Dynafin: An electric cycloidal propulsion system with aquatic-inspired blade design.

1.2.1 Thrust-producing kinematics

Fish swimming modes can be categorized based on morphological characteristics, kinematics, and locomotor behavior, [42] and [5]. Figure 1.10 contains a schematic representation of the four distinctive fish locomotion modes. Joint experimental and numerical research suggests that *thunninform* swimming, illustrated in Figure 1.11, is the most efficient. *Thunninform* swimming is a culminating point in the evolution of swimming designs, and we encounter it among varied groups of vertebrates (teleost fish, sharks, and marine mammals), which have evolved, astonishingly, under different circumstances.

This highly efficient method of swimming attracts attention due to its potential to provide artificial systems with superior propulsion characteristics compared to other vehicles equipped with conventional propellers. The robotic fish 'RoboTuna' shown in Figure 1.12 was developed initially by Barret [43], [44] in MIT, was shaped after an actual tuna and combined oscillating foil/tail movements with *carangiform* body kinematics. This prototype, that continued to be built upon years on, showcased all the advantages of bio-inspired thrusters for autonomous underwater vehicle (AUV) propulsion. Mean propulsive efficiencies as high as 91% have been reported for the RoboTuna [42], based on the optimal body motions deduced from an optimization study using genetic algorithms. Its success spawned further work in the area of swimming robots [8].

Typically, *thunninform* bio-inspired thrusters consist of a relatively stiff caudal fin; shaped like a tapered hydrofoil with moderate sweep-back, curved leading edge and sharp trailing edge. Fish et al. [45] provides abundant information on cetacean fluke morphology. The thruster traces an oscillating path, propelling the AUV forward, that is characterized by a peak-to-peak amplitude, a tail-beat frequency and a wavelength. This combination of out-of-phase heave/pitch produces the thrust-producing trajectory shown in Figure 1.11.

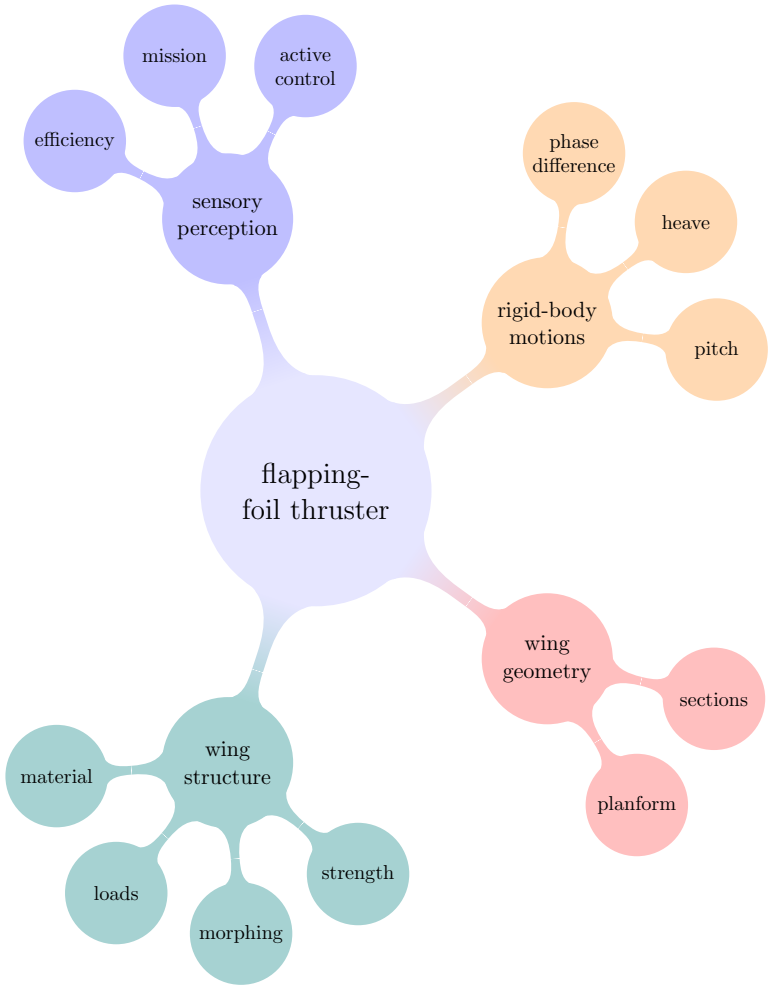

Figure 1.9: Important aspects for the design of bio-inspired flapping thrusters.

In most engineering applications and experimental works, harmonic functions are used for heave and pitch motions,

$$y(t) = A_y \sin(2\pi f t), \tag{1.1}$$

$$\theta(t) = A_\theta \sin(2\pi f t + \phi_\theta). \tag{1.2}$$

Esfahani et al. [46]-[47] used CFD to study the effects of other non-harmonic fish-inspired trajectories on the propulsive efficiency of flapping foils, with encouraging results.

The main factors determining the relative contributions of momentum transfer mechanisms to thrust and resistance are 1) Reynolds number, 2) reduced frequency, and 3) shape. Reynolds number Re is defined as the ratio of inertial and viscous

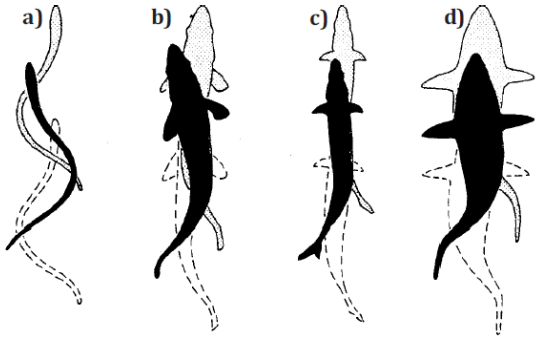

Figure 1.10: Body/caudal fin propulsion swimming modes from primitive to derived: (a) *anguilliform*, (b) *sub-carangiform*, (c) *caragiform* and (d) *thunninform*, adapted from Sfakiotakis et al. 1999 [42].

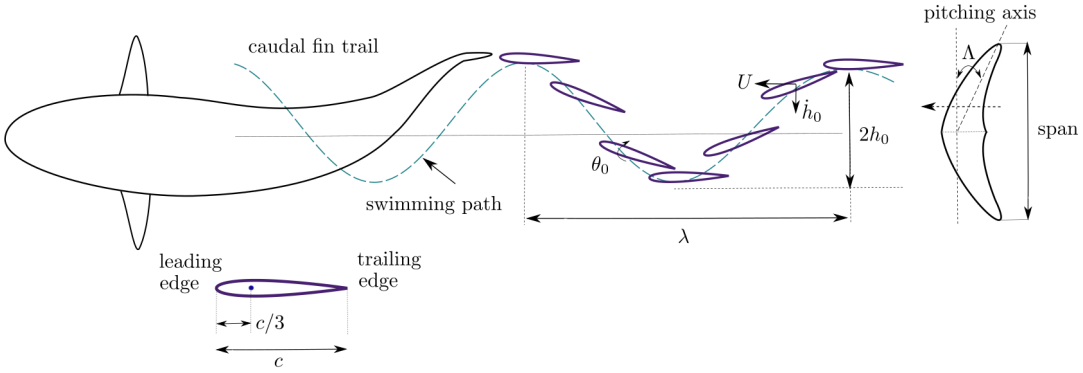

Figure 1.11: Schematic representation of the *thunniform* swimming mode.

forces,

$$Re = \frac{LU}{\nu}, \tag{1.3}$$

where L is a characteristic length, U is the swimming velocity, and ν is the kinematic viscosity of water. The reduced frequency k indicates the importance of unsteady (time-dependent) effects in the flow and is defined as

$$k = 2\pi \frac{fL}{U}, \tag{1.4}$$

where f is the oscillation frequency, L is the characteristic length, and U is the swimming velocity. In some works, the Strouhal number, defined as

$$St = \frac{2fA_y}{U}, \tag{1.5}$$

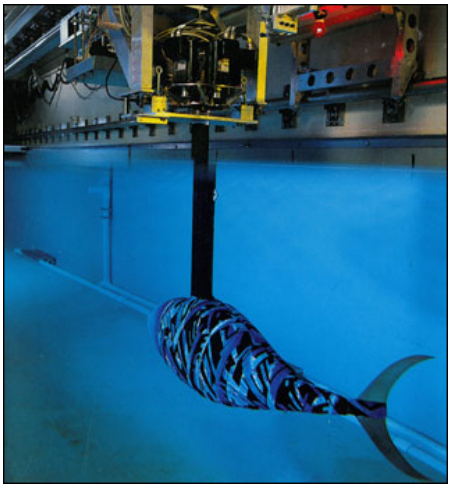

Figure 1.12: Built to simulate the action of a fish, RoboTuna metallic prototype in MIT towing tank basin; courtesy of Sam Ogden.

is used alternatively as a measure of unsteadiness, with A_y denoting the peak-to-peak amplitude.

Froude efficiency, namely swimming efficiency, is defined as,

$$\eta = \frac{\langle T \rangle U}{\langle P \rangle}, \tag{1.6}$$

where U is the mean forward velocity, $\langle T \rangle$ is the time-averaged produced thrust, and $\langle P \rangle$ power is required to sustain the prescribed motion of the device. Thrust production efficiency of oscillating foils is maximized for Strouhal numbers $0.25 - 0.35$, based on the experiments of Triantafyllou et al. 1991 [48] in the early 90's. A summary of experimental biologist's observations published in [49] reveals that Strouhal numbers in nature lie between $0.2 - 0.4$, which is indeed an extraordinary finding.

Experiments revealing the hydro-mechanics of fish-like propulsion

Notably, many of the pioneering experimental works on thrust-producing oscillating foils were conducted at MIT focus and focused on investigating the hydro-mechanics of fish-like propulsion, see [49],[50], [51] and [52]. The examined wings are made of stiff materials and performed a combination of harmonic heave and pitch motions that yielded thrust-producing effective angle of attack profiles. A characteristic experimental configuration in shown in Figure 1.13 related to the work in [50]. In the review by Triantafyllou et al. [53], fluid mechanics-based scaling laws are derived on theoretical, numerical, and experimental grounds, provid-

ing valuable directions for assessing artificial flapping-foil systems. Recent experimental studies concerning rigid flapping foils focus on unsteady motion analysis, characterization of large-scale vortex structures, and investigation of tandem foil configurations, see [54].

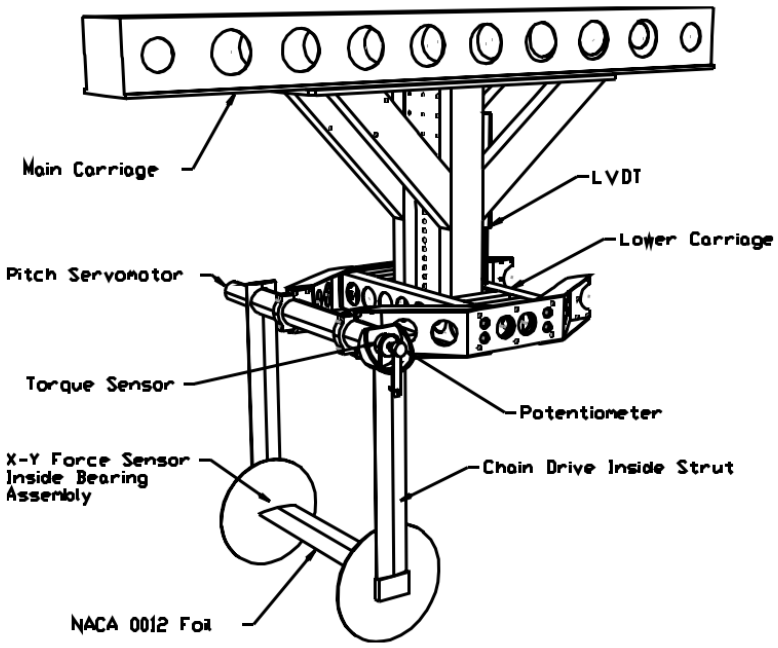

Figure 1.13: View of the test carriage used in the experiments by Read et al. [50], which oscillates the foil in flapping motion while moving horizontally in the towing tank.

Numerical models for hydrodynamics

Depending on the application, numerical models facilitate the analysis of various wing configurations and, when used alongside experiments, provide a better understanding of the system's hydro-mechanics. Ideal-flow-based models are a cost-effective alternative to CFD; enabling fast simulations and achieving engineering accuracy for hydrodynamic load predictions. Their applicability covers 3D, unsteady hydrodynamic simulations on general planform shapes assuming attached flow conditions.

Historically, models based on Prantl's lifting line theory were the first to be developed for lift predictions on large aspect ratio wings. Extensions of lifting line theory allow for unsteady simulations and consideration of curved planform shapes; as discussed in the recent works of Bird et al. 2020 [55] and Reid 2020

[56], respectively. In the follow-up work by Bird et al. 2020 [57], extreme benchmark cases for the unsteady lifting line theory (ULLT); involving large-amplitude kinematics at low Reynolds numbers, are examined and compared against experimentally validated CFD simulations for $Re = 10,000$. The findings emphasize on the applicability of ideal-flow models and their extremely low computational cost.

Then, models based on lifting surface theory emerged to improve lift and induced-drag predictions on small aspect ratio wings. The earliest works treated lifting flows around arbitrary 3D bodies for aerodynamic applications [58], and later, the works of notable scientists such as [59], [60] covered the lack of comprehensive text for boundary element methods (BEM). The BEM is still used today due to the advantages it holds over other popular numerical methods, with applications not only limited to lifting-flow problems, see, e.g., [61], [39], [62], [63]. These advantages are:

- Dimensionality reduction, i.e., discretization schemes are implemented only on the boundary, and thus approximate solutions to the 3D problem are equivalent to the determination of unknowns on the specified 2D boundary. Weak formulation.
- Straightforward handling of unbounded domain problems; in case closed boundaries are contained, all flow generated information satisfies the infinity condition by construction.
- Analytical or semi-analytical calculation of integral terms significantly reduces the computational cost.
- For lifting flow problems, the boundary values of the initially unknown potential field and its derivative contain all the physical information required to evaluate pressure and velocity on the whole domain.
- Solution of the corresponding initial boundary value problem yields the boundary values of the potential field and its derivative.

The accuracy of hydrodynamic load predictions, as obtained using ideal-flow models, can improve further without considerably increasing the computational cost, through viscous corrections based on empirical formulas.

In addition, an extension of such boundary element models allows the study of intricate wing geometries with morphing capabilities (i.e., active & passive wing shape modification) and their effect on the hydro-mechanics of propulsion with low computational cost compared to solvers that require meshing on the whole domain, such as computational fluid dynamics or finite elements. The motivation for using these tools comes from the fact that studies of flapping thrusters with bio-mimetic features have the potential to inspire future technological solutions that are environmentally friendly and have enhanced efficiency.

1.2.2 Wing geometry

The work by Fish et al. 1998 [45] provides abundant inspiration regarding the morphology of cetacean flukes. Wing geometry is also closely related to wing performance. The non-dimensional aspect ratio (AR) is one measure used to correlate a wing planform to its performance. By definition, the aspect ratio equals the square of the wingspan divided by the wing area. For a rectangular wing, it holds that $AR = s^2/(sc)$, where c is the chord length at the root and s is the span. Regarding planform shapes, a simple parameterization consisting of the sweep angle Λ and the taper ratio $\lambda_r = c_t/c_r$, i.e., defined as the ratio of tip chord c_t to root chord c_r, are two parameters that can be used to define various wing configurations, as discussed in [59]. This representation, shown in Figure 1.14, is also followed in the present work for its simplicity and close resemblance to cetacean fluke shapes.

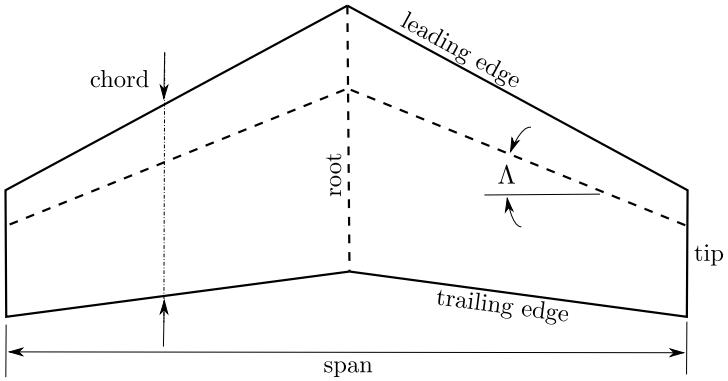

Figure 1.14: Nomenclature for planform parameterization based on taper ratio and sweep.

However, fins in nature have more complex shapes with variable chord lengths and noticeable variations along the span, as discussed in [64] and [32]. Aspect ratio is also a measure of agility and maneuverability for both artificial and natural swimmers (or fliers), with smaller values, for instance, $AR < 3$, suggesting advanced maneuverability and higher values $AR > 5$ observed on wings with excellent steady-state forward flight capabilities.

In addition, fins found in nature may also exhibit intricate morphology in the leading edge region, which affects the wing's overall performance [65], [66]. The humpback whale pectoral fins, with their distinct tubercle leading edge (TLE), shown in Figure 1.17, are an excellent example of a mechanism for delaying and restricting span-wise separation, tonal noise, and dynamic stall at high effective angles of attack. Tubercles serve as vortex generators; suppressing flow separation and improving maneuvering, as observed experimentally in [67], [68] and [69].

These findings have recently motivated the design of tidal turbine blades with tubercle leading edge [70] and novel appendages for yachts, such as the Club Swan 50 twin-rudder concept. A hub-less thruster for the yachting sector inspired from humpback whales has been developed by BlueNav [71], featuring tubercle-inspired tip and striations along blade body as shown in Figure 1.17. Also, from the neighboring field of aeronautics, the review [65] and experimental study [67] discuss similar findings. Some prototypes for small aerial vehicles with TLE wings have also emerged [72].

Figure 1.15: (a)

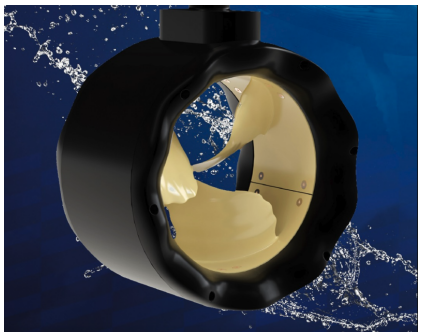

Figure 1.16: (b)

Figure 1.17: (a) Humpback whale pectoral fins with tubercles and (b) BlueNav hub-less thruster featuring tubercle-inspired tips and striations on blade body [71].

1.2.3 Passively morphing wings

Fins found in nature are deformable and can adapt to hydrodynamic load excitation; exploiting intrinsic musculature that allows for active shape control. These observations drastically open the 'shape' space compared to the analysis and design of non-deforming wings. Many publications focus on the effects of flexibility on the performance of flapping thrusters, supporting the development of artificial swimming robots using new materials and advanced actuation. A summary of notable experimental and numerical works follows in Tables 1.1 and 1.2.

Experimental studies

The findings from Prempraneerach et al. 2003 [73] suggest that properly selected chord-wise flexibility can significantly enhance the propulsive efficiency of flapping thrusters, even up to 36%, compared to rigid foils with the penalty of a small loss in thrust. They also introduced a non-dimensional flexibility parameter to derive a scaling law for flexibility effects. Indications that properly selected material

properties enhance the performance are also present in Heathcote et al. 2004 [74] experiments for purely heaving foils.

Heathcote et al. 2008 [75] note that the range for which Strouhal numbers are beneficial for the efficiency overlaps with the range of Strouhal numbers $0.2 - 0.4$ found in nature.

Efficiency maximization can also be correlated with resonance effects and modal analysis. In Paraz et al. 2014 [76], response curves representing the relative thin plate tip amplitude with respect to the forcing frequency, exhibit peaks of resonance for the natural modes of the purely heaving plate in the flow. Additionally, for plates with uniform material properties, flexural rigidity within the examined range has only minor effects on the response curves, when the forcing frequency is normalized with the first natural mode. However, forcing amplitude significantly affects the response indicating strongly nonlinear behavior, which needs to be taken into consideration for the development of fluid structure interaction (FSI) models.

In the experiments from Richards et al. 2015 [77], it was observed that maximum efficiency occurs at a frequency ratio resulting in both a beneficial phasing of the deformation, with respect to the drive motion, and the maximum deflection. Flapping (i.e. heave and pitch) kinematics were shown to increase the efficiency while reducing the thrust, compared to a purely heaving study case. In addition, an increase of the forcing amplitude, corresponding to the drive motion, was found to cause the frequency ratio, providing maximum efficiency, to shift toward lower values.

Kancharala et al. 2016 [78] performed water tunnel experiments on real and fabricated caudal fins, to investigate effects of stiffness variation on thrust and efficiency. The fabricated fins were constructed using carbon fiber reinforced composites (CFRC) using various layer scheme configurations; mimicking stiffness measurements (i.e., in the sense of EI) obtained from real fish fins (trout, red/vermilion snapper). The findings suggest that the self-propelled flapping fin prototypes based on bio-inspired stiffness variation outperformed the ones corresponding to a constant layer scheme resulting in uniform EI stiffness. It was also observed that optimal selection of the stiffness variation profile produces greater thrust and enhances the propulsive efficiency.

The experimental work by Quinn et al. 2015 [79] stands out since it addresses the problem of efficiency maximization for the case of flexible thrusters experimentally. In their study, a simple gradient-based optimization approach is shown to lead to significant improvement in the efficiency of a flexible plate with Young's modulus $E = 3.9GPa$. Some of the design variables considered include the Strouhal number, heaving amplitude, and maximum pitch angle. The multi-dimensionality and multi-modality of the efficiency space revealed, via the

experiments, that flexible propulsors are prime candidates for optimization routines.

Theoretical models

Some experimental works also address the applicability of theoretical models to the prediction of flexible-foil resonance phenomena and structural response in joint frameworks that allow for the validation of the proposed models via comparisons against the available measurements. For instance, in Alben et al. 2012 [89], the self-propulsion water tunnel experiments at $Re = 10^3 - 10^5$ on purely heaving flexible panels serve as the basis for theoretical model verification. They propose a 2D model that consists of an in-extensible elastic equation *strongly coupled* with inviscid thin-airfoil theory. A good agreement between the model and experimental measurements is observed in terms of (i) deformed shape/ wavelength predictions and (ii) dependence of swimming speed on foil length, rigidity, and the corresponding flows. It is noted that 3D effects are significant, however the model is sufficient for scaling law derivation in this context.

In Quinn et al. 2014 [83], the small deflection of the examined heaving flexible panel is modeled using the Euler-Bernoulli beam equation. The solution of the equation is expressed using modal decomposition, and the natural modes are correlated with the deformed shapes of the flexible panels obtained from the experiments. Four constant-thickness panels with different flexural rigidities were examined, to account for flexibility effects. Emphasis is given to resonance phenomena and efficiency peaks. It was observed that as the heaving frequency increases, higher modes are actuated. Flexibility affects the frequency at which resonance peaks are observed.

Modal analysis based on the Euler-Bernoulli beam equation is also considered in Paraz et al. 2016 [90]. The experimental setup in [90] consists of a flexible panel actuated at the leading edge, with end-plates restricting 3D flow phenomena. The beam equation is coupled with unsteady airfoil theory to formulate a *weakly nonlinear* model. Hydrodynamic pressure is based on Theodorsen's theory. The model can produce acceptable predictions in terms of the tip response amplitude as a function of forcing frequency over a range that includes the first two resonance peaks for the coupled system. Damping terms are added to the linear model equations in order to improve numerical predictions. Their findings also suggest that nonlinearities and 3D effects should be taken into account through numerical simulations to enable predictions for wings with moderate/small aspect ratios, which are typically found in nature.

Even though CFD simulations are gaining ground in the field, recent works that tackle the FSI problem using analytic approaches still provide valuable insight. A great example is the analytical model from Fernandez-Feria & Alaminos-Quesada

Table 1.1: Experimental investigation of flexibility effect on the propulsive efficiency of flapping thrusters.

Authors	Medium	Inflow	Kinematics	Flow	Structural info	Geometry	Study
Prempraneerach et al. 2003 [73]	fresh water	yes	heave/pitch, St=0.1-0.45, Re=4E-4	2D, end plates	urethane rubber, E=0.3-5E-5 Pa	NACA 0014	AoA profiles
Heathcote et al. 2004 [74]	air	no	heave	3D	steel plates, constant thickness	airfoil/plate combination	tip-response, thrust/efficiency
Heathcote et al. 2007 [80]	fresh water	0-0.45m/s	heave, Re=9,000-27,000	3D	steel plates, constant thickness	airfoil/plate combination	tip-response, thrust/efficiency
Heathcote et al. 2008 [75]	fresh water	yes	heave, Re=10,000-30,000	3D	PDMS foil with $1mm$ sheet core (steel/aluminium)	NACA 0012	spanwise flexibility
Riggs et al. 2010 [81]	fresh water	no	pitch	3D	rubber	bio-inpired thickness, NACA 0012	thrust/efficiency
Barannyk et al. 2012 [82]	fresh water	0.22m/s	heave/pitch	3D, free surface	acrylic (0.0420-3.30GPa), PDMS (flexible)	flat plate (rigid/flexible part)	thrust/efficiency
Quinn et al. 2014 [83]	fresh water	yes	heave, Re=7,800-46,800	3D	$\{82, 1.7, 3.8\}GPa$	flat plate	modal analysis, thrust/efficiency
Paraz et al. 2014 [76]	fresh water	yes	heave, Re=12,000	2D	$\{0.018, 0.028\}Nm$	flat plate	tip response, resonance

Table 1.2: Experimental investigation of flexibility effect on the propulsive efficiency of flapping thrusters.

Authors	Medium	Inflow	Kinematics	Flow	Structural info	Geometry	Study
Moored et al. 2014 [84]	fresh water	0.06m/s	pitch	3D	EI=4.2E-4 up to 1.1E-2 Nm^2	flat plate	vorticity field, wake patterns, cfd
Cleaver et al. 2014 [85]	fresh water	0.43m/s	pitch, Re=30,000	2D end-plate	stainless steel, aluminum, polyester, vinyl	NACA 0012/flexible TE	tip response, drag reduction
Richards et al. 2015 [77]	fresh water	yes	heave/pitch	3D	steel sheet core/silicone rubber foil	plate, rounded-LE	thrust/efficiency
Iverson et al. 2019 [86]	fresh water	yes	heave/pitch, Re=80,000	3D	steel sheet core/silicone rubber foil	plate, rounded-LE	flow patterns, shed vorticity, chordwise flexibility
Lucas et al. 2015 [87]	fresh water	self-propulsion	heave/pitch, Re=21,000-115,000 St=0.20-0.25	3D	segmented	plate	non-uniform stiffness
Kancharala et al. 2016 [78]	fresh water	self-propulsion	heave/pitch	3D	carbon fiber composite	plate	varying EI, layer optimization
Pratz et al. 2017 [88]	fresh water	yes	pitch, Re=9,250	3D	EI=1.12-7.4E-3Nm^2	teardrop TE/plate	flow patterns, hydrodynamic forces

2021 [91]. In the theoretical models presented previously, the foil is actuated at the leading edge, whereas in [91] a framework for the analysis of a thin flexible foil that undergoes prescribed heaving/pitching motions about any pivot location is presented. The model is based on linear potential flow and the Euler-Bernoulli beam equation using a quartic approximation for the deflection. This allows for the analytic calculation of the deformation amplitude, thrust force, input power, and propulsive efficiency in terms of stiffness, mass ratio, frequency, pivot location, and kinematic parameters.

In the follow-up work by Sanmiguel-Roja & Fernandez-Feria 2021, [92], linear theory predictions are compared against cfd results, for purely plunging flexible foils, illustrating that the analytical model is a reliable and useful guide for the design of underwater flexible flapping-foil thrusters. In addition, a practical chart that relates the optimal flapping frequency to the actuation point, the stiffness, and the mass ratios of the hydrofoil is provided.

Numerical models

Experimental works serve as a database for validating new computational tools that are on the surge and suggest that the response of flexible thrusters is non-linear, meaning that passive deformations affect the hydrodynamic force excitation and vice-versa. In that sense, coupling methodologies are required for numerical models to capture this FSI problem. From low-order methods, see, e.g., [63], [93], to higher-fidelity simulations such as [94] and [94], researchers have been able to predict the response of wings under hydrodynamic and inertial excitation with inspiring results, see, e.g., a summary in Table 1.3. The structural models used range from beams, plates/shells, and solids, whereas the numerical study of passively deforming oscillating foils also requires reformulating computational fluid dynamics models.

Coupling can either be *weak* or *strong*, depending on whether iterative schemes are employed to solve the problem. Strong coupling requires the use of iterative methods that tackle non-linear equations. Depending on the problem formulation, the coupling can also be considered *monolithic* or *partitioned*. Partitioned approaches use separate numerical tools and couple them through information exchange along their boundaries, see, e.g.,[63],[94]. In a strongly coupled/partitioned scheme, the loads and movements for each physical time step are transmitted between the computational programs, enabling all non-linear contributions from the hydro- and structural dynamics. In weak/partitioned coupling, information is exchanged between the fluid/structure boundaries once per time step, as discussed in [95]. On the other hand, monolithic coupling tackles the full set of equations and requires tailor-made mathematical formulations for each problem setup, which is rare for works on passively deforming hydrofoils.

What type of coupling should we use for our FSI? The appropriate methodology depends on the density of the fluid medium. Daniel et al. 2002 [96] suggest that for the case of passively morphing wings immersed in high-density fluids, such as water, accurate predictions of the wing's response require a solution to the complete (full) set of equations coupling fluid and solid dynamics. This argument is also supported by Zhu 2007 [63]. On the other hand, studies of animal flight show that weak (or loose) coupling may suffice for many aero-elastic applications.

Table 1.3: Numerical works on FSI for passively morphing wing thrusters.

Authors	Fluid	Structure	Coupling
Zhu 2007 [63]	potential (BEM)	thin plate, uniform material, rectangular (FDM)	strong, partitioned
Zhu and Shoele 2008 [93]	potential (BEM)	Euler-Bernoulli beams (FDM), fish planform, skeleton-strengthened fin	strong, partitioned
Dai et al. 2012 [97]	viscous (CFD)	plate with frame, homogeneous (FEM)	strong, partitioned
Ducoin and Young 2013 [95]	viscous (CFD)	2-dof bend/twist, rectangular wing (FEM)	weak, partitioned
Liao et al. 2019 [98]	viscous (CFD)	solid (FEM), composite (CFRP) cantilevered wing	weak, partitioned
Luo et al. 2020 [94]	viscous (CFD)	solid, fin, non-uniform stiffness (CalculiX FEM, brick elements)	strong, partitioned (preCISE)
Wang at al. 2020 [99]	viscous, shear flow (LBM)	plate, large-deformations (FEM, DKT)	strong, partitioned

1.2.4 Flexible propulsors with enhanced performance

Flexible propulsors may be prime candidates for optimization routines, however, hydro-structural optimization remains a challenging field of research due to its multi-disciplinary nature. Notable works include Wills et al. 2007 [100], where a computational framework that exploits models with different geometric and physical fidelity levels for designing high-performance flexible aerial vehicle wings is proposed. For the fluid-structure interaction (FSI) problem, they used an unsteady lifting-line formulation in conjunction with beam models for the wing surfaces. This framework is suitable for both direct and inverse wing design problems.

In their work, Garg et al. 2017 [101] discuss the importance of high-fidelity FSI simulations and multi point optimization for the design of flexible hydrofoils with optimal performance. The optimization problem involves the minimization of hydrofoil drag-coefficient under constraints, including cavitation suppression. The hydro-structural solver consists of a 3D nearly incompressible Reynolds-averaged Navier–Stokes equations (RANSE) solver strongly coupled with a 3D structural finite-elements. The structure is a solid homogeneous isotropic material with a linear elastic response, and the use of adjoint optimization makes the cost of gradient calculation nearly independent of the total number of the structural design variables. Experimental verification of the optimal hydrofoil is performed in their follow up work [102] with great results. By enriching the structural model to account for fiber orientation effects (CFRP), Liao et al. 2021 [103] designed a cavitation-free wing with minimum drag using a high-fidelity computational tool for the FSI problem and adjoint-based optimization. Their findings suggest that an optimal selection of fiber angle balances the bend-twist coupling and modifies the directional strength to reduce the susceptibility to excessive deformation and material failure for wings with a sweep angle.

The above works suggest that a lower-fidelity method that tackles the fully coupled FSI problem can become instrumental both in terms of predicting the hydro-elastic response of flexible fins but also by enabling the cost-effective hydro-structural optimization of flexible wings, taking into account stiffness variability, wing planform shape, unsteady hydrodynamic loading, and kinematic parameters. The development of an FSI tool, combined with optimization at a cost-effective level, lies at the core of this dissertation. Research on this field fills in the gap and advances the scarcity of these models in the literature, see Table 1.3. Chapters 2, 3, and 4 of the present contain material related to the computational tools that were developed for this purpose; with emphasis on leading to the fully coupled *FlexWing3D* solver that is introduced in this work. The solutions to optimization problems arising from the optimal tuning of geometric, kinematic, and stiffness properties of flexible flapping foils, with a focus on performance maximization, are addressed using a gradient-based method, sequential-quadratic programming algorithm that is suitable for handling nonlinear constraints, and also is part of many standard libraries for optimization. Sensitivity calculations are performed for simplicity using standard finite difference schemes.

1.3 Hydrofoil cavitation

Cavitation is a multi-phase phenomenon defined by the appearance of vapor cavities inside an initially homogeneous liquid medium, which occurs in different situations depending on the flow configuration and the physical properties of the fluid

itself, as discussed in Franc & Mickel 2006 [104]. The liquid medium breaks down in the low-pressure region of lifting surfaces, such as the suction sides of propeller blades and hydrofoils. These vapor structures tend to disturb and modify the basic flow around the lifting surface as they develop, resulting in adverse effects such as induced noise, vibration, structural failure, and a drop in performance, see Carlton 2018 [105].

Extensive experimental work allows the physical aspects of the many forms of cavitation to be understood and essentially contributes to the formation of an accurate database for validating computational methods, i.e., [106], [107], [108] and [109]. Multi-phase flow CFD has become increasingly popular in the last several years and enables researchers to gain further insight into the physical mechanisms driving cavitation phenomena. Some of these works include numerical methods developed to predict specific forms of cavitation, such as partial or sheet cavitation [110], cloud cavitation [111], [112] and [113], super-cavitation [114] and tip-vortex cavitation [115] and [116]. In Ji et al. [117], emphasis is given to the cavitation shedding dynamics evolution and the cavitation-vortex interaction using Large Eddy Simulation (LES) coupled with a homogeneous cavitation model, and the analysis of pressure fluctuations and the transition from attached sheet to cloud cavitation. Another interesting multi-scale Eulerian-Lagrangian approach for simulating a cavitating turbulent flow around the Clark-Y hydrofoils is presented in Wang et al. 2021 [118], where results of bubble dynamics analysis are also provided.

Certain cavitation forms, such as partial or sheet cavitation, can be predicted with acceptable accuracy using lower fidelity methods in the context of viscid-inviscid models, see, e.g., [119] and [120] or purely potential-based methodologies, see, e.g., Bal et al. 2001 [121]. Literature shows that the main points in partial cavitation simulations are the cavity detachment position tuning and the wake modeling downstream of the cavity [120]. Mass transfer between water vapor and the water generates unsteadiness and instabilities in the wake downstream of the attached cavity, which is characterized by a two-phase turbulent zone based on the discussions in [117], [120]. This zone is perturbed moderately in certain flow configurations, for which a steady solution is possible. In this case, numerical results obtained with viscous models for the attached cavity region agree quite satisfactorily with experimental observations. Moreover, an attached cavity would develop from a sharp leading edge, and in the case of a smoother leading edge, the cavity would detach at a point downstream of the laminar boundary-layer separation point Celik et al. [122].

Despite neglecting viscosity phenomena, purely potential-based methods yield acceptable results if they are used in conjunction with a cavity termination model to bring numerical results closer to validated CFD simulations or experimental

data, see, e.g., the discussion in Celik et al. 2014 [122]. Particularly in potential-based methods, the solver is used in conjunction with a geometric criterion to determine the initially unknown shape of the cavity, modeled as a free streamline. Problem unknowns can include either the cavity length or the cavitation number, depending on the problem setup. In cases where the cavitation number is considered known, an iterative scheme is employed to locate the cavity surface and determine its length, until the exact boundary conditions are satisfied on all portions of the foil/cavity and free surface boundaries.

Lower-fidelity methods remain a valuable tool in the prediction of cavitation phenomena. Some advantages include their low computational cost and the "natural" boundary conditions imposed in potential-based formulations. Higher-fidelity models often require careful tuning of various parameters to yield accurate results; see, e.g., the work by Lee et al. 2021 [123] for marine propeller cavitation. On the other hand, potential-based methodologies are suitable for the early stages of lifting surface design and analysis, with simulations performed on personal computers instead of high-performance computing resources. These methodologies also provide the basis for fast extensible algorithms capable of addressing multi-disciplinary problems, such as the effects of unsteady partial cavitation on the hydro-elastic stability of a two-degree-freedom hydrofoil [124].

1.3.1 Free-surface effects

Hydrofoil performance during operation in proximity to the free surface is of utmost importance for the stability and performance of foiling yachts and crafts. The lift generated by hydrofoil appendages raises the hull and reduces the crafts' wetted surface [125]. Consequently, a significant reduction in resistance is achieved, allowing for high-speed cruising of the craft at fuel efficiency. Moreover, the interaction of water waves with varying currents is essential for the design and development of flapping-foil systems for the exploitation of marine renewable energy resources, see e.g., [41] and the detailed reviews in Xiao & Zhu 2014 [40], Xing & Yang 2023 [9], especially if these devices are to be mounted onto sea-going vessels, Filippas & Belibassakis 2022 [12], Ntouras et al. 2022 [126]. These suggest that the physics behind hydrofoil performance at low submergence needs to be addressed for engineering applications.

Experimental work on submerged lift-producing hydrofoils is rather limited, and historically one of the first experiments conducted by Duncan 1983 [127] back in 1983, on a NACA 0012 hydrofoil at a $5deg$ angle of attack for different submergence depths with an aim to study the induced free surface waves and the associated breaking and non-breaking wave resistance, still serves as a standard verification case for emerging numerical methods. Applications of flapping-foil energy extraction devices have led to an increase in experimental analysis on the

matter, see, e.g., Barranyk et al. 2012 [128] where a flexible oscillating plate is studied experimentally as an energy extraction device at different depths of submergence, and even though the operation principle, between flow energy converters and hydrofoil craft appendages, differs, such works can also serve as validation cases for numerical models.

Regarding the study of hydrofoils beneath the free surface, potential-based methods remain popular for this type of analysis, see, e.g., the 3D method introduced in Filippas & Belibassakis [129], [12], and continue to emerge, i.e., for instance the recent 2D model in Chen 2012 [130] where, due to the cost-effective nature of the models and their accuracy in predictions. However, their applicability is limited to cases without wave breaking and where submergence depths remain moderate, typically up to $h/c \leq 1.0$, with h denoting submergence depth and c hydrofoil chord.

Viscous solvers are extensively used in predicting hydrodynamic loading on submerged hydrofoils. For instance we address two recent works in these topics. Pernod et al. 2023 [131] performed numerical simulations based on unsteady RANSE and confirm that at high proximity to the free surface, i.e., $h < 0.5c$, significant modification of the pressure field around the foil is evident, and even the lift is swapped to downward, highlighting the importance of considering the effect of finite submergence to compute foils' hydrodynamic forces. Moreover, in Petikidis & Papadakis 2023 [132], where the performance of a fully passive flapping foil device for energy harvesting in a free surface flow is examined via CFD simulations, it was shown that regular waves with a frequency close to the natural mode of the device aided energy harvesting.

However, when it comes to modeling the performance of hydrofoils operating beneath the free surface under cavitation regimes, the relevant works in the literature are limited. Notable works based on multi-phase flow CFD include [133], [134], and [135]. Regarding computational tools based on purely potential methods, i.e., Faltinsen & Semenov 2008 [136] and Bal et al. 2001 [121] are also characteristic.

Compared to higher-fidelity solvers, potential-based methods can treat the effects of a free surface on lifting surfaces operating in finite submergence depth along with certain cavitation phenomena concurrently with relatively low additional computational costs. Therefore, to further investigate this topic, which is relevant to the operation of hydrofoils, the present work addresses the problem of partially cavitating hydrofoils moving steadily under a free surface via an inverse problem formulation based on ideal flow assumptions.

1.3.2 Sensitivity calculation via the adjoint-method

Within the thesis context, and addressing the topic of partially cavitating hydrofoils operating beneath the free surface that is relevant to the preliminary design of

flapping foils, we introduce a mathematical model based on ideal-flow theory and inverse design (ID) for hydrofoils in 2D domains. The objective function follows the assumption of constant pressure on the cavity boundary, i.e., typical for cavitation prediction ideal-flow solvers. Upon solution of the optimization problem, the strengths of velocity potential on the hydrofoil (including the attached cavity) and the linearized free-surface boundaries are determined, along with the shape of attached cavity, dictated by the objective function. Hydrofoil/cavity boundary parameterization tool uses B-splines and the coordinates of control points included in the design variable vector [137]. Upon solution of the optimization problem, given the attached cavity extent, the cavitation number and cavity shape are determined.

For the optimization problem solution, we used a gradient-based algorithm with sensitivity derivative estimates obtained using the continuous adjoint method. The adjoint method is very cost-effective, especially for large numbers of design variables, compared to the number of objective functions (i.e., in our case, only one objective function is considered), as it requires only two solver evaluations per optimization cycle to produce the sensitivity derivative estimates for each design variable. The primary and adjoint boundary value problems are solved numerically at each optimization cycle using the source/vorticity BEM solver based on [58], [59].

This research example, contained in Chapter 5 of the present, revealed insightful aspects of continuous adjoint-based boundary element methods. The developed computational tool *PCavPreMod* is validated against comparison with other works and experimental data, constituting a new methodology for partial cavitation prediction with free-surface effects. Moreover, it has the potential of extension to account for 3D (i.e., sheet cavitation) and transient effects.

1.4 Design and optimization methods

As the available computational power and resources increase worldwide, the number of engineering problems that numerical simulations can tackle also increases. Increased computational power combined with the utilization of parallel processing systems and new algorithms makes it possible to simulate numerically detailed models of various technologies and to incorporate multi-disciplinary optimization (MDO) in the design process to yield solutions with superior performance, see Thévenin & Janiga 2008 [138]. Especially, research related to the field ship energy-saving devices and propulsion systems, where multiple contradictory design criteria must be taken into consideration, is a prime candidate for multi-disciplinary optimization (MDO) applications.

Each optimization process starts with the problem statement, using formula-

tions that typically lie into one of the following categories:

- Direct Numerical Optimization (DNO)
- Inverse Design (ID)

Direct Numerical Optimization (DNO) couples design-variable parameterization with computational tools in an iterative process in order to produce an optimal solution that maximizes (or minimizes) the objective function and satisfies the problem constraints. On the contrary, as the name suggests, the concept of Inverse Design (ID) reverses the conventional design process, allowing new materials and compounds to be 'reverse-engineered' simply by inputting a set of desired properties and characteristics and then using an optimization algorithm to generate a predicted solution. For instance, relating to hydrodynamic analysis, this could be a fluid dynamic characteristic, such as the pressure distribution.

Typically, the solution to an optimization problem can be determined using various algorithms. These lie in two dominant categories, the gradient-based methods and the evolutionary approaches, depending on whether differentiation of the objective function with respect to the design variables is a requirement during the optimization process. In addition, *hybrid algorithms* constitute another category that has emerged in an attempt to bring the best of both worlds, i.e., gradient and evolutionary, which are currently getting attention due to their versatility for MDO applications, see, e.g., [139]-[140] on airfoil shape optimization.

1.4.1 Recent progress in ship design

Decarbonization of shipping by 2050 mandates that ship design adapts to a new reality by incorporating holistic approaches and life cycle considerations aiming at robust designs under uncertainties. Holistic ship design is introduced in Papanikolaou 2010 [141], where the use of advanced optimization techniques for the computer-aided generation, exploration and selection of optimal ship designs is discussed with emphasis on the conflicting requirements resulting from the design constraints and optimization criteria (merit or objective functions), reflecting the interests of ship design stake holders that are inherent to the whole process.

Following this idea, in the recent work by Nikolopoulos & Boulougouris 2020 [142] a new holistic ship optimization framework is proposed where the geometrical model lies at the core of their methodology and various modules targeting stability, strength, powering and propulsion, safety, economics and even operation simulation are considered.

Modern approaches to ship design, which also target the aspect of propulsion and resistance to some extent via numerical towing tank simulations, have been shown to lead to reduced required powering, improved environmental protection,

increased safety, and partly innovative designs. In a sense, the traditional design approaches, see, e.g., [143], nowadays have been enriched and merged with MDO frameworks, advanced computer-aided design software, and numerical simulation tools.

In that sense, methodologies that address the optimization of a ship propulsion subsystem can easily be incorporated into the holistic ship design approach due to the modular nature of the developed frameworks. Related to the optimization of propulsion systems and hydrofoil appendages, various methods have been developed, see, e.g., [144] on the design optimization of a PBCF propeller, [145] on an IGA-BEM for 2D hydrofoil optimization and [146] on a shape-informed dimensional reduction approach in hydrofoil modeling that is useful in optimization, paving the way for more efficient ship propulsion.

1.4.2 Gradient-based and evolutionary approaches

Gradient-based methods

Gradient-based methods consider a baseline (reference) design and use information obtained from the objective function derivative to each design variable, i.e., defined as sensitivities, to alter the design variable vector toward objective function minimization without violating the constraints. *Steepest descent* is one of the oldest and most widely known methods for minimizing a general nonlinear function, see Pironneau 1983 [147]. It is easy to implement and also available in most optimization libraries. However, improving the performance and versatility of gradient-based algorithms remains an active field of research.

The core of gradient-based methods lies in sensitivity derivative calculation, the most computationally expensive aspect of this methodology. Regarding sensitivity derivative calculation, *standard finite difference schemes* may be a simple approach for producing estimates. However, this comes with a penalty in the overall computational time and potential rounding errors. The required computational time is proportional to the order of the finite difference scheme used, assuming that the finite difference stencil dictates the number of solver evaluations.

Other methods for sensitivity calculation include *complex number approaches* and the more sophisticated *adjoint-based methods*, see, e.g., Thévenin & Janiga 2008 [138]. Sensitivity calculation using complex numbers is not prone to rounding errors and requirements in terms of computational time are similar to estimations based on finite differences. However, development time is proportionally greater compared to implementations based on finite differences, since the main solver needs to be extended for complex number variables.

Adjoint-based methods, on the other hand, are the most cost-effective concerning sensitivity calculation when the number of design variables is greater than

the number of objective functions, which is typically the case for engineering applications, see, e.g., Papoutsis-Kiachagias et al. 2014 [148] on the continuous adjoint-method formulation with application to hydraulic turbomachines. They can produce sensitivity derivative estimates at each optimization cycle at the computational cost of two solver evaluations while remaining independent of the total number of design variables. These methods require significant efforts for their mathematical derivation and additional time invested into code development to produce the equivalent adjoint solver but yield high-quality sensitivity derivative estimates at a fraction of the computational cost required by other methods. Finally, adjoint formulations enable optimization studies based on computationally demanding high-fidelity solvers, such as computational fluid dynamics (CFD) and finite element methods (FEM) for structural problems. Various commercial and open-source software (see ANSYS, CAESES, OpenFOAM) with high-fidelity simulation tools contain modules for adjoint-based sensitivity analysis and optimization.

Evolutionary approaches

Evolutionary approaches also known as genetic algorithms (or stochastic optimization methods), are inspired by evolution theory and observations of nature's optimization processes. Key characteristics of these methods include random number generation, gene editing, elitism, population, and generation concepts, see, e.g. Sloss & Gustafson 2020 [149]. One advantage of randomized search algorithms, compared to gradient-based algorithms, is that they succeed at locating the global optimum solution while the latter are prone to get trapped in local optima.

Genetic algorithms require significantly more computational resources to emulate nature's evolution process when compared to gradient-based methods. Each generation requires hundreds of candidate solution evaluations, resulting in excessive CPU time due to the excessive number of costly solver evaluations, see, e.g., Giannakoglou 2002 [150]. However, evolutionary approaches can become efficient and effective by exploiting techniques that rely on surrogate (or approximation) models. These models serve as a substitute for the exact and costly solver evaluations. They are constructed using a limited number of solver evaluations at carefully selected design points and continuously gain ground along with the progress in artificial intelligence.

Notable works include the following: Asouti et al. 2023 [151] investigate the adequacy of radial basis function (RBF)-based models as surrogates in uncertainty quantification (UQ) and CFD shape optimization. Kampolis et al. 2007 [152] propose multilevel optimization strategies based on metamodel-assisted evolutionary algorithms targeted toward computationally expensive problems. Kyriacou et al. 2014 [153] addresses efficient PCA-driven EAs and metamodel-assisted EAs with

applications in turbomachinery.

One of the few works relating to flexible hydrofoil applications is the study in Sacher et al. 2018 [154]. MDO via the proposed surrogate-based model is used for the design of a deformable hydrofoil for the 35th America's Cup. The objective functions consist of minimization of hydrofoil drag and cavitation mitigation at selected sailing conditions (boat speed and lifting force). A 2D, nonlinear, fluid-structure interaction (FSI) solver predicts drag values and cavitation criteria. The solver consists of a static vortex lattice method for the fluid flow with viscous boundary layer equations and a nonlinear elasticity solver for the deformations of the elastic components of the foil. Their successful approach suggests that multiple-fidelity computational tools can contribute to superior and realizable designs using MDO approaches.

Efficiency enhancement of marine propellers via reformation of blade tip-rake distribution

The use of gradient-based optimization algorithms based on standard finite difference schemes for sensitivity calculation remains a valuable tool when coupled with low-fidelity solvers for objective function evaluation. Matlab optimization toolbox provides various tools for the solution of engineering problems. Particularly, the *fmincon* solver is a sequential programming algorithm capable of handling nonlinear constraints. Familiarization with this tool has been accomplished within the context of a study on enhancing the efficiency of marine propellers using optimization techniques and geometry reformation. This study was motivated by the increasing attention on efficient ship propulsion systems and energy-saving devices supported by the short state-of-the-art review on Section 1.1.

In Anevlavi at al. 2023 [155], the effects of blade tip-rake reformation on the performance of marine propellers using a low-cost potential-based vortex-lattice method (VLM), calibrated and validated by the high fidelity artificial compressibility CFD-RANS solver MaPFlow [126], [156]. The primary focus of this study lies on determining whether the low-cost VLM, in conjunction with a multi-dimensional parametric model for the tip-rake and pitch/camber distributions, can produce a propeller geometry with improved efficiency.

Due to the availability of experimental and numerical data, the NSRDC 4381-82 propellers were selected as reference geometries. Torque minimization serves as the objective function in the gradient-based optimization procedure under a thrust constraint, which translates into efficiency enhancement at the selected design advance ratio. The optimized 4381 propeller yields a +1.1% improvement in efficiency based on CFD-RANS, whereas for the modified skewed 4382 propeller, the efficiency gain is +0.5%. The performance enhancement is also evident at a region near the design advance ratio. The results suggest that the exploitation of

low-cost VLM solvers can significantly reduce the CFD simulations required in the optimization process and thus can be effectively used for the design of propellers with tip-rake reformation.

1.5 Thesis outline

The thesis is divided in two Parts, corresponding to the distinct engineering problems addresses within the context of bio-mimetic propulsion applications. Part I, containing Chapters 2-4, focuses on the development of numerical tools for the analysis and optimization of morphing wing thrusters. Part II, containing Chapter 5, introduces the problem of partially cavitating hydrofoils including free surface effects and addresses the formulation of a new continuous adjoint BEM-based optimization method for the prediction of partial cavitation on hydrofoils steadily moving beneath the free surface. Optimization applications based on Direct Numerical Optimization (DNO) can be found in Chapters 2 and 4 referring to the performance enhancement of bio-mimetic flapping thrusters with active and passive morphing capabilities respectively, whereas an Inverse Design (ID) approach is followed for the mathematical formulation of hydrofoil cavitation model presented in Chapter 5. Part III contains Chapter 6 addressing concluding remarks and future work directions.

Chapter 2 deals with the extension of the unsteady boundary element method introduced in Filippas & Belibassakis 2022 [12], to study actively morphing flapping thrusters. Verification of the developed computational tool $3d$BEM is performed through a series of comparisons against other works found in the literature. Friction drag corrections are included in the modeling via empirical coefficients. The wings under study follow a thrust-producing flapping trajectory (heave/pitch) and undergo prescribed (but arbitrary) active morphing. Optimal tuning of geometric and kinematic parameters is performed via a series of optimization studies using the *3dBEM* solver, indicating that significant performance enhancement is achieved via optimally tuned morphing features.

Chapter 3 introduces the Kirchhoff-Love thin plate theory model and the corresponding numerical implementation $2d$FEM based on DKT finite elements, following the work in Karperaki 2021 [157], along with indicative comparisons for validation. This model is used for the structural idealization of wings, thus flexural rigidity variability is included in the formulation to account for thickness profile effects and the use of functionally graded materials. Rayleigh damping is included in the modeling.

Chapter 4, addresses the problem of passively morphing wings and the development of the cost-effective numerical tool *FlexWing3D* suitable for tackling the fluid-structure interaction (FSI) problem. The proposed method follows a parti-

tioned approach, where the potential solver *3dBEM* is strongly coupled with the thin-plate finite element solver *2dFEM*. The FSI tool is validated and numerical results concerning the effect of elasticity on the propulsive performance of flexible flapping thrusters are presented. Optimization studies targeting hydrofoil shape, kinematics, and material properties are included, indicating that proper material selection and material properties distribution can yield favorable passive deformations that enhance propulsion metrics.

Chapter 5 deals with the inverse problem formulation for the case of partially cavitating hydrofoils in 2D domains operating steadily beneath the free surface. Inverse problem solution is obtained using a gradient-based method with sensitivity derivative estimates based on the continuous adjoint method. Verification of the numerical tool *PCavPreMod* is accomplished via a series of comparisons against other works, both numerical and experimental. Finally, submergence and Froude number effects on cavitation number, cavity volume, and shape are investigated. The Chapter contains a description of the developed methodology and material that has been published in Anevlavi & Belibassakis 2022 [158], in compliance with Elsevier copyright policy.

A final Chapter is included to provide concluding remarks, summarize the findings and also address future work directions, highlighting that although emphasis is given to the performance of bio-mimetic wing thrusters, the computational tools that were developed within the context of this work (*FlexWing3D*, *PCavPreMod*) can facilitate the preliminary design of foil-based wave/current energy-saving devices in general.

1.6 Original contributions

Morphing in nature also occurs through active deformation, so incorporating this feature into the design of wing thrusters expands their range of applications. Emphasizing only the hydrodynamics, optimization studies referring to a realistic autonomous underwater vehicle propulsion scenario were conducted, assuming two distinct active morphing thruster concepts, to investigate whether propulsive performance enhancement is achievable via optimal tuning of morphing and flapping parameters. These were the concepts of (1) active hydrofoil-section adjustment and (2) a combination of span-wise bend and twist morphing. A gradient descent approach based on sequential quadratic programming (SQP) is used for optimal tuning of design variables (including planform shape, flapping, and morphing parameters), targeting efficiency maximization under thrust and effective angle of attack constraints.

Our findings indicate that the optimal thruster with chord-line morphing exhibits up to 25% efficiency gain, whereas the results for a wing concept featuring

span-wise bend and twist show an improvement of 9%. The studies performed with the proposed *3dBEM* computational tool give evidence on its capabilities and suggest that it can support the preliminary design and optimization process of actively morphing flapping-foil thrusters. The above provided essential validation required before developing the FSI model where the *3dBEM* undertakes hydrodynamic pressure predictions.

The geometry of wings operating as marine thrusters implies that a plate model is suitable for extracting useful information about the structural response of lifting surfaces with a moderate-to-low aspect ratio. For that purpose, the thin plate finite element solver *2dFEM* written in C/C++, which also allows consideration of the wing's thickness profile in the sense of flexural rigidity variability and load distribution, has been developed for dynamic elastic response predictions. Boundary conditions are introduced as additional equations using a new approach based on Lagrange multipliers. An inverse distance weighting (IDW) method, also known as Shepard interpolation, is implemented to map distributed load and thickness profile data onto the unstructured mesh consisting of Discrete Kirchhoff Triangles (DKT). These 9-dof elements provide excellent accuracy for thin plate predictions and have the lowest computational cost compared to other plate elements.

One advantage of DKT elements is their suitability for general thin plate formulations, including the Föppl–von Kármán equation for problems of large deflections. In addition, the DKT element can be directly extended to the Discrete Shear Triangle (DST) that is compatible with First Order Shear Deformation Theory (FSDT), allowing for simulations involving moderately thick plates (or equivalently finite wings with thicker sections) as well as laminate composites. Extensive validation of 2dFEM covers modal analysis and static response benchmarks for various thickness profiles and boundary conditions. The plate model can be easily used as an external module in FSI frameworks, targeting applications of bio-mimetic thrusters and other wave/current energy-saving devices.

The main contribution of the present thesis is the development of a low-cost FSI model addressing the fully coupled non-linear problem of passively morphing wings operating as marine thrusters. The new computational tool *FlexWing3D*, written in C/C++, consists of the unsteady boundary element solver *3dBEM* for hydrodynamic pressure predictions and the thin plate finite element solver *2dFEM* for elastic response analysis. The partitioned BEM-FEM scheme exploits information exchange between the two solvers and performs interpolation using the IDW method to map data between the different meshes where it is required. Comparisons against experimental works found in the literature support the validity of the present scheme and illustrate its prediction capabilities.

Effects of chord-wise flexibility on a thruster in flapping mode suggest that passive deflections enhance the propulsive performance at the expense of thrust.

Span-wise bending did not yield performance enhancement in the examined range of parameters. An improved thickness profile is determined using optimization, and results suggest that hydrofoils that are more slender near the trailing edge outperform NACA profiles in flapping-foil propulsion applications. Finally, the low computational cost and acceptable accuracy of the *FlexWing3D* method allow for design-space investigations using a typical workstation, for which higher-fidelity hydrodynamic would be, in some cases, computationally prohibitive.

To summarize the author's contributions in terms of scientific publications produced within the context of this thesis, the list of peer-reviewed publications is provided below.

(P1) D. Anevlavi, E.S. Filippas, A. Karperaki and K.A. Belibassakis, 'A nonlinear BEM-FEM coupled scheme for the performance of flexible flapping-foil thrusters', *J. Mar. Sci. Eng.*, 8(1), 2020.
https://doi.org/10.3390/jmse8010056

(P2) D. Anevlavi and K.A. Belibassakis, 'An adjoint optimization prediction method for partially cavitating hydrofoils', *J. Mar. Sci. Eng.*, 9(9), 2021.
https://doi.org/10.3390/jmse9090976

(P3) D. Anevlavi and K.A. Belibassakis, 'Analysis of partially cavitating hydrofoils under the free surface using BEM-based adjoint optimization', *Applied Mathematical Modeling*, 112, 415-435, 2022.
https://doi.org/10.1016/j.apm.2022.07.033

(P4) D. Anevlavi, S. Zafeiris, G. Papadakis and K.A. Belibassakis, 'Efficiency enhancement of marine propellers via reformation of blade tip-rake distribution', *J. Mar. Sci. Eng.*, 11(11), 2023.
https://doi.org/10.3390/jmse11112179

(P5) D. Anevlavi, E. Filippas and K.A. Belibassakis, 'A GPU-accelerated 3dBEM supporting the optimization of actively morphing flapping-foil thrusters with application to AUV propulsion', *Ocean Engineering*, 300, 117513, 2024.
https://doi.org/10.1016/j.oceaneng.2024.117513

(P6) D. Anevlavi and K.A. Belibassakis, 'A strongly coupled BEM-FEM fluid-structure interaction model for flexible wing thrusters', *To be submitted in July 2024.*

Finding have also been presented in the following international conferences and published in the corresponding proceedings.

(C1) D. Anevlavi and K.A. Belibassakis, 'Prediction model for partially cavitating foils based on sensitivity derivatives', CIMNE 2021, 02-04 Jun, Edinburgh, Scotland, 2021 (virtual).

(C2) D. Anevlavi and K.A. Belibassakis, 'Flapping-foil thruster design with optimal flexural rigidity profile based on a coupled BEM-FEM model', IMAM 2022, *19th International Congress of the International Maritime Association of the Mediterranean*, 26-29 Sept, Istanbul, Turkey, 2022 (virtual).

(C3) D. Anevlavi and K.A. Belibassakis, 'Effects on partially cavitating hydrofoils in finite submergence depth via an adjoint-based prediction method' IMAM 2022, *19th International Congress of the International Maritime Association of the Mediterranean*, 26-29 Sept, Istanbul, Turkey, 2022 (virtual).

(C4) D. Anevlavi, E.S. Filippas, A. Karperaki and K.A. Belibassakis, 'Optimization of a flexible flapping-foil thruster based on a coupled BEM-FEM model' OMAE 2022, *41st International Conference on Ocean, Offshore and Arctic Engineering*, 05-10 June, Hamburg, Germany, 2022.

(C5) D. Anevlavi and K.A. Belibassakis, 'An adjoint optimization method for partially cavitating hydrofoils with free-surface effects' MARTECH 2022, *6th International Conference on Maritime Technology and Engineering*, 24-26 May, Lisbon, Spain, 2022 (virtual).

(C6) D. Anevlavi, E.S. Filippas and K.A. Belibassakis, 'Energy-minimizing kinematics for actively morphing flapping foil thrusters' SOME 2023, *8th International Symposium on Ship Operations, Management and Economics*, 07-08 March, Athens, Greece, 2023.

(C7) D. Anevlavi, E.S. Filippas and K.A. Belibassakis, 'Hydrodynamic optimization of actively deforming flapping-foil thrusters for AUV propulsion' EUROGEN 2023, *15th ECCOMAS Thematic Conference on Evolutionary and Deterministic Methods for Design, Optimization and Control*, 01-03 June, Chania, Crete Greece, 2023. (Book of Abstracts)

(C8) D. Anevlavi, E.S. Filippas, A. Karperaki and K.A. Belibassakis, 'Hydroelastic analysis of flapping-foil thrusters using a partitioned BEM-FEM' EURODYN 2023, *7th International Conference on Structural Dynamics*, 02-05 July, Delft, Netherlands, 2023.

(C9) Δ. Ανεβλαβή, Α. Καρπεράκη, Ε. Φίλιππας, Κ. Μπελιμπασάκης, 'Υδροελαστική ανάλυση βιομιμητικών προωθητήρων μέσω συζευγμένης μεθόδου συνοριακών και πεπερασμένων στοιχείων' ΡΟΗ 2024, *12ο Πανελλήνιο Συνέδριο Φαινομένων Ροής Ρευστών*, 15-16 Απριλίου, Θεσσαλονίκη, Ελλάδα, 2024.

Part I

Analysis and optimization of morphing thrusters

Chapter 2

Hydrodynamic model for actively morphing wings

List of symbols

XYZ	Cartesian global (earth-fixed) coordinate system
xyz	Cartesian local (body-fixed) coordinate system, centered at the pitch rotation axis
h_0	heave amplitude in meters
θ_0	pitch amplitude in rad
$h(t)$	instantaneous heave in m
$\theta(t)$	instantaneous pitch in rad
ω	angular frequency in rad/s
f	frequency in Hz
T_p	harmonic motion period in s
ψ	pitch phase difference in rad
c	chord length in m
s	span length in m
$AR = s^2/Area$	aspect ratio
$Str = 2fh_0/U$	Strouhal number
X_R	pitch pivot point as % of the chord
U	forward motion velocity in m/s
$s(t)$	instantaneous forward motion in m
$\alpha_{eff}(t)$	effective angle of attack in rad
$f_s(t), f_o$	ramp function and ramp function coefficient
$C_L(t)$	instantaneous lift coefficient
$C_T(t)$	instantaneous thrust coefficient
$C_M(t)$	instantaneous moment coefficient

$C_p(\mathbf{x};t)$, $p(\mathbf{x};t)$	pressure coefficient, pressure in Pa
ρ	fluid density in kg/m^2
$\mathbf{n}(\mathbf{x};t)$	normal unit vector
$D(t)$	fluid flow domain
$\partial D_B(t)$, $\partial D_W(t)$	wing and wake surface boundaries
DtN	Dirichlet-to-Neumann operator
η	propulsive efficiency
$\mathbf{V}(\mathbf{x};t)$	velocity in m/s
$\Phi(\mathbf{x};t)$	velocity potential
μ_W	velocity potential jump on the wake
$\mu_K(\mathbf{x};t)$	velocity potential jump on Kutta strip
$G(\mathbf{x}_0\|\mathbf{x})$, $\partial_n G(\mathbf{x}_0\|\mathbf{x})$	Green's function and its normal derivative
NEC, NEA	number of chordwise, spanwise panel elements
dt	time-step in s
A_c	chord-line morphing amplitude in m
G_1, F_1	spanwise bending, twist mode
$\beta(\mathbf{x};t)$	local vertical bending in m
$\gamma(\mathbf{x};t)$	local hydrodynamic twist angle in rad
ψ_β	spanwise bending phase difference in rad
ψ_γ	spanwise twist phase difference in rad
ψ_c	chord-line adjustment phase difference in rad
K_1, K_2	Courant numbers
$k_G = \pi f c/U$	reduced frequency
U_o	constant inflow velocity in m/s
α_0	fixed hydrodynamic twist angle in rad

2.1 Background

Technologically, the use of active wing morphing, i.e., wing shape modification, for the control of lifting surfaces was initially introduced in aeronautics as a means of meeting the varying demands of flight scenarios by keeping the aircraft *trimmed* (in moment equilibrium) and controlling its direction of flight [59]. One of the Wright brothers' contributions, applied to the famous Wright glider, was the invention of a system for varying the camber of their wings by warping via tugging wires attached to wing-tip corners. In 1980, Glenn Curtis was the first to use hinged ailerons to provide differential lift on the wings, a system used widely in most aircraft since then, including later products of the Wrights. Flapped wings can increase the total lift without requiring the whole aircraft to change its inclination to the direction of flight. It became clear that multi-element airfoils were here to stay, and their proper design remains a challenge to the aerodynamicist today.

Since the 80s, technologies for active wing morphing in the aviation industry have matured and the geometrical parameters of a morphing solution are conveniently classified as (1) *planform morphing*, (2) *out-of-plane morphing* and (3) *airfoil section adjustment*; see, e.g., the recent reviews from [159] and [160]. The demands of aviation may differ from fish locomotion, however, the abundant literature on actively morphing airfoils and wings provides valuable insight for the present study, which aims to reveal interesting trends for the energy-minimizing kinematics for hydrofoils in thrust-producing mode.

In the aviation industry *planform morphing* (span, sweep, chord) in the form of variable sweep has proven successful, particularly in enabling military aircraft to fly at supersonic speeds, albeit with a large weight penalty [159]. Sweep has positive effects on boundary layer transition and dynamic stall behavior of finite wings.

Out-of-plane morphing (twist, dihedral/gull, span-wise bending) is probably the least common type of morphing solution, perhaps with the exception of wing twists. The twist is the oldest shape morphing, but was discarded for almost 80 years to prevent aeroelastic problems. Advances in aerospace materials (composites) have made twist morphing possible. In addition, twist morphing (similar to camber morphing) can serve multiple tasks simultaneously, such as alleviating gust and maneuver load; increasing the lift coefficient, and replacing conventional control surfaces [59]. Most of the research has been focused so far on actively tailoring the wing elasticity to achieve the desired twist; moreover, traditional actuation systems have been adopted in most of the studies that reached the wind tunnel test stage.

State-of-the-art multidisciplinary optimization (MDO) studies of aircraft wings deal with actuation mechanisms, structural analysis, aerodynamic simulations, and techno-economic aspects. Various approaches have been proposed for MDO, and

taking into account the complexity of simulations, design detail, and contradictory criteria, this new field of research is certainly getting a lot of attention, see, e.g., [101].

However, from the abundant literature on the topic, it is evident that airfoil section morphing (camber, thickness), and more specifically *camber morphing*, is the dominant research topic in subsonic aerodynamic applications when compared to the planform and out-of-plane morphing methods, see e.g. [161], [162], [163] and [164]. The research in airfoil morphing, which includes camber and thickness distribution changes, is dominated by the camber morphing concepts.

Applications of actively morphing wings in the field of naval architecture are limited. They can be found among technologies of wing stabilizers with actively controlled flaps, such as the type-S retractable fin stabilizer by [165], and the anti-rolling MR-Series of [166]. In addition, new designs have emerged from the studies conducted for the America's Cup racing sailboats, where safety factors are kept to a minimum in order to attain maximum performance [167]. Many racing and fast-cruising foiling sailboats use state-of-the-art actively controlled foils and appendages; see, e.g., the methodology proposed by [168] for the sea-keeping of a flying yacht or the split-flap concept for the T-foil of a sailing yacht [169].

Within the research community, there is an explicit distinction between studies focused primarily on (1) producing working prototypes of actively morphing wings and (2) research that aims to reveal the physical principles of efficiency enhancement due to the incorporation of certain bio-mimetic features via numerical computations. The first approach is directly linked to the most recent advances in smart materials research, including developments in actuation technology, constitutive laws, modeling, optimization, control, and failure prediction, which demand more purposeful steps to progress variable-geometry wings. 'According to studies at NASA, it will take another 20-30 years before skies could be filled by aircraft more similar to birds, having wings without discrete control surfaces that can change their shape in a smart way' [170]. On the other hand, the development of computational tools that can accurately simulate the flow around actively morphing wings is in demand and has been able to produce valuable results that facilitate the development of working prototypes.

In general, this requires reformulating models that originate from the field of computational fluid dynamics in order to derive the dynamic models needed for the design and also for the control systems of the thruster device [6]. In recent years, computational fluid dynamics (CFD) has been extensively used to investigate the unsteady flow phenomena in oscillating wings with active deformation. Both Navier-Stokes-based methods and ideal-flow approaches have been assigned the task of predicting the hydrodynamic loads on oscillating actively morphing wings that move within a fluid. The verification of newly developed numerical

tools is essential, prior to conducting studies using them to derive insight into the physics behind aquatic locomotion.

In [171], the effects of a prescribed harmonic time-varying chord-line morphing profile on the propulsive efficiency of a hydrofoil using CFD were investigated and compared results with the reference hydrofoil that undergoes a prescribed heaving and pitching motions.

Chapter 2 contains the extension of an ideal-flow *3dBEM* model for the hydrodynamic analysis of actively morphing wings. Concerning the kinematics, studied wings undergo arbitrary but prescribed motions, including rigid-body dynamics and morphing. The proposed *3dBEM* solver is capable of hydrodynamic pressure and integrated load predictions for finite wings, operating at small-to-moderate angles of attack with acceptable accuracy. Moreover, *3dBEM* includes a linear wake model and free wake analysis. The free-wake model gives better predictions for cases of large unsteadiness. The required computational cost is lower compared to higher-fidelity viscous-RANS. Moreover, all simulations presented in this work were performed using a workstation with an NVIDIA GPU exploited for parallel computation.

The examples included here refer to various flapping-foil propulsion scenarios. Therefore, I begin with the kinematic model and the distinction between the rigid-body motions, i.e., heave, pitch, and the active morphing kinematics incorporated into the model to provide additional bio-mimetic features. These morphing parameters can enhance the propulsive efficiency of the flapping thruster with proper tuning, see e.g. [79].

Then, I provide the mathematical model for the case of unsteady flows around wings that perform arbitrary but prescribed kinematics. This model serves as the basis for boundary element implementation that yields the GPU-accelerated *3dBEM* solver used to study morphing wings. The present model is compared against other numerical and experimental works for validation, highlighting its strengths and limitations. The proposed model provides useful predictions of thrust coefficient and efficiency at small-to-moderate angles of attack.

Finally, results of optimization studies concerning proper tuning of geometric, kinematic, and morphing parameters for performance enhancement under thrust angle of attack constraints are discussed. These efficient flapping thruster designs with morphing capabilities are proposed for the propulsion system of a concept autonomous underwater vehicle (AUV). Some of the results are published in [172] and including them is in accordance with Elsevier copyright policy. The proposed methodology is suitable for the preliminary design actively morphing wing thrusters with a wide range of applications, ranging from the propulsion of AUVs, renewable-energy systems for wave/current energy harvesting or even large-scale projects for augmenting ship propulsion in waves [129], [39], [126] and [12].

2.2 Wing kinematics

The wing of chord length c and span s is assumed to be fully submerged within the fluid medium, and any interactions with other boundaries, including wavy free-surface effects, are considered negligible. The wing performs prescribed rigid-body motions (heave, pitch) superimposed with arbitrary but prescribed morphing[1], i.e., instantaneous changes in wing shape.

The whole formulation is set to an earth-fixed reference frame and a global coordinate system XYZ, while an auxiliary moving body-fixed coordinate system xyz is used as a reference for changes in shape due to active morphing. A schematic representation of a wing cross section including the nomenclature used to describe the rigid-body kinematics is shown in Figure 2.1. Heave and pitch motions are based respectively on the following harmonic functions,

$$h(t) = h_0\, sin(\omega t), \tag{2.1}$$
$$\theta(t) = \theta_0\, sin(\omega t + \psi), \tag{2.2}$$

where h_0 denotes the amplitude of heave motion in meters, θ_0 the amplitude of pitch motion in radians and ω the forcing frequency in rad/s. In our case the selected phase difference is set to $\psi = -90^o$ and negative pitch angles correspond to nose-up rotations. The period of motion in seconds can be obtained from the forcing frequency $\omega = 2\pi f$ as $T_p = 1/f$. This is based on observations suggesting that this is the optimal phase difference, [173], [53]. The pivot axis for the pitch motion is placed at $X_R = c/3$ from the leading edge (LE). A forward translation motion denoted as $s(t)$ (toward the negative X-axis) given by,

$$s(t) = -Ut, \tag{2.3}$$

simulates the AUV propulsion scenario for which free-stream velocity is set to zero and shear current effects are negligible. Moreover, the effective angle of attack due to the flapping is,

$$a_{eff}(t) = -\theta(t) - tan^{-1}(\dot{h}(t)/U), \tag{2.4}$$

where $\dot{h}(t)$ denotes the heaving velocity, see Hover et al. [51].

Assuming that the morphed wing geometry denoted as $\mathbf{x}$, is defined in a body-fixed coordinate system xyz, then the following transformation can be used to derive the morphed wing position in the global reference frame, denoted as $\mathbf{X}$,

$$\mathbf{X} = \mathbf{Q} \cdot \mathbf{x} + \mathbf{T}, \tag{2.5}$$

[1]Details on the active morphing modes studied in the present can be found in Sec. 2.5.1.

where

$$\mathbf{Q} = f_s(t) \begin{bmatrix} cos\,\theta(t) & 0 & -sin\,\theta(t) \\ 0 & 1 & 0 \\ sin\,\theta(t) & 0 & cos\,\theta(t) \end{bmatrix}, \quad \mathbf{T} = f_s(t) \begin{bmatrix} s(t) \\ 0 \\ h(t) \end{bmatrix}, \tag{2.6}$$

with $\mathbf{Q}$ is the rotation matrix for the pitch motion with respect to the selected pivot point and $\mathbf{T}$ the translation matrix considering both heaving and forward motion. In addition, $f_s(t) = 1 - exp(-f_o(t/T_p)^2)$, where T_p is the period of harmonic motion, denotes a ramp function permitting smooth transition from rest to the fully developed state of oscillatory motions. At $f_o = 1.5$, when $t/T_p > 2$, the wing's motion is fully developed and is not affected further by the filter.

A schematic representation of an actively morphing wing in the body-fixed xyz and global XYZ coordinate systems is shown in Figure 2.2. I note that the rigid-body motions are taken into consideration via Eq. (2.5) and are expressed in the global coordinate system XYZ. A snapshot of the linearized trailing wake is also included in the figure for visualization purposes since it is part of the boundary mesh used in the *3dBEM* numerical tool that is described in the next section.

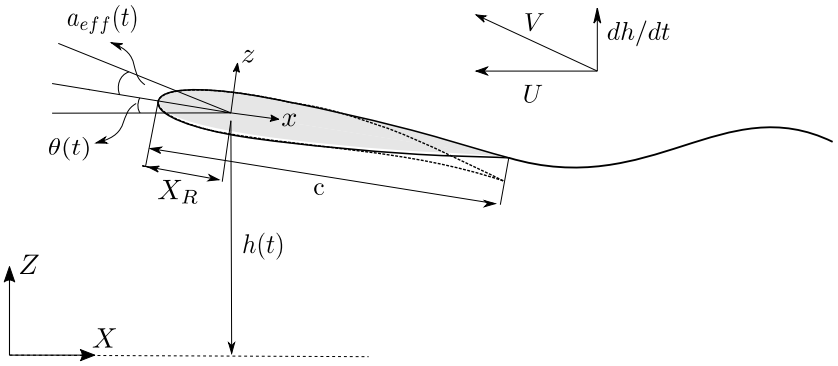

Figure 2.1: Nomenclature for flapping-foil kinematics on a wing cross section in the global XZ and local xz coordinate systems. The morphed instance of the wing is represented with a dotted line.

2.3 Propulsive performance metrics

The instantaneous lift (C_L), thrust (C_T) and moment (C_M) coefficients, with respect to the pivot axis, are calculated using,

$$C_L(t) = \frac{L(t)}{0.5\rho U^2 cs} = -\frac{1}{A}\int_{\partial D_B} C_p\, \mathbf{n}\cdot\mathbf{i}_y dS, \tag{2.7}$$

$$C_T(t) = \frac{T(t)}{0.5\rho U^2 cs} = \frac{1}{A}\int_{\partial D_B} C_p\, \mathbf{n}\cdot\mathbf{i}_x dS, \tag{2.8}$$

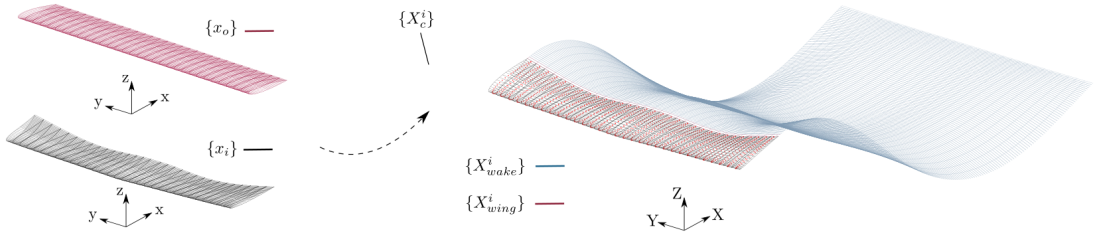

Figure 2.2: Body-fixed xyz and global XYZ geometry definitions for an actively morphing wing, with $\{\mathbf{x}_o\}$ representing points on the undeformed wing surface, $\{\mathbf{x}_i\}$ point coordinates on the morphed wing surface and $\{\mathbf{X}_c^i\}$ control point coordinates on the morphed wing/wake in the global system.

$$C_M(t) = \frac{M(t)}{0.5\rho U^2 c^2 s} = -\frac{1}{Ac}\int_{\partial D_B} C_p\, \mathbf{n}\cdot\mathbf{r}(x|x^*)dS, \tag{2.9}$$

where A denotes the planform surface area, c the chord length, s the span and $\mathbf{r}(x|x^*)$ the reference vector for moment calculation.

To estimate the propulsive (Froude) efficiency η of an actively morphing flapping thruster, it is essential to take into consideration not only the power required to sustain the rigid-body motions but also the power for morphing. The efficiency is calculated as follows,

$$\eta = \overline{C}_{P_{out}}/\bar{C}_{P_{in}}, \tag{2.10}$$

where $\overline{C}_{P_{out}} = P_{out}/(0.5\rho U^3 A)$, $\bar{C}_{P_{in}} = P_{in}/(0.5\rho U^3 A)$ and

$$P_{out} = \frac{1}{T_p U}\int_0^{T_p} T(t)U dt, \tag{2.11}$$

$$P_{in} = \frac{1}{T_p U}\int_0^{T_p} P_h(t) + P_\theta(t) + P_{morph}(t)dt, \tag{2.12}$$

with T_p denoting the period of harmonic motion, $T(t)$ the instantaneous thrust and U the forward motion velocity. The mean input power P_{in} required by the oscillating system per period of motion can be expressed using

$$P_h(t) = L(t)\dot{h}(t), \tag{2.13}$$

$$P_\theta(t) = M(t)\dot{\theta}(t), \tag{2.14}$$

with $\dot{h}$, $\dot{\theta}$ denoting the heave/pitch velocities. The power component responsible for sustaining the active morphing, following [171] and [173], is estimated as

$$P_{morph}(t) = \frac{1}{A}\oint_{\partial D_B} C_p \mathbf{n}\cdot\mathbf{V}_{morph} ds, \tag{2.15}$$

where C_p is the pressure coefficient, $\mathbf{V}_{morph}$ the velocity component due to the morphing. Morphing velocity[2] can be calculated as the difference between total and rigid-body motion velocity. Thus,

$$\mathbf{V}_{morph}(\mathbf{x};t) = \mathbf{V}_{total}(\mathbf{x};t) - \mathbf{V}_{rigid}(\mathbf{x};t). \tag{2.16}$$

2.3.1 Friction-drag correction

Consideration of friction drag effects can be included using the following empirical formula that comprises of two coefficients, the skin-friction resistance component and another related to the effective angle of attack from [129],

$$C_r(t) = C_F + C_a(Re)\alpha_{eff}^2(t), \quad C_F = \frac{0.0858}{[log_{10}Re - 1.22]^2}, \tag{2.17}$$

with

$$C_{Tvisc}(t) = C_r(t) + C_T(t), \quad \eta = \bar{C}_{Tvisc}/\bar{C}_{Pwtot}. \tag{2.18}$$

The friction coefficient increases at higher angles of attack, leading to better predictions. The corrections are implemented during the post-processing phase on the instantaneous thrust coefficient and then on the efficiency after averaging for the last period of the simulation. Formulation of other coefficients targeting effects, such as leading-edge separation, will also improve our predictions, assuming that adequate data from either CFD or experiments are available. This extension is left for future work.

2.4 Unsteady lifting flows around actively morphing wings

Concerning the hydrodynamic analysis of actively morphing flapping-foil thrusters, an existing 3D unsteady boundary element model from Filippas and Belibassakis [12] has been reformulated within the context of this thesis. The model in [12] is suitable for the prediction of hydrodynamic loads on finite-span wings that undergo flapping-type motions at small-to-moderate effective angles of attack, suggesting that the flow remains attached. The initial version of the computational tool consists of a three-dimensional boundary element method (BEM) for unsteady lifting flows around wings operating beneath the wavy free surface. However, in the present work, software extension addresses the case of flapping wings that are

[2]Velocities due to rigid-body motions are calculated analytically, whereas for the total velocity a third-order finite difference stencil is implemented.

fully submerged within the fluid medium and leaves free surface effects for future work.

The BEM code exploits parallel programming techniques on graphics cards (GPUs), which leads to a significant reduction in the required computational time. In Papadakis et al. [174] and Filippas et al. [175], extensive comparisons between the three-dimensional GPU-accelerated *3dBEM* and the unstructured-grid RANS solver MaPFlow suggest that the present potential code is capable of accurate predictions concerning hydrodynamic loads for the case of rigid flapping-foils. It is highlighted that the *3dBEM* is very cost-effective as it provides a good compromise between the required accuracy and computational time. For example, in Papadakis et al. [174], the computational cost of 3D-RANS simulations required approximately 5 hours on 120 CPUs while detached-eddy simulations (DES) required 12 hours on 1000 CPUs. Coarse-mesh simulations using the *3dBEM* required 88 sec using 1.3GB of VRAM. The simulations refer to a wing with aspect ratio $AR = 6$, NACA 0012 sections, $c = 0.1m$, Strouhal number $Str = 0.3$, heaving amplitude $h_0 = 0.75c$ and Reynolds number $Re = 4 \cdot 10^4$.

Therefore, our efforts here build upon a cost-effective computational code and aim to extend its capabilities in terms of enabling the analysis and optimization of actively morphing flapping-foil thrusters. The benefits of using potential-based solvers for the problem of energy-minimizing kinematics for animal flight are addressed in [170] and [176], where tuning of active morphing parameters is accomplished via optimization where a vortex-lattice method is used to evaluate the performance of each candidate thruster.

The low computational cost of the proposed GPU-accelerated *3dBEM* allows for the completion of an optimization study on morphing thrusters using an AMD Ryzen 9 3900XT workstation equipped with an NVIDIA GeForce RTX 3080 (10GB VRAM) within a few days, referring to gradient-based optimization and also depending on the total number of design variables, see Sec. 2.6 of the present. Contributions of the thesis related to GPU-BEM solver extension are summarized below:

1. Numerical calculation of the wing body boundary velocities $\mathbf{V}_{total}(\mathbf{x}; t)$ using a (backward) finite difference scheme of third order, exploiting parallel programming in CUDA.

2. Re-generation of wing mesh at each time step, in order to account for morphing effects.

3. Re-calculation of induction coefficients at each time step, in order to account for morphing effects.

4. Evaluation of the propulsive performance metrics for the case of actively morphing wings, including $\mathbf{V}_{morph}(\mathbf{x};t)$ estimation.

2.4.1 Mathematical formulation

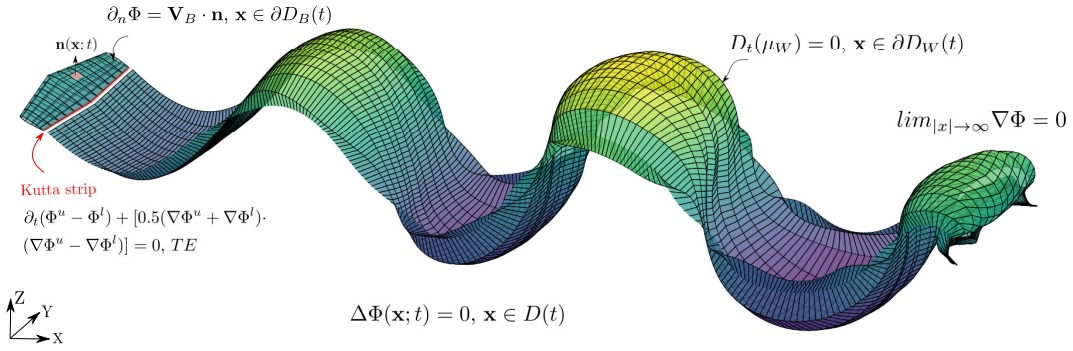

Figure 2.3: Computational domain and boundary conditions for the unsteady lifting-flow problem of morphing flapping wings in the global coordinate system XYZ.

The lifting flows studied in the present, under an ideal fluid assumption[3], are modeled as inviscid and incompressible. In the present work, the wing and wake boundaries, which are denoted as $\partial D_B(t)$ and $\partial D_W(t)$ respectively, are consequently modeled as surfaces of potential discontinuity. A schematic representation of the wing and wake boundaries is provided in Figure 2.3. The wing undergoes arbitrary but prescribed motions, including rigid-body kinematics and morphing (i.e. changes in shape). The wake boundary represents the trailing-vortex sheet, emanating from the sharp trailing edge, and is modeled as a free-shear layer with non-zero vorticity.

The velocity potential $\Phi(\mathbf{x};t)$ is defined as a twice continuous differentiable function in $D(t)$ and its derivative yields the (disturbance) velocity field as $\mathbf{V}(\mathbf{x};t) = \nabla\Phi$. Regarding the present formulation, the velocity potential $\Phi(\mathbf{x};t)$ is considered an initially unknown scalar field. The governing equation (Laplace),

$$\Delta\Phi(\mathbf{x};t) = 0, \quad \mathbf{x} \in D(t), \tag{2.19}$$

represents the conservation of mass for incompressible and irrotational fluid flows.

[3]Ideal-flow in 2D translates into the assumptions of an incompressible, inviscid and irrorational fluid. However, the irrotationality assumption is not valid for 3D problems.

Concerning the boundary conditions, on the wing surface a flow tangency condition must hold,

$$\partial_n \Phi(\mathbf{x};t) = \mathbf{V}_B(\mathbf{x};t)\cdot\mathbf{n}(\mathbf{x};\mathbf{t}), \quad \mathbf{x}\in\partial D_B(t), \tag{2.20}$$

where $\partial_n\Phi(\mathbf{x};t) = \nabla\Phi(\mathbf{x};t)\cdot\mathbf{n}$ denotes the directional derivative of the velocity potential, $\mathbf{n}$ is the unit normal to the body boundary pointing toward $D(t)$ and $\mathbf{V}_B(\mathbf{x};t)$ is the total body velocity. For the present initial boundary value problem (IBVP) formulation the disturbance potential and velocity fields vanish at large distances from the body, in the sense of a radiation condition.

It is important to note that the velocity term $\mathbf{V}_B(\mathbf{x};t)$ on the *rhs* of Eq. (2.20) refers to known quantities, since the kinematics are prescribed. On the other hand, for passively morphing wings, i.e. free to deform under hydrodynamic load excitation, the total velocity consists of rigid-body motion induction terms and velocity components due to elastic deformation. The elastic response of the wing is dependent on its shape at each instant and vice-versa. In that sense the flow-tangency condition becomes implicitly non-linear because the body boundary $\partial D_B(\mathbf{x};t)$ and the velocities $\mathbf{V}_B(\mathbf{x};t)$ are initially unknown quantities. More details regarding the extension of BEM solver for the fluid structure interaction simulations are contained in Chapter 4.

Furthermore, dynamic and kinematic boundary conditions should be satisfied on the wake $\partial D_W(t)$. The dynamic boundary condition mandates that a free-shear layer cannot carry loading and thus the pressure at both sides of it should be the same,

$$p_W^u(\mathbf{x};t) = p_W^l(\mathbf{x};t), \quad \mathbf{x}\in\partial D_W(t). \tag{2.21}$$

At the same time, the upper and lower sides of a shear layer cannot be separated to two distinct surfaces, thus the velocity component normal to the wake surface should also be continuous,

$$\partial_n\Phi^u(\mathbf{x};t) = \partial_n\Phi^l(\mathbf{x};t), \quad \mathbf{x}\in\partial D_W(t). \tag{2.22}$$

The superscripts *"u", "l"* are used to denote the wake's upper and lower side respectively, while the indices *"B", "W"* are used to denote values of the potential field and its derivative at the wing surface and wake respectively. Bernoulli's equation in the inertial reference frame,

$$\frac{p(\mathbf{x};t)}{\rho} + \partial_t\Phi(\mathbf{x};t) + \frac{1}{2}[\nabla\Phi(\mathbf{x};t)]^2 = 0, \quad \mathbf{x}\in D(t), \tag{2.23}$$

can be used to derive information about the pressure from velocity data. A detailed derivation of Bernoulli's equation on a body-fitted reference frame; which is useful to hydrodynamic pressure calculation on the wing, can be found in Filippas 2019

[37]. The above expression is nonlinear since the term $[\nabla\Phi(\mathbf{x};t)]^2$ is retained. Moreover, Eq. (2.23) when used in conjunction with the dynamic and kinematic boundary conditions on the wake, namely Eqs. (2.21)-(2.22) yields,

$$\frac{D\mu_W(\mathbf{x};t)}{Dt} = 0, \quad \mathbf{x} \in \partial D_W(t), \tag{2.24}$$

where $D(\cdot)/Dt = \partial_t(\cdot) + \mathbf{V}_W^m \cdot \nabla(\cdot)$ denotes the material derivative based on the mean total velocity $\mathbf{V}_W^m = 0.5(\nabla\Phi_W^u + \nabla\Phi_W^l)$ on the trailing wake and $\mu_W = \Phi_W^u - \Phi_W^l$ the potential jump on the wake. Based on this relation, the trailing wake $\partial D_W(t)$ evolves in time as a material curve whose exact motion becomes part of the solution, thus introducing an implicit non-linearity. Details concerning the derivation can be found in [12].

A free wake model requires that the trailing-vortex sheet evolves in time as a material surface, which leads to a significant increase of the required computational time. This feature is included in the present version of the computational code.

For the simplified wake model, the generated vortex sheet emanates parallel to the bisector of trailing edge and assumes the shape of trailing-edge path. Linearization of wake dynamics simplifies the problem and provides satisfactory predictions in flows of low/moderate unsteadiness.

A schematic comparison between the free and simplified wake models for the time-evolution of a trailing vortex sheet in two-dimensions is shown in Figure 2.4, where the free-wake model is shown with the blue vectors denoting the potential jump and the dashed line corresponds to the simplified wake model. This visualization of free-wake reveals the famous von Kármán vortex-street formation corresponding to thrust-producing foil kinematics.

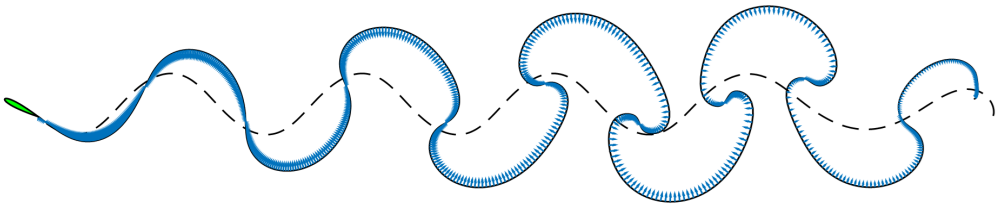

Figure 2.4: Time-evolution of a trailing vortex sheet in two-dimensions based on the free-wake (blue curve) and linearized (dashed line) models adapted from [177].

For lifting flows, enforcement of the Kutta condition is also required in order to fix the circulation at each time instant. In the present work, a non-linear (quadratic) pressure-type Kutta condition, requiring zero pressure difference at the trailing edge, is enforced at the trailing edge,

$$\partial_t(\Phi^u - \Phi^l) + 0.5(\nabla\Phi^u + \nabla\Phi^l) \cdot (\nabla\Phi^u - \nabla\Phi^l) = 0, \tag{2.25}$$

$$\mathbf{x}(\xi,\eta) \in \partial D_B(t), \ (\xi,\eta) \to (\xi_{TE},\eta_{TE}). \tag{2.26}$$

Based on Eqs. (2.19),(2.20) and (2.22) the weakly singular boundary integral equation (BIE) is obtained, which holds for each point on the body boundary, with $\mathbf{x}_0 \in \partial D_B(t)$, as follows[4],

$$\frac{1}{2}\Phi_B(\mathbf{x}_0;t) + \int_{\partial D_B(t)} \Phi_B(\mathbf{x};t)\partial_n G(\mathbf{x}_0|\mathbf{x})ds(\mathbf{x}) \tag{2.27}$$
$$= \int_{\partial D_B(t)} b(\mathbf{x};t)G(\mathbf{x}_0|\mathbf{x})ds(\mathbf{x}) - \int_{\partial D_W(t)} \mu_W(\mathbf{x};t)\partial_n G(\mathbf{x}_0|\mathbf{x})ds(\mathbf{x}),$$

where μ_W denotes the dipole intensity, or potential jump, on the wake. Equation (2.27) above is formulated using the fundamental solution of 3d Laplace equation known as Green's function and its directional derivative. They are defined respectively as

$$G(\mathbf{x}_0|\mathbf{x}) = -\frac{1}{4\pi}\frac{1}{r(\mathbf{x}_0|\mathbf{x})}, \quad D(t) \subseteq R^3, \tag{2.28}$$

$$\partial_n G(\mathbf{x}_0|\mathbf{x};t) = -\frac{1}{4\pi}\frac{\mathbf{r}(\mathbf{x}_0|\mathbf{x})\cdot\mathbf{n}(\mathbf{x};t)}{[r(\mathbf{x}_0|\mathbf{x})]^3}, \quad D(t) \subseteq R^3, \tag{2.29}$$

with

$$\mathbf{r}(\mathbf{x}_0|\mathbf{x}) = \mathbf{x}_0 - \mathbf{x}, \quad r(\mathbf{x}_0|\mathbf{x}) = ||\mathbf{x}_0 - \mathbf{x}||_2, \tag{2.30}$$

where the latter is an Euclidean metric.

Regarding the initial boundary value problem, Eq. (2.27) and Eq. (2.25) form a system of nonlinear equations with respect to the unknown velocity potential field and the dipole intensity on the Kutta-strip. To solve this non linear system of equations, a general iterative method such as the Newton-Raphson can be used. Following the work of Filippas and Belibassakis [12], these equations are combined to form a single dynamic equation with respect to the unknown dipole intensity of the Kutta-strip, denoted with μ_K, as discussed in Section 2.4.2 that follows. This dynamic equation is treated more efficiently, in terms of computational time compared to the other approach based on general iterative methods, using a time-stepping methodology.

2.4.2 Discrete formulation and solution of the boundary integral equation

Regarding the spatial discretization, the following assumptions are made:

- C^0 representation of the wing/wake boundaries based on bilinear quadrilateral elements, as shown in Figure 2.5 and defined in Appendix A.

[4]Multiplier 1/2 suggests that the weak form is valid on smooth portions of the boundary; otherwise a multiplier $1/\alpha$ needs to be used instead, where α is defined by the local angle.

- The velocity potential, its normal derivative and potential jump on the wake at each time step are approximated by piece-wise constant distributions,

$$\begin{aligned} \Phi_B(\mathbf{x};t) &= \Phi_{Bi}(t), \quad i = 0, 1, ..., N_B - 1, \\ \partial_n \Phi_B(\mathbf{x};t) &= \partial\Phi_{Bi}(t), \quad i = 0, 1, ..., N_B - 1, \\ \mu_W(\mathbf{x};t) &= \mu_{Ww}(t), \quad w = 0, 1, ..., N_W(t) - 1. \end{aligned} \tag{2.31}$$

- Finally, following a collocation scheme, the BIE in Eq. (2.27) is satisfied in a finite number of points. To avoid singularities, the centroid of each element are chosen as collocation (or control) points.

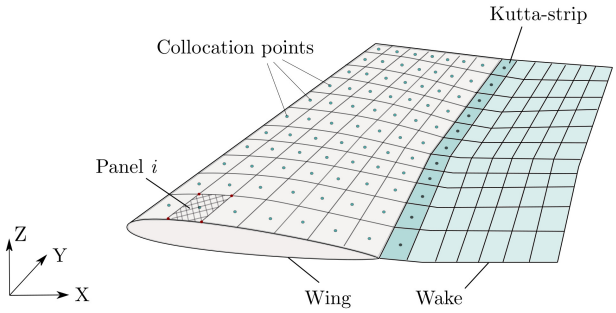

Figure 2.5: Schematic of a wing and its wake discretized into quadrilateral panels in the global coordinate system XYZ.

Up to this point, the boundary $D(t)$ consists of the body boundary and the trailing vortex sheet i.e. $\partial D(t) = \partial D_B(t) \cup \partial D_W(t)$. In $\partial D_W(t)$ at the vicinity of trailing edge there is a transitional region where the trailing vortex sheet transform from a free surface to a bound surface. In the sequel that region will be termed Kutta-strip and will be denoted as $\partial D_K(t)$ and with $\partial D_W(t)$ I will denote the remaining free boundary. Moreover, in the discretized model, Kutta-strip is approximated by N_K boundary elements distributed along the span. Wing body is discretized into N_B elements total with NEA elements in the spanwise direction and NEC elements chordwise.

The discretized form of Eq. (2.27) is as follows

$$\mathcal{D}_B^{pot}(t) \cdot \mathbf{\Phi}_B(t) = \mathcal{S}_B^{pot}(t) \cdot \mathbf{b}(t) + \mathcal{D}_{B,K}^{pot}(t) \cdot \boldsymbol{\mu}_K(t) + \mathcal{D}_{B,W}^{pot}(t) \cdot \boldsymbol{\mu}_W, \tag{2.32}$$

where $\mathcal{D}_B^{pot}(t), \mathcal{S}_B^{pot}(t), \mathcal{D}_{B,K}^{pot}(t), \mathcal{D}_{B,W}^{pot}(t)$ are potential induction-factor matrices, with S denoting source or single-layer integrals, and with D denoting dipole or double-layer integrals. It is important to note that in the case of actively morphing wings,

the self-induction coefficients must be re-calculated to consider effects of mesh deformation.

Particularly, $\mathcal{D}_B^{pot}(t), \mathcal{S}_B^{pot}(t)$ model body-body interactions, while the additional terms involving matrices $\mathcal{D}_{B,K}^{pot}(t), \mathcal{D}_{B,W}^{pot}(t)$ model wake-body interactions and the definition of the above matrices can be found in [37]. Terms with bold denote vectors containing values of piecewise-constant functions on he panel elements representing boundary fields such as $\mathbf{\Phi}_B = \{\Phi_{Bj}\}$, $\mathbf{b} = \{b_j\}$, $\boldsymbol{\mu}_K = \{\mu_{Kk}\}$, $\boldsymbol{\mu}_W = \{\mu_{Ww}\}$. By multiplying both side of Eq. (2.27) with $\left(\mathcal{D}_B^{pot}(t)\right)^{-1}$ I derive,

$$\mathbf{\Phi}_B(t) = \mathcal{G}(t) \cdot \mathbf{b}(t) + \mathcal{Z}(t) \cdot \boldsymbol{\mu}_K(t) + \mathcal{P}(t) \cdot \boldsymbol{\mu}_W, \tag{2.33}$$

where

$$\mathcal{G}(t) = \left(\mathcal{D}_B^{pot}(t)\right)^{-1} \cdot \mathcal{S}_B^{pot}(t),\ \mathcal{Z}(t) = \left(\mathcal{D}_B^{pot}(t)\right)^{-1} \cdot \mathcal{D}_{B,K}^{pot}(t)\right)^{-1} \cdot \mathcal{D}_{B,W}^{pot}(t).$$

This mapping, namely the discrete Dirichlet-to-Neumann (DtN) operator, connects the potential (Dirichlet data) with the velocity potential on the body boundary $\partial D_B(t)$ (Neumann data). However it contains the unknown values of the dipole intensity on the Kutta-strip $\boldsymbol{\mu}_K$ (Dirichlet data) which is part of the wake $\partial D_W(t)$. Apart from the Kutta-strip, the wake boundary introduces memory effects through the term $\mathcal{P}(t) \cdot \boldsymbol{\mu}_W$. The background field velocity effects are included in the term $\mathbf{b}$, as described in Eq. (2.20).

Finally, a system of, spatially and temporarily, non-local differential equations with both explicit and implicit non-linearity in the following form[5]

$$d_t \boldsymbol{\mu}_K = \mathbf{f}\big(\boldsymbol{\mu}_K\big), \tag{2.34}$$

is used to describe the dynamics of an oscillating wing. This system of equations is derived using the appropriate part of the DtN map in Eq. (2.33) and the pressure-type Kutta condition in its discrete form; see also Sec. 2.8 from [37].

Time integration

The numerical solution of the aforementioned evolution equation is obtained using the fourth-order Adams-Bashford-Moulton (ABM) linear multistep method. Assuming that the vector of unknowns in the previous time-step t is denoted as $\mathbf{U}(t) = \boldsymbol{\mu}_K(t)$, then the solution in the current step is obtained using the predictor/corrector formulas below,

$$\mathbf{U}(t+dt) = \mathbf{U}(t) + \frac{dt}{24}\Big[9\mathbf{f}_{pre}(t+dt) + 19\mathbf{f}(t) - 5\mathbf{f}(t-dt) + \mathbf{f}(t-2dt)\Big], \tag{2.35}$$

[5]To be precise, the expression holds as $d_t\boldsymbol{\mu}_K = \mathbf{f}\big(\boldsymbol{\mu}_K, t\big)$, where dependence on time t originates from the enforced flapping kinematics; via information that is passed to the problem through a body boundary flow-tangency condition.

with predictor step

$$\mathbf{f}_{pre}(t+dt) = \mathbf{f}_{t+dt}\Big(\mathbf{U}_{pre}(t+dt)\Big), \tag{2.36}$$

$$\mathbf{U}_{pre}(t+dt) = \mathbf{U}(t) + \frac{dt}{24}\Big[55\mathbf{f}(t) - 59\mathbf{f}(t-dt) + 37\mathbf{f}(t-2dt) - 9\mathbf{f}(t-3dt)\Big],$$

where terms relating to current t and previous time steps $t-dt$, $t-2dt$, $t-3dt$ are used. The ABM scheme requires the calculation of only two derivative equations at each time, and assuming that a fine discretization in time/space is used good convergence is achieved, since the error is of order (dt^5) where dt is the time-step.

Body velocity calculation

Total velocity on each collocation point is calculated using a third-order (backward) finite difference stencil. Thus, consequent morphed configurations of the wing in XYZ from the previous time steps need to stored. Morphing velocities can be calculated using Eq. (2.16) by subtracting velocity components due to rigid-body motions $\mathbf{V}_{rigid}(\mathbf{x};t)$ (i.e., for which analytical formulas can be exploited) from the total velocity $\mathbf{V}_{total}(\mathbf{x};t)$. The latter is calculated numerically using a forward, third-order finite difference scheme.

2.5 Numerical results and verification

The source code of the developed *3dBEM* solver is written in $C/C++$ with CUDA kernel functions that exploit the parallel computation capabilities of modern NVIDIA GPUs. In addition, a Matlab script ($interfaceBEM.m$) is written for pre/post-processing purposes serves as the interface. Matlab is proprietary software, however it our pre/post-processing modules can be easily replaced with Python which is open-source.

All computations within the context of this thesis were performed on an AMD Ryzen 9 3900XT workstation with 32GB RAM equipped with an NVIDIA GeForce RTX 3080 (10GB VRAM) that launched in 2020, see Figure 2.6. The latter is gaming graphics card however it can be exploited for parallel scientific computations. Simulations using the present tool can also be performed in other workstations equipped with an NVIDIA GPU after minor modifications in the $makefile$ used for source code compilation.

The study cases in Table 2.2 are selected for validating the extended *3dBEM* with emphasis on predicting hydrodynamic forces and the propulsive performance of actively morphing flapping-foils. In all cases, a constant inflow velocity U_∞ is considered. Regarding the performance metrics, these refer to mean values concerning the last flapping-cycle of three-period simulations. Depending on the

simulation parameters, the free wake model can be used to improve predictions at flows with high unsteadiness. Unless stated otherwise a linearized wake model is assumed. The accuracy at which the pressure-type condition is satisfied depends on the temporal and spatial discretization. In the examples presented here, the maximum pressure difference on the trailing edge lies between $10^{-2} - 10^{-3}$.

Overall, the GPU-accelerated *3dBEM* performed well in the comparisons. Indicating that the developed numerical tool works best at attached-flow conditions, as expected. Significant discrepancies were evident between our predictions and the last study case against the experiment in [178], where viscous phenomena are not negligible.

Figure 2.6: NVIDIA GeForce RTX 3080 (10GB).

Table 2.2: Validation studies for actively morphing wings.

id	Flapping	Morphing	Data	Medium
1	heave, pitch	chord-line	numerical, 2D-BEM [177]	fresh water
2	heave	spanwise bending	experiment [75]	fresh water
3	-	spanwise bending fixed twist angle	numerical (inviscid), Euler solution [173]	air
4	-	spanwise bending	experiment [178]	air

2.5.1 Chordwise and spanwise morphing profiles

Hydrofoil-section adjustment. Abundant literature on the matter gives inspiration for the design of hydrofoil-section adjustment technologies for flow control, see, e.g., [161], [162],[163] and [164]. State-of-the-art research in airfoil morphing, which includes camber and thickness distribution changes, is dominated by camber morphing concepts. In flapping-foil applications, hydrofoil sections have zero

camber, in order to maintain symmetry in the loading during up- and down-stroke motions. The same holds for ship fin stabilizer technologies and other foiling-vessel appendages.

Considering the above, a scenario of time-varying chord-line morphing is introduced instead of camber morphing. The hydrofoil-section adjustment profile is uniform in the spanwise direction. A snapshot of a morphed hydrofoil section, based on a NACA 0012 thickness profile, is shown schematically in Figure 2.7. The normalized chord-line deformation profile is defined as,

$$\begin{aligned} y_c(t) &= 0, && x/c \in [0, X_R] \\ &= \frac{A_c}{c}\frac{(x - X_R)^2}{(1 - X_R)^2} \cdot sin(\omega t + \psi_c), && x/c \in (X_R, 1], \end{aligned} \tag{2.37}$$

where A_c/c denotes the amplitude of morphing, ψ_c the phase difference, and $\{\mathbf{x}_o\}$ the reference-wing coordinates (with no morphing) in the body-fixed coordinate system xyz. Morphing is restricted to the part between pitch pivot point X_R and the trailing edge (TE). Moreover, maximum displacement occurs at the TE. The

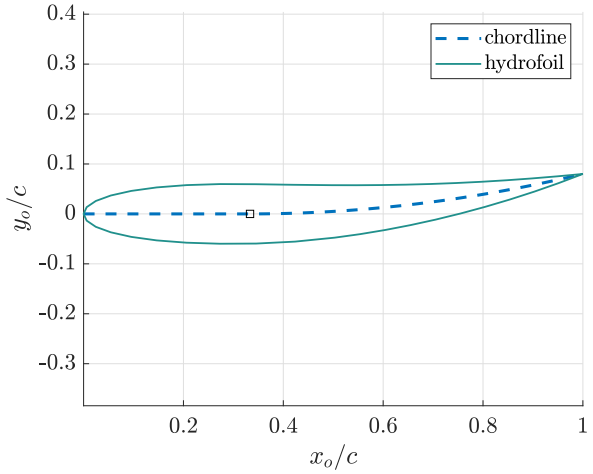

Figure 2.7: Snapshot of a NACA 0012 hydrofoil with chord-line morphing, based on Eq. (2.37) at $t = 0s$ with $Ac = 0.08c$, $\psi_c = 90^o$ and pivot location $X_R = c/3$ shown with a black square.

above equation, when multiplied with the chord length, gives the $y-$coordinates of the morphed chord-line profile. Frequency ω is kept the same as rigid-body motion equations for simplicity, even though the effects of morphing frequency on flapping-foil performance have technological interest and are included in future work extensions.

Spanwise bend and twist. Regarding the out-of plane morphing, I introduce the linear bending mode G_1 and the quadratic twist mode F_1 in Stanford and Beran [170],

$$G_1 = 2|y|/s, \tag{2.38}$$
$$F_1 = (2|y|/s)^2, \tag{2.39}$$

where $y \in [-s/2, s/2]$. Each mode is then multiplied with a harmonic amplitude to yield a time-varying morphing shape as follows,

$$\beta(\mathbf{x}; t) = \beta_1(t) \cdot G_1(\mathbf{x}), \tag{2.40}$$
$$\gamma(\mathbf{x}; t) = \gamma_1(t) \cdot F_1(\mathbf{x}), \tag{2.41}$$

with

$$\beta_1(t) = A_b \, sin(\omega t + \psi_b), \quad \gamma_1(t) = A_\gamma \, sin(\omega t + \psi_\gamma), \tag{2.42}$$

where A_b, A_γ denote the amplitudes of bending displacement and hydrodynamic twist respectively. Similarly, ψ_b, ψ_γ are the corresponding phase differences. Again, the frequency ω is kept the same as rigid-body motion equations for simplicity. A schematic representation of the above modes is provided in Figure 2.8.

The phase differences between the morphing modes and the rigid-body motions play a significant role in terms of propulsive performance. In [179], a detailed parametric study reveals the existence of optimum values for the phase difference of active spanwise bending for the case of low-aspect-ratio flapping thrusters. It is important to note that although morphing parameters, such as the bending amplitude and the phase differences, are considered known quantities within the context of actively morphing wings, proper tuning is expected to yield enhanced propulsive performance. This is the subject of Section 2.6 of the present work, where optimal tuning is accomplished via optimization.

Finally, passive bend/twist coupling in real aeroelastic applications, for instance, in wind turbine installations, can also lead to instabilities and structural failure. This needs to be considered in future applications involving actively-morphing thrusters with spanwise bend/twist capabilities.

Morphed wing shape To sum up, the wing shape considering both hydrofoil-section adjustment and out-of-plane bend/twist in the body-fixed coordinate system xyz is represented via the following transformation,

$$\{\mathbf{x}\} = \mathbf{Q}_{twist} \cdot \left(\mathbf{x}_o - \mathbf{X}_R\right) + \mathbf{X}_R + \mathbf{T}, \tag{2.43}$$

where

$$\mathbf{Q}_{twist} = f_s(t) \begin{bmatrix} cos\,\beta(\mathbf{x};t) & 0 & -sin\,\beta(\mathbf{x};t) \\ 0 & 1 & 0 \\ sin\,\beta(\mathbf{x};t) & 0 & cos\,\beta(\mathbf{x};t) \end{bmatrix}, \quad \mathbf{T} = f_s(t) \begin{bmatrix} 0 \\ \cancel{\gamma_b^s(\mathbf{x};t)} \\ \gamma(\mathbf{x};t) \end{bmatrix},$$

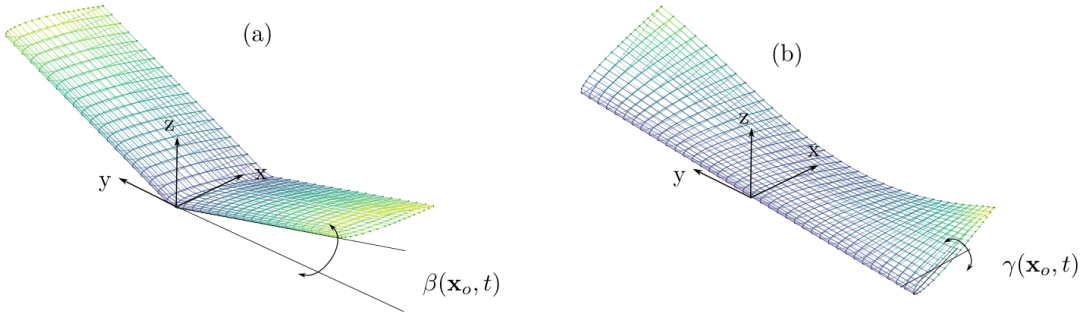

Figure 2.8: Schematic representation of the instantaneous spanwise (a) bend and (b) twist morphing modes in the body-fixed coordinate system xyz. Nose-down twist morphing corresponds to $\gamma(\mathbf{x}; t) > 0$.

where $\mathbf{x}_o$ denotes the wing configuration based on the instantaneous chord-line morphing, $\mathbf{X}_R = [x_R, y_R, z_R]^T$ is the translation required for the enforcement of hydrodynamic twist $\mathbf{Q}_{twist}$ in $xz-$plane with respect to the selected pivot point and $\mathbf{T}$ the bending displacement. In our simulations, $\mathbf{X}_R = [x_R, 0, 0]^T$ typically with $x_R = 1/3c$. Ramp function, $f_s(t) = 1 - exp(-f_o(t/T_p)^2)$ is used to permit a smooth transition from rest to the fully developed state of oscillatory motions. The order of transformations is important for reproducibility. Moreover, the above transformation can be written more compactly as

$$\{\mathbf{x}\} = \mathbf{Q}'_{morph} \cdot \{\mathbf{x}_o\} + \mathbf{T}'_{morph}, \tag{2.44}$$

where $\mathbf{Q}'_{morph}$ and $\mathbf{T}'_{morph}$ represent the rotation and translation matrices considering all morphing motions.

Regarding the bending displacement, in Stanford and Beran 2010 [170] the implementation of a foreshortening correction via an addition displacement in the $y-$axis denoted as $\gamma_b^s(\mathbf{x}; t)$ is proposed. If the amplitude of bending motion remains small, neglecting this correction is justified.Otherwise, if not explicitly stated in the simulations no corrections have been implemented.

In addition, effective angle of attack calculations for actively morphing wings need to take into consideration both the hydrodynamic twist and bending displacements. Thus, the extended Eq. (2.4) becomes,

$$\alpha_{eff}(\mathbf{x}; t) = -\big[\theta(t) + \beta(\mathbf{x}; t)\big] - tan^{-1}\Big(\frac{\dot{h}(t) + \dot{\gamma}(\mathbf{x}; t)}{U}\Big). \tag{2.45}$$

2.5.2 Chordwise morphing

Temporal discretization dt is selected based on the following *Courant* numbers, in order to avoid the occurrence of numerical instabilities,

$$K_1 = \frac{U dt}{dx_{Kutta}} < K_1^{max}, \quad K_2 = \frac{\sqrt{U^2 + (\omega c)^2} dt}{dx_{Kutta}} < K_2^{max}, \tag{2.46}$$

where dx_{Kutta} is the average Kutta-strip panel length in the direction of chord and K_1^{max},K_2^{max} are user-defined parameters with typical values within the range $0.7 - 1.2$. Both Courant numbers are independent of the total number of panels in the direction of span, therefore NEA is tuned so as to yield panel element aspect ratios ~ 1.

The purpose of this study is to provide representative information on the overall computational time using different simulation parameters. Table 2.3 contains information regarding the computational time of three-cycle simulations based on different combinations of mesh size, wake model, and DtN re-calculation mode. Regarding the latter, induction coefficient matrix must be re-evaluated at each time step for simulations of morphing wings. However, since it increases the overall computational time, simulations without DtN re-calculation are also performed to investigate whether it could be omitted without great loss in accuracy. More precisely, the required computational time is the average among results of performing the same simulations several times.

Table 2.3: Required computational time. Simulation of a flapping-wing (rigid) with $c = 0.33m$, $s = 1.0m$, $h_0 = 0.75c$, $\theta_0 = 23^o$, $\psi = -90^o$ and $Str = 0.26$.

id	NEA	NEC	$dt/T_p(\%)$	DtN re-calc	Wake	Time [s]	[min]
0	31	60	0.5	no	linear	177	3
1	31	60	0.5	yes	linear	300	5
2	31	60	0.5	yes	free	918	15
3	31	120	0.31	no	linear	841	14
4	31	120	0.31	yes	linear	1417	24
5	31	120	0.31	yes	free	4253	75

Comparison with 2D-BEM

The first test case is selected to verify that the extended computational tool is capable of capturing chord-line morphing effects on the propulsive performance of flapping wings. Results of GPU-accelerated *3dBEM* are compared against predictions obtained using the 2D-BEM from Anevlavi et al. 2020 [177]. Comparisons between two and three-dimensional solvers serve as preliminary benchmark cases. Finite wings with orthogonal planforms and high aspect ratios can be modeled

using 2D theory, by assuming that downwash effects are negligible [59]. Moreover, wing geometry and incident flow are assumed uniform in the direction of span.

The parameters that characterize the examined scenario are summarized in Table 2.4. For the 3D simulations two aspect ratios are examined, $AR = \{6, 12\}$. The wing undergoes prescribed flapping and forward motion defined in Eq. (2.5) superimposed with active chord-line adjustment based on Eq. (2.37). Morphing is uniform in the direction of span, thus comparisons between the solvers are justified.

For the 2D simulations, I used $dt/T_p = 0.5/100$ and $NEC = 60$ panels concerning the discretization. The same parameters are used in 3D simulations, along with $NEA = 8AR$. Courant parameter is set to $K_1^{max} = 1.0$. Figure 2.9 shows consequent instances of the wing's root section, i.e. where $y = 0$, on the flapping trajectory.

Figure 2.10 contains the instantaneous thrust $C_T(t)$, lift $C_L(t)$, and moment $C_M(t)$ coefficients obtained using the two and three-dimensional BEM solvers. The time histories are in good agreement, and it is observed, as expected, that *3dBEM* predictions on the wing with $AR = 12$ are closer to 2D results compared to the prediction on $AR = 6$. Simulations with the $AR = 6$ lead to time histories with a slight swift to the left (i.e. phase difference) when compared to the 2D results. However, increasing the aspect ratio reduces the observed phase difference, suggesting that results on a wing with $AR > 12$ will bring 3D simulations even closer to the 2D idealization. This is in accordance with classic aerodynamic theory and proves the validity of *3dBEM* in predicting the performance of a flapping wing with active chord-line adjustment.

Table 2.4: Motion parameters for comparison with 2D-BEM.

Geometry	$c = 1m$, NACA 0012
Aspect ratio	$AR = \{6, 12, \infty\}$
Flapping motion	$h_0 = 0.75c$, $\theta_0 = 23^o$, $\psi = -90^o$
Strouhal number	$Str = 0.23$
Morphing	$A_c = 0.08c$, $\psi_c = 0^o$

Mesh sensitivity

Additional simulations were performed for the finite wing with $AR = 6$ to investigate mesh sensitivity effects based on morphing wing simulations. This is not intended to be a complete sensitivity analysis, but rather a study that provides a quantification of the accuracy achieved using different simulation parameters related to mesh and wake dynamics. Table 2.5 contains information regarding

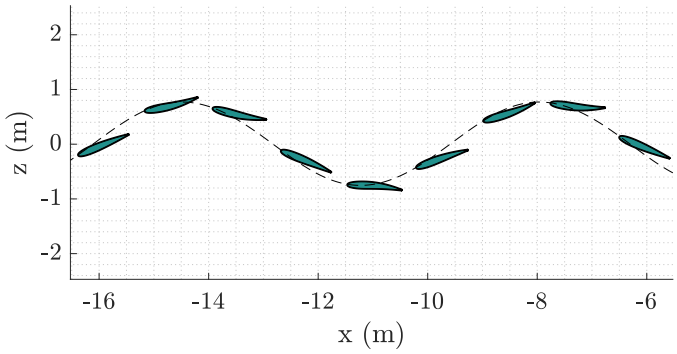

Figure 2.9: Morphed instances of the flapping-wing root section for the test case in Table 2.4.

mesh size, DtN re-calculation mode, wake dynamics, etc. Results suggest that analysis with and without DtN re-calculation shows deviations of 2% concerning predictions for mean thrust coefficient and efficiency. The less computationally expensive simulation ($id = 4$) refers to a coarse mesh and linear wake analysis without DtN re-calculation, which results in a 1.1% loss of accuracy compared to the fully resolved simulations ($id = 0$). These settings reduce the required computational time with an acceptable loss in accuracy, which is useful to the optimization studies on morphing wings discussed in Section 2.6.

Table 2.5: Effects of simulation parameters in the case of a chord-line morphing wing with $AR = 6$.

id	dt/T_p (%)	NEC, NEA	DtN	Wake	Time [s]	$\overline{C}_T$	Diff (%)	η	Diff (%)
2D	0.5	60,-	yes	linear	3.62	0.2267		0.6253	
3D									
0	0.38	80,55	yes	free	6129.7	0.2335	-	0.5465	-
1	0.38	80,55	yes	linear	1870.6	0.2314	0.90	0.5380	1.57
2	0.38	80,55	no	linear	1242.1	0.2661	-1.10	0.5516	-0.92
3	0.50	60,49	yes	linear	682.92	0.2265	3.10	0.5320	2.72
4	0.50	60,49	no	linear	442.47	0.2309	1.12	0.5462	0.05

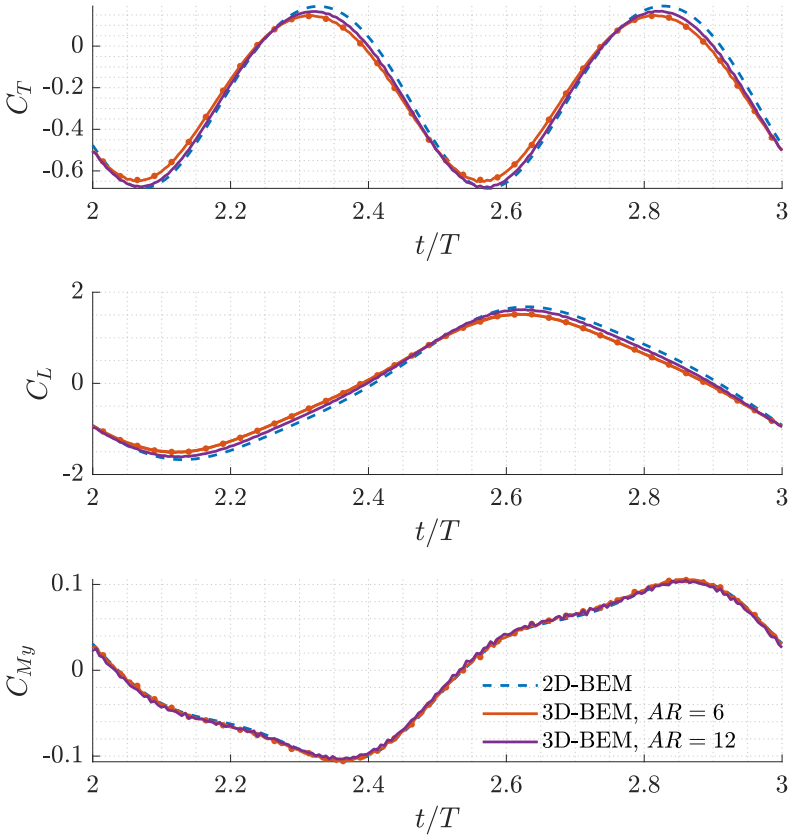

Figure 2.10: Instantaneous thrust (C_T), lift (C_L) and moment (C_{My}) coefficients for the test case in Table 2.4.

2.5.3 Heaving wing with spanwise bending

Furthermore, to verify that our method can predict the effects of active spanwise bending on the propulsive performance of heaving wing I have selected the following test case from the experiments in Heathcote et al. 2008 [180]. A schematic representation of the wing kinematics examined in the experiment is shown in Figure 2.11. The wings have NACA 0012 sections, aspect ratio $AR = 3$, and main dimensions $c = 0.1m$, $s = 0.3m$. Regarding the heaving motion, the wing is actuated at its root with $s_{ROOT}(t) = h_0 cos(\omega t)$, $h_0 = 0.175c$, see also 2.11. The inflow velocity is constant and the wing morphs passively under hydrodynamic load excitation. Measurements of deflection reveal that the bending profile can be modeled using a first-order mode. Moreover, in [180] measurements of the tip

amplitude and phase difference with respect to the heaving motion are provided. It is also important to note that the examined wings are labeled as 'inflexible', 'flexible', and 'very flexible' based on their flexural rigidity.

In our simulations, the whole wing is considered, thus $s = 0.6m$ and $AR = 6$. The flow is symmetric with respect to the $yz-$plane as shown in Figure 2.12, where a snapshot of the simulated wing with free wake is provided. The vertical skeg is included for visualization purposes. The symmetry plane is included for visualization purposes. Table 2.6 contains geometric and kinematic parameters for this test case.

The mesh consists of $NEC = 60$, and $NEA = 5AR$ panels in the chordwise and spanwise direction respectively. Free wake analysis is used and the time step is set to $dt/T_p = 0.45\%$. Inflow velocity is $U = 0.3m/s$ at Reynolds number $Re = 3 \cdot 10^4$ where kinematic viscosity is $\nu = 10^{-6}m^2/s$.

Figure 2.13 contains *3dBEM* predictions for mean thrust coefficient per-unit-span $\overline{C}_T = \overline{T}/(0.5\rho U^2 c)$ as a function of reduced frequency $k_G = \pi f c/U$ and the corresponding experimental data from [180]. In particular, Figure 2.13 [left] contains our inviscid predictions which overpredict the thrust, however, they are found to be in accordance with the experimental data in terms of trends. Improved predictions are accomplished using the friction-drag coefficient defined in Eq. (2.17) after calibration with the experimental data as shown in Figure 2.13 [right]. Calibration of the coefficients is performed *heuristically* using *trial-error*. Friction drag correction comprises a skin-friction resistance coefficient and another dependent on the effective angle of attack [129]. Implementation of friction-drag corrections is performed in the post-processing phase. To sum up, this comparison further supports the validity of our method in predicting out-of-plane morphing effects on the propulsive performance of wings.

Table 2.6: Motion parameters for the scenario from [180].

Dimensions	$c = 0.1m$, $s = 1.2m$
Sections	NACA 0012
Heave amplitude	$h_0 = 0.175c$
Inflow velocity	$U = 0.3m/s$
Reduced frequency	$k_G = (0.5, 1.75)$
Spanwise bending	$A_b(k_G)$, $\psi_b(k_G)$ in [180]

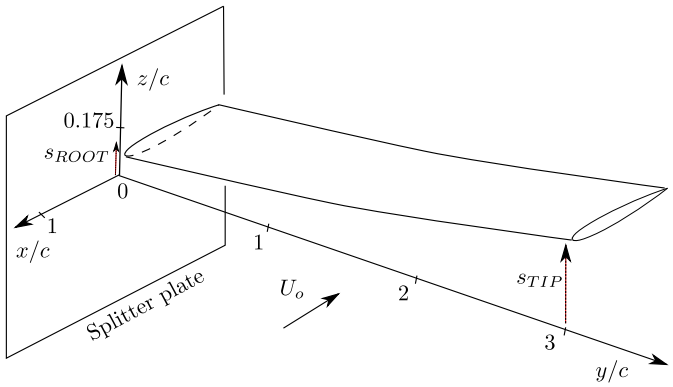

Figure 2.11: Schematic representation of the heaving and spanwise bending wing from the experiments in Heathcote et al. 2008 [180].

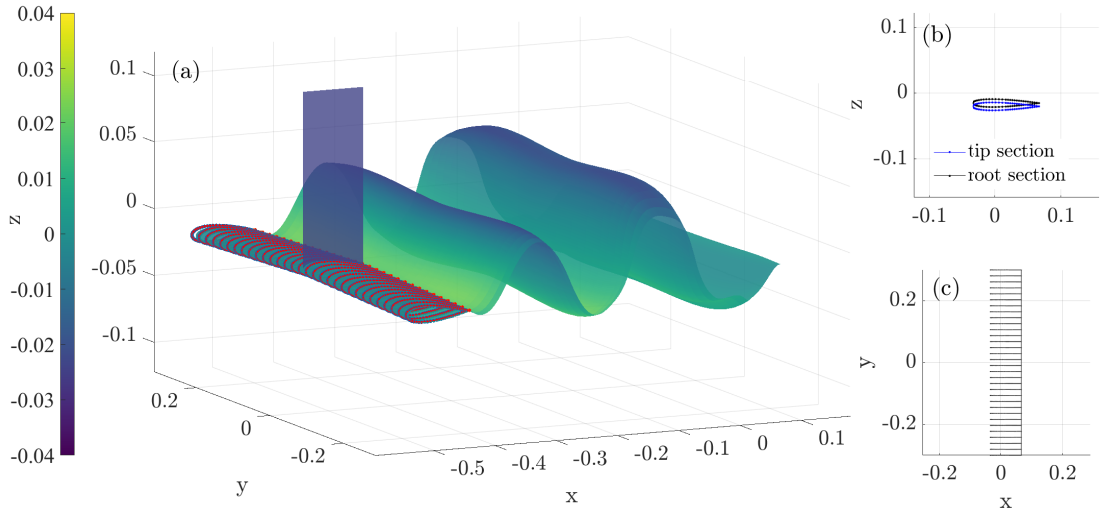

Figure 2.12: Snapshot of numerical simulations using the present method for comparison against [180]: (a) free-wake formation, (b) instantaneous root/tip sections and (c) planform shape.

2.5.4 Examples inspired from bird flight

Wing kinematics based on spanwise bend/twist morphing lie at the heart of bird flight [6]. Bird-flight applications open a new world concerning physics, mainly due to the different mission targets that require both thrust and lift production during each flapping cycle. In addition, the maneuvering capabilities of birds depend highly on active morphing, i.e., bend and twist manipulation. Studies on this topic reveal interesting aerodynamic effects and provide abundant inspiration

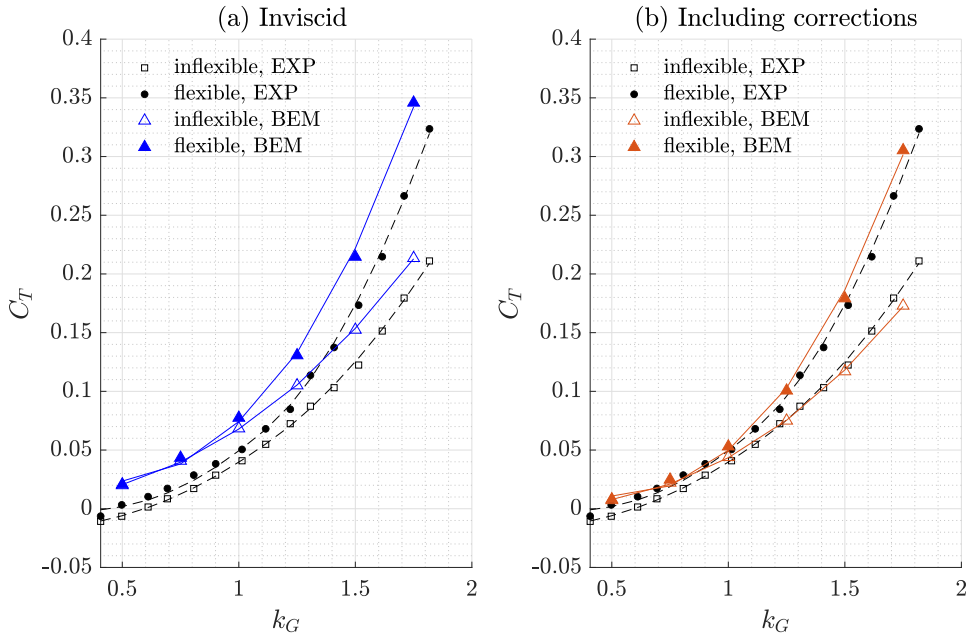

Figure 2.13: Comparison with experimental data from [180] for a heaving and spanwise bending wing. GPU-accelerated *3dBEM* results without [left] and including friction-drag correction with $C_F = 0.0081$ and $C_a = 0.185$ [right].

for future applications of both micro-aerial and underwater autonomous vehicles.

Motivated by this, I selected a relevant study from the numerical work of Neef & Hummel 2001 [173], concerning a wing at a high-cruising speed that undergoes active bend and twist mimicking bird flight. In their work, the propulsive performance of the wings is predicted using a numerical solver based on the solution of inviscid Euler equations. The propulsion scenario selected for comparison and verification refers to a wing that undergoes active spanwise bending and has a fixed twist angle to ensure that adequate lift is also provided during flight. The parameters of motion and the wing geometry are summarized in Table 2.7 for reproducibility of the results.

The wing operates at a reduced frequency $k_G = 2\pi fc/(2U) = 0.1$ with $f = 3s^{-1}$. Negative twist angle corresponds to a nose-up hydrodynamic twist at the tip. In simulations performed with the present computational tool, the morphing kinematics are emulated using the following expressions,

$$\beta(\mathbf{x};t) = f_s\, A_b sin(\omega t) G_1(\mathbf{x}), \quad A_b = 0.5s\, tan(15^o), \tag{2.47}$$

$$\gamma(\mathbf{x};t) = f_s(t)\, \alpha_0 G_1(\mathbf{x}), \quad \alpha_0 = -4^o, \tag{2.48}$$

where $f_s(t)$ denotes the ramp function permitting smooth transition between rest and the fully developed motion. Regarding the discretization, a fine mesh with

Table 2.7: Motion parameters for comparison against [173].

Orthogonal planform	$c = 0.16m$, $s = 1.28m$
Aspect ratio	$AR = s/c = 8$
Sections	NACA 0012
Heave, pitch	$h_0 = \theta_0 = 0$
Bending amplitude	$A_b = 0.5s\,tan(15^o)$
Fixed twist angle	$\alpha_0 = -4^o$
Forward motion	$U = 15m/s$

$dt/T_p(\%) = 0.125$, $NEA = 49$ and $NEC = 60$ was used. The required computational time for each simulation was approximately 1.25 hours, including free-wake analysis and DtN re-calculation. For wings operating at high cruising speeds fine temporal discretization must be used to avoid numerical instabilities (i.e., arising from the linear multi-step method used to solve the IBVP described in Sec. 2.4.2.

Figure 2.14 contains predictions of the instantaneous lift and thrust coefficients for the scenario with parameters summarized in Table 2.7. The comparison includes results obtained using the present method, numerical solution from the Euler equation solver in [173], and the unsteady vortex-lattice (UVLM) predictions from [176]. It is important to note that the latter neglects wing thickness. The presence of a non-zero twist angle results in lift production, as shown in Figure 2.14a. Particularly, lift production during the flapping cycle can be beneficial for maneuvering and should be included in the design criteria of bio-inspired wing devices for future applications in autonomous underwater vehicles (AUVs).

It is observed that the present method over predicts thrust coefficient time history peaks by 3%, whereas lift predictions are in very good agreement with the solution from [173]. This discrepancy can be attributed to an under-prediction in terms of tip-vortex swirling strength or induced drag, which is relatively strong as shown in the flow fields provided in [173].Tip-vortex swirling is not modeled in the present *3dBEM* formulation, however simulations based on free wake dynamics can capture vortex sheet swirling up to a degree. Since all models are inviscid, this comparison provides additional verification, that the present method is capable of predicting bend/twist effects on the performance of wings.

Finally, an extreme test case from the experimental work in Fejtek & Nehera 1980 [178] is included to investigate the limitation of the present method. This process is motivated by Bird et al. 2021 [57], where their findings establish that ideal-flow models, such as the unsteady lifting-line theory, still provide a useful solution for low-Reynolds-number $Re = 1{\cdot}10^4$, large-amplitude kinematics problems, via comparisons against experimentally validated fluid dynamics simulations.

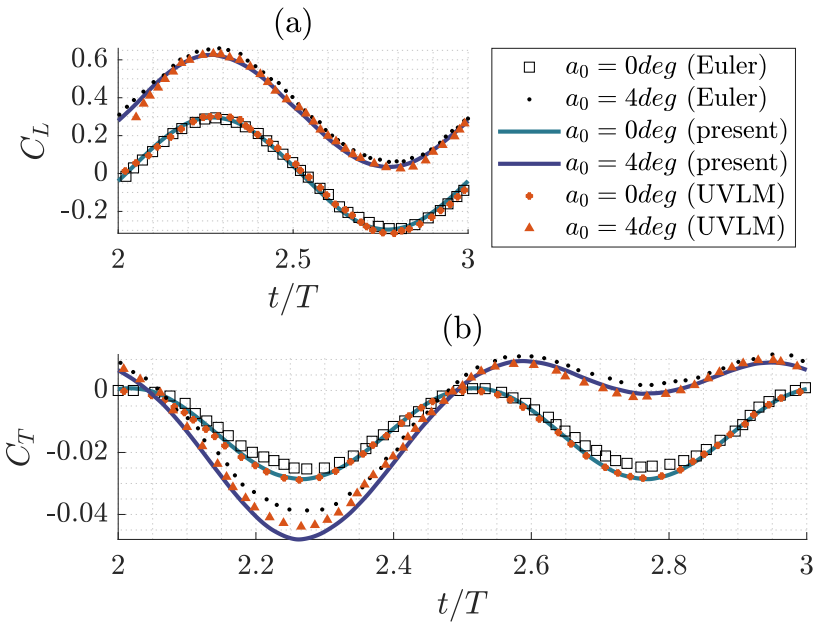

Figure 2.14: Comparison between the present method and results from [173].

The experiments in [178] are also inspired by bird flight and are one of the early experiments in this field as discussed in [181]. They conducted wind tunnel measurements on a high camber NACA 8313 wing with orthogonal planform, a blunt tip, and main dimensions $c = 76mm$, $s = 305mm$ corresponding to an aspect ratio of $AR = 4$. Concerning the manufacturing materials, the wing was shaped from a solid balsa plank and covered with a shrink-tight plastic film. No deflections were observed during the experiments. Figure 2.15 contains information regarding the experimental setup and wing kinematics. It is clamped at the root and performs an enforced $1-$dof motion mimicking the flapping (i.e. plunging) of bird flight with an amplitude of 45^o. The inflow velocity is constant and equal to $U_o = 21.4m/s$, whereas the angle of incidence with respect to the wing's leading edge is zero. The forcing and reduced frequencies are $f = 3.3s^{-1}$ and $k = \omega c/(2U) = 0.03082$ respectively.

In *3dBEM* simulations, the whole wing of aspect ratio $AR = 8$ is simulated, as shown in 2.16. The kinematics are modeled using the linear bending mode defined in Eq. (2.38). The flow in our simulations is symmetric with respect to the $xz-$plane, thus ground-effects present in the experiments are accounted for in the numerical modeling. In Vest & Katz 1996 [181], where a 3D potential-based method is proposed for flapping wing analysis, the same simulation setup is followed and their results are also taken into consideration.

Figure 2.17 contains the instantaneous lift and thrust coefficients obtained us-

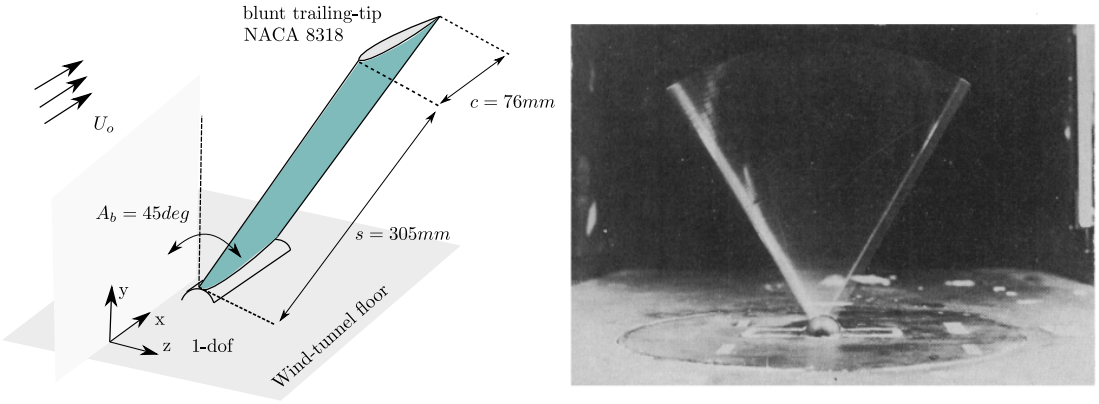

Figure 2.15: (a) Schematic representation of the wing kinematics and (b) snapshot of wind tunnel experiments in [178].

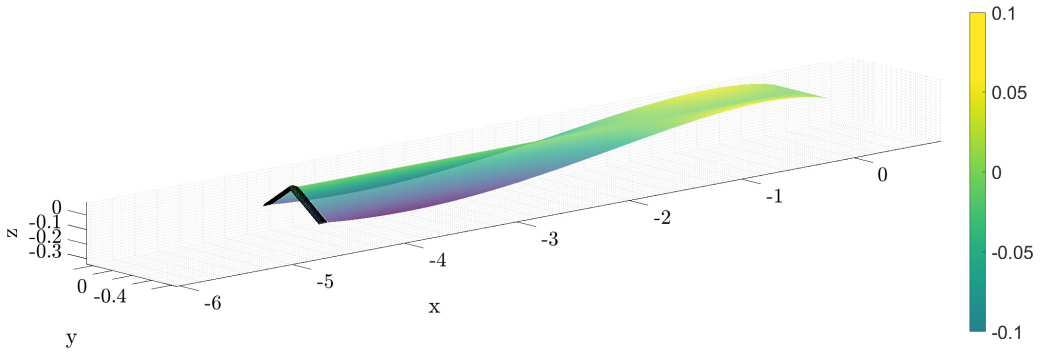

Figure 2.16: Snapshot of the simulated wing during the downstroke motion. Comparison against Fejtek & Nehera 1980 [178]. The colorbar refers to the wake's $z-$coordinates. The wing is shown with black.

ing the present method, including numerical results from [181] and the experimental data from [178]. Concerning the present method, the data shown in Figure 2.17 refer to inviscid results without friction-drag corrections, for comparison against the inviscid predictions of Vest & Katz in [181]. Viscous phenomena are dominant, especially during the downstroke, as suggested in [181], which explains the discrepancies between potential-based predictions and the experiment. Instantaneous lift is over predicted throughout the flapping cycle with greater deviations near the peaks. Simulations with *3dBEM* show a second positive peak during downstroke, suggesting that thrust is generated; results that are in accordance with [181] potential-based predictions. However, it is interesting that in the ex-

periments, during the downstroke drag is generated.

Regarding mean lift and thrust coefficients, I have included in Figure 2.17 the *3dBEM* predicted values using dashed lines and the corresponding experimental value with solid lines. The mean lift coefficient is in good agreement with the experiment, whereas mean thrust is over predicted. Present findings are contradictory to experimental results, since measurements from [178] suggest that drag is generated during each flapping cycle. Even though the 'plunging' motion is inspired from bird flight, it is evident from the experiments that birds must exploit additional mechanisms; including twist morphing that is not examined in this scenario, to generate thrust throughout each flapping cycle. If emphasis is to be given on thrust predictions, results show that a new model needs to be formulated in order to capture the dynamics of this particular bird flight scenario.

To sum up, the operational regime of bio-inspired thrusters based on flapping foils refers to small-to-moderate effective angles of attack where viscous phenomena are not dominant. In this regime, the present method provides a good compromise between computational cost and accuracy in hydrodynamic load prediction. This is supported by the summary of verification-study results presented previously.

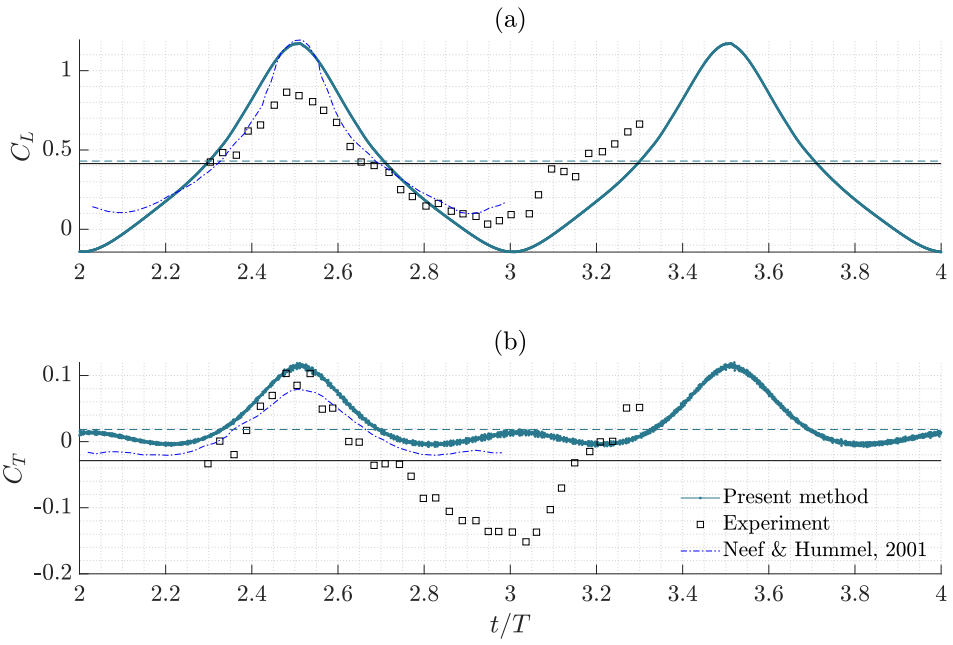

Figure 2.17: Comparison between *3dBEM*, numerical results from the potential method [181] and experimental data [178] for (a) lift and (b) thrust coefficients. Constant inflow velocity of $U_o = 21.4m/s$.

2.6 Enhancing the performance of an actively morphing thruster via optimization

Aiming towards the design of an eco-friendly propulsion system for AUVs, the concept thruster shown schematically in Figure 2.18 is considered. The wing undergoes prescribed out-of-phase heave and pitch motions, relating to the *thunniform* swimming mode depicted in Figure 1.11, superimposed with active morphing in the sense of either (i) hydrofoil adjustment or (ii) spanwise bend-twist.

Regarding the device prototype, the flapping-foil kinematics can be emulated using a robotic-arm type mechanism with two degrees of freedom based on elbow/wrist servomotors. Replicating the active morphing, would require additional internal mechanisms or the use of smart materials, see [182]. However, our focus here does not lie on the structural aspects, but rather on the investigation of efficiency enhancement due to optimal tuning of design parameters affecting the planform shape and the kinematics (i.e., rigid-body, morphing) motivated by the findings in [6], [160].

Regarding the AUV body geometry and design cruising speed, the propulsion scenario studied in [183] with $U = 2.52m/s$ is also considered here. Details concerning the propulsion scenario are provided in Table 2.8. The AUV body is modeled for simplicity as a prolate speroid with $(5:1:1)$. The total resistance of the vehicle consists of a friction-drag (based on the ITTC curve) $C_F = R_F/(0.5\rho U^2 S_{wet})$ and a wave-resistance component, which is calculated using the methodology presented in [61]. This analysis yields a thrust requirement of $\overline{C}_T = 0.32$ corresponding to the design cruising speed. Detailed calculations using a higher-fidelity method were not considered necessary using the preliminary design phase, thus the above calculations are adequate for deducing the thrust requirement.

Moreover, to quantify the performance gain obtained from the optimal tuning of the selected design parameters, a reference flapping-foil thruster, which satisfies the thrust requirement, is also considered. Relevant information regarding the reference wing geometry and flapping kinematics is summarized in Table 2.8. It is important to note that the reference thruster performs only rigid-body motions and does not morph. The reference wing has an orthogonal planform of moderate aspect ratio $AR = 3$ and NACA 0012 sections, which are assumed uniform in the direction of span.

The following section is dedicated to the study of actively morphing wings for the propulsion scenario presented above and the optimal tuning of geometric and kinematic parameters for efficiency maximization. The following section contains information regarding the optimization problem formulation. Studies are performed for each morphing type, and their findings are discussed in the sections

that follow.

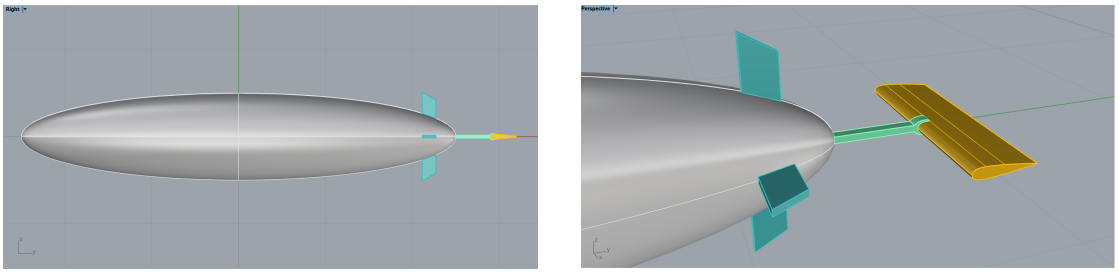

(a) Side view (b) Perspective

Figure 2.18: Schematic representation of the AUV body (as a prolate spheroid) and reference thruster configuration, including stern fin-rudder appendages.

Table 2.8: Propulsion scenario for the concept AUV.

Geometry	Prolate spheroid $(5:1:1)$	Froude number	$Fr(L_{OA}) = 0.36$
Length overall	$L_{OA} = 5m$	Friction-resistance	$C_F = 0.0025$
Surface	$S_w = 12.55m^2$	Wave-resistance	$C_W = 0.0058$
Submergence depth	$d/L_{OA} = 0.16$	Total-resistance $C_{TOT} = C_F + C_W$	$C_{TOT} = 0.0083$
Cruising speed	$U = 2.52m/s$	Thrust req.	$C_{Treq} = 0.32$

Table 2.9: Geometry and kinematics of reference flapping-foil.

Dimensions	$c = 0.33m$, $s = 1.0m$	Strouhal number $(Str = 2h_0 f/U)$	$Str = 0.26$
Sections	NACA 0012	Aspect ratio	$AR = s/c = 3$
Heave amplitude	$h_0 = 0.75c$	Planform area	$cs = 0.33m^2$
Pitch amplitude	$\theta_0 = 23.30^o$	Efficiency	$\eta = 0.64$
Pivot axis	$X_R = c/3$	Mean thrust	$\bar{C_T} = 0.32$
Phase difference	$\psi = -90^o$	Angle-of-attack (maximum)	$a_{eff}^{max} = 15^o$

2.6.1 Optimization problem formulation

Concerning the morphing flapping-foil concept, the wing planform is modeled using two parameters: the sweep angle Λ and the taper ratio $\lambda_r = c_t/c_r$, see Moran [59]. For simplicity, hydrofoil sections are assumed uniform in the direction of span. The use of more complex models for wing geometry parameterization, including the variability of thickness profiles in the direction of span, is left as future work. Regarding the kinematics, I assume that the wing follows a flapping trajectory and performs active morphing in the sense of either (i) hydrofoil adjustment or (ii) span-wise bend-twist.

Design variables. The design-variable vector,

$$b_n \in DS = \{b_n \in R_n \,|\, l_b \leq b_n \leq u_b\}, \tag{2.49}$$

with DS denoting the design space as an n-dimensional bounding box and l_b,u_b the lower/upper bounds respectively, contains parameters from the following categories:

- planform geometry (Λ, λ_r),
- rigid-body kinematics (h_0, θ_0, Str),
- hydrofoil-section morphing (A_c, ψ_c),
- spanwise bend/twist (A_b, A_γ, ψ_b, ψ_γ).

Optimal tuning of geometric and kinematic parameters is accomplished via the solution of an optimization problem on efficiency maximization under thrust and effective-angle constraints.

Objective function. Efficiency maximization,

$$\eta = U\overline{T}/P_{in}, \tag{2.50}$$

where $\overline{T}$ is the mean thrust force and P_{in} the input power required to sustain the wing's prescribed motions (flapping, morphing) under the resulting hydrodynamic loads. The objective function corresponds to the maximization of Froude efficiency, whereas the required thrust and maximum allowable effective angle of attack are included as constraints.

Constraints. Thrust requirement,

$$(1-p)C_{Treq} \leq \overline{C}_T \leq (1+p)C_{Treq}, \tag{2.51}$$

where p denotes a tolerance parameter for the thrust constraint that is set to $p = 3\%$ for all optimization studies that follow. Mean thrust is calculated using time history data from the last flapping-cycle of motion, and the constraint is valid for the inviscid value. However, the viscous-corrected mean thrust ($\overline{C}_{Tvisc}$) and efficiency (η_{visc}), for each candidate design, is also to be provided alongside the optimization results; see also Sec. 2.3.1 on friction drag corrections.

Moreover, since the effective angle of attack can serve as an indication of flow separation and dynamic-stall phenomena, an additional constraint is included to limit the maximum angle during operation. The corresponding constraint is,

$$\{\alpha_{eff}^{root}, \alpha_{eff}^{tip}\} \leq \alpha_{max}, \tag{2.52}$$

where α_{eff}^{tip}, α_{eff}^{root} are the instantaneous effective angles of attack at the tip and root respectively, evaluated using Eq. (2.45). The maximum effective angle of attack is set to 15^o for all optimization studies, assuming that this value corresponds to largely attached flows where the present an ideal-flow hydrodynamic model provides load predictions of acceptable accuracy.

The sweep angle does not affect the dimensions of chord and span, however taper ratio changes the planform area. In order to maintain the same wing surface, for comparison purposes, I keep the root chord fixed and re-define the span based on the taper ratio λ_r using,

$$s = 2S_{ref}/(c_r + c_r\lambda_r), \quad c = c_r^{ref} = 0.33m. \tag{2.53}$$

The above expression is not formulated as a constraint but rather as a limitation to the admissible set of design variables.

The examined cruising speed is relatively low and therefore the device is at no risk of cavitation. However, if higher speeds were to be examined, or operation close to the free surface, cavitation prevention criteria should be taken into consideration, see, e.g. [184].

The Reynolds number for this study is $Re = 861,600$ and the coefficients for friction-drag corrections, i.e. $C_F = 0.0039$ and $C_a = 0.13$, where calibrated via comparisons against Heathcote et al. 2008 [75] as discussed in Section 2.5.3. A typical three flapping-cycle simulation based on the linear wake model, without DtN re-calculation and a coarse discretization ($NEA = 8AR$, $NEC = 40$ and $K_1^{max} < 1.0$) requires $2-16min$ on an AMD Ryzen 9 3900XT workstation equipped with an NVIDIA GeForce RTX 3080 (10GB VRAM).

All optimization studies are run using the Matlab 2022a sequential quadratic programming (sqp) algorithm *fmincon* that is suitable for handling nonlinear constraints. For sensitivity and Hessian computations, the default option of forward differences is used. Very small step-sizes where found produce rounding errors and loss of precision even for double-precision arithmetic. Therefore, the selection of

an appropriate step-size is important prior to each optimization study based on sensitivity calculation using finite differences.

Moreover, gradient-based methods are prone to locate local optima. For engineering applications where emphasis is given on improving the reference design, this behavior is not problematic. However, an easy way to alleviate this issue is to perform the same optimization study several times, starting from different initial points using a random number generator, and to select the best candidate design out of all the solutions obtained. An optimization study stops either when the maximum number of solver calls has been reached or when converged is achieved.

2.6.2 Case 1. Chord-line morphing

For this optimization study I introduce the following design-variable vector $b_n = \{\Lambda, \lambda_r, A_r, \psi_c, Str\}$. The first two parameters are the sweep angle and taper ratio, referring to the planform shape. Then I include the amplitude of chord-line morphing and the corresponding phase difference defined in Eq. (2.37). Strouhal number is also included in the design-variable vector to ensure that the thrust requirement constraint can be satisfied. Table 2.10 contains a summary of the design-variable bounds used in this study and the optimal set of parameters as deduced from the optimization process that is discussed below. It is important to note that *fmincon* optimizer requires the determination of lower/upper bounds, however that is not the case for other gradient-based algorithms.

Table 2.10: Case 1. Design-variable bounds and optimal solution.

Description	Design variables b_n	Lower bound l_b	Optimal	Upper bound u_b
Sweep angle	Λ (deg)	0	18	25
Taper ratio	λ_r	0	1.0	1.0
Morphing amplitude	A_c/c	-0.12	0.12	0.12
Phase difference	ψ_c (deg)	0	165	180
Strouhal number	Str	0.23	0.25	0.30

Taking into consideration that gradient-based algorithms are prone to locate locally optimum solutions, I performed the same optimization study four times starting from different initial points. The maximum allowable number of solver evaluations per optimization set to $N = 300$ and the required CPU/GPU-time for all (4) optimization studies was approximately three days on our workstation, taking into consideration that each solver evaluation requires approximately $15min$.

Even though the optimization is performed using coarse mesh, linear wake model and no DtN re-calculation to save computational time, the results summarized in Table 2.11 refer to fully resolved simulations including free wake analysis, finer grids ($NEA = 9AR$, $NEC = 60$, $K_1^{max} < 1.0$) and DtN re-calculation at each time step. Coarser grids still provide engineering accuracy, however for completeness to optimization results based on finer grids and dynamic wake modeling are included. The first column of Table 2.11 contains information regarding the initial and final design variable values and below the corresponding propulsive performance metrics; in the sense of viscous corrected propulsive efficiency (η_{visc}), mean thrust coefficient ($\overline{C}_T$) based on ideal-flow predictions, viscous corrected mean thrust coefficient ($\overline{C}_{Tvisc}$) and maximum effective angle (α_{eff}) in degrees.

The best solution is deduced from the second optimization study and corresponds to $b_n = \{20^o, 1.0, 0.12, 165^o, 0.25\}$ after rounding, with a performance gain compared to the reference thruster of +16.25%. The initial solution with $id = 1$ in Table 2.11 is the reference thruster. Overall, the findings reveal that a positive amplitude for the chord-line morphing at a phase difference between $150 - 170^o$ is highly beneficial to the propulsive efficiency. Optimal Strouhal number is for this propulsion scenario is slightly lower than the reference design and equals $Str = 0.25$.

Table 2.11: Case 1. Optimization results.

	Init.				Optim.			
id	1	2	3	4	1	[2]	3	4
Λ (deg)	0.0	20.0	24.08	11.2	0.03	19.9	23.9	11.2
λ_r	1.00	0.356	0.742	0.273	0.275	1.000	1.000	0.253
s (m)	1.00	1.47	1.14	1.57	1.56	1.00	1.00	1.59
A_c/c	0.00	-0.019	-0.114	0.041	0.078	0.117	0.120	0.120
ψ_c (deg)	0.00	164.8	152.8	141.3	73.5	164.2	167.3	156.4
Str	0.260	0.286	0.295	0.265	0.239	0.251	0.251	0.254
η_{visc}	0.67	0.534	0.366	0.693	0.702	0.806	0.794	0.761
$\overline{C}_T$	0.328	0.381	0.376	0.341	0.314	0.316	0.312	0.311
$\overline{C}_{Tvisc}$	0.291	0.337	0.329	0.303	0.282	0.281	0.276	0.276
α_{eff} (deg)	15.93	18.58	19.55	16.48	13.68	14.88	14.97	15.00

Regarding the planform shape, it seems that the rectangular wing ($\lambda_r = 1.0$) yields best performance and that sweep angles do not affect significantly the results since they remains close to the initial value for all studies apart from $id = 1$. This behavior could be either attributed to the selection of step-sizes for sensitivity calculation using finite differences leading to rounding errors, or the dominant nature of the other design variables in terms of their effect on the objective function.

Moreover, sequential programming algorithms often search for a solution that satisfies the constraints by favoring the lower/upper bounds. This can be evident in the solution of $id = \{2, 3\}$ where the taper ratio receives its upper-bound value, and also $id = \{3, 4\}$ where the morphing amplitude also receives its upper-bound value. If that is the case for $id = 1$ and the value of sweep angle (i.e. receiving its lower-bound value), it is important to further investigate this matter.

To investigate further the effects of sweep angle on the propulsive performance of the chord-line morphing flapping-foil, I performed a parametric study with results shown in Figure 2.19 concerning the best candidate with design-variable vector $b_n = \{\Lambda, 1.0, 0.12, 165^o, 0.25\}$. The thrust coefficient and the propulsive efficiency are shown as functions of sweep angle suggesting the existence of an optimal value in terms of efficiency maximization at $\Lambda = 15^o$. Since the latter peak value corresponds to a thrust coefficient that is close to the lower-bound for the required thrust, I selected for the candidate thruster a sweep angle of $\Lambda = 18^o$. This value enhances the performance and has a smaller divination from original sweep $\Lambda = 19.9^o$ that was deduced from the optimization study for $id = \{2\}$ in Table 2.11.

To sum up, the propulsive performance of the reference and optimal thrusters with chord-line morphing are summarized in Table 2.12, where a performance gain of $+25.37\%$ is achieved via this optimization methodology.

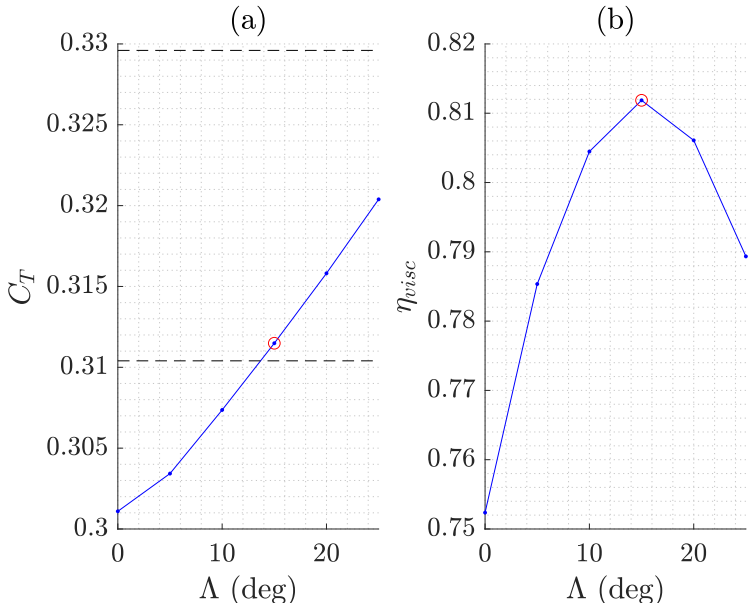

Figure 2.19: Effects of sweep angle on (a) mean thrust and (b) viscous-corrected efficiency for the candidate thruster with chord-line morphing. The region of feasible solutions is defined using dashed lines [left].

Table 2.12: Case 1. Comparison between reference and optimal designs. Optimization is performed with thrust requirement $\overline{C}_{Treq} = 0.32$.

Design variables	Reference	Optimal	
Λ (deg)	0.0	18.0	
λ_r	1.00	1.00	
s (m)	1.00	1.00	
A_c/c	0.00	0.120	
ψ_c (deg)	0.00	165	
Str	0.260	0.250	
Performance			Diff(%)
η_{visc}	0.67	0.84	+25.37%
$\overline{C}_T$	0.328	0.310	-5.5%
$\overline{C}_{Tvisc}$	0.291	0.275	-5.5%
α_{eff} (deg)	15.9	14.8	-6.9%

An interesting finding is deduced from the study of chord-line morphing profiles for the optimal thruster. Figure 2.20 contains snapshots of the wing's root section on the flapping trajectory, revealing that maximization of efficiency is achieved when the morphed shape of the chord-line is aligned with the flapping trajectory. That is the case of passively morphing wings, where proper tuning of the phase difference between wing deformation and flapping motions can enhance the propulsive performance, see, e.g. Anevlavi et al. 2020 [177].

Figure 2.21 shows a snapshot of the *3dBEM* simulations for the optimal wing design with chord-line morphing. The free-wake formation behind the wing is shown on the left, where roll-up effects are clearly evident. Red color is used to highlight the Kutta-strip. Moreover, the tip and root sections of the wing are provided on the right along with a schematic representation of the planform shape based on $c = 0.33m$, $s = 1.0m$ and sweep angle $\Lambda = 18^o$.

To examine the origin of efficiency gain I present a comparison between the instantaneous lift, thrust and moment coefficients of the reference and optimal thruster design in Figure 2.22. The corresponding planform shapes are also shown schematically. Introducing chord-line morphing leads to a phase difference that is beneficial to the efficiency without drastic reduction in the mean thrust. It is important to note, that for technological applications a more accurate estimation of power required to sustain the flapping and morphing motions is essential for predictions of efficiency.

For completeness, Figures 2.23-2.24 contain pressure coefficient envelopes for the reference and optimal thruster respectively, at selected sections along the span

and at four time instances during the last flapping-cycle of the motion. These post-processing results highlight the capabilities of *3dBEM* in terms of predicting the hydrodynamic pressure. Suggesting that this computational tool can be exploited for the analysis and optimization of bio-inspired thrusters with application to autonomous underwater vehicles.

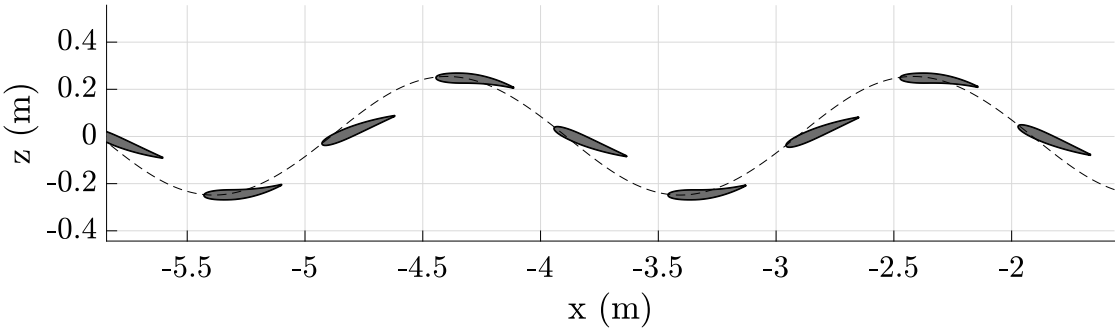

Figure 2.20: Case 1. Morphed chord-line instances for the optimal thruster on the flapping-foil trajectory, denoted with a dashed line

.

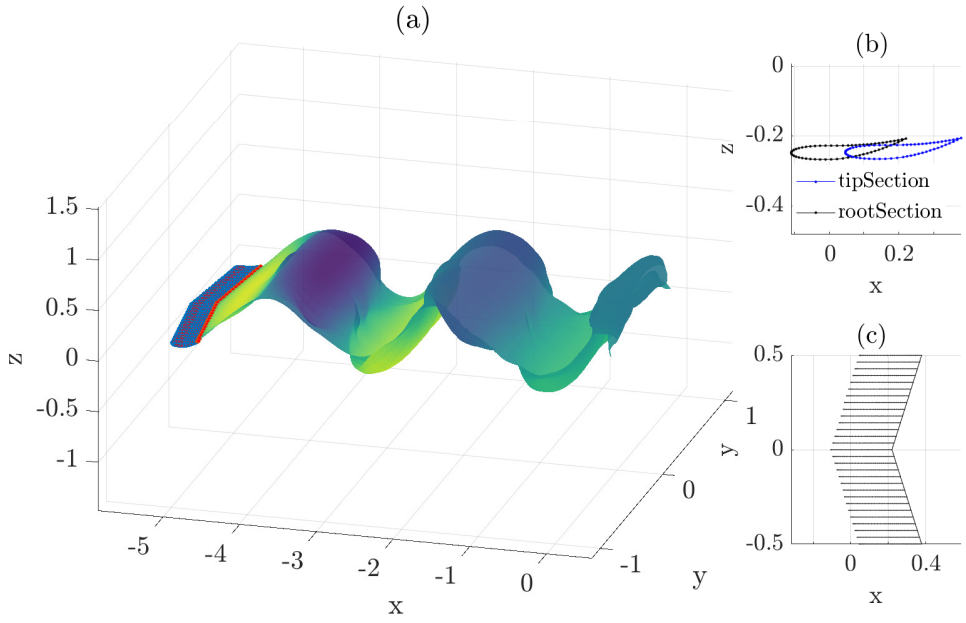

Figure 2.21: Case 1. (a) Free-wake formation for the optimal thruster with chord-line morphing, (b) root/tip sections and (c) planform shape.

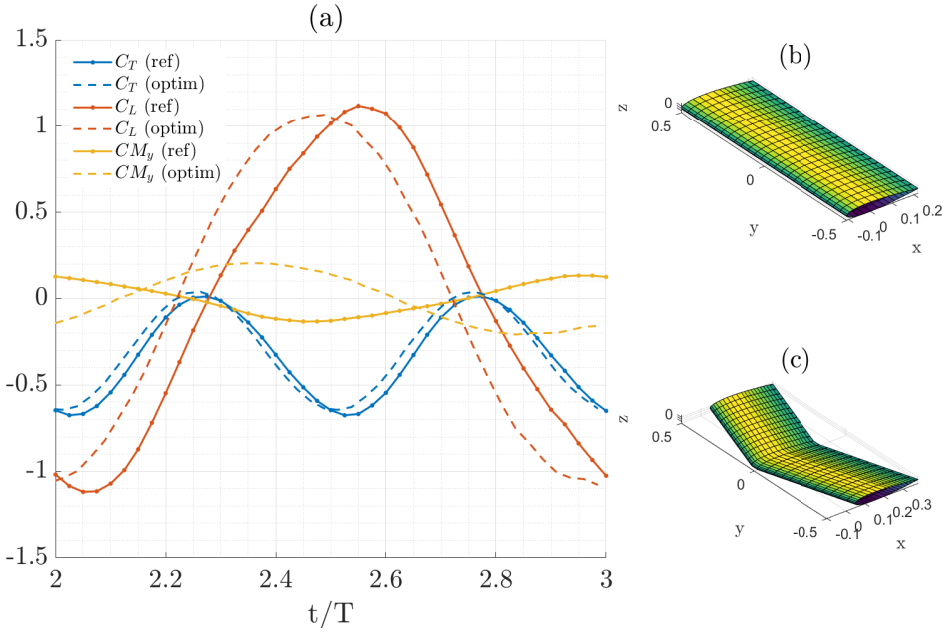

Figure 2.22: Case 1. (a) Instantaneous propulsive coefficients, (b) reference planform and (c) optimal planform.

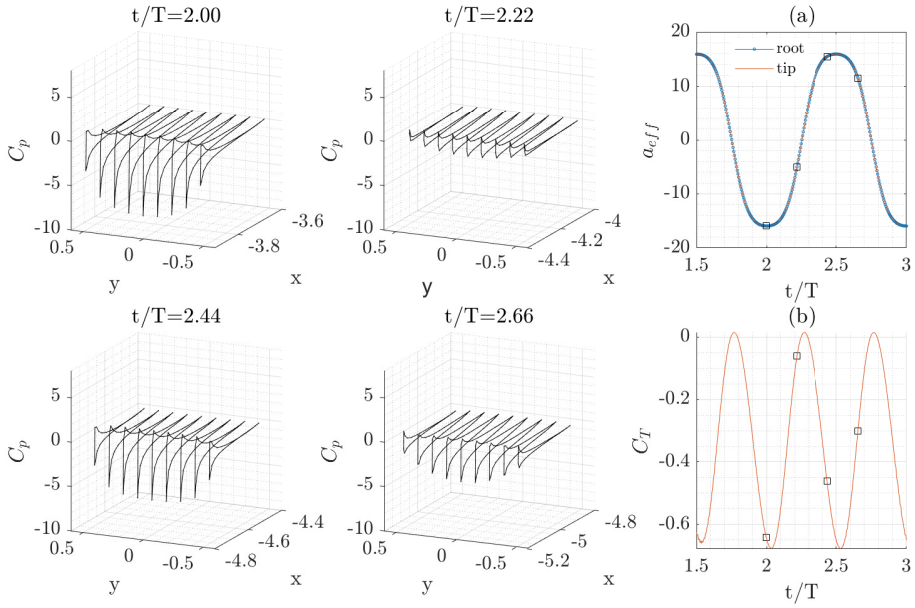

Figure 2.23: Case 1. Pressure coefficient envelopes on the reference wing [left]. Effective angle of attack and thrust time-history [right].

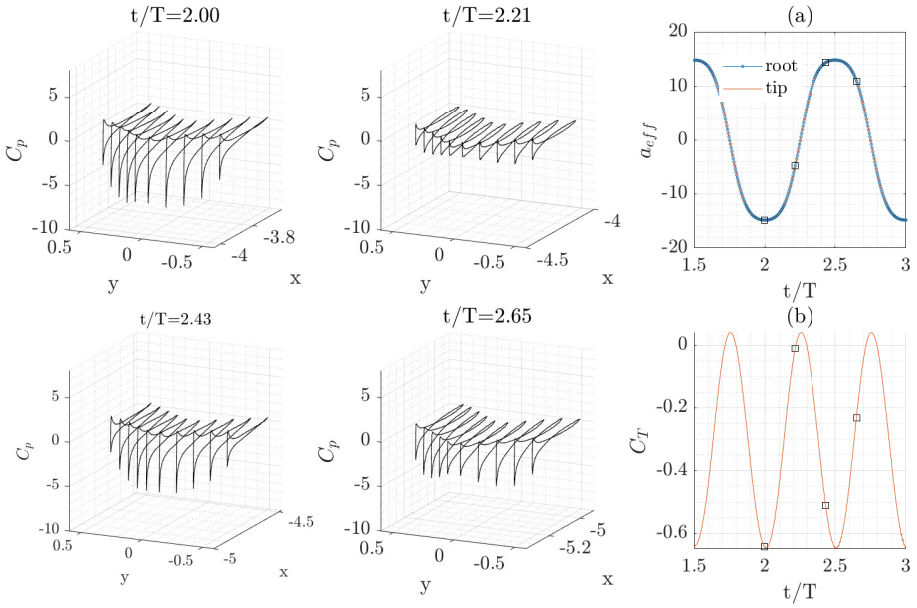

Figure 2.24: Case 1. Pressure coefficient envelopes on the optimal wing [left]. Effective angle of attack and thrust time-history [right].

2.6.3 Case 2. Spanwise bend and twist morphing

In this section, I focus on the effects of out-of-plane morphing, in the sense of active bend/twist, and their potential to enhance the propulsive performance of the flapping-foil thrusters in the selected propulsion scenario. Sweep angle has been set to the optimal value of $\Lambda = 18^o$ based on Case 1 presented in the previous section. Span-wise bending contributes significantly to the thrust production, as shown in the experiments conducted by [180]. This is also evident from bird flight studies, where twist is mainly responsible for maneuvering and weight balancing.

A direct extension of the design-variable vector used in Case 1 for this scenario would be, i.e. $b_n = \{\lambda_r, A_b, \psi_b, A_\gamma, \psi_\gamma, Str\}$. However it fails to produce a feasible design solution with enhanced propulsive performance. Thus, a redefinition of the design-variable vector so that it also includes the heave/pitch amplitudes is considered. To sum up, the design-variable vector for this case study is defined as $b_n = \{\lambda_r, A_b, \psi_b, A_\gamma, \psi_\gamma, Str, h_0/c, \theta_0\}$. Table 2.13 contains a summary of the lower/upper bounds of each parameters along with the optimal solution deduced from the optimization studies.

For this scenario I performed two optimization studies; starting from different initial points, and selected the best candidate thruster among the two. Optimization results are summarized in Table 2.14. The reference design is included as an

Table 2.13: Case 2. Design-variable bounds and optimal solution.

Description	Design variables b_n	Lower bound l_b	Optimal	Upper bound u_b
Taper ratio	λ_r	0.25	0.55	1.0
Bend amplitude	A_b (deg)	-15	5.3	15
Bend phase diff.	ψ_b (deg)	0	16	180
Twist amplitude	A_γ (deg)	-8	-2.5	8
Twist phase diff.	ψ_γ (deg)	0	110	180
Strouhal number	Str	0.23	0.25	0.30
Heave amplitude	h_0/c	0.25	1.0	1.00
Pitch amplitude	θ_0 (deg)	5	25.9	35

initial point corresponding to the study with $id = \{1\}$, whereas the study with $id = \{2\}$ start from a randomly generated initial design-variable vector.

The best candidate solution, after rounding, yields a +7.5% efficiency enhancement with moderate loss of thrust that lies within the tolerance percentage of 3%. The corresponding vector is $b_n = \{5.3^o, -2.5^o, 16^o, 110^o, 0.25, 1.0, 25.9^o, 0.55\}$. Optimization is performed based on low-computational-cost *3dBEM* simulations. For completeness, the performance metrics of the final thruster, that are summarized in Table 2.14, refer to simulations including free-wake analysis, DtN re-calculation and a finer mesh ($NEC = 60$, $NEA = 9AR$, $K_1^{max} < 1.0$) to exploit the most out of the engineering accuracy provided by the ideal-flow model.

The optimal taper ratio $\lambda_r = 0.55$ and selected sweep angle $\Lambda = 18^o$ produce a crescent-like shape, indicating that a bio-mimetic planform are beneficial to the efficiency of wings with active bend/twist. The planform shape is shown schematically in Figure 2.25, where it is evident that its span is greater than the reference geometry and $s = 1.29m$. This is essential to keep the planform surface a constant for comparison purposes.

Table 2.15 contains details regarding the propulsive performance of reference and optimal designs for comparison purposes. Regarding the effective angle of attack, it is evident that the selection of heave/pitch and Strouhal numbers in the optimal design are responsible for the large reduction of the maximum angle at the root. Concerning, the value of effective angle at the tip, it is slightly lower than the upper-bound set for the optimization study and within acceptable limits.

Moreover, Figure 2.25 contains the instantaneous lift, thrust and moment coefficients for the reference and optimal thrusters. Introducing active morphing in the sense of spanwise bend/twist also yields a phase difference that is beneficial to

Table 2.14: Case 2: Optimization study results.

		Init.		Optim.	
id	Ref.	1	2	1	2
A_b (deg)	0.0	0.0	9.70	1.73	5.28
A_γ (deg)	0.0	0.0	1.94	-2.34	-2.50
ψ_b (deg)	0.0	0.0	57.01	4.73	15.9
ψ_γ (deg)	0.0	0.0	171	34.75	110.6
Str	0.260	0.260	0.234	0.258	0.250
h_0/c	0.75	0.75	0.75	0.99	1.00
θ_0 (deg)	23.30	23.30	23.30	25.04	25.91
λ_r	1.00	1.00	1.00	0.56	0.55
s (m)	1.00	1.00	1.00	1.28	1.29
η_{visc}	0.67	0.67	0.811	0.698	0.735
$\bar{C}_T$	0.328	0.328	0.315	0.301	0.312
$\bar{C}_{Tvisc}$	0.296	0.296	0.285	0.284	0.285
α_{eff}^{root} (deg)	15.93	15.93	12.80	14.00	12.46
α_{eff}^{tip} (deg)	15.93	15.93	25.87	14.84	14.83

the efficiency with an acceptable reduction in thrust.

It is important to note that, optimal selection of the phase difference; between the morphing motions and the enforced flapping kinematics, yields the performance enhancement. This phenomenon is also observed in the previous study (Case 1) with results shown in Figure 2.22. On the left, I present a schematic representation of the wing mesh for the reference and optimal designs. The results suggest that when active bend/twist morphing is incorporated into the design a crescent-like planform contributed to efficient propulsion. On the contrary, a taper ratio did not enhance the performance of a thruster with chord-line morphing as shown in the previous study (Case 1) results.

Moving on to Figure 2.26, it contains a schematic representation of the free wake formation, the instantaneous root/tip sections and the planform shape. From root/tip section position in the global coordinate system, we can observe that indeed the optimal design has sweep and taper. In this particular snapshot, both bend and twist motions are evident.

Finally, Figure 2.27 shows the instantaneous morphed wing shape along its flapping trajectory, with the colorbar (on the right) denoting the z-coordinates, aiming to provide additional information regarding the flapping and morphing kinematics of the device.

Table 2.15: Case 2. Comparison between reference and optimal thrusters.

Design variables	Reference	Optimal	
Λ (deg)	0.0	18.0	
λ_r	1.00	0.55	
s (m)	1.00	1.28	
A_b	0.00	5.3	
A_γ	0.00	-2.50	
ψ_b (deg)	0.00	16.00	
ψ_γ (deg)	0.00	110	
h_0/c	0.75	1.00	
θ_0 (deg)	23.30	25.90	
Str	0.260	0.250	
Performance			Diff(%)
η_{visc}	0.67	0.72	+7.5%
$\overline{C}_T$	0.3280	0.3103	-5.4%
$\overline{C}_{Tvisc}$	0.2906	0.2707	-5.4%
α_{eff}^{root} (deg)	15.93	12.47	-22%
α_{eff}^{tip} (deg)	15.93	14.8	-6.9%

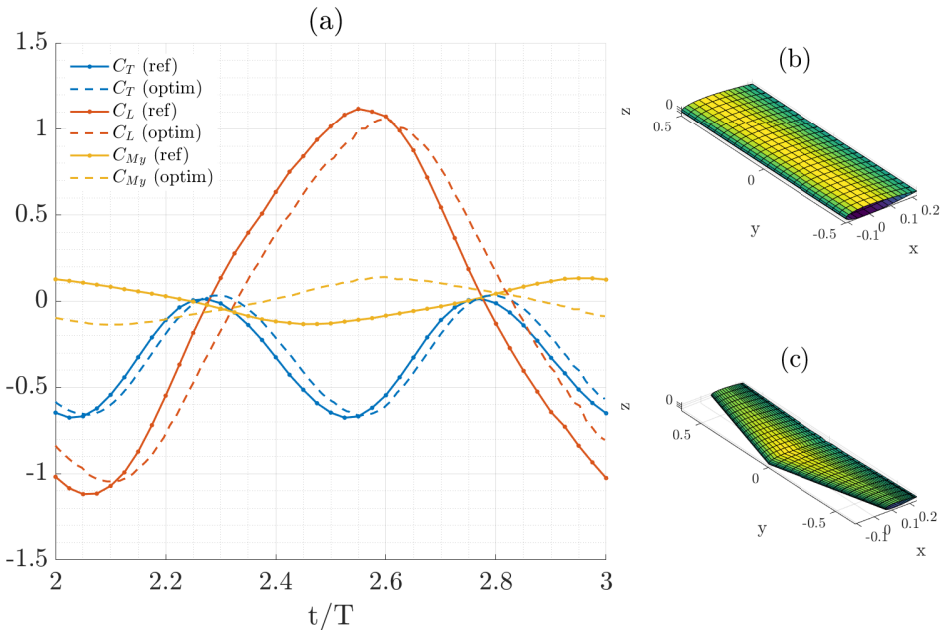

Figure 2.25: Case 2. (a) Comparison of instantaneous thrust, lift and moment coefficients, planform shape for (b) reference and (c) optimal thrusters respectively.

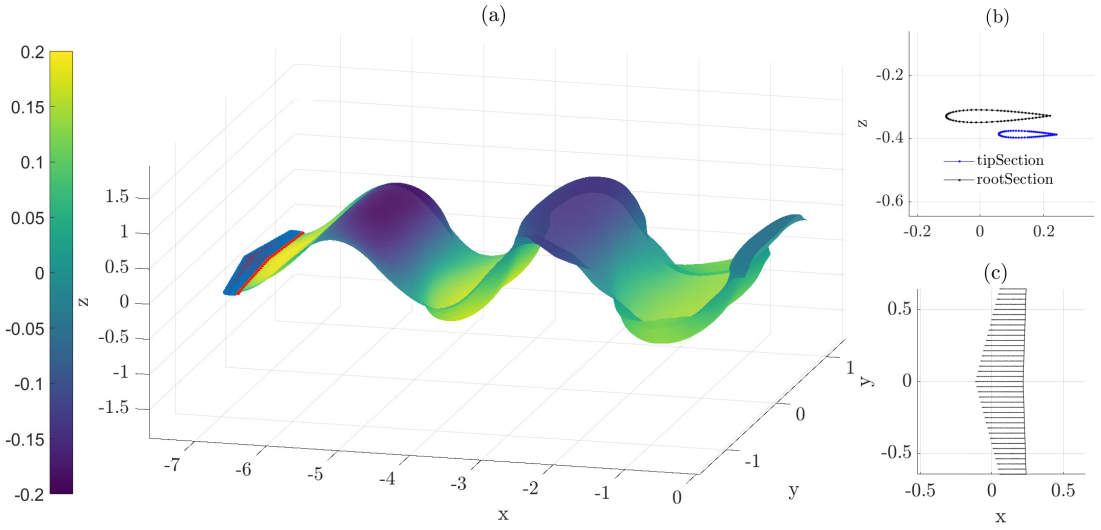

Figure 2.26: Case 2. (a) Free-wake formation behind the optimal thruster with active out-of-plane morphing, (b) root/tip sections and (c) planform shape with $\Lambda = 18^o$, $\lambda_r = 0.55$.

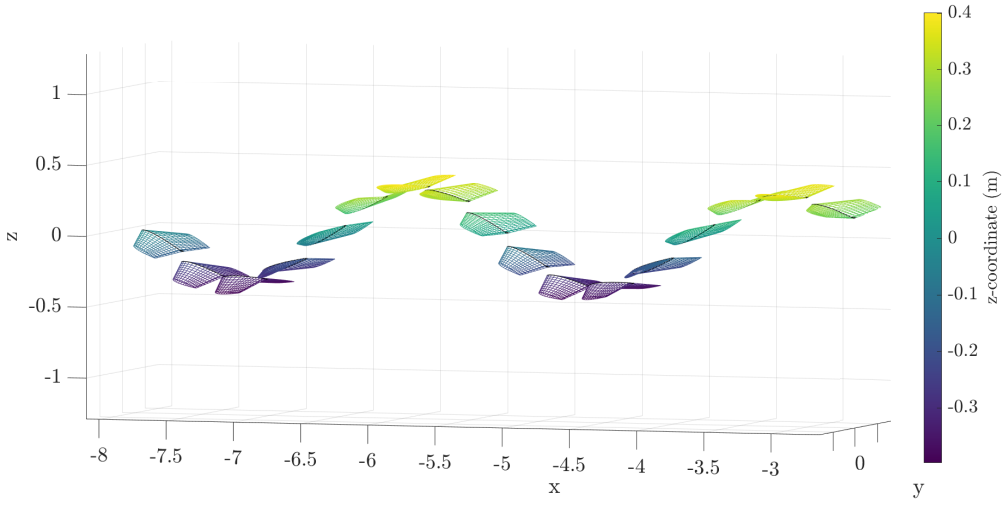

Figure 2.27: Case 2. Snapshots of the wing's morphed shapes during its flapping-type motion. The color-bar refers to the z-coordinate in global system XYZ.

2.7 Discussion and future extensions

This Chapter focuses on the study of active morphing effects on the propulsive performance of flapping thrusters with application to AUVs. The examined morphing effects are (1) hydrofoil adjustment and (2) spanwise bending/twisting during each flapping cycle of motion. To produce flapping-foil designs with improved performance, in the sense of Froude efficiency maximization under certain thrust and effective angle of attack constraints which are dictated by the adopted realistic propulsion scenario described in our paper, two optimization studies are conducted. A gradient-based solver is used and the design-variable vector contains geometric (sweep angle, taper ratio) and kinematic parameters, such as the heave/pitch amplitudes and forcing frequency (Strouhal number), alongside the active morphing parameters.

To enable fast and efficient optimization studies, targeting quantities related to hydrodynamic pressure and propulsive performance metrics for cases of actively morphing flapping-foils, I developed the *3dBEM* solver as an extension to the GPU-BEM version in Filippas et al. [12]. Particularly for the optimization, hundreds of solver evaluations are performed using a desktop within a few days using the proposed tool, whereas higher-fidelity simulations based on traditional Reynolds-Averaged Navier-Stokes equation (RANSE) based solvers would require significantly more computational time and resources. The aforementioned optimization studies support the argument that optimal tuning of morphing parameters indeed leads to a significant propulsive efficiency gain. From the perspective of hydrodynamics, the optimal selection of morphing parameters produces wing designs with enhanced propulsive efficiency delivering the required thrust.

Although ideal-flow models are able to provide low-cost and accurate predictions, enabling the optimization of efficiency via proper tuning of various geometric and kinematic parameters, a detailed analysis of the optimal designs using viscous CFD is essential for the detailed analysis of future technological applications. Therefore, CFD studies concerning operation and off-design conditions including modeling of flow separation phenomena and dynamic stall are added as future work directions.

The findings of our investigation suggest that a wing prototype with a trailing-edge flap is the most promising solution for the efficient propulsion of a small-scale AUVs. I propose the study and manufacturing of a bio-mimetic thruster with an actively controlled trailing-edge flap mechanism. The performance of the concept thruster can be be studied with the developed numerical tool *3dBEM*, additional viscous CFD simulations and towing tank experiments to provide proof of concept.

Concerning the direction of extending the present computational tool, the following aspects are proposed:

- **Free surface effects.** The mathematical formulation presented in [12] includes modeling of free surface effects and waves; affecting the performance of wings moving beneath the free surface through perturbation of the velocity profiles (i.e. due to forward motion) in the sense of a wave-induced gust. The present version of the computational code can be extended to incorporate the solver module that treats the problem of a wing operating beneath the free surface and in waves. This analysis is important for applications of wings operating as thrust-augmentation devices for ships with energy-harvesting capabilities, and AUV thrusters operating at small submergence depths. Modeling free-surface effects with viscous solvers increases further the required computational cost, thus the present extension is important since the final results would be competitive against commercial software for such applications, especially if it enables the fast hydrodynamic optimization of foils.

- **Performance predictions for complex wing geometries and marine propellers.** In nature, the cross-sectional shapes along the spanwise direction exhibit noticeable variations in camber and thickness. This is also evident in the design of aircraft wings where airfoils differ along spanwise positions, see [32]. The geometric representation of the wing can be enriched in order to account for more complex wing geometries. Parametric models for wings have been developed using Computer-Aided-Design software, that can be exploited for this purpose. The same holds for the extensions including models of marine propellers, that can be treated using the mathematical formulation behind the *3dBEM* computational tool.

- **Viscous-inviscid interaction.** The adoption of boundary-layer corrections to potential flow solvers enriches the obtained solutions from the physical point of view, [145]. In Riziotis & Voutsinas 2008 [185], a model for strong viscous-inviscid interaction coupling allows for hydrofoil performance predictions including boundary-layer and and wake shear layer evolution effects. In addition, separation effects are also modelled by introducing a second wake originating, namely a 'double-wake' model, from the separation point that is provided as part of the boundary layer solution. This particular model for instance could be implemented in a strip-wise manner to enrich the predictions of the developed *3dBEM*, allowing improved predictions at off-design points.

- **Sensitivity calculation via the adjoint method.** The standard finite difference schemes used to evaluate the sensitivity derivatives via consecutive solver calls, even for gradient-based algorithms, which are considered to be less computationally intensive than algorithms based on evolution-approach

(i.e. genetic algorithm), require computational time that is proportional to the number of design variables. Therefore, the use of an adjoint GPU-accelerated *3dBEM* solver would allow for more detailed geometric and kinematic optimization studies regardless of the number of design variables used. The surface of the wing could be parametrized using NURBS, see, e.g., [145], [186] and then integrated into the adjoint *3dBEM* optimization framework.

The *3dBEM* computational tool can also be integrated into a fluid structure interaction (fsi) framework to address the problem of flexible wings that deform passively under hydrodynamic load excitation following a partitioned approach. This is the subject of Chapters 3-4 that follow. Regarding the prospect of engineering applications on flexible foils, the literature review presented in Chapter 1 suggests that proper tuning of the material properties of the flexible wing can yield favorable deformation, i.e., changes in shape due to loading, that can enhance the device's performance. This approach lies within the state-of-the-art design of large wing turbines, where optimal selection of rigidity leads to a significant reduction in structure weight and aerodynamic loads. Relevant works are based on the use of composite materials for custom rigidity properties. However, within the context of this thesis, our effort is focused on the development of a fluid structure interaction solver for flexible wing analysis. Other extensions, concerning the use of composites and inverse design for tailor-made elasticity are left as future work.

Chapter 3

Hydromechanics of thin elastic plates

List of symbols

xyz	Cartesian local (body-fixed) coordinate system
u, v, w	displacement field
$w_0(x, y)$	field of vertical bending displacement in m
$\epsilon_{xx}, \epsilon_{yy}, \gamma_{xy}$	field of linear strains
$\sigma_{xx}, \sigma_{yy}, \sigma_{xy}$	field of stresses in Pa
$q(x, y)$	distributed load in Pa
E	Young modulus in Pa
ν	Poisson's ratio
$D(x, y)$	flexural rigidity
$h(x, y)$	thickness distribution
ρ_s	material density in kg/m^2
U_b, U_s	bending and transverse shear strain energy
$\mathbf{H}_x(\xi, \eta)$, $\mathbf{H}_y(\xi, \eta)$	Discrete Kirchhoff Triangle (DKT) shape functions
$\mathbf{q}$	global nodal unknown vector
N_{elem}	number of DKT elements
Δt	time-step
$\mathbf{M}_{loc}$, $\mathbf{M}_{glob}$	local and global mass matrix
$\mathbf{K}_{loc}$, $\mathbf{K}_{glob}$	local and global stiffness matrix
$\mathbf{f}_{loc}$, $\mathbf{F}_{glob}$	local and global load vector
$\mathbf{C}_{glob}$	global proportional damping matrix

3.1 Background

The main dimensions of the object under study often dictate appropriate structural idealizations for the analysis always with a focus on the application. Typically, for wings with relatively high aspect ratios, such as aircraft wings and applications of aero-elasticity, three-dimensional beam models can be used. The main focus of the present work lies in predicting the structural response of low-to-moderate aspect ratio wings under hydrodynamic pressure excitation. Thus, a thin plate idealization is most appropriate as suggested in Zhu (2017) [63], Dai et al. (2012) [97] and Wang et al. (2020) [63], where similar models are proposed for the analysis of flexible plates in the context of fluid-structure interaction. In our model, the homogeneous and isotropic plate has two identical faces whose dimensions (breadth, length) are considerably greater than the thickness. To account for stiffness variation effects in the context of classical thin plate models, spatial variation of thickness and Young's modulus is introduced.

The subject of plate bending based on the Kirchhoff and Mindlin plate theories for a variety of transverse loading and boundary conditions has been studied by numerous investigators, see, e.g., Wang et al. [187], Timoshenko & Krieger [188] and Reddy [189]. Standard texts on plate theory also contain derivations of closed-form solutions for the stress resultants and deflections for some plate cases, for instance, Timoshenko & Krieger [188]. However, for most engineering applications where exact solutions cannot be obtained, the designer can draw on very general finite element software to solve their plate bending problems. Commercial packages usually provide classical (or Kirchhoff) plate theory (CPT) elements and first-order shear deformation (or Mindlin) plate theory (FSDT) elements that are designated for plate analysis. The latter type of element allows for the effect of transverse shear deformation.

Recent versions of commercial software, such as ANSYS, favor analysis using multi-purpose shell elements that are able to capture the physics behind plates of various geometries under general loading conditions. Despite the computational cost these elements have gained popularity due to their versatility. In our era, modern software retrieves information on the computer architecture and exploits parallelization, for instance CPU multi-threading and parallel computing on graphics cards/accelerators. Nevertheless, the use of commercial software may enable detailed and accurate simulations of complex structures, which is important for the final stages of engineering and manufacturing, but proprietary software does not allow modifications of the source code. Thus, within the context of this thesis, it was decided that the in-house finite element solver developed in Karperaki 2021 [157] based on Discrete Kirchhoff Triangles (DKT) would be extended to address the dynamic analysis of wings modeled as thin plate structures with thickness variability.

3.2 Classical Plate Theory (CPT)

Plate theories are formally derived from the representation of displacement field components through the plates' thickness, using polynomial representations. In Wang et al. [187], the classical plate theory (CPT) for the case of pure bending is based on,

$$u(x, y, z) = -z\frac{\partial w_0}{\partial x}, \tag{3.1}$$

$$v(x, y, z) = -z\frac{\partial w_0}{\partial y}, \tag{3.2}$$

$$w(x, y, z) = w_0(x, y), \tag{3.3}$$

where (u, v, w) are the displacement components along the (x, y, z) coordinate directions, respectively, and w_0 is the transverse deflection of a point on the mid-plane (i.e., $z = 0$).

The displacement field in (3.1) is formulated under Kirchhoff's hypothesis for plate kinematics. The neutral plane coincides with the mid-surface of the structure, and the kinematic assumptions imply that,

1. straight transverse normals, which are perpendicular to the neutral mid-plate, remain straight and normal after deformation - *normal orthogonality assumption*,

2. points on the neutral line move only vertically,

3. transverse normals do not elongate after deformation,

4. normal transverse stresses are assumed negligible - *plane stress assumption*.

The fourth point carries the dimensional reduction to two dimensions. Figure 3.2 contains a geometric illustration of kinematic consideration.

A direct extension to first-order deformation theory (FSDT) by Mindlin, relaxes the orthogonality assumption and allows constant rotation of the straight transverse normals, which remain straight but not orthogonal after deformation while the rest of CPT kinematic assumptions hold [187], [190]. The additional rotations referred to as shear angles allow predictions of thin-to-moderately thick plates and can also be extended to treat problems of composite and laminate plates as discussed in Reddy [191]. This interesting direct extension is left for future work.

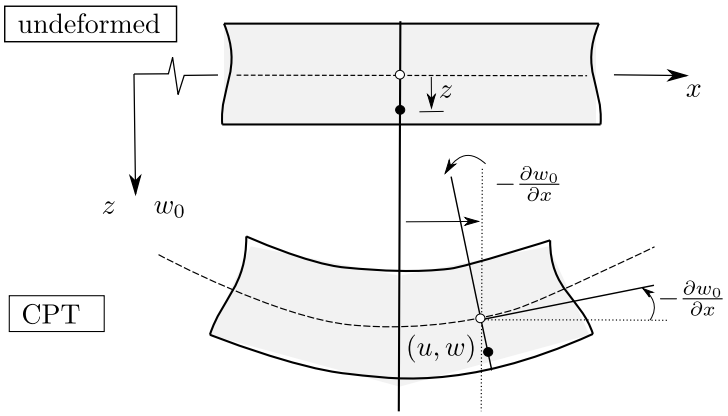

Figure 3.1: Undeformed and deformed geometries in CPT theory adapted from Wang et al. [50].

3.2.1 Equations of equilibrium

The non-zero linear strains associated with the displacement field in Eqs. (3.1) are,

$$\epsilon_{xx} = \frac{\partial u}{\partial x} = -z\frac{\partial^2 w_0}{\partial x^2}, \tag{3.4}$$

$$\epsilon_{yy} = \frac{\partial v}{\partial y} = -z\frac{\partial^2 w_0}{\partial y^2}, \tag{3.5}$$

$$\gamma_{xy} = \left(\frac{\partial v}{\partial x} + \frac{\partial u}{\partial y}\right) = -2z\frac{\partial^2 w_0}{\partial x \partial y}, \tag{3.6}$$

where $(\epsilon_{xx}, \epsilon_{yy})$ are the normal strains and γ_{xy} is the shear strain. Equilibrium equation holds as,

$$\frac{\partial^2 M_{xx}}{\partial x^2} + 2\frac{\partial^2 M_{xy}}{\partial x \partial y} + \frac{\partial^2 M_{yy}}{\partial y^2} + q(x, y) = 0, \quad in \quad \Omega_0, \tag{3.7}$$

As discussed in Zienkiewicz [192], the thin constrained theory is widely used in practice and is adequate for various structural problems. Even though it should not be taken 'literally' as the true behavior near supports or where local load action is important and three-dimensional elasticity phenomena become dominant.

3.2.2 Governing equation in terms of deflection

The corresponding expressions for the stresses are,

$$\sigma_{xx} = \frac{E(x,y)}{1-\nu^2}(\epsilon_{xx} + \nu\epsilon_{yy}), \tag{3.8}$$

$$\sigma_{yy} = \frac{E(x,y)}{1-\nu^2}(\epsilon_{yy} + \nu\epsilon_{xx}), \tag{3.9}$$

$$\sigma_{xy} = G(x,y)\gamma_{xy} = \frac{E(x,y)}{2(1-\nu)}\gamma_{xy}, \tag{3.10}$$

where $E = E(x,y)$ denotes the Young's modulus distribution, $G = G(x,y)$ the shear modulus distribution, and ν Poisson's ratio. Using Eqs. (3.8)-(3.10) and carrying out the indicated integration over the plate thickness, I arrive at

$$\begin{aligned} M_{xx} &= \int_{-h/2}^{h/2} \sigma_{xx} z dz = \frac{E(x,y)}{1-\nu^2}\int_{-h/2}^{h/2}(\epsilon_{xx} + \nu\epsilon_{yy}) z dz \\ &= -D(x,y)\Big(\frac{\partial^2 w_0}{\partial x^2} + \nu\frac{\partial^2 w_0}{\partial y^2}\Big), \end{aligned} \tag{3.11}$$

$$\begin{aligned} M_{yy} &= \int_{-h/2}^{h/2} \sigma_{yy} z dz = \frac{E(x,y)}{1-\nu^2}\int_{-h/2}^{h/2}(\epsilon_{yy} + \nu\epsilon_{xx}) z dz \\ &= -D(x,y)\Big(\nu\frac{\partial^2 w_0}{\partial x^2} + \frac{\partial^2 w_0}{\partial y^2}\Big), \end{aligned} \tag{3.12}$$

$$\begin{aligned} M_{xy} &= \int_{-h/2}^{h/2} \sigma_{xy} z dz = G(x,y)\int_{-h/2}^{h/2}\gamma_{xy} z dz \\ &= -(1-\nu)D(x,y)\frac{\partial^2 w_0}{\partial x \partial y}, \end{aligned} \tag{3.13}$$

where $D = D(x,y)$ is the flexural rigidity distribution

$$D(x,y) = \frac{E(x,y)h(x,y)^3}{12(1-\nu^2)}, \tag{3.14}$$

Assuming that the wing's thickness profile $h = h(x,y)$ is provided, an exact representation of the lifting surface geometry can be modeled via stiffness variability effects. Bio-mimicry suggests that fins in nature have variable stiffness and material properties. The present CPT formulation can also consider stiffness variability effects due to Young modulus variation, which is also useful when modeling func-

tionally graded materials. Substituting (3.11)-(3.13) to (3.7) yields,

$$\frac{\partial^2}{\partial x^2}\Big[D\Big(\frac{\partial^2 w_0}{\partial x^2}+\nu\frac{\partial^2 w_0}{\partial y^2}\Big)\Big]+2(1-\nu)\frac{\partial^2}{\partial x\partial y}\Big[D\frac{\partial^2 w_0}{\partial x\partial y}\Big] + \frac{\partial^2}{\partial y^2}\Big[D\Big(\nu\frac{\partial^2 w_0}{\partial y^2}+\frac{\partial^2 w_0}{\partial x^2}\Big)\Big]+q(x,y)=0. \tag{3.15}$$

The first term in (3.15) can be expanded as follows,

$$\begin{aligned}\frac{\partial^2}{\partial x^2}\Big[D\Big(\frac{\partial^2 w_0}{\partial x^2}+\nu\frac{\partial^2 w_0}{\partial y^2}\Big)\Big] &= \frac{\partial}{\partial x}\frac{\partial}{\partial x}\Big[D\Big(\frac{\partial^2 w_0}{\partial x^2}+\nu\frac{\partial^2 w_0}{\partial y^2}\Big)\Big] \qquad (3.16)\\ &= \frac{\partial}{\partial x}\Big[\frac{\partial D}{\partial x}\Big(\frac{\partial^2 w_0}{\partial x^2}+\nu\frac{\partial^2 w_0}{\partial y^2}\Big)+D\Big(\frac{\partial^3 w_0}{\partial x^3}+\nu\frac{\partial^3 w_0}{\partial x\partial y^2}\Big)\Big]\\ &= \frac{\partial^2 D}{\partial x^2}\Big(\frac{\partial^2 w_0}{\partial x^2}+\nu\frac{\partial^2 w_0}{\partial y^2}\Big)+\frac{\partial D}{\partial x}\Big(\frac{\partial^3 w_0}{\partial x^3}+\nu\frac{\partial^3 w_0}{\partial x\partial y^2}\Big)\\ &+\frac{\partial D}{\partial x}\Big(\frac{\partial^3 w_0}{\partial x^3}+\nu\frac{\partial^3 w_0}{\partial x\partial y^2}\Big)+D\Big(\frac{\partial^4 w_0}{\partial x^4}+\nu\frac{\partial^4 w_0}{\partial x^2\partial y^2}\Big).\end{aligned}$$

The second term in (3.15),

$$\begin{aligned}2(1-\nu)\frac{\partial^2}{\partial x\partial y}\Big[D\frac{\partial^2 w_0}{\partial x\partial y}\Big] &= 2(1-\nu)\frac{\partial}{\partial x}\frac{\partial}{\partial y}\Big[D\frac{\partial^2 w_0}{\partial x\partial y}\Big] \qquad (3.17)\\ &= 2(1-\nu)\frac{\partial}{\partial x}\Big[\frac{\partial D}{\partial y}\frac{\partial^2 w_0}{\partial x\partial y}+D\frac{\partial^3 w_0}{\partial x\partial y^2}\Big] \qquad (3.18)\\ &= 2(1-\nu)\Big[\frac{\partial^2 D}{\partial x\partial y}\frac{\partial^2 w_0}{\partial x\partial y}+\frac{\partial D}{\partial y}\frac{\partial^3 w_0}{\partial x^2\partial y}\\ &+\frac{\partial D}{\partial x}\frac{\partial^3 w_0}{\partial x\partial y^2}+D\frac{\partial^4 w_0}{\partial x^2\partial y^2}\Big].\end{aligned}$$

The third term (3.15) can be expanded as follows,

$$\begin{aligned}\frac{\partial^2}{\partial y^2}\Big[D\Big(\nu\frac{\partial^2 w_0}{\partial x^2}+\nu\frac{\partial^2 w_0}{\partial y^2}\Big)\Big] &= \frac{\partial}{\partial y}\frac{\partial}{\partial y}\Big[D\Big(\nu\frac{\partial^2 w_0}{\partial x^2}+\frac{\partial^2 w_0}{\partial y^2}\Big)\Big] \qquad (3.19)\\ &= \frac{\partial}{\partial y}\Big[\frac{\partial D}{\partial y}\Big(\nu\frac{\partial^2 w_0}{\partial x^2}+\frac{\partial^2 w_0}{\partial y^2}\Big)+D\Big(\nu\frac{\partial^3 w_0}{\partial y\partial x^2}+\frac{\partial^3 w_0}{\partial y^3}\Big)\Big]\\ &= \frac{\partial^2 D}{\partial y^2}\Big(\nu\frac{\partial^2 w_0}{\partial x^2}+\frac{\partial^2 w_0}{\partial y^2}\Big)+\frac{\partial D}{\partial y}\Big(\nu\frac{\partial^3 w_0}{\partial y\partial x^2}+\frac{\partial^3 w_0}{\partial y^3}\Big)\\ &+\frac{\partial D}{\partial y}\Big(\nu\frac{\partial^3 w_0}{\partial y\partial x^2}+\frac{\partial^3 w_0}{\partial y^3}\Big)+D\Big(\nu\frac{\partial^4 w_0}{\partial y^2\partial x^2}+\frac{\partial^4 w_0}{\partial y^4}\Big)\Big].\end{aligned}$$

Finally the CPT equation for variable flexural rigidity becomes,

$$\begin{aligned}&\nabla^4 w_0 + \nabla^2 D\nabla^2 w_0 + 2\nabla D\cdot\nabla(\nabla^2 w_0) \\ &-(1-\nu)(\partial_{xx}D\partial_{yy}w_0 - 2\partial_{xy}D\partial_{xy}w_0 + \partial_{yy}D\partial_{xx}w_0) = q(x,y).\end{aligned} \tag{3.20}$$

Or in a more compact form using the following identity from vector calculus

$$\begin{aligned}\nabla^2(D\nabla^2 w_0) &= \nabla\cdot\nabla(D\nabla^2 w_0) \\ &= \nabla\cdot(\nabla D\nabla^2 w_0 + D\nabla\cdot(\nabla^2 w_0)) \\ &= \nabla^2 D\nabla^2 w_0 + \nabla D\cdot\nabla(\nabla^2 w_0) + \nabla D\cdot\nabla(\nabla^2 w_0) + D\nabla^4 w_0 \\ &= D\nabla^4 w_0 + \nabla^2 D\nabla^2 w_0 + 2\nabla D\cdot\nabla(\nabla^2 w_0).\end{aligned} \tag{3.21}$$

The above form of is suitable for static analysis, whereas for dynamic modeling an additional term needs to be added in Eq. (3.20), see also Karperaki [157],

$$\begin{aligned}&\rho_s h(x,y)\partial_t^2 w_0 + \nabla^2(D\nabla^2 w_0) \\ &-(1-\nu)(\partial_{xx}D\partial_{yy}w_0 - 2\partial_{xy}D\partial_{xy}w_0 + \partial_{yy}D\partial_{xx}w_0) = q(x,y;t),\end{aligned} \tag{3.22}$$

where ρ_s denotes the material density and $h(x,y)$ is the plate thickness. Note that the forcing term on the *rhs* is also time-varying to model transient response.

3.2.3 Boundary conditions

In our formulation, the plate is symmetric with respect to the $xz-$plane and fully submerged within the liquid medium. The side faces of the plate are free from loading, whereas displacements and slopes are zero at the support configuration in the vicinity of the axis of symmetry. This configuration is responsible for transmitting the enforced rigid-body motions to the plate as a whole.

Conditions enforced on the primary variables (i.e., generalized displacements: w_0, $\partial w_0/\partial n$) constitute essential (or geometric) boundary conditions, whereas conditions enforced on the secondary variables (i.e., generalized forces V_n, M_{nn}) constitute natural (or force) boundary conditions. The latter is expressed in terms of the normal and tangential coordinates (n,s) on the plate boundary [187].

At a free edge (F), which is not geometrically restrained in any way, the generalized displacements of the mid-plane are not equal to zero,

$$w_0 \neq 0, \quad \frac{\partial w_0}{\partial n} \neq 0. \tag{3.23}$$

However, the edge may have applied forces and/or moments

$$V_n = Q_n + \frac{\partial M_{ns}}{\partial s} = \hat{V}_n, \qquad M_{nn} = \hat{M}_{nn}, \tag{3.24}$$

where quantities with a hat are specified forces/moments and V_n is the effective shear force. For free rectangular plates, $M_{ns} = 0$, hence no corner forces are developed.

A fixed or clamped edge (C) is fully geometrically restrained,

$$w_0 = 0, \quad \frac{\partial w_0}{\partial n} = 0. \tag{3.25}$$

Therefore, the forces and moments on a fixed edge are not known a priori (i.e., they are reactions to be determined as a part of the analysis). For clamped rectangular plates, $M_{ns} = 0$, hence no corner forces are developed.

At a simply supported edge (S),

$$w_0 = 0, \quad M_{nn} = \hat{M}_{nn}, \tag{3.26}$$

where $\hat{M}_{nn}$ is the applied normal bending moment on the edge. For simply supported rectangular plates, a reacting force of $2M_{ns}$ is developed at each corner of the plate.

3.3 Numerical implementation using finite elements

The fourth-order partial differential equations (PDE) in Eq. (3.20) and (3.22), referring to static and transient response respectively, along with a set of boundary conditions can be solved to obtain the solution in terms of the unknown transverse bending deflection $w_0(x, t; y)$. Modal analysis can also be performed numerically for in-vacuo frequency prediction under the selected boundary conditions. The numerical solution of the above problems is performed via finite element analysis, see, e.g., Hughes [193], Zienkiewicz & Taylor [192] and the standard text by Fung & Tong [194].

Producing the weak formulation for plates from the pde is quite tedious, thus the finite element formulation is derived from a Hamiltonian principle. In general, the problem of thin plates associated with fourth-order differential equations leads to a potential energy functional that contains second derivatives of the unknown function $w_0(x, t; y)$, thus the shape functions need to be characterized by C^1 continuity, i.e. the shape function and its first derivatives are continuous, which is a rather strong restriction. Polynomial expressions with many dofs are required to satisfy the strict C^1 requirement and things become even more difficult when popular schemes that work well for 1D problems, such as the Hermite interpolation functions, can not be extended to triangular meshes.

In the literature, non-conforming techniques based on *mixed formulations* have emerged over the years to construct triangle elements with few dofs that converge

to the classical thin plate solution and essentially bypass the strict C^1 continuity restriction. In the present work, the reliable and efficient Discrete Kirchhoff Triangle (DKT) introduced in Batoz et al. [195], Batoz & Lardeur [190] and [196] is selected. This triangular flat element having displacements and rotations at the corner nodes as degrees of freedom is particularly appealing for practical reasons, including modeling arbitrary plate geometries and general supports with low computational cost.

3.3.1 Discrete Kirchhoff Triangle (DKT)

The Discrete Kirchoff Triangle (DKT) is a non-conforming element with nine degrees-of-freedom (dof), three on each node. The independent quantities are the mid-surface deflection w_0, and the rotations β_x, β_y with respect to $x-$ and $y-$axis respectively as shown in Figure 3.3.1 following the sign convention adopted in Batoz et al. [195].

Before presenting details regarding the DKT element, I briefly summarize the theory of plates using matrix notation. The kinematic assumptions of small displacement theory are,

$$u = z\beta_x(x,y), \quad u = z\beta_y(x,y), \quad w = w(x,y), \tag{3.27}$$

where β_x, β_y are the rotations of a normal to the undeformed middle surface corresponding to the $x-z$ and $y-z$ planes respectively. In thin plate theory $\beta_x = -\partial_x w$, $\beta_y = -\partial_y w$. The bending strains (linear through thickness) are,

$$\boldsymbol{\epsilon}_b = z\boldsymbol{\kappa}, \tag{3.28}$$

where $\boldsymbol{\kappa}$ is the three-component curvature vector,

$$\boldsymbol{\kappa} = \begin{bmatrix} \partial_x \beta_x \\ \partial_y \beta_y \\ \partial_x \beta_y + \partial_y \beta_x \end{bmatrix}. \tag{3.29}$$

The transverse shear strains (constant through thickness) are,

$$\boldsymbol{\gamma} = \begin{bmatrix} \partial_x w + \beta_x \\ \partial_y w + \beta_y \end{bmatrix}. \tag{3.30}$$

Plane stress assumption holds, i.e. $\sigma_z = 0$, and no coupling between σ_b and transverse shear strains is considered, thus

$$\boldsymbol{\sigma}_\mathbf{b} = \begin{bmatrix} \sigma_x \\ \sigma_y \\ \tau_{xy} \end{bmatrix} = z \begin{bmatrix} D_{11} & D_{12} & D_{13} \\ & D_{22} & D_{23} \\ (sym) & & D_{33} \end{bmatrix} \boldsymbol{\kappa} = z\mathbf{D}\boldsymbol{\kappa}, \tag{3.31}$$

and

$$\boldsymbol{\sigma}_{\mathbf{s}} = \begin{bmatrix} \tau_{xz} \\ \tau_{yz} \end{bmatrix} = \begin{bmatrix} E_{13} & E_{23} \\ E_{23} & E_{33} \end{bmatrix} \boldsymbol{\gamma} = \mathbf{E}\boldsymbol{\gamma}, \tag{3.32}$$

where the E_{ij}, $i, j = 1, 3$ are the components of three-dimensional elasticity matrix,

$$D_{ij} = E_{ij} - \frac{E_{i3}E_{3i}}{E_{33}}. \tag{3.33}$$

Based on all the above, kinematic assumptions and material description, the strain energy is,

$$U = U_b + U_s, \tag{3.34}$$

where

$$U_b = \frac{1}{2}\int_A \boldsymbol{\kappa}^T \mathbf{D}_b \boldsymbol{\kappa}^T \, dxdy, \tag{3.35}$$

$$U_s = \frac{1}{2}\int_A \boldsymbol{\gamma}^T \mathbf{D}_s \boldsymbol{\gamma}^T \, dxdy, \tag{3.36}$$

represent the bending and transverse shear contributions respectively. The matrices $\mathbf{D}_b$, $\mathbf{D}_s$ are functions of the thickness $h(x, y)$ and of elastic properties. Variable A refers to the area of plate's middle surface. For the case of isotropic (homogeneous) plates with thickness variability,

$$\mathbf{D}_b = \frac{E(x,y)h(x,y)^3}{12(1-\nu)} \begin{bmatrix} 1 & \nu & 0 \\ & 1 & 0 \\ (sym) & & \frac{1-\nu}{2} \end{bmatrix}, \quad \mathbf{D}_s = \frac{E(x,y)h(x,y)k}{2(1+\nu)} \begin{bmatrix} 1 & 0 \\ 0 & 1 \end{bmatrix}. \tag{3.37}$$

The explicit expressions for U_b, U_s are,

$$U_b = \int_A \frac{Eh^3}{24(1-\nu)} \Big[\partial_x\beta_x^2 + \partial_y\beta_y^2 + 2\nu\partial_y\beta_y^2\partial_x\beta_x^2 + \frac{1-\nu}{2}(\partial_y\beta_x + \partial_x\beta_y)^2\Big] dxdy, \tag{3.38}$$

$$U_s = \int_A \frac{Ehk}{4(1+\nu)} \Big[(\partial_x w + \beta_x)^2 + (\partial_y w + \beta_y)^2\Big] dxdy. \tag{3.39}$$

The E and v are the Young's modulus and Poisson's ratio, and k is the shear correction factor usually taken as 5/6.

The transverse shear energy U_s is negligible for the kinematic assumptions, i.e. relating rotations to transverse displacement under *Kirchhoff hypothesis*. However, if shear energy is retained, the lock-free Discrete Shear Triangle (DST) for thick plates can be formulated as discussed later in Batoz & Lardeur [190]. The DST element as expected leads to the aforementioned DKT via degeneration. The benefits of using these two reliable and cost-effective elements are illustrated in the work of Karperaki [157], where finite element models of both are exploited for calculations involving simulations of large floating structures in waves.

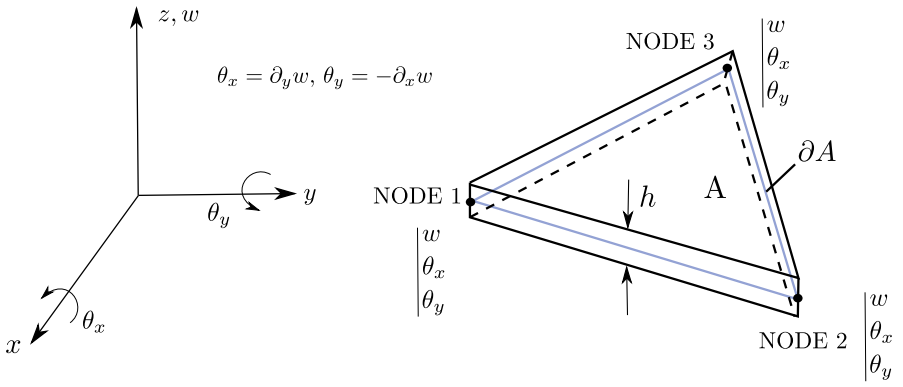

Figure 3.2: Nine dof triangular plate bending element from Batoz et al. [195]. Element edges are denoted as ∂A.

The kinematic assumptions in DKT formulation are to be introduced in a discrete way along the edges of an element to ensure compliance with the kinematic assumptions. Only C_0 continuity requirements need to be satisfied. Particularly, the Discrete Kirchhoff Triangle (DKT) formulation in [195] consists of the following,

1. Total rotations β_x, β_y are approximated using quadratic Lagrange functions over the element,i.e.

$$\beta_x = \sum_{i=1}^{6} N_i \, \beta_{x_i}, \quad \beta_y = \sum_{i=1}^{6} N_i \, \beta_{y_i}, \tag{3.40}$$

   where β_{x_i}, β_{y_i} are the nodal values at the corners $(i = 1, 2, 3)$ and mid-nodes $(i = 4, 5, 6)$, the $N_i(\xi, \eta)$ are the shape functions and ξ, η the are coordinates in the element's local coordinate system. Definition of the shape functions can be found in Batoz et al. (1980) [195] and in Appendix B for completeness.

2. Thin plate kinematic assumptions are imposed at the corner and mid-nodes respectively,

$$\beta_x + \partial_x w = 0, \; \beta_y + \partial_y w = 0, \quad \textit{at nodes } 1, 2, 3 \tag{3.41}$$

$$\beta_{s_\kappa} + \partial_{s_\kappa} w = 0, \quad \kappa = 4, 5, 6. \tag{3.42}$$

3. Hermite interpolation is used for w along the edges,

$$w_{s_\kappa} = -\frac{2}{3l_{ij}} w_i - \frac{1}{4} \partial_{s_i} w + \frac{3}{2l_{ij}} w_j - \frac{1}{4} \partial_{s_j} w, \tag{3.43}$$

   with κ denoting the mid-node of side ij and l_{ij} equal to the length of corresponding edge.

4. A linear variation of β_n is imposed along the sides, i.e.

$$\beta_{n_\kappa} = 0.5(\beta_{n_i} + \beta_{n_j}), \tag{3.44}$$

where $4, 5, 6$ denote the mid-node of sides 23, 31 and 12, respectively, see Batoz et al. [190].

From the above relations, by assuming a cubic variation of w along the sides, $w_{,s}$ follows a quadratic variation and so does β_s. Since $w_{,s}$ matches β_s at three points along each side, the Kirchhoff hypothesis (i.e. $\gamma_s = \beta_s + w_{,s} = 0$) is satisfied along each of the three boundary edges ∂A. Also, convergence toward the classical thin plate solution is obtained since the transverse shear strain energy is neglected, and because the Kirchhoff hypothesis is satisfied align the element boundary.

To obtain β_x and β_y in terms of the nodal dof vector,

$$\mathbf{U}^T = [w^{(1)} \;\; \theta_x^{(1)} \;\; \theta_y^{(1)} \;\; w^{(2)} \;\; \theta_x^{(2)} \;\; \theta_y^{(2)} \;\; w^{(3)} \;\; \theta_x^{(3)} \;\; \theta_y^{(3)}], \tag{3.45}$$

where $\theta_x = \partial_y w$, $\theta_y = -\partial_x w$ expressing the rotations with respect to the $x-$ and $y-$axis respectively holds for compatibility, the following relations are needed on each side,

$$\begin{bmatrix} \beta_x \\ \beta_y \end{bmatrix} = \begin{bmatrix} c & -s \\ s & c \end{bmatrix} \begin{bmatrix} \beta_n \\ \beta_s \end{bmatrix}, \tag{3.46}$$

and

$$\begin{bmatrix} w_{,s} \\ w_{,n} \end{bmatrix} = \begin{bmatrix} c & s \\ s & -c \end{bmatrix} \begin{bmatrix} \theta_n \\ \theta_s \end{bmatrix}, \tag{3.47}$$

where $c = cos(\mathbf{x}, \mathbf{n}_{ij})$ and $s = sin(\mathbf{x}, \mathbf{n}_{ij})$ in Figure B from Appendix B.

Consequently, the corresponding Discrete Kirchoff Triangle (DKT) shape function vectors $\mathbf{H_x}$, $\mathbf{H_y}$ (with nine components each) are defined so that they comply with all the above assumptions. Definition of shape functions $\mathbf{H_x}$, $\mathbf{H_y}$ and their derivatives is provided in Batoz et al. [195] and Appendix B for completeness. To obtain rotations in terms of the nodal dofs,

$$\beta_x = \mathbf{H_x}^T(\xi, \eta)\mathbf{U}, \tag{3.48}$$

$$\beta_y = \mathbf{H_y}^T(\xi, \eta)\mathbf{U}. \tag{3.49}$$

The curvatures can now be computed as,

$$\boldsymbol{\chi} = [\partial_x \beta_x \;\; \partial_y \beta_y \;\; \partial_y \beta_x + \partial_x \beta_y]^T = \mathbf{B_b}\mathbf{U}, \tag{3.50}$$

with

$$\mathbf{B_b} = \begin{bmatrix} \partial_x H_x^T \\ \partial_y H_y^T \\ \partial_y H_x^T + \partial_x H_y^T \end{bmatrix} = \begin{bmatrix} H_{x,\xi}^T \xi_{,x} + H_{x,\eta}^T \eta_{,x} \\ H_{y,\xi}^T \xi_{,y} + H_{y,\eta}^T \eta_{,y} \\ H_{x,\xi}^T \xi_{,y} + H_{x,\eta}^T \eta_{,y} + H_{y,\xi}^T \xi_{,x} + H_{y,\eta}^T \eta_{,x} \end{bmatrix}, \tag{3.51}$$

where using curvilinear system notation,

$$\xi_{,x} = \frac{y_{,\eta}}{J}, \quad \xi_{,y} = -\frac{x_{,\eta}}{J}, \quad \eta_{,x} = -\frac{y_{,\xi}}{J}, \quad \eta_{,y} = \frac{x_{,\xi}}{J}, \tag{3.52}$$

for which the Jacobian $J = x_{,\xi}y_{,\eta} - y_{,\xi}x_{,\eta}$ equals twice the size of each triangular element. More details regarding the expression above can be found in Batoz et al. [195].

Stiffness matrix

By means of Eqs. (3.34) and (3.3.1) the minimization principle involving the total potential energy functional, $\delta U = 0$, yields the element stiffness matrix expression,

$$\mathbf{K}_{loc} = \int_A \mathbf{B_b}^T \mathbf{D_b} \mathbf{B_b} \, dA. \tag{3.53}$$

If the thickness and material properties are constant over the element, then exact integration of $\mathbf{K}_{loc}$ is obtained using three points for numerical integration located inside the DKT element assuming Gauss quadrature.

Mass matrix

In the Discrete Kirchhoff Triangle, the rotations are represented by quadratic surfaces, and the lateral deflection (i.e. bending displacement) by cubic curves that are defined only on the edges. As it is not possible to define a consistent mass matrix for this element and therefore the pseudo-consistent mass matrix definition introduced in Sydenstricker et al. [196] is implemented.

Particularly, a cubic polunomial defines the lateral deflections w in the triangle's interiors and on the edges coincides with the curves used in DKT,

$$w = \mathbf{N_w} \mathbf{U}, \tag{3.54}$$

where $\mathbf{N_w} = \mathbf{LW} \cdot \mathbf{HW}$ following the notation in Sydenstricker et al. [196]. The mass matrix is expressed as,

$$\mathbf{M}_{loc} = \rho h \int_A \left(\mathbf{N_w}^T \mathbf{N_w} + \frac{h^2}{12} \mathbf{H_x}^T \mathbf{H_x} + \frac{h^2}{12} \mathbf{H_y}^T \mathbf{H_y} \right) dA, \tag{3.55}$$

where $\mathbf{N_w}$ are shape functions defined in Sydenstricker et al. [196] for the field of bending displacements using a pseudoconsistent formulation. The mass matrix includes rotary inertia terms involving the β_x, β_y shape functions, see, e.g. [197].

Load vector

For distributed loads, the value f_z corresponding to the element centroid is assumed constant over the whole triangle and the nodal load vector is,

$$\mathbf{f}_{loc} = f_z \frac{A_e}{3} < 1\ 0\ 0\ 1\ 0\ 0\ 1\ 0\ 0 >^T . \tag{3.56}$$

3.3.2 Integration and interpolation

In practice, most of the integrals (encountered frequently) either cannot be evaluated analytically or the evaluations are very lengthy and tedious. Numerical integration methods are preferred and the ones that employ Gaussian quadrature techniques, which were originally designed for one-dimensional cases, are used extensively. This family of quadrature has gained popularity since the formulas are simple to implement and they guarantee exact integration for polynomials less than a specified degree.

Gaussian quadrature naturally extends to two- and three-dimensional rectangular domains according to the notion of Cartesian product. Mapping techniques allow for the implementation of Gaussian quadrature to triangular domains. A Table summarizing the coordinates and weights for 3, 7 and 13-point integration over triangular domains can be found in Bathe [198] and the integration formula holds as,

$$\int\int F dr ds = \frac{1}{2} \sum c_i F(r_i, s_i), \tag{3.57}$$

where c_i denotes the weights, (r_i, s_i) the corresponding domain coordinates and $F(r_i, s_i)$ the function evaluation at the integration points.

An interpolation scheme is also essential for mapping information, such as thickness and distributed load, onto the triangle mesh. The inverse distance weighting (IDW) scheme defined in Shepard [199] is implemented for that purpose. Given a set of sample points $\{\mathbf{x}_i, u_i \,|\, for\ \mathbf{x}_i \in R_n, u_i \in R\}_{i=1}^N$, the IDW interpolation function denoted as $u(\mathbf{x}) : R^n \rightarrow R$ is defined as follows,

$$\begin{aligned} u(\mathbf{x}) &= \frac{\sum_{i=1}^N \omega_i(\mathbf{x}) u_i}{\sum_{i=1}^N \omega_i(\mathbf{x})}, \quad && if\ d(\mathbf{x}, \mathbf{x}_i) \neq 0,\ for\, all\, i \\ &= u_i, && if\ d(\mathbf{x}, \mathbf{x}_i) = 0,\ for\, some\, i, \end{aligned} \tag{3.58}$$

with

$$\omega_i = \frac{1}{d(\mathbf{x}, \mathbf{x_i})^p}, \tag{3.59}$$

where $\mathbf{x}$ denotes an interpolated (arbitrary) point, $\mathbf{x}_i$ is an interpolating (known) point, d is a given distance (metric operator) from the known point $\mathbf{x}_i$ to the

unknown point $\mathbf{x}$, N is the total number of known points used in interpolation and p is a positive real number, called the power parameter.

Scattered data interpolation will also be useful for coupling the *2dFEM* solver with the hydrodynamic solver *3dBEM* (see Chapter 2) for addressing problems of fluid-structure interaction. Moreover, since the above interpolation scheme can be implemented to each $\mathbf{x}$ independently, the routine is parallelizable. The development of a CUDA kernel for accelarating the computations related to interpolation with IDW is left as a future extension.

3.3.3 Global matrix assembly

The mesher provides all relevant information regarding the properties of each triangle and its neighbors, for the generated unstructured mesh. Each triangle is characterized by three nodes and nine degrees of freedom are assigned to it (three per node). The process for global matrix assembly based on the LM array described in Hughes [193] is implemented in the developed plate solver. First, the element nodal data array – which relates local to global node numbers – is defined as

$$IEN(a, e) = A, \tag{3.60}$$

in which a is the local node number, e is the element number, and A is the global node number. The dimensions of IEN are $M = 3$, $N = N_{elem}$. The destination array is defined as

$$ID(i, A) = P, \tag{3.61}$$

in which i the local dof number and P is the global equation number. Finally, the location matrix is defined as

$$LM(k, e) = ID(i, IEN(a, e)), \tag{3.62}$$

where k is an index from $1 - 9$, since LM has dimensions $M = 9$, $N = N_{elem}$.

3.3.4 Static and dynamic problems

The structural governing equation residuals in discretized form, with respect to $\mathbf{q}(x, y; t)$ representing the vector of unknowns in terms of transverse deflection and rotations, can be written as,

$$\mathbf{M}_{glob} \frac{d^2\mathbf{q}}{dt^2} + \mathbf{C}_{glob} \frac{d\mathbf{q}}{dt} + \mathbf{K}_{glob}\, \mathbf{q} = \mathbf{F}_{glob}(t), \tag{3.63}$$

with

$$\mathbf{q} = [w^{(1)}, b_x^{(1)}, b_y^{(1)}, ..., w^{(i)}, b_x^{(i)}, b_y^{(i)}]^T, \quad i = \{1, 2, ..N_{nodes}\}, \tag{3.64}$$

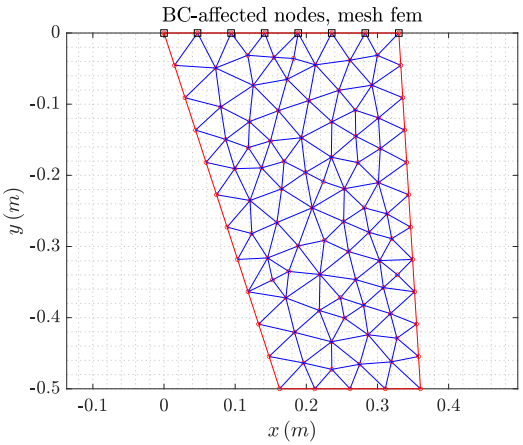

Figure 3.3: Unstructured mesh with $N_{elem} = 167$ elements generated using Delaunay triangulation. Black squares denote the nodes affected by the boundary conditions.

where i denotes the global node number in the planar mesh assumed to coincide with mid-surface of the plate and N_{nodes} is the number of DKT nodes in the mesh. Assuming that $N_{GEN} = 3N_{nodes}$ represents the total number of global unknowns, then $\mathbf{M}_{glob}$ denotes the linear structural global mass matrix of size $N_{GEN} \times N_{GEN}$, $\mathbf{K}_{glob}$ is the global stiffness matrix of size $N_{GEN} \times N_{GEN}$, $\mathbf{C}_{glob}$ is the global damping matrix of same size, and $\mathbf{F}_{glob}(t)$ is the global load vector of size $N_{GEN} \times 1$. The latter represents a pressure distribution that acts on the plate mid-surface and it is assumed to be time-varying; similar to the vector of unknowns that is also time-varying.

Plate boundary conditions. In the present study I consider the boundary condition types introduced previously in Sec. 3.2.3 and particularly the case of simply supported and fully clamped edges. Since these boundary conditions are not satisfied a priori (i.e. in a weak form), they are enforced by means of additional constraints. This approach is easy to implement and yields satisfactory results in terms of accuracy as shown in the verification studies presented in Sec. 3.4. Enforcing a fixed support at a node translates into setting the corresponding dofs to zero,

$$w^{(i)} = \theta_x^{(i)} = \theta_y^{(i)} = 0, \tag{3.65}$$

whereas for simply supported nodes only the transversal deflection is set to zero,

$$w^{(i)} = 0. \tag{3.66}$$

Satisfaction of the above boundary conditions is achieved by using the method of Lagrange multipliers leading to augmented global matrices which are formulated to

include the constraints, referring to the enforced boundary conditions, as additional equations.

Following a semi-discrete notation the augmented Eq. (3.63) takes the form,

$$\mathbf{M}_{aug}\frac{d^2\mathbf{q}_{aug}}{dt^2}+\mathbf{C}_{aug}\frac{d\mathbf{q}_{aug}}{dt}+\mathbf{K}_{aug}\,\mathbf{q}_{aug}=\mathbf{F}_{aug}(t). \tag{3.67}$$

Similarly, the vector of unknowns is also augmented to accommodate the extra equations, i.e.,

$$\mathbf{q}_{aug}=\begin{bmatrix}\mathbf{q}\\ \boldsymbol{\lambda}\end{bmatrix}, \tag{3.68}$$

where $\mathbf{q}$ is the matrix of nodal unknowns with size $N_{GEN}\times 1$ introduced previously in Eq. (3.68), $\boldsymbol{\lambda}$ is an $N_s\times 1$ matrix containing the Lagrange multiplies to be defined upon solution of the problem and N_s denotes the number of dofs associated with the boundary conditions.

An augmented stiffness matrix is introduced as,

$$\mathbf{K}_{aug}=\begin{bmatrix}\mathbf{K}_{glob} & (\mathbf{K}_L)^T\\ \mathbf{K}_L & [0]_{N_s\times N_s}\end{bmatrix}, \tag{3.69}$$

where matrix $\mathbf{K}_L$ has a size $N_s\times N_{GEN}$ and carries the implementation of Lagrange multipliers for enforcing the boundary conditions as constrains. Its transpose is used on the upper right portion of the augmented stiffness matrix. Moreover, the rows of $\mathbf{K}_L$ are defined as,

$$row_j=[\underbrace{0,...,0,}_{B_{dof}(j-1)}\ 1,\ 0,...,0\,],\quad j=\{1,...,N_s\}, \tag{3.70}$$

assuming that matrix $\mathbf{B_{dof}}$ contains the global indices of the nodal unknowns affected by the boundary conditions and has a size of $1\times N_s$. Also, the augmented force and mass matrices are defined as follows,

$$\mathbf{M}_{aug}=\begin{bmatrix}\mathbf{M}_{glob} & [0]_{N_s\times N_{GEN}}\\ [0]_{N_s\times N_{GEN}} & [0]_{N_s\times N_s}\end{bmatrix}, \tag{3.71}$$

$$\mathbf{F}_{aug}(t)=\begin{bmatrix}\mathbf{F}_{glob}(t)\\ [0]_{N_s\times 1}\end{bmatrix}. \tag{3.72}$$

From now on the global matrices are defined based on their augmented formulation and the same holds for the Rayleigh damping (see Sec. 3.3.4), that is defined using the augmented stiffness and mass matrices.

This process presented above implies that the constraints are enforced using Lagrange multipliers and following a more rigorous mathematical notation starting from the weak form we can derive the discrete form of the above equations. This approach deteriorates the condition number of the mass matrix, however the system of equations can be solved with the EIGEN sparse matrix linear solvers (LU factorization, QR factorization) using double precision arithmetic.

Rayleigh proportional damping

Classical viscous damping, also known as Rayleigh or proportional damping, is defined using a linear combination of mass and stiffness. The damping matrix $\mathbf{C}_{aug}$ is given by,

$$\mathbf{C}_{aug} = a\,\mathbf{M}_{aug} + b\,\mathbf{K}_{aug}, \tag{3.73}$$

where $a, b \in R$ are the constants of proportionality. Mass and stiffness matrices are denoted as $\mathbf{M}_{aug}$, $\mathbf{K}_{aug}$ respectively. The stiffness-proportional term contributes damping that is linearly proportional to the response frequency, whereas the mass-proportional term contributes damping that is inversely proportional to the response frequency. An example of damping ratios as a function of natural frequency is presented in Figure 3.3.4, where the first portion of the curve shows non-linearity and beyond that the curve becomes linear.

Despite its simplicity, one of the less attractive features of Rayleigh damping is that the damping ratio ζ varies with response frequency. Especially for systems with many degrees of freedom, the selection of meaningful Rayleigh damping coefficients prior to each analysis is not straightforward.

In this work, I follow the methodology described in Chowdhury & Dasgupta [200] since it produces rational estimates for damping coefficients $a, b \in R$ that take into consideration that modal mass participation decreases at higher modes. The selection methodology begins with modal analysis and identification of the significant modes ($= m$), i.e. the natural frequencies f_i. Then, I select a damping ratio ζ_1 for the first mode, and a ratio ζ_m for the m-th significant mode. For intermediate modes i, i.e., $1 < i < m$, damping ratios ζ_i are based on linear interpolation,

$$\zeta_i = \frac{\zeta_m - \zeta_1}{f_m - f_1}(f_i - f_1) + \zeta_1, \tag{3.74}$$

whereas for modes greater than m, i.e., $m < i < 2.5m$, damping ratio values are extrapolated using,

$$\zeta_i = \frac{\zeta_m - \zeta_1}{f_{m+1} - f_1}(f_i - f_1) + \zeta_1. \tag{3.75}$$

Based on the above set of data, I obtain $b_i \in R$ as,

$$b_i = \frac{2\zeta_1 f_1 - 2\zeta_i f_i}{f_1^2 - f_i^2}. \tag{3.76}$$

Then by substituting this value into the following expression I obtain $a \in R$,

$$a_i = 2\zeta_1 f_1 - b_i f_1^2. \tag{3.77}$$

Repeating the process in Eqs. (3.76)-(3.77) for the first and $n = 2.5m-$th mode yields two sets of Rayleigh damping coefficients denoted as (a_1, b_1), $(a_{2.5m}, b_{2.5m})$.

An averaging process is then used as a better approximation for the final Rayleigh coefficients,

$$a = 0.5(a_1 + a_{2.5m}), \quad b = 0.5(b_1 + b_{2.5m}). \tag{3.78}$$

For instance, if $m = 2$, then the higher mode examined for damping ratios is the $n = 5$-th mode and a modal analysis considering at least five natural frequencies is sufficient.

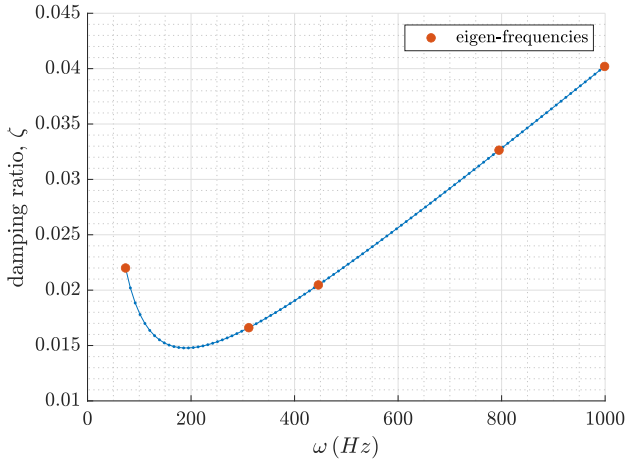

Figure 3.4: Example of Rayleigh proportional damping for $\zeta_1 = \zeta_2 = 0.022$. The first five natural frequencies given as input as shown with circles.

Time integration of equivalent 1st-order system

We can produce an equivalent system of first order equations, considering for simplicity that $\mathbf{q}$ denotes the augmented vector of unknowns defined in Eq. (3.68), by setting

$$\mathbf{u} = \begin{bmatrix} \dot{\mathbf{q}} \\ \mathbf{q} \end{bmatrix}, \tag{3.79}$$

and bring the dynamic equation into the form

$$\begin{bmatrix} \mathbf{M}_{aug} & 0 \\ 0 & \mathbf{I} \end{bmatrix} \cdot \dot{\mathbf{u}} + \begin{bmatrix} \mathbf{C}_{aug} & \mathbf{K}_{aug} \\ -\mathbf{I} & 0 \end{bmatrix} \cdot \mathbf{u} = \begin{bmatrix} \mathbf{F}_{aug}(t) \\ 0 \end{bmatrix}, \tag{3.80}$$

where $\mathbf{I}$ is the identity matrix. Based on the above and assuming that $\dot{\mathbf{u}} = \mathbf{f}(t, \mathbf{u}(t))$, where Δt denotes the time step, counter $n = \{1, ..., n_{max}\}$ for the time step index, the standard Crank-Nicolson method hold as,

$$\mathbf{u}_n = \mathbf{u}_{n-1} + \frac{1}{2}\Delta t\Big(\mathbf{f}(t_{n-1}, u_{n-1}) + \mathbf{f}(t_n, u_n)\Big). \tag{3.81}$$

Time integration of the 2nd-order system

To avoid handling a second-order system of equations, one can implement the Newmark method, considering for simplicity that $\mathbf{q}$ denotes the augmented vector of unknowns defined in Eq. (3.68) One advantage of not reducing to a system of first-order equation is that Newmark method results in matrices with better condition numbers. It is formulated in a predictor/corrector manner, depending on whether the last terms in the expressions below are retained,

$$\dot{\mathbf{q}}_n = \dot{\mathbf{q}}_{n-1} + (1-\gamma)\Delta t\, \ddot{\mathbf{q}}_{n-1} + \gamma \Delta t\, \ddot{\mathbf{q}}_n, \tag{3.82}$$

$$\mathbf{q}_n = \mathbf{q}_{n-1} + h\dot{\mathbf{q}}_{n-1} + \Delta t^2 \left(\frac{1}{2} - \beta\right)\ddot{\mathbf{q}}_{n-1} + \Delta t^2\, \beta \ddot{\mathbf{q}}_n, \tag{3.83}$$

where γ, β are quadrature parameters; typical values include $\gamma = 1/2$, $\beta = 1/6$ (linear interpolation) and $\gamma = 1/2, \beta = 1/4$ (averaging). The last term in the above expressions when omitted denotes the predictor formulas and when included the corrector expressions.

To implement the Newmark Method, I write the dynamic equation for the $n-$th time step and substitute the predictor equations above into Eq. (3.67) to produce,

$$\begin{aligned}
&\Big[\mathbf{M}_{aug} + \gamma\Delta t\, \mathbf{C}_{aug} + \beta\Delta t^2\, \mathbf{K}_{aug}\Big]\ddot{\mathbf{q}}_n = \mathbf{F}_{aug}(t)_n \\
&- \mathbf{C}_{aug}\Big[\dot{\mathbf{q}}_{n-1} + (1-\gamma)\Delta t\, \ddot{\mathbf{q}}_{n-1}\Big] \\
&- \mathbf{K}_{aug}\Big[\mathbf{q}_{n-1} + \Delta t\, \dot{\mathbf{q}}_{n-1} + \Delta t^2 \left(\frac{1}{2} - \beta\right)\ddot{\mathbf{q}}_{n-1}\Big].
\end{aligned} \tag{3.84}$$

Implementation of the predictor/corrector Newmark time integration requires the following steps,

1. Considering that the time step Δt is uniform, then we can factor once and store the expression $\Big[\mathbf{M}_{aug} + \gamma\Delta t\, \mathbf{C}_{aug} + \beta\Delta t^2\, \mathbf{K}_{aug}\Big]$,
2. The above system of equations is solved with respect to $\ddot{\mathbf{q}}_n$ and
3. The result is then substituted to the corrector expressions in Eqs. (3.82)-(3.83) to refresh predictions for the velocity and displacement respectively.

This method requires initial conditions for the acceleration, velocity and displacement $\ddot{\mathbf{q}}_{n-1},\ \dot{\mathbf{q}}_{n-1},\ \mathbf{q}_{n-1}$ to obtain estimates for the $n-$th time step (assuming that $n = 1$ at the first time step). In addition, the forcing term at $n-$the time step is needed. In cases where the forcing terms equals to zero at the first time step, estimates for the acceleration need to be produced, i.e. using Eq. (3.84) in conjunction with data for the displacement and velocity to start the time marching.

3.4 Numerical results and verification

The *2dFEM* source code is written in C/C++, routines from the standard LAPACK and BLAS libraries are used for vector/matrix operations and linear solution of sparse systems is performed using the EIGEN library. Pre- and post-processing is conducted in Matlab 2022a. Regarding the mesh generation, the Delaunay triangulation (DT) routine from the Matlab PDE Toolkit is used. All computations were performed in an AMD Ryzen 9 3900XT workstation with 32GB RAM equipped with an NVIDIA GeForce RTX 3080 (10GB VRAM).

In this section I examine problems of modal analysis for rectangular plates of constant and linearly varying thickness assuming boundary conditions that are of interest to validate DKT stiffness/mass matrices. Comparison against Navier analytic solution for a rectangular plate is included for completeness to validate the forcing vector. Finally, a study case involving a plate with varying thickness and distributed load resembling the geometry and loading condition of a wing operating as marine thruster is examined and our results compared against ANSYS Mechanical.

3.4.1 Eigenvalues and mesh sensitivity

The equation treated in the sense of modal analysis via finite elements holds as,

$$\mathbf{M}_{aug}\,\frac{d^2\mathbf{q}}{dt^2} + \mathbf{K}_{aug}\,\mathbf{q} = 0, \tag{3.85}$$

where $\mathbf{q}$ is the vector of structural displacements and rotations and $\mathbf{M}$ is the augmented mass matrix, $\mathbf{K}$ is the augmented stiffness matrix (see also Sec. 3.3.4). Assuming harmonic nodal displacements/rotations I derive the generalized eigenproblem,

$$\mathbf{K}_{aug}\,\boldsymbol{\phi} = \boldsymbol{\omega}^2\,\mathbf{M}_{aug}\boldsymbol{\phi}, \tag{3.86}$$

where ω_n the free vibration frequencies in rad/s, $\sqrt{\omega_n^2}/(2\pi)$ the eigenvalues in Hz and $\boldsymbol{\phi}_n$ the corresponding modal shape (eigen)vector, see Bathe [198].

Rectangular plates with constant thickness. In Leissa [201] comprehensive and accurate analytical results concerning the free vibration problem of rectangular plates with constant thickness based on the CPT model. All possible combinations (21) of clamped, simply supported, and free edge conditions are considered, suggesting that this work is indeed a standard reference for benchmarking in the field.

Verification of the FEM begins with comparisons against the closed-form solutions for the free vibration problem of an isotropic, homogeneous rectangular

plate with constant thickness. The following boundary conditions are considered: clamped along edges (C-C-C-C), simply supported along edges (S-S-S-S), all edges clamped and all other edges free from loading (C-F-F-F).

Regarding the boundary condition symbolism, concerning a more general example, SS-C-SS-F notation refers to a rectangular plate with the edges $x = 0$, $y = 0$, $x = a$, $y = b$ having simply-supported, clamped, simply supported, and free boundary conditions, respectively.

The completely clamped and simply supported cases are frequently used as a test problem for analytical methods because of the simplicity of the boundary conditions. Cantilever plate case is included as a benchmark since it is linked directly to technological applications involving lifting and stabilizing surfaces in the marine and aerospace industries. Table 3.2 summarizes the benchmark parameters. The comparison is performed concerning the frequency parameter $\lambda = \omega a^2 \sqrt{\rho/D}$, thus the plate properties are included to support that this study case lies within the assumptions of thin plate theory for $a/h \leq 0.1$.

Modal analysis using the *2dFEM* solver is performed using coarse and fine meshes to obtain additional information regarding mesh sensitivity and convergence. The results for all meshes, i.e. $N_{elem} = \{334, 1336, 5344\}$, are summarized in Tables 3.3-3.5 for then thin plate benchmark case. The modal frequencies obtained via numerical computations are arranged in ascending order. The coarse and fine grids are provided in Figure 3.5.

Table 3.2: Plate properties of thin plate for comparison with [201],[202].

Material properties		Geometry	
Young's modulus	$E = 210GPa$	dimensions	$a = b = 10m$
Poisson's ratio	$\nu = 0.3$	thickness	$h = 0.01m$
density	$\rho = 7850kg/m^3$	aspect ratio	$a/b = 1$
surface-density ($\rho_A = \rho h$)	$\rho_A = 78.5kg/m^2$	thickness/chord	$h/a = 0.001$

The comparison between our finite element model and the benchmark solutions from Leissa [201] suggest that our DKT solver is capable of predicting the eigenfrequencies with good accuracy as shown in Tables 3.3-3.5. It is worth mentioning that as the mesh becomes finer, convergence is achieved; however each natural frequency has its own rate of convergence. This behavior is attributed to the orientation of triangles in the unstructured mesh, since it may affects convergence.

The accuracy improves for finer mesh discretizations as expected, ensuring h-convergence. In Tables 3.3-3.4, the intermediate mesh discretization with $N_{elem} = 1336$ the accuracy is of the order of 1.0%, whereas for the fine mesh with $N_{elem} =$

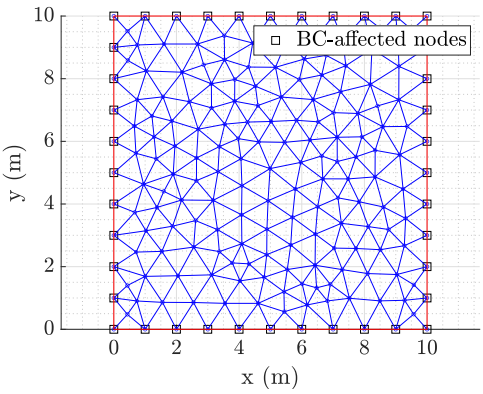

(a) $N_{elem} = 334$

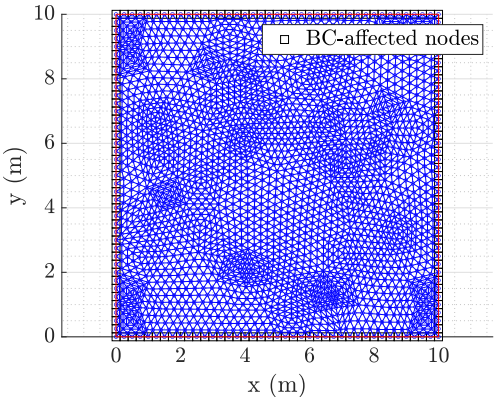

(b) $N_{elem} = 5344$

Figure 3.5: Modal analysis using (a) coarse and (b) fine mesh, with black squares indicating the boundary nodes.

5344 an accuracy of 0.2% is achieved. The results show that accuracy depends both on the discretization and boundary conditions.

Table 3.3: Frequency parameters $\lambda = \omega a^2 \sqrt{\rho h/D}$ for C-C-C-C rectangular plate with constant thickness.

id	Leissa [201]	DKT (334)	Diff(%)	DKT (1336)	Diff(%)	DKT (5344)	Diff(%)
1	35.992	36.0121	-0.0558	35.9927	-0.0019	35.9870	0.0139
2	73.413	73.6732	-0.3544	73.4735	-0.0824	73.4138	-0.0011
3	73.413	73.6961	-0.3856	73.4812	-0.0929	73.4159	-0.0040
4	108.27	109.1788	-0.8394	108.4826	-0.1964	108.2833	-0.0123
5	131.64	132.9158	-0.9692	131.9773	-0.2562	131.6832	-0.0328
6	132.24	134.8479	-1.9721	132.9123	-0.5084	132.3826	-0.1078

This is evident from Table 3.5 where the fine mesh yields an accuracy of the order of 0.70%. The C-F-F-F boundary conditions are considered more demanding than the fully-clamped case. Eigen-function contour plots are provided for completeness in Figures 3.6-3.8 related to all the examined boundary conditions. Each mode is accompanied by a color bar referring to the bending deflection w in the $z-$axis. These benchmarks verify the population of stiffness and mass matrices in the source code.

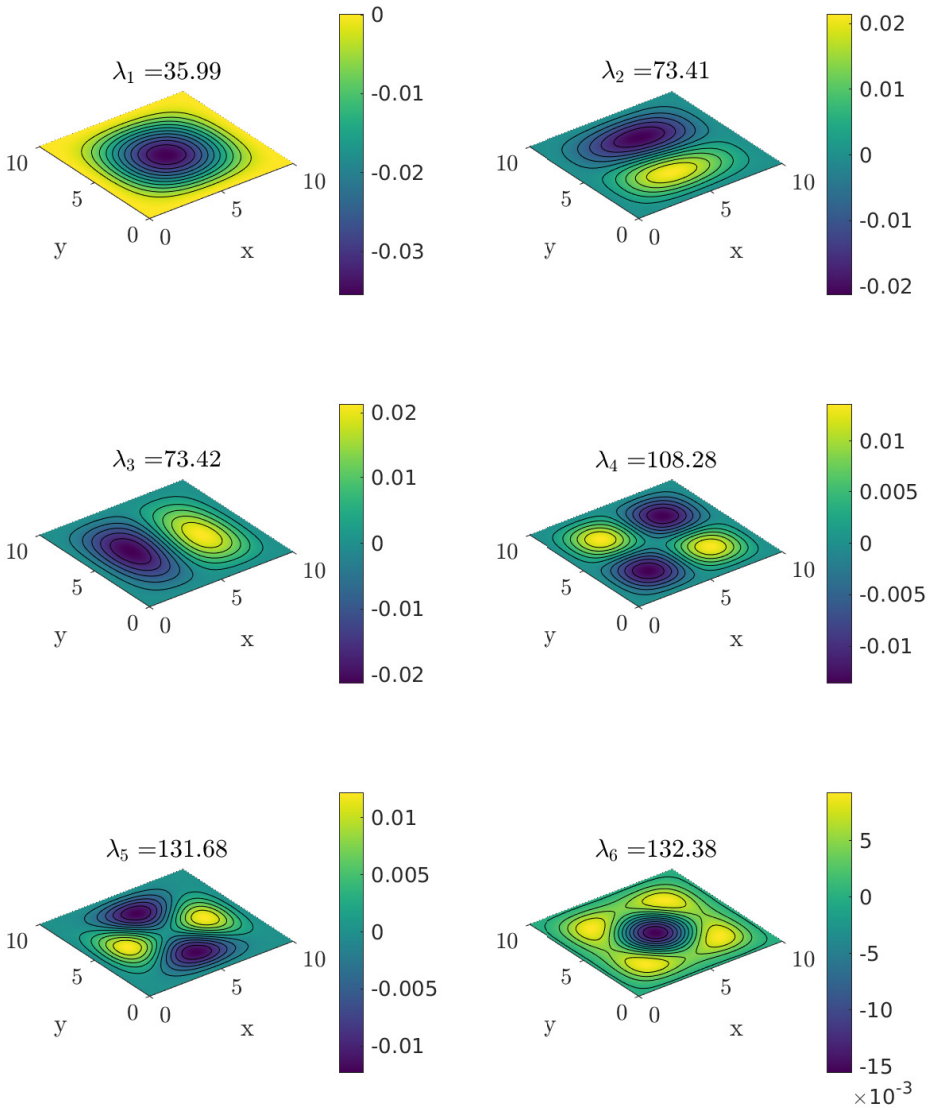

Figure 3.6: Eigenfunction contour plots for C-C-C-C results from Table 3.3 with color bar refering to the $z-$coordinate.

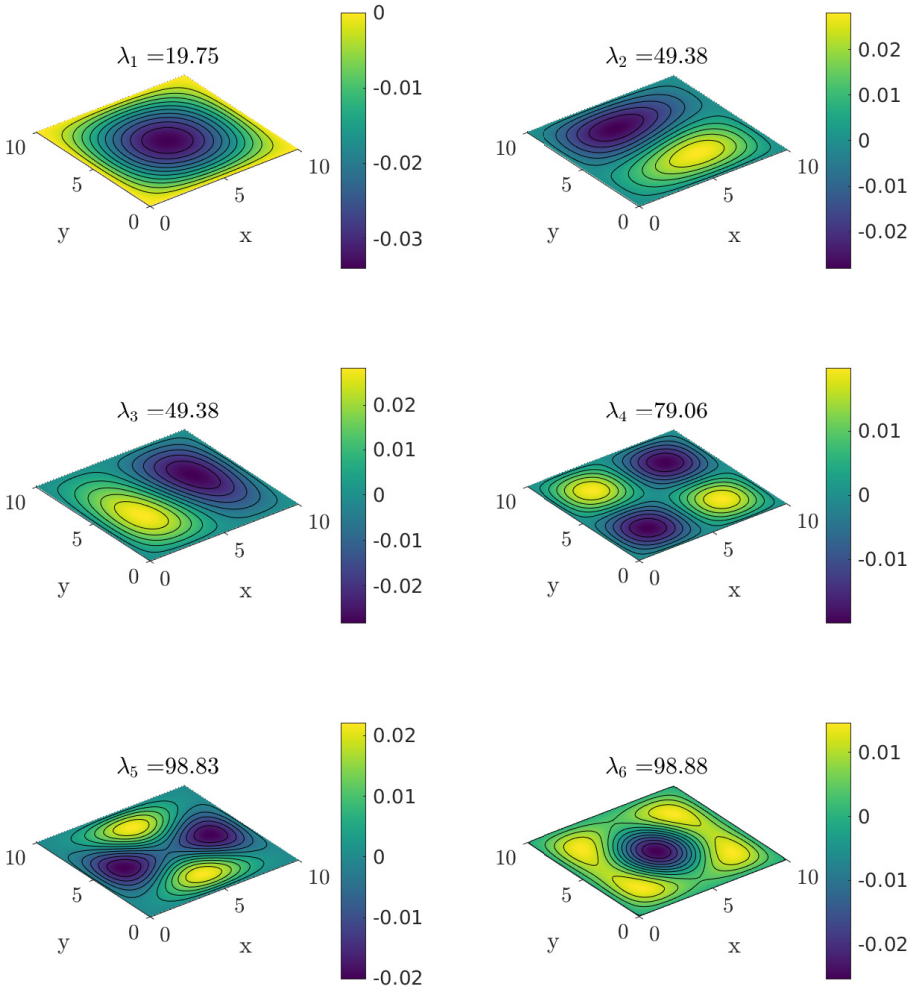

Figure 3.7: Eigenfunction contour plots for S-S-S-S results from Table 3.4 with color bar refering to the $z-$coordinate.

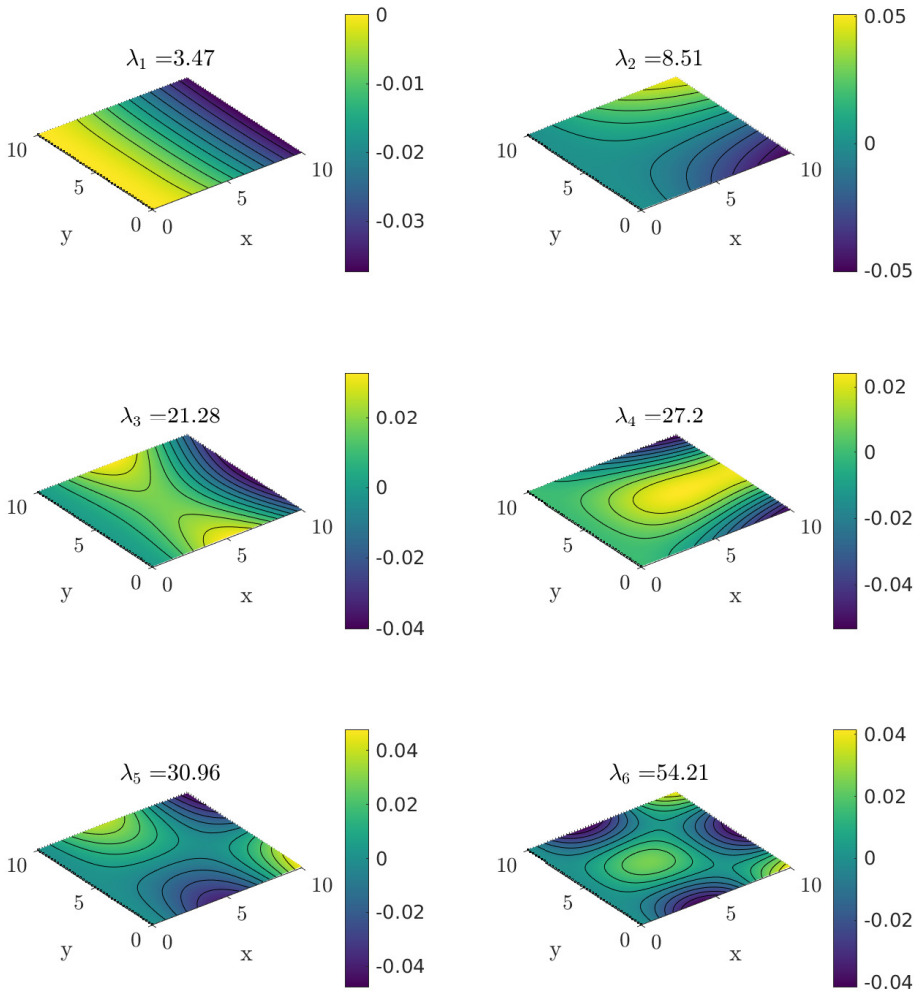

Figure 3.8: Eigenfunction contour plots for C-F-F-F results from Table 3.3 with color bar refering to the $z-$coordinate and plate clamped along $x = 0$.

Table 3.4: Frequency parameters $\lambda = \omega a^2\sqrt{\rho h/D}$ for S-S-S-S rectangular plate with constant thickness.

id	Leissa [201]	DKT (334)	Diff(%)	DKT (1336)	Diff(%)	DKT (5344)	Diff(%)
1	19.7392	19.8320	-0.4701	19.7626	-0.1185	19.7451	-0.0299
2	49.3480	49.8485	-1.0142	49.4771	-0.2616	49.3804	-0.0657
3	49.3480	49.9212	-1.1615	49.4947	-0.2973	49.3847	-0.0744
4	78.9568	80.5741	-2.0483	79.3722	-0.5261	79.0610	-0.1320
5	98.6960	100.6417	-1.9714	99.2081	-0.5189	98.8250	-0.1307
6	98.6960	101.5332	-2.8747	99.4196	-0.7332	98.8773	-0.1837

Table 3.5: Frequency parameters $\lambda = \omega a^2\sqrt{\rho h/D}$ for C-F-F-F rectangular plate with constant thickness

id	Leissa [201]	DKT (334)	Diff(%)	DKT (1336)	Diff(%)	DKT (5344)	Diff(%)
1	3.4917	3.4674	0.6959	3.4702	0.6157	3.4708	0.5986
2	8.5246	8.4045	0.2358	8.5059	0.2194	8.5062	0.2158
3	21.429	21.2803	0.6939	21.2835	0.6790	21.2838	0.6776
4	27.331	27.1772	0.5627	27.1947	0.4987	27.1977	0.4877
5	31.111	31.0194	0.2944	30.9730	0.4436	30.9590	0.4886
6	54.443	54.6274	-0.3387	54.3050	0.2535	54.2140	0.4206

Rectangular plates with linearly varying thickness. For the analysis of plates with thickness variation, in our implementation each DKT element receives information concerning the local thickness on its centroid. Thus, thickness is assumed constant within each element. Shepard interpolation with parameter $p = 2.55$ is used to assign thickness values to each element based on scattered thickness data.

In Katsikadelis & Sapountzakis [202] results concerning the free vibration of linearly tapered plates along the $x-$axis based on a boundary element method are presented. The thickness profile in SI units is defined as,

$$h(x, y) = h_o(1 + \tau_x \frac{x}{a}), \quad x \in [x_o, x_1] = [0, a]. \tag{3.87}$$

where $\tau_x = h_1/h_o - 1$ denotes the taper ratio and $h_o = h(0, y)$, $h_1 = h(a, y)$ are known values. Based on the above profile, the thickness along $x = 0$ is less than thickness along $x = a$, i.e. $h_o < h_1$.

The case of a fully-clamped plate with properties based on Table 3.2 is selected

for comparison. Table 3.6 contains frequency parameter results obtained from the present method and compared against Katsikadelis & Sapountzakis [202] and Kuttler at al. [203]. The latter consists of a finite element model based on the CPT with which our predictions are in very good agreement (0.3% accuracy).

The deviations observed regarding the comparison against Katsikadelis & Sapountzakis [202] results are more evident in higher frequencies and can be attributed to their numerical implementation using boundary elements. It is important to note that results in [202] deviate (up to 3.95%) from the analytic solution in Leissa [201] for C-C-C-C thin rectangular plates with constant thickness. Since, our method is in excellent agreement (0.1% accuracy) with Leissa [201] for this standard case as shown in Table 3.3, the deviations observed for the linearly tapered case are justified. Regarding the C-F-F-F rectangular plate with linear taper

Table 3.6: Frequency parameters $\Omega = \omega a^2\sqrt{\rho_A(h_o)/D(h_o)}$ for C-C-C-C rectangular plate with taper ratio $\tau_x = 0.2$ ($h_o = 0.01m$, $h_1 = 0.012m$).

	$\tau_x = 0.2$			$\tau_x = 0.4$		
id	Katsikadelis [202]	Kuttler [203]	DKT (5344)	Katsikadelis [202]	Kuttler [203]	DKT (5344)
Ω_1^2	$0.1553{\cdot}10^4$	$0.1559{\cdot}10^4$	$0.1557{\cdot}10^4$	$0.1827{\cdot}10^4$	$0.1837{\cdot}10^4$	$0.1832{\cdot}10^4$
Ω_2^2	$0.6182{\cdot}10^4$	$0.6443{\cdot}10^4$	$0.6471{\cdot}10^4$	$0.7251{\cdot}10^4$	$0.7605{\cdot}10^4$	$0.7587{\cdot}10^4$
Ω_3^2	$0.6212{\cdot}10^4$	$0.6469{\cdot}10^4$	$0.6483{\cdot}10^4$	$0.7383{\cdot}10^4$	$0.7632{\cdot}10^4$	$0.7630{\cdot}10^4$
Ω_4^2	$0.1390{\cdot}10^5$	$0.1407{\cdot}10^5$	$0.1411{\cdot}10^5$	$0.1639{\cdot}10^5$	-	$0.1664{\cdot}10^5$

in the $x-$axis, relevant results are also presented in Shufrin & Eisenberger [204]. The thickness profile along the $x-$axis in their study is based on,

$$h(x, y) = h_o(1 - \tau_x \frac{x}{a}), \quad x \in [x_o, x_1] = [0, a]. \tag{3.88}$$

where τ_x denotes the taper ratio. Based on the above profile $h_o > h_1$. Regarding the plate properties I consider data from Table 3.2, however the thickness is assumed to be on the limit of moderately thick plates with $h_o/a = 0.1$, since [204] examines standard and higher-order plate models.

Table 3.7 contains the comparison results against the CPT model in Shufrin & Eisenberger [204]. We can observe that the first two frequencies are predicted with good accuracy, whereas for higher frequencies discrepancies are evident.

Table 3.8 contains results concerning the C-C-C-C case with $\tau_x = 0.25$ for reference, where it is shown that for the standard case a deviation of up to 3% is observed at higher frequencies. Deviations can be attributed to the interpolation scheme based on which the distributed thickness properties are assigned to each

element in our solver and also consideration of boundary conditions via augmentation of the system of equations. The C-F-F-F problem is considered challenging and taking into consideration that I compared against another numerical model, the results overall lie within acceptable limits.

Table 3.7: Frequency parameters $\lambda_s = \omega a^2 \sqrt{\rho h_o / D(h_o)}/\pi^2$ for C-F-F-F rectangular plate with taper ratio $\tau_x = 0.5$ ($h_o = 1.0m$, $h_1 = 0.5m$).

id	Shufrin [204]	DKT (5344)	Diff(%)
1	0.3859	0.3816	1.13
2	0.7563	0.7541	0.29
3	1.8485	1.7598	4.79
4	1.9438	1.9924	-2.50
5	2.4184	2.3659	2.17
6	4.0317	3.9625	1.71

Table 3.8: Frequency parameters $\lambda_s = \omega a^2 \sqrt{\rho h_o / D(h_o)}/\pi^2$ for C-C-C-C rectangular plate with taper ratio $\tau_x = 0.25$ ($h_o = 1.0m$, $h_1 = 0.75m$).

id	Shufrin [204]	DKT (5344)	Diff(%)
1	3.1767	3.1630	0.43
2	6.4650	6.3801	1.31
3	6.4782	6.3920	1.33
4	9.5610	9.3505	2.20
5	11.5702	11.2599	2.68
6	11.6375	11.3580	2.40

The eigenfunction contours are included in Figure 3.9 for comparison purposes against Figure 3.8, where we can observe the effects of linear thickness variation on the nondimensional frequencies and the eigenfunctions. All the above test cases support the validity of the developed numerical tool for thin tapered plate analysis.

3.4.2 Static response

The system of equations treated via finite element analysis is,

$$\mathbf{K}_{aug}\,\mathbf{q} = \mathbf{F}_{aug} \tag{3.89}$$

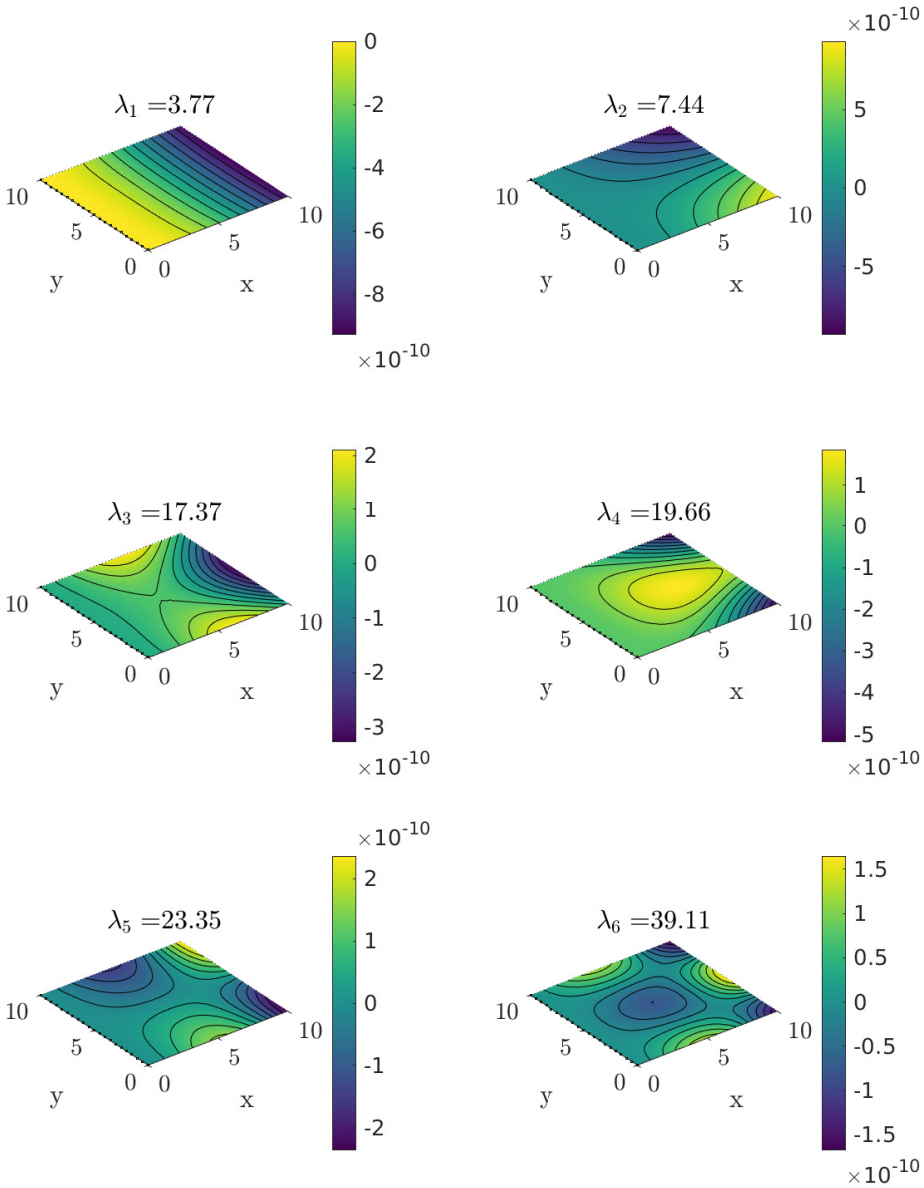

Figure 3.9: Eigenfunction contour plots for C-F-F-F results from Table 3.7 with color bar referring to the $z-$coordinate.

where q is the vector of structural displacements/rotations, $\mathbf{K}$ is the augmented stiffness matrix and $\mathbf{F}$ the augmented load vector in Pa (see also Sec. 3.3.4).

Navier solution for S-S-S-S rectangular plate. Next, the static solution under (i) uniform and (ii) concentrated loading scenarios is considered. For the simply supported plate with constant thickness, numerical results are compared against analytical solutions. Navier solutions for the S-S-S-S rectangular plate case are derived by means of Fourier series representations [188]. For the case of uniform load, the plate deflection is expressed as

$$w(x,y) = \frac{16p_0}{D\pi^6} \sum_{n=1,3,5..} \sum_{n=1,3,5..} \frac{sin(m\pi x)sin(n\pi y)}{mn(m^2/a^2 + n^2/b^2)^2}, \tag{3.90}$$

where a, b are the $x-$ and $y-$expanded dimensions respectively. For the concentrated load positioned at (ξ, η) the deflection reduces to,

$$w(x,y) = \frac{16p_0}{Dab\pi^6} \sum_{n=1,3,5..} \sum_{n=1,3,5..} \frac{sin(m\pi\xi/a)sin(n\pi\eta/b)sin(m\pi x/a)sin(n\pi y/b)}{mn(m^2/a^2 + n^2/b^2)^2}. \tag{3.91}$$

Setting $p_o = 100N$ and keeping a large number of terms to ensure convergence, the results for $(\xi, \eta) = (5, 5)$ are presented in Table 3.9 and Figure below. The plate properties are provided in Table 3.2, and a mesh of $N_{elem} = 1336$ is considered.

Regarding the sign convention of the present formulation, loads and displacements are positive when directed towards the positive z-axis. The results are in excellent agreement with the analytical solution. The selected test case illustrates that concentrated load conditions lead to higher bending displacement compared to the same load uniformly distributed along the surface of the plate.

Table 3.9: Maximum bending displacement w_0^{max} (m) for static load cases.

	Timoshenko [188]	DKT (1336)	Diff(%)
concentrated	$0.6015{\cdot}10^{-2}$	$0.6034{\cdot}10^{-2}$	+0.3070
uniform	$0.2111{\cdot}10^{-2}$	$0.2108{\cdot}10^{-2}$	-0.1427

Rectangular plate with constant thickness under distributed load. The following test case is included to verify that the present numerical tool is capable of predicting bending displacements under distributed load conditions. I compared results obtained with the *2dFEM* solver against ANSYS Mechanical 2023

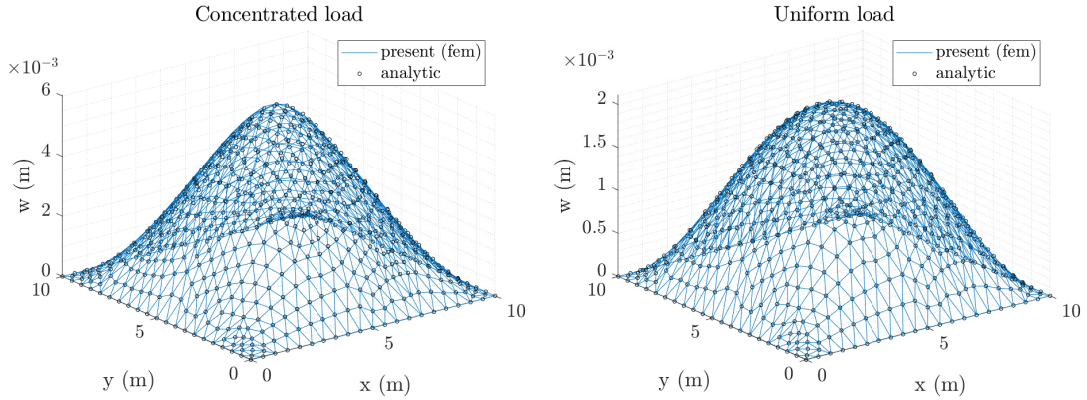

(a) $p_o = 100N$ (b) $p_o = 1Pa$

Figure 3.10: Comparison with Navier solution in [188] for S-S-S-S rectangular plate with properties in Table 3.2 under (a) concentrated and (b) uniform load.

R2 (Student) for a rectangular plate with properties shown in Table 3.2 under a distributed load given by,

$$f_x = \frac{1}{s}\sqrt{2\pi}\, exp\Big(-0.5[(x_0 - m)/s]^2\Big), \quad x_0, y_0 \in [-1, 1], \tag{3.92}$$

$$x = a \cdot 0.5(1 - x_0), \quad y = b \cdot 0.5(y_0 + 1),$$

where $s = 0.2$,$m = 0.6$ are parameters and a, b are the main plate dimensions. The distributed load over the plate surface is shown schematically in Figure 3.11. For this example, Shepard interpolation parameter $p = 5.55$ is considered for mapping the distributed load data onto the fem plate elements.

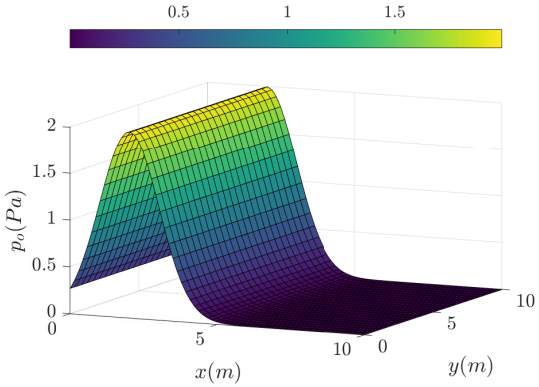

Figure 3.11: Distributed load scenario for *2dFEM*. Positive load yields bending deflection in the same direction.

Regarding the boundary conditions C-F-F-F (clamped along $x = 0$) and F-F-C-F (along $x = a$) are considered. This distribution in Eq. (3.92) resembles the hydrodynamic loading of a wing that undergoes a prescribed flapping motion, these boundary conditions are of value. Particularly, C-F-F-F models a flapping wing that is actuated from its leading edge. Similarly, F-F-C-F models a T-foil scenario, where due to symmetry only the half wing is simulated and the clamped edge corresponds to the location of the vertical skeg.

ANSYS Mechanical is a commercial software that is used worldwide for education and industry applications. It is important to note that the sign convention in ANSYS Mechanical differs from *2dFEM* since negative pressure yields positive bending displacements. For comparison purposes, we used the legacy SHELL36 element which is very similar to the DKT for thin plates. In Geometry < Surface Body < Commands (APDL), the following lines can be added to control the element used in the simulations and plate thickness

$$
\begin{aligned}
&et,\ matid,\ SHELL63\\
&etcontrol,\ set,\ on\\
&r,\ matid,\ 0.01
\end{aligned}
$$

The distributed load is imported as tabulated data (in .csv format) using the 'External Data' from the 'Component Systems' in ANSYS Workbench and it is linked to the Setup, see also the ANSYS GUI in Figure 3.15. Similarly, for the case of variable thickness plates, tabulated data can be imported using 'External Data' to incorporate distributed thickness profiles into the analysis. However, in this case, it is linked to the 'Model'.

The static response of the plate as obtained using the *2dFEM* is shown in Figures 3.12-3.12 for the F-F-C-F and C-F-F-F boundary conditions respectively. Table 3.4.2 summarized results for the maximum bending displacement from *2dFEM* and ANSYS. For the simulations, 20000 SHELL63 elements were used to achieve maximum accuracy. The present method is in excellent agreement with ANSYS results.

The corresponding ANSYS contour plots shown in Figure 3.14 for both scenarios agree with the results in Figures 3.12-3.12, supporting the above statement. Moreover, the results highlight effects of boundary conditions on static response.

Rectangular plate with variable thickness under distributed load. In addition, the case of a rectangular plate with thickness variation in the $x-$axis under the distributed load is examined. The thickness profile is based on the NACA 0012 hydrofoil section. The profile is based on the hydrofoil section superimposed with a filter function that increases the values near leading/trailing edges to ensure

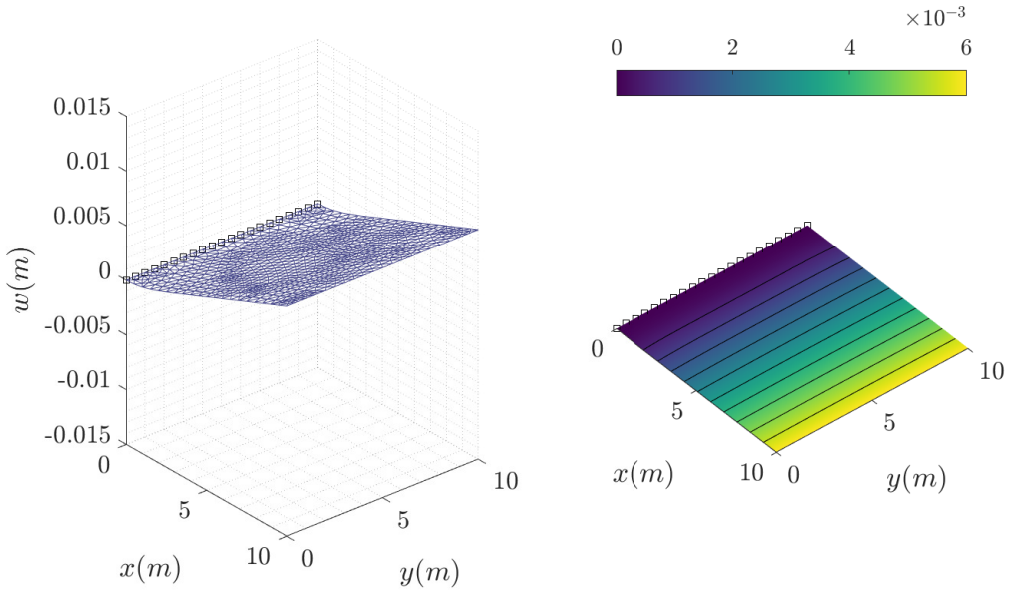

Figure 3.12: Bending displacement [left] and contour [right] for the C-F-F-F plate under distributed load.

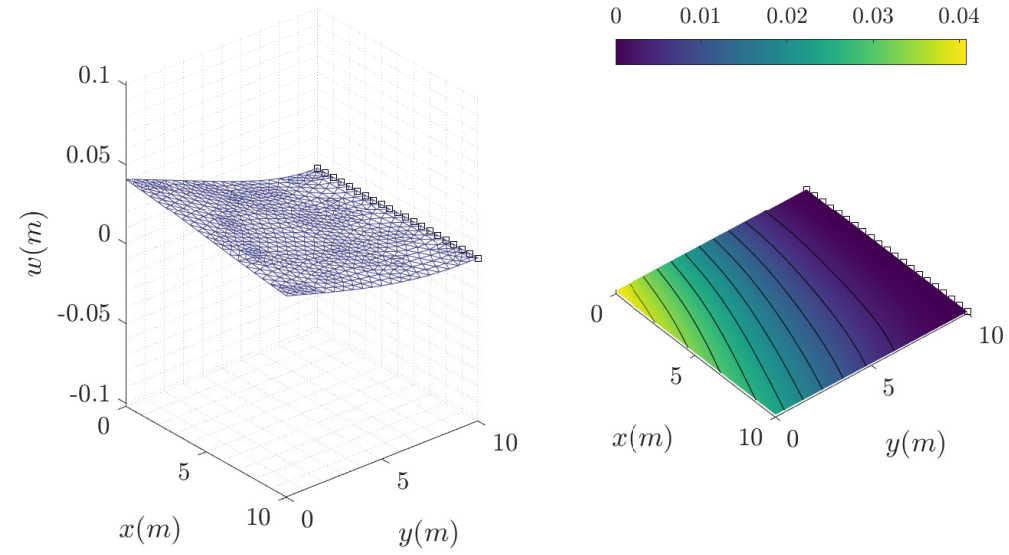

Figure 3.13: Bending displacement [left] and contour [right] for the F-F-C-F plate under distributed load.

Table 3.10: Maximum bending displacement $w_0^{max}\,(m)$ for distributed load case.

	ANSYS SHELL63	DKT (1336)	Diff(%)
C-F-F-F	0.005974	0.006009	0.58
F-F-C-F	0.040813	0.040846	0.08

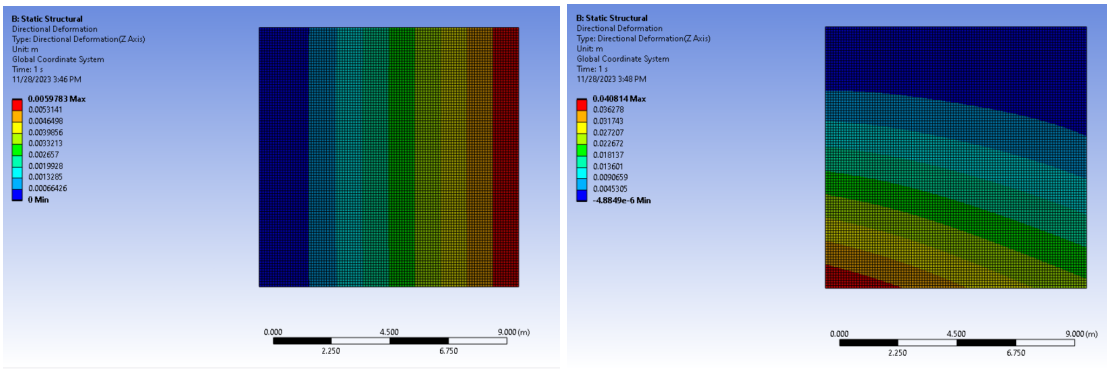

(a) (b)

Figure 3.14: ANSYS contour plots for bending displacement: (a) C-F-F-F and (b) F-F-C-F plates with constant thickness $h = 0.01m$ under distributed load.

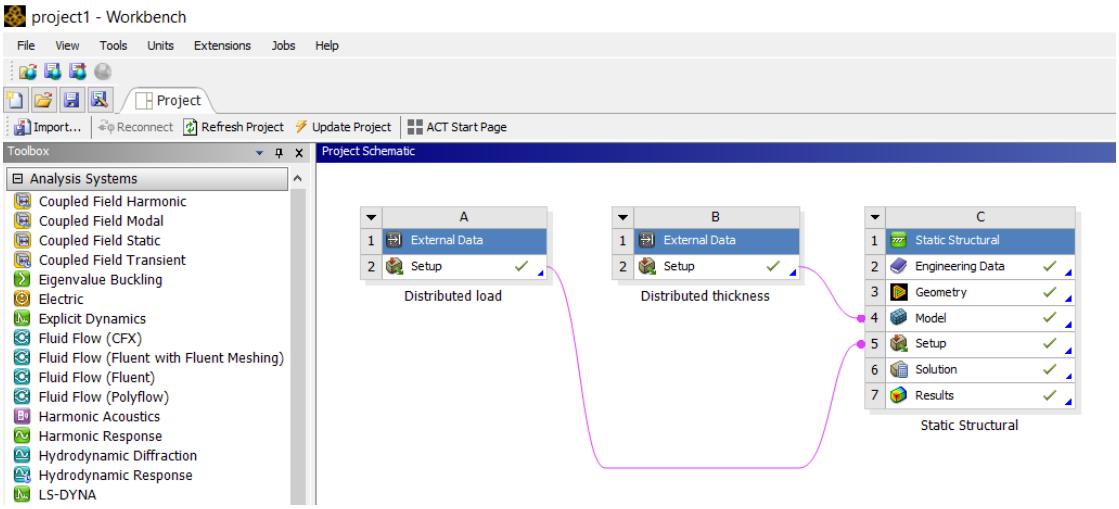

Figure 3.15: Static Structural with 'External Data' in ANSYS Workbench.

finite thickness near the edges. A normalized filter function given by,

$$f_2(x_{naca}) = \frac{f_1(x_{naca})}{max|f_1(x_{naca})|}, \quad f_1(x_{naca}) = x_{naca}^2, \tag{3.93}$$

is used in conjunction with,

$$h_{naca} = 2\,(0.1\,y_{naca} + 0.01\,f_2(x_{naca})), \tag{3.94}$$

where $(x_{naca},\, y_{naca})$ denote the NACA 0012 hydrofoil section coordinates, to describe the thickness distribution shown schematically in Figure 3.16. Please note that the through thickness, hence the multiplication with two, is taken into consideration for simulations with finite elements.

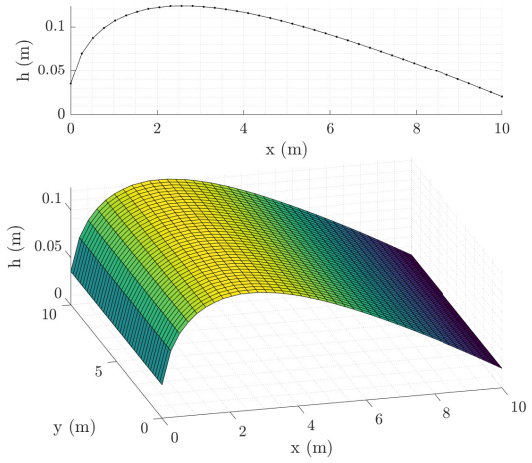

Figure 3.16: Distributed thickness based on hydrofoil section.

It was not possible to use SHELL63 elements for plates with thickness variability and instead, a mesh of 20000 SHELL181 elements was used. Table 3.11 summarizes results for maximum bending displacement, where good agreement between the present method and ANSYS is observed. Deviations are attributed to the element selection and accuracy lies within acceptable limits. Both pressure and thickness distributions are uniform in the $y-$axis, thus the contour plots for this case are similar to the previous case and only the magnitude of bending displacement is different.

These comparisons suggest that the developed finite element solver *2dFEM* is suitable for static response predictions for thin tapered plates under distributed load conditions. The interpolation scheme based on the Shepard method is sufficient. Taking this a step further, the same solver is capable of predicting the dynamic response of flexible plates as discussed in the following section.

Finally, I consider the following case,

$$h_{naca} = 2\,(y_{naca} + 0.01\,f_2(x_{naca})), \tag{3.95}$$

which is at the limit of thin plates, since $h(x,y)/a \leq 0.12$. Results obtained using *2dFEM* and ANSYS for F-F-C-F are summarized in Table 3.12 regarding the maximum bending displacement. The present model is suitable for predictions where $h/a < 0.1$, otherwise higher-order elements need to be taken into consideration to account for shear deformation effects. In Karperaki [157] finite element models based on shear deformation theory are formulated, thus incorporating these elements into the *2dFEM* solver to improve predictions on moderately-thick plates is left for future work.

Table 3.11: Maximum bending displacement $w_0^{max}\,(m)$ due to distributed load for plate with $h(x,y)/a \leq 0.012$.

	ANSYS SHELL181	DKT (5334)	Diff(%)
C-F-F-F	$1.2989{\cdot}10^{-5}$	$1.3457{\cdot}10^{-5}$	3.5
F-F-C-F	$3.9368{\cdot}10^{-5}$	$3.9268{\cdot}10^{-5}$	0.33

Table 3.12: Maximum bending displacement $w_0^{max}\,(m)$ due to distributed load for plate with $h(x,y)/a \leq 0.12$.

	ANSYS SHELL181	DKT (5334)	Diff(%)
F-F-C-F	$4.6067{\cdot}10^{-8}$	$4.4886{\cdot}10^{-8}$	2.35

3.5 Discussion and future extensions

In this Chapter, I propose a thin plate model (CPT) with flexural rigidity variability for the hydromechanics of wings operating as marine thrusters. For the numerical analysis of static and dynamic problems related to general plate configurations is based on a finite element method using the low-cost 3-node Discrete Kirchhoff Triangle (DKT).

The *2dFEM* solver is developed in C/C++ and various verification studies are presented to support the validity of the developed scheme. Verification studies included modal analysis of tapered plates and static solutions. These studies involve the global matrices, refer to various standard boundary conditions and prove that the *2dFEM* is suitable for predictions on thin plates with thickness variability.

Direct extensions related to the numerical implementation include:

- **GPU-acceleration.** Enabling parallel computation using CUDA kernel functions for sparse matrix handling, i.e., for instance using the cuSPARSE() library, and faster scattered data interpolation using the Shepard method, to decrease the overall computational time.

- **Adaptive mesh generation for shapes with curved boundaries.** Triangulation in the current version of the *2dFEM* solver is based on the Delaunay triangulation routine included in Matlab 2022a PDE Toolbox. The latter is adaptive and can capture plate geometries with curved boundaries, thus strategic efforts in mesh adaptability would potentially add value to the analysis of plates with complex shapes and thickness variability. In addition, the development or integration of an open-source adaptive mesher would facilitate cross-platform portability and enable optimization studies involving design variables that target plate geometry and boundary conditions.

- **Failure criteria.** Evaluation of various failure criteria is important to the selection of appropriate materials when designing a structure. For instance, the von Mises yield criterion suggests that the yielding of materials begins when the second deviatoric stress invariant reaches a critical value. In material science and engineering, this criterion provides a simple indication for failure due to yielding, which is expected to occur when von Mises stress reaches a critical (or maximum) value, i.e., typically this value is the material's yield strength. This is part of a plasticity theory that applies best to ductile materials, such as metals, and suggests that before yielding the materials' response is assumed to be elastic.

$$\sigma_v = \sqrt{\sigma_{xx}^2 - \sigma_{xx}\sigma_{yy} + \sigma_{yy}^2 + 3\sigma_{xy}^2} < \sigma_{max}. \tag{3.96}$$

  Evaluating the von Mises criterion requires straight-forward post-processing related to calculating the stress components in Eqs. (3.8), and due to its simplicity is widely used, see, e.g., Garg et al. [101] where the above is included in the constraints for a high-fidelity multi-point hydro-structural optimization for a 3-D hydrofoil.

All the above implementations are direct and can be addressed with relative ease. Future extensions that are considered more demanding, yet open the field of future applications where the *2dFEM* solver can be useful, include the following:

- **Large deflections.** Enriching the thin plate model by retaining non-linear terms to address problems of moderate rotations, or even large deflections using the Föppl–von Kármán equations. This model is derived from strain-displacement relations (von Kármán strains) corresponding to the three-dimensional Lagrangian Green strain tensor. Neglecting higher-order terms

but retaining the following and assuming small strains/moderate rotation,

$$\left(\frac{\partial w}{\partial x}\right)^2, \quad \left(\frac{\partial w}{\partial y}\right)^2, \quad \frac{\partial w}{\partial x}\frac{\partial w}{\partial y}, \tag{3.97}$$

allows for accurate predictions on more flexible wings. Especially for cases where the forcing frequency is high, evaluating the above terms (in the post-processing phase) and comparing them to the unit reveals whether the examined scenario violates the assumption of small strains/small rotations of the present *2dFEM* model.

- **Moderately thick plates.** The Discrete Kirchhoff triangle (DKT) can be directly extented to the Discrete Shear Triangle (DST), that addresses the problem of moderately thick plates as it is compatible with the Reissner-Midlin or namely First-order Shear Deformation Theory (FSDT), see also Batoz & Lardeur (1989) [190] and Batoz & Katili [205]. This type of element is also studied in Karperaki (2021) [157] where numerical models for large floating structures are developed. Essentially, extension to FSDT theory allows for more accurate predictions in cases where the ratio of thickness to chord (or span) lie above $h/a > 0.1$.

- **Composite plates.** Sandwich plate (core, facings) formulations, or laminated composite plates in general, based on CPT and FSDT, have also been studied. For instance, Reddy [191] introduces extensions of the above theories to cases of laminated composite plates and shells, and Wang [187] emphasizes extensions related to sandwich plates. Lifting surfaces made of composite materials are prime candidates for rapid manufacturing, allowing for more experiments at lower cost, which is not the case for wings constructed using metals. In addition, manufacturing smaller-scale aquatic-inspired thrusters using composite materials via layering (hand lay-up, molding, etc.) are cheaper, supporting the above argument. Considering also that the optimal selection of composite layers can produce wings with tailor-made rigidity distributions suggests that theories able to capture the physics behind composite structures are extremely valuable to the design of these devices.

- **Higher-order terms and non linearity.** Enrich the elastic equation model by including higher order terms and other types of nonlinear damping to improve predictions. Thin plate models for large displacements are also an interesting field for research.

- **Higher-fidelity fluid-structure interaction.** Moreover, coupling the plate model, or an extended version of it, with a hydrodynamic solver opens the

field of potential applications. The development of a fluid-structure interaction solver for passively morphing lifting surfaces is the topic of our next Chapter 4, however it is important to note that coupling the developed model with a viscous CFD solver would allow for the analysis of flexible flapping thrusters at operating conditions where viscous effects are dominant. Studies on resonance and hydro-elastic instabilities are also of interest considering the potential use of flexible lifting surfaces as small-scale autonomous underwater vehicle appendages related to maneuvering and propulsion applications [182], or even wave/current source energy harvesting devices [40], [9].

Chapter 4

A strongly coupled fluid-structure interaction model for flexible wing thrusters

List of symbols

XYZ	Cartesian global (earth-fixed) coordinate system
xyz	Cartesian local (body-fitted) coordinate system
U	forward motion velocity in m/s
$w_0(\mathbf{x};t)$	field of bending deflection
ΔC_p	hydrodynamic pressure difference
n	time-step iteration index
κ	internal loop iteration index
$\mathbf{J}$	Jacobian matrix
$\mathbf{R}$	residual equation
$\mathbf{Q}$	load vector

4.1 Background

Conventionally most lifting surfaces for a variety of applications have been made of metallic alloys, mainly due to the strict requirements for rigid body response of highly-loaded thin structures. However, one increasingly popular alternative is composite materials and depending on the application it is now possible to design composite hydrodynamic lifting surfaces with passive shape adaptability that leads to performance enhancement; see, e.g., Sacher et al. (2018) [154] and Liao et al. (2021) [103].

Motivated by this prospect I emphasize on developing a model for the hydroelastic analysis of passively deforming wings operating as bio-mimetic thrusters and explore various design concepts that have the potential to yield enhanced efficiency. Literature suggests that cost-effective computational tools suitable for performance predictions on flexible flapping wing thrusters are considered valuable to the design process of similar bio-inspired devices. Particularly, the findings in Garg et al. (2017) [206] highlight that the design optimization process of flexible hydrofoils and lifting-surfaces requires in general coupled hydrodynamic and structural analysis to achieve truly optimal, physically realizable, and structurally sound designs. Their work is directly linked to the final stages of lifting surfaces design and testing, therefore a combination of high-fidelity computational tools and experiments is used.

The study in Stanford et al. (2010) [170], where potential-based tools are used for the hydrodynamic analysis of actively morphing wings for animal flight scenarios, suggests that lower-fidelity numerical tools may help alleviate the burden of paring down the field of design variables to those of particular importance, when used alongside higher-fidelity models. It is also mentioned that potential-based solver may even be used alone during the search process, if it is thought that the tool is able to adequately capture the physical process that drives the design concept.

This Chapter is dedicated to the methodology that was developed for the fluid-structure interaction problem of passively morphing wings with emphasis on flapping-foil marine thrusters. The numerical tool that is developed, *FlexWing3D*, consists of the unsteady boundary element method *3dBEM* (see Chapter 2) and the thin plate finite element solver *2dFEM* (see Chapter 3) following a partitioned approach for a strongly coupled scheme. Both solvers have been introduced previously, therefore here emphasis is given on the coupling algorithm. Parallel computation techniques are exploited for by the hydrodynamics solver, however the finite element tool could also benefit from CUDA kernel functions, but this is left for future development.

4.2 Fluid-structure interaction

Following a partitioned approach, I use the potential (*3dBEM*) and finite element (*2dFEM*) solvers, which were initially developed to treat each sub-problem separately but are extended here, to address the fluid-structure interaction problem via a data exchange strategy that takes place at each time-step. The physical problem addressed is implicitly nonlinear since the hydrodynamic forces affect the field of bending displacements and vice-versa. In the literature coupling schemes for partitioned solvers are typically categorized as,

- ***Weak coupling***: Data is exchanged once per time-step during the simulation. Deformations from the previous step are used to generate the wing mesh for the current time-step.

- ***Strong coupling***: Data is exchanged during each time-step until convergence is achieved by means of criteria set for each study, which involves sub-iterations at each time-step or even additional evaluations using each of the sub-solvers.

A weak coupling scheme is not sufficient for capturing the basic mechanisms of the fluid-structure interaction problem involving a lifting surface submerged in water, thus we are 'obliged' to follow a strongly coupled approach.

At each time-step, the analysis begins with predictions for hydrodynamic pressure coefficient on the wing's surface. Then, I calculate the difference in pressure between the upper and lower sides of the wing's surface. Load data are then transferred to the structural solver via interpolation (inverse distance weighting - IDW), after using the centroid of each triangle on the finite element mesh. The structural solver then produces predictions for the vertical bending displacement and the slopes. An example is shown in Figure 4.1. Then displacement field data are used to reconstruct the deformed wing surface section-wise as shown in the Figure, also by implementing the IDW scattered data interpolation method. This is the first time during each time-step that the residual equation is evaluated, which is formulated based on the time-marching scheme used for the structural problem. If convergence criteria are satisfied, then I proceed to the next time-step. Otherwise, Newton-Raphson internal iterations begin to bring the residual equation closer to zero. When convergence is achieved the solver re-evaluates hydrodynamic loads and proceeds to the next time-step. This process is described schematically in Figure 4.2.

The numerical tool is validated via comparisons against experimental data, corresponding to Studies 1-2. Then additional results are provided to showcase the capabilities of *FlexWing3D* regarding the analysis of thrusters in flapping mode. Study 3 is dedicated to effects of chord-wise flexibility, where by selecting appropriate boundary conditions chord-line deflections become dominant. Finally, an optimization study targeting the thickness profile of the flexible wing thruster is presented.

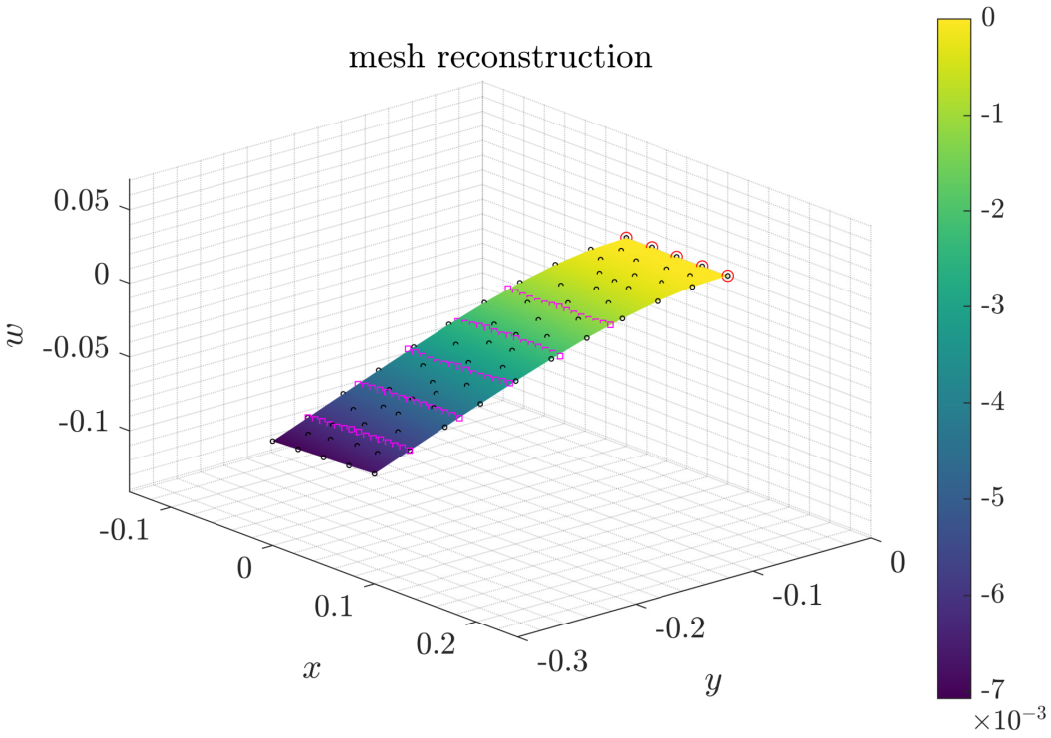

Figure 4.1: Extraction of chord-line data via IDW interpolation on finite element solution for bending displacement in the local coordinate system xyz. Mesh reconstruction data for hydrodynamic solver. The half wing shape, clamped at $y = 0$, is 'exaggerated' for visualization purposes.

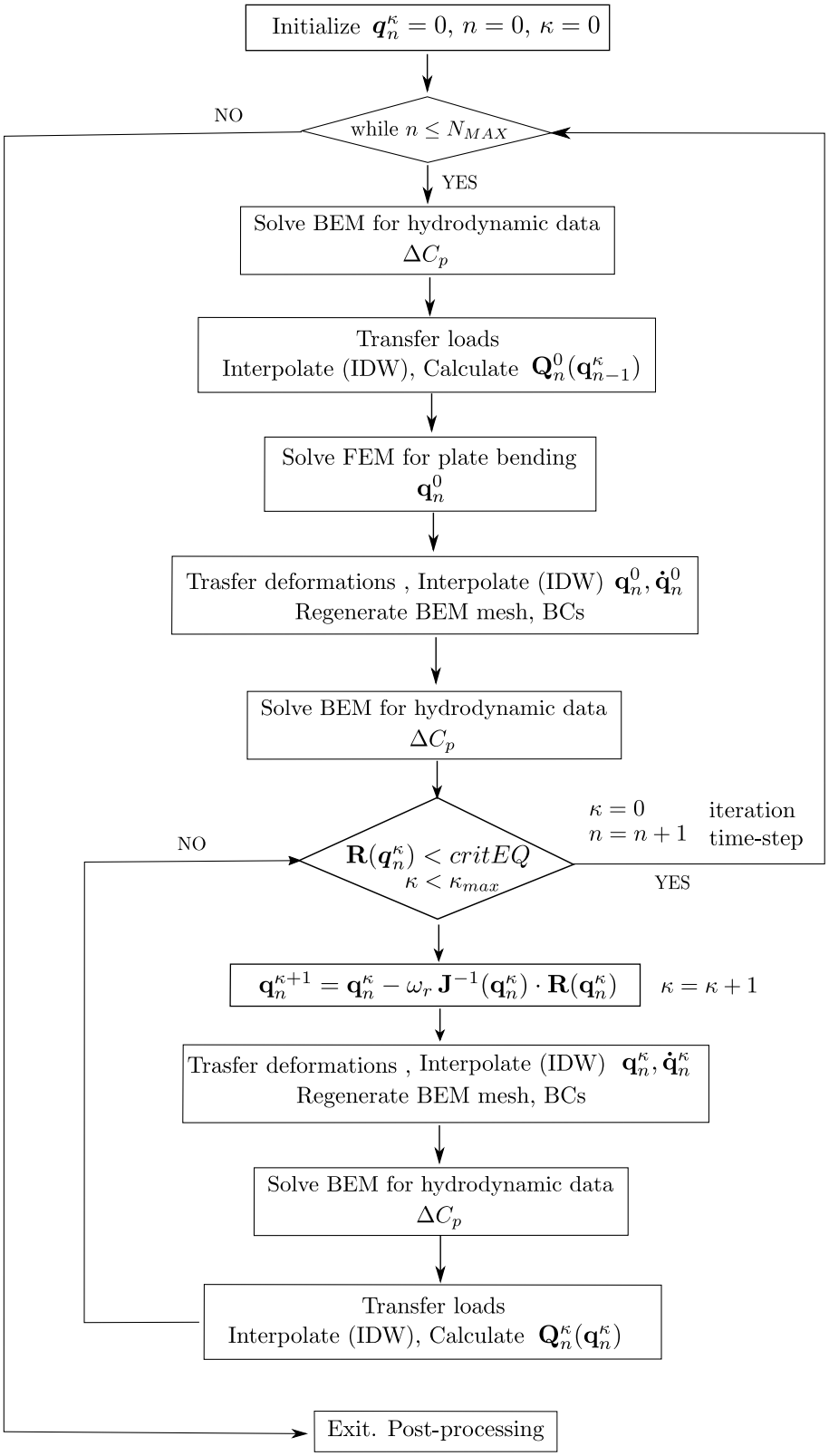

Figure 4.2: Flowchart for strongly coupled fsi bem-fem simulations with $\mathbf{q}_n^\kappa$ representing the solution of elastic problem at time-step n referring to sub-iteration κ.

4.2.1 Fluid-flow solver (*3dBEM*)

The wing and wake boundaries, denoted as $\partial D_B(t)$, $\partial D_W(t)$ respectively, are modeled as surfaces of potential discontinuity in a global coordinate system XYZ. The wing undergoes prescribed rigid-body motions and is free to deform passively. The wake boundary represents the trailing vortex sheet emanating from the sharp trailing edge and is modeled as a free shear layer with non-zero vorticity.

The formulation of an initial boundary value problem (IBVP) is based on potential theory and boundary integral equations (BIE), see also Chapter 2 for more details. Laplace serves as the governing equation for the total velocity potential,

$$\Delta\Phi(\mathbf{x};\boldsymbol{w}_0,t)=0, \quad \mathbf{x}\in D(t). \tag{4.1}$$

where $\boldsymbol{w}_0$ denotes the mid-surface deflection[1] of the wing modeled as a thin plate.

For this boundary value problem, a flow-tangency condition must hold on the body boundary,

$$\partial_n\Phi(\mathbf{x};\boldsymbol{w}_0,t)=\mathbf{V}_B(\mathbf{x};\boldsymbol{w}_0,t)\cdot\mathbf{n}(\mathbf{x};\boldsymbol{w_0},\mathbf{t}), \quad \mathbf{x}\in\partial D_B(t), \tag{4.2}$$

where $\partial_n\Phi(\mathbf{x};\boldsymbol{w}_0,t)=\nabla\Phi(\mathbf{x};\boldsymbol{w}_0,t)\cdot\mathbf{n}$ denotes the directional derivative of the velocity potential, $\mathbf{n}$ is the unit normal to the body boundary pointing toward $D(t)$ and $\mathbf{V}_B(\mathbf{x};\boldsymbol{w}_0,t)$ is the instantaneous velocity of the wing due to oscillatory motions and elastic deformations.

The underlying coupling mechanism between the hydrodynamic and structural problems is introduced via the boundary condition, which is enforced on the wing's surface. Particularly, the total body velocity used to formulate the tangential boundary condition in Eq. (4.2) consists of a rigid-body and bending displacement velocity components and is expressed on each control point on $\partial D_B(t)$ as follows,

$$\mathbf{V}_B=f_s(t)\Big(\mathbf{V}_{rigid}+\mathbf{n}_z\cdot\frac{d\boldsymbol{w}_0}{dt}\Big), \quad \mathbf{n}_z=(-sin\theta(t),0,cos\theta(t)), \tag{4.3}$$

where the second term is a vector product that is used to map the displacement velocity from the local system to the global. The ramp function $f_s(t)$ is used for a smooth transition between rest to the fully developed unsteady motion. The $\theta(t)$ denotes the instantaneous pitch angle - due to prescribed rigid-body motions, $\boldsymbol{w}_o$ the field of mean surface bending displacements and d/dt refers to the rate of change with respect to the body-fixed reference frame. In cases where pitch angle $\theta(t)$ is very small, the normal vector introduced above simplifies to $\mathbf{n}_z=(0,0,1)$.

[1] Consideration of the $\boldsymbol{w}_0$ using a semicolon expression represents the implicit non-linearity introduced to the hydrodynamics problem due to the effect of wing deflections on hydrodynamic loading and vice-versa.

To close the problem, a non-linear (quadratic), pressure-type Kutta condition requiring zero pressure difference at the trailing edge is enforced,

$$\partial_t(\Phi^u - \Phi^l) + 0.5(\nabla\Phi^u + \nabla\Phi^l)\cdot(\nabla\Phi^u - \nabla\Phi^l) = 0, \tag{4.4}$$

$$\mathbf{x}(\xi,\eta) \in \partial D_B(t),\ (\xi,\eta) \to (\xi_{TE},\eta_{TE}). \tag{4.5}$$

The above form of the pressure-type Kutta condition can be derived by using the approximate Bernoulli's theorem on the body at upper and lower sides of the trailing edge in conjunction with the assumption that wake evolves in time as a material curve based on the mean velocity. Linearization of wake dynamics yields a simplified wake model, where the generated vortex sheet emanates parallel to the trailing edge bisector; tracing the trailing edge path. Alternatively, the free wake model formulated in the present assumes that the wake evolves in time as a material surface (i.e. moving with the mean velocity). The latter is to be used for simulations at higher Strouhal numbers where the flow is characterized by strong unsteadiness.

Following a formulation that is direct with respect to the velocity potential, the weakly singular Boundary Integral Equation (BIE), which holds for each $x_0 \in \partial D_B(t)$ is derived using the above information[2],

$$\begin{aligned}\frac{1}{2}\Phi_B(\mathbf{x}_0;\boldsymbol{w}_0,t) + \int_{\partial D_B(t)} \Phi_B(\mathbf{x};\boldsymbol{w}_0,t)\partial_n G(\mathbf{x}_0|\mathbf{x})ds(\mathbf{x}) \\ = \int_{\partial D_B(t)} b(\mathbf{x};\boldsymbol{w}_0,t)G(\mathbf{x}_0|\mathbf{x})ds(\mathbf{x}) \\ - \int_{\partial D_W(t)} \mu_W(\mathbf{x};\boldsymbol{w}_0,t)\partial_n G(\mathbf{x}_0|\mathbf{x})ds(\mathbf{x}),\end{aligned} \tag{4.6}$$

where μ_W denotes the potential jump on the wake. Equation (4.6) above is formulated using the fundamental solution of 3d Laplace equation known as Green's function and its directional derivative.

For the numerical solution of the 3D, unsteady and nonlinear problem an efficient, both in terms of computational time and space complexity, the GPU-accelerated element method *3dBEM* developed in this work is used. The pressure-type Kutta condition serves as the basis of constructing a dynamical system equation with respect to the unknown potential jump on the Kutta-strip $\mu_K(\mathbf{x};\boldsymbol{w}_0,t)$ while other kinematic boundary conditions along with the BIE are used as constraints. Particularly, the discretized form of the BIE based on a low-order piecewise-constant approximation is used as an algebraic constraint by means of the *DtN*

[2]Multiplier 1/2 suggests that the weak form is valid on smooth portions of the boundary; otherwise a multiplier $1/\alpha$ needs to be used instead, where α is defined according to the local boundary angle.

operator; leading to an evolution equation with respect to the potential jump on the Kutta-strip,

$$d_t \boldsymbol{\mu}_K = \mathbf{f}\big(\boldsymbol{\mu}_K; \boldsymbol{w}_0\big). \tag{4.7}$$

Starting from a given initial condition, for instance at rest, a time-stepping method is applied to obtain the numerical solution. Calculation of the generalized forces is obtained, without further assumptions, using pressure integration. The latter is calculated via the approximate Bernoulli equation. In the present study, the numerical solution is obtained using a higher-order Adams-Bashford-Moulton (ABM) scheme. At time t, knowing $\mathbf{U}(t) = \boldsymbol{\mu}_K(t)$, I proceed to the next time step using,

$$\mathbf{U}(t+dt) = \mathbf{U}(t) + \frac{dt}{24}\Big[9\mathbf{f}_{pre}(t+dt) + 19\mathbf{f}(t) - 5\mathbf{f}(t-dt) + \mathbf{f}(t-2dt)\Big], \tag{4.8}$$

with predictor step

$$\mathbf{f}_{pre}(t+dt) = \mathbf{f}_{t+dt}\Big(\mathbf{U}_{pre}(t+dt); \boldsymbol{w}_0(t+dt)\Big), \tag{4.9}$$

$$\mathbf{U}_{pre}(t+dt) = \mathbf{U}(t) + \frac{dt}{24}\Big[55\mathbf{f}(t) - 59\mathbf{f}(t-dt) + 37\mathbf{f}(t-2dt) - 9\mathbf{f}(t-3dt)\Big],$$

where $\boldsymbol{w}_0$ denotes the bending deformation of the wing modeled as a plate. Terms in the expression above related to the current t and previous time steps, i.e., $t-dt$, $t-2dt$, $t-3dt$, remain unaltered during the NR-scheme iterations. Semicolon expression on the predictor step indicates implicit dependence to the solution $\boldsymbol{w}_0$ that comes from the finite element solver. Thus, only $\mathbf{U}(t+dt)$ and $\mathbf{f}_{pre}(t+dt)$ are updated during NR iterations.

Bernoulli's equation on an inertial reference frame holds as,

$$\frac{p(\mathbf{x};t)}{\rho} + \partial_t\Phi(\mathbf{x};t) + \frac{1}{2}[\nabla\Phi(\mathbf{x};t)]^2 = 0, \quad \mathbf{x} \in D(t). \tag{4.10}$$

The same expression referring to a body-fitted reference frame, that moves with the morphing wing, is used to calculate the hydrodynamic pressure; see also [175], [37] for more details on the derivation of Bernoulli's equation for a moving reference frame. After the solution has been obtained for the current time step, post-processing begins to derive the pressure coefficient on the wing and of course the pressure-difference ΔC_p that serves as the loading vector for the finite element analysis. Evaluating the maximum pressure difference on the upper and lower sides of the wing boundary near the trailing edge serves as a criterion for examining whether Kutta condition is satisfied. Depending on the simulation parameters, if this quantity exceeds unity numerical instabilities start to emerge and the simulation terminates.

Propulsive performance metrics

The instantaneous lift (C_L), thrust (C_T) and moment (C_M) coefficients are calculated using Eqs. (2.7)-(2.9). Unlike propulsive performance studies on actively morphing wings, the fluid structure interaction problem of passively deforming thrusters requires the following formula for the propulsive efficiency metric η,

$$\eta = \overline{C}_{P_{out}}/\bar{C}_{P_{in}}, \tag{4.11}$$

with

$$\overline{C}_{P_{out}} = \frac{P_{out}}{0.5\rho U^3 A}, \quad P_{out} = \frac{1}{T_p U}\int_0^{T_p} T(t)U\,dt, \tag{4.12}$$

$$\bar{C}_{P_{in}} = \frac{P_{in}}{0.5\rho U^3 A}, \quad P_{in} = \frac{1}{T_p U}\int_0^{T_p} \Big(L(t)\dot{h}(t) + M(t)\dot{\theta}(t)\Big)\,dt, \tag{4.13}$$

where A denotes the wing's surface, T_p the period of harmonic motion, $T(t)$ the thrust, $L(t)$ the lift, $M(t)$ the moment, $\dot{h}$, $\dot{\theta}$ the heave, pitch velocities and U the forward motion velocity. Effects of passive morphing on body velocities are embedded into the pressure coefficient term which is used to evaluate lift, thrust and moment, thus the above expression for the P_{in} is appropriate, see also [63], [75].

4.2.2 Structural solver (*2dFEM*)

The structural model used here is a 2D plate finite element solver. Especially for marine thrusters designed for small-scale autonomous underwater vehicles with low-aspect ratio wings, this structural idealization is suitable for capturing chord-wise and span-wise flexibility effects. Moreover, it can also be used for moderate-to-large aspect ratio wings.

The passive deformation caused by hydrodynamic pressure and inertial forces is solver in a local body-fitted coordinate system xyz using Kirchhoff's plate model, known as Classical Plate Theory (CPT), based on the small displacement assumption, see also Chapter 3. A direct consequence of the employed strain-displacement relation of CPT is the zeroing of shear deformation that restricts the applicability of this model to "thin" configurations, see also [189] for higher-order plate theories allowing varying degrees of shear deformation. The vertical bending equation of motion (in the z-direction) for plates with non-uniform rigidity is the following 4−th order PDE,

$$\begin{aligned}&\nabla^2(D\nabla^2 w_0) + \rho_s\tau(\mathbf{x})\partial_t^2 w_0 \\ &-(1-\nu)(\partial_{xx}D\partial_{yy}w_0 - 2\partial_{xy}D\partial_{xy}w_0 + \partial_{yy}D\partial_{xx}w_0) = Q(\mathbf{x};t), \quad \mathbf{x}\in\Pi\end{aligned} \tag{4.14}$$

where $D(\mathbf{x}) = E(\mathbf{x})h^3(\mathbf{x})/(12(1-\nu^2))$ denotes the flexural rigidity, $E(\mathbf{x})$ is the Young's modulus, ν Poisson's ratio, ρ_s the material density, $\tau(\mathbf{x})$ plate thickness and w_0 the bending deflection with respect to the reference plane.

Note that the forcing term on the *rhs* is also time-varying to model transient response. Particularly, the forcing term consists of the hydrodynamic pressure difference term and the fictitious forces terms due to use of a body-fitted coordinate system,

$$Q(\mathbf{x};t) = Q_{hydro}(\mathbf{x};t) + Q_{fictitious}(\mathbf{x};t). \tag{4.15}$$

The hydrodynamic pressure term is obtained from the boundary element solver (wingBEM) as,

$$Q_{hydro}(\mathbf{x}) = 0.5\rho_f U^2 \Delta C_p, \tag{4.16}$$

where ρ_f is the fluid density, U the forward velocity of the wing and ΔC_p the pressure difference between the upper and lower sides of the wing projected to the mean surface.

As mentioned previously, fictitious forces are also included in the modeling to account for non-inertial nature of the body-fixed coordinate system based on which finite elements are formulated, thus

$$Q_{fictitious}(\mathbf{x}) = -m(\mathbf{x})\Big(w_0(\mathbf{x};t)\dot{\theta}^2 + x\ddot{\theta}(t) + \ddot{h}(t)cos\theta(t)\Big), \tag{4.17}$$

where $m(\mathbf{x}) = \rho_s\tau(\mathbf{x})$, see also Priovolos & Belibassakis [183] for fictitious force derivation. The latter formula takes a problem-specific form and is linearized for simplicity.

The above fourth order PDE is complimented by a set of natural and/or essential conditions on each edge. The latter involve some of the primary variables, i.e. the deflection w (vertical motion) and the rotations $\partial_x w$,$\partial_y w$, and express geometric considerations. Natural conditions on the other hand involve expressions of secondary variables which are known as stress resultants and the stress couples referring to shear forces, bending and twisting moments.

The numerical treatment of Eq. (4.14) is sought after by means of FEM that essentially targets the equivalent C^1 variational problem. The smoothness requirements on the approximate solution poses difficulties as the construction of conforming FEM schemes becomes challenging. Interesting accounts on the subject can be found in [192]. For the numerical solution I developed a finite element solver (FEM) based on DKT (Discrete Kirchhoff Triangle) elements. The DKT follows a C^0 formulation (Reissner-Mindlin) and satisfies the geometric Kirchhoff assumptions. The extended global equation that is derived from the Galerkin scheme using FEM assembly techniques, local-to-global numbering and Gaussian quadrature is treated via the Newmark method for time integration.

In Anevlavi et al. 2020 [177] the coupling algorithm for the strongly coupled fluid-structure interaction problem is formulated using the Crank-Nicolson method for time integration. The extension of this methodology is included in Appendix C, however it was found to be more computationally intensive compared to the coupling scheme based on the Newmark method thus it is not used but included for completeness.

Numerical solution using Newmark

Alternatively, the solution can be obtained via the Newmark method, which is one of the most widely used multi-step time integration algorithm for structural analysis. Considering for simplicity that $\mathbf{q}$ denotes the augmented vector of unknowns defined in Eq. (3.68), at each time step I begin with the predictor step,

$$\dot{\mathbf{q}}_n^{pre} = \dot{\mathbf{q}}_{n-1} + (1-\gamma)dt\ddot{\mathbf{q}}_{n-1}, \tag{4.18}$$

$$\mathbf{q}_n^{pre} = \mathbf{q}_{n-1} + dt\dot{\mathbf{q}}_{n-1} + dt^2\Big(\frac{1}{2} - \beta\Big)\ddot{\mathbf{q}}_{n-1}, \tag{4.19}$$

where γ, β are quadrature parameters; typical values include $\gamma = 1/2$, $\beta = 1/6$ (linear interpolation) and $\gamma = 1/2, \beta = 1/4$ (averaging).

Following the notation introduced in Chapter 3, the matrices shown below correspond to the augmented format including the boundary conditions as addition equations in the form of constraints using Lagrange multipliers, i.e. $\mathbf{M} = \mathbf{M}_{aug}$, $\mathbf{K} = \mathbf{K}_{aug}$, $\mathbf{F} = \mathbf{F}_{aug}(t)$ and $\mathbf{q} = \mathbf{q}_{aug}$. This ensures that the global motions of the wing that undergoes prescribed heave and pitch are transferred via the fixed support boundary conditions assumed here.

To implement the Newmark Method, I write the dynamic equation for t_{n+1} and substitute the equations above to produce,

$$\Big[\mathbf{M} + \gamma dt\mathbf{C} + \beta dt^2\mathbf{K}\Big]\ddot{\mathbf{q}}_{\mathbf{n}} = \mathbf{F}_n - \mathbf{C}\cdot\dot{\mathbf{q}}_n^{pre} - \mathbf{K}\cdot\mathbf{q}_n^{pre}, \tag{4.20}$$

Then, I calculate the corrector step that is used in the next time-step,

$$\dot{\mathbf{q}}_n = \dot{\mathbf{q}}_n^{pre} + \gamma dt\ddot{\mathbf{q}}_n, \tag{4.21}$$

$$\mathbf{q}_n = \mathbf{q}_n^{pre} + dt^2\beta\ddot{\mathbf{q}}_n. \tag{4.22}$$

For the numerical implementation,

1. the forcing vector consists of the hydrodynamic loads and the fictitious forces terms, see Eqs. (4.16) and (4.17),

2. if the time step dt is uniform, then $\mathbf{M} + \gamma h\mathbf{C} + \beta dt^2\mathbf{K}$ can be factored once,

3. then solve the above system of equations for $\ddot{\mathbf{q}}_{n+1}$.

This method requires initial conditions for the acceleration, velocity and displacement $\ddot{\mathbf{q}}_n,\ \dot{\mathbf{q}}_n,\ \mathbf{q}_n$ at the first time step. Also, information referring to loading from the proceeding time step is needed. In our case, if forcing at the first time step is zero, then an estimate for the acceleration needs to be produced using Eq. (4.20). This occurs only at the first time step.

Coupling scheme. Following the above time-marching scheme the residual equation treated holds as,

$$\mathbf{R}(\ddot{\mathbf{q}}_n^{\kappa}) = \Big[\mathbf{M} + \gamma dt\mathbf{C} + \beta dt^2\mathbf{K}\Big] \cdot \ddot{\mathbf{q}}_{\mathbf{n}} - \mathbf{F}_n + \mathbf{C} \cdot \dot{\mathbf{q}}_n^{pre} + \mathbf{K} \cdot \mathbf{q}_n^{pre}. \tag{4.23}$$

Setting the residual expression to vanish,

$$\mathbf{R}(\ddot{\mathbf{q}}_n^{\kappa}) \to 0, \tag{4.24}$$

is pursued using the Newton-Raphson method and successively approximated via,

$$\ddot{\mathbf{q}}_n^{\kappa+1} = \ddot{\mathbf{q}}_n^{\kappa} - \omega_r\, \mathbf{J}^{-1}\Big(\ddot{\mathbf{q}}_n^{\kappa}\Big) \cdot \mathbf{R}\Big(\ddot{\mathbf{q}}_n^{\kappa}\Big), \quad \kappa = \{0, 1, ..., \kappa_{MAX}\}, \tag{4.25}$$

where $\omega_r \leq 1.0$ denotes a relaxation factor and unless stated otherwise I assume $\omega_r = 0.98$. The matrix $\mathbf{J}$ is the Jacobian of function $\mathbf{G} : R^N \to R^N$ where N denotes the total number of unknowns for the structural problem,

$$J_{ij} = \frac{\partial R_i}{\partial \ddot{\mathbf{q}}_j}, \quad \mathbf{R}(\ddot{\mathbf{q}}) = [R_1(\ddot{\mathbf{q}}_n^{\kappa}), R_1(\ddot{\mathbf{q}}_n^{\kappa}), ..., R_N(\ddot{\mathbf{q}}_n^{\kappa})]. \tag{4.26}$$

The calculation of Jacobian matrix requires knowledge of the partial derivatives of the scalar components $R_i(\ddot{\mathbf{q}})$ of the function $R(\ddot{\mathbf{q}})$. These components are numerically approximated via a central differences scheme,

$$\frac{\partial R_i}{\partial \ddot{q}_j^{\kappa}} \simeq \frac{R_i(\ddot{q}_j^{\kappa} + h_j) - R_i(\ddot{q}_j^{\kappa} - h_j)}{2h_j}, \tag{4.27}$$

assuming that the step-size h_j is sufficiently small. In practice it is selected as a small percentage of $|\ddot{q}_j|$, for instance $h_j = 0.001|\ddot{q}_j|$. Calculation of the Jacobian is indeed the most computationally expensive part of the simulation.

Although various criteria can be established to monitor the Newton-Raphson convergence at each time step, I found *heuristically* that the following criterion yields a good compromise between accuracy and iteration number,

$$max|\mathbf{R}(\ddot{\mathbf{q}}^{\kappa})| < critEQ, \quad crtiEQ = \lambda\, max(\mathbf{T}),\ \lambda = 1e^{-3}, \tag{4.28}$$

where

$$\mathbf{T} = \Big[T_1, T_2, T_3, T_4\Big], \tag{4.29}$$

$$T_1 = \frac{1}{N}\sum_{i=1}^{i=N} abs\Big[[\{\mathbf{M}\} + \gamma dt\{\mathbf{C}\} + \beta dt^2\{\mathbf{K}\}] \cdot \ddot{\mathbf{q}}_{\mathbf{n}}\Big]_{i-th},$$

$$T_2 = \frac{1}{N}\sum_{i=1}^{i=N} abs\Big[- \{\mathbf{F}\}_n\Big]_{i-th},$$

$$T_3 = \frac{1}{N}\sum_{i=1}^{i=N} abs\Big[+ \{\mathbf{C}\} \cdot \dot{\mathbf{q}}_n^{pre}\Big]_{i-th},$$

$$T_4 = \frac{1}{N}\sum_{i=1}^{i=N} abs\Big[+ \{\mathbf{K}\} \cdot \mathbf{q}_n^{pre}\Big]_{i-th}.$$

In this formulation, coarse mesh equals approximately 2 hours per simulation, therefore coupling is based on the Newmark time integration method. Simulations verify that both approaches (Crank-Nicolson, Newmark) give the same predictions, therefore unless stated otherwise I present results based on the latter which is more cost-effective.

4.3 Verification and numerical results

This section contains results of various representative study cases, out of which Studies 1-2 are selected for validation purposes. Results concerning quantities of interest, such as the bending deflection w_0 and the mean thrust coefficient C_T, are obtained using the developed computational tool and then compared against experimental results from the literature. Study 3 is included to investigate chordwise flexibility effects on a flapping wing. The linearized wake model is used for the simulations.

Tuning of Rayleigh damping coefficients is based on *2dFEM* predictions for the first in-air natural frequencies of the wings modeled as a plate including thickness variability to account for the hydrofoil section. However, in cases where the natural frequencies of the coupled system are provided, i.e. obtained via experimental testing, they can be used instead of the in-air mode predictions for proportional damping coefficient selection.

4.3.1 Study 1. Flexible wing under heaving excitation

The study case considered here is derived from the experimental work of Heathcote et al. 2008 [180], where wings with orthogonal planform are placed within a flow

and actuated at one edge. The wings undergo prescribed heaving motion and deform passively under hydrodynamic load excitation. The tip amplitude and phase angle of deflection are recorded.

Details regarding the experimental setup can be found in Sec. 2.5.3. However, for completeness some information that is useful for the simulation results presented are included. In [180], the tested wings have NACA 0012 sections, aspect ratio $AR = 3$ and main dimensions $c = 0.1m$, $s = 0.3m$. The heave profile is given by $s_{ROOT}(t) = h_0 cos(\omega t)$, $h_0 = 0.175c$ and the inflow velocity is $U = 0.3m/s$ at Reynolds number $Re = 30,000$. The forcing frequency is defined as $k_G = \pi f c/U$ where $\omega = 2\pi f$. It is important to note that the examined wings are labeled as 'inflexible', 'flexible' and 'very flexible' based on their rigidity. The 'inflexible' wing is constructed using nylon and two steel beams placed near the aft part to increase rigidity. The 'flexible' wing is made of PDMS with $1mm$ steel sheet are core, see Figure 4.3.1.

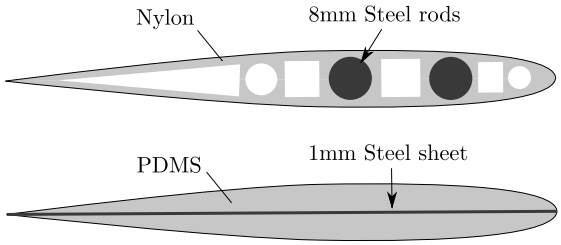

Figure 4.3: Wings tested in Heathcote et al. 2008 [180].

Regarding the structural idealization, the 'flexible' wing is modeled as a rectangular plate made of steel with constant thickness, i.e. $h = 1mm$. The material properties for structural steel are Young's modulus $E_1 = 210GPa$, Poisson's ratio $\nu = 0.28$ and density $\rho_s = 7850kg/m^2$. The boundary conditions considered are F-F-C-F. Modal analysis in vacuo serves as the basis for Rayleigh proportional damping coefficient tuning. Assuming that for the first and second eigenfrequency damping ratios of $\zeta_1 = 0.011$, $\zeta_2 = 0.018$ are used, then the corresponding Rayleigh coefficients are $a_1 = 0.173481$, $b_1 = 0.000383$. Another set of Rayleigh damping coefficients $a_2 = 3.576952$, $b_2 = 0.006462$ corresponding to higher ratios of $\zeta_1 = \zeta_2 = 0.022$ is also tested for completeness.

Regarding the finite element simulations, the plate's geometry corresponds to a wing of $c = 0.1m$, $s = 0.3m$. However, hydrodynamic load calculations are based on simulations concerning the whole wing with main dimensions $c = 0.1m$, $s = 0.6m$. Symmetry of the flow ensures compatibility with the experimental case.

The propulsive performance metrics correspond to the average values during the last flapping cycle of a three-period simulation. Regarding the discretization, I used $NEC = 40$ (chordwise), $NEA = 5AR$ (spanwise) panel elements for the

GPU-BEM spatial discretization, $N_{elem} = 110$ DKT triangles for the finite element mesh and a shared time-discretization of $(dt/T_p)\% = 0.40$. The meshes used are depicted in Figure 4.6. The fsi scheme based on the Newmark method is implemented for time integration, whereas scattered data interpolation is performed via Shepard's Inverse Distance Weighting, see Sec. 3.3.2. Each simulation requires approximately $137min \sim 2.5hrs$ on our workstation. The Jacobian does not change significantly during internal iterations and typically up to three cycles are sufficient for convergence.

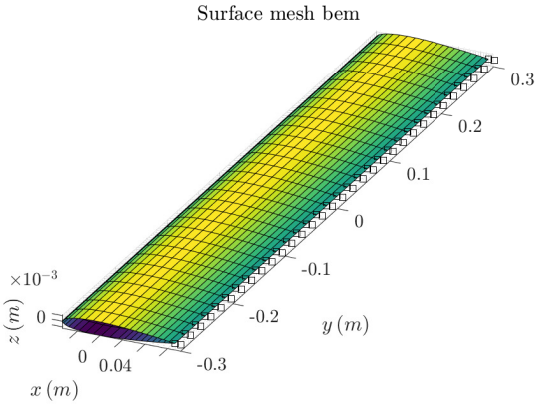

Figure 4.4: (a)

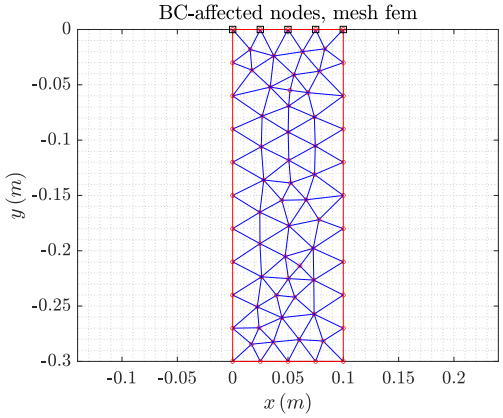

Figure 4.5: (b)

Figure 4.6: Meshes used in the validation study against Heathcote et al. [75]: (a) Structured quadrilateral BEM mesh for the whole wing, (b) Unstructured DKT FEM mesh for the half wing. Black squares denote the clamped nodes in FEM simulations.

In Figure 4.7, I compare the mean thrust predictions obtained with the coupled scheme against experimental data for the flexible wing at reduced frequency, denoted as k_G, within the range $\{0.4 - 1.82\}$; corresponding to Strouhal number between $\{0.0557 - 0.2028\}$. It is observed that the present FSI model reproduces the parabolic form of forcing frequency k_G effects on the mean thrust coefficient. Predictions obtained with the *FlexWing3D* over predict mean thrust coefficient at low frequencies, whereas for higher k_G values thrust is under predicted.

Moreover, in Figure 4.8, I compare maximum tip amplitude and the corresponding phase lag predictions against PIV data from [75] for the same range of reduced frequency. Tip amplitude is predicted well, however for higher frequencies phase lag is under predicted. The examined range of reduced frequency (i.e. in the sense of Strouhal number) suggests that ideal-flow predictions are applicable with engineering accuracy. Thus, discrepancies between phase lag predictions; affecting directly the mean thrust coefficient, are attributed to the structural idealization

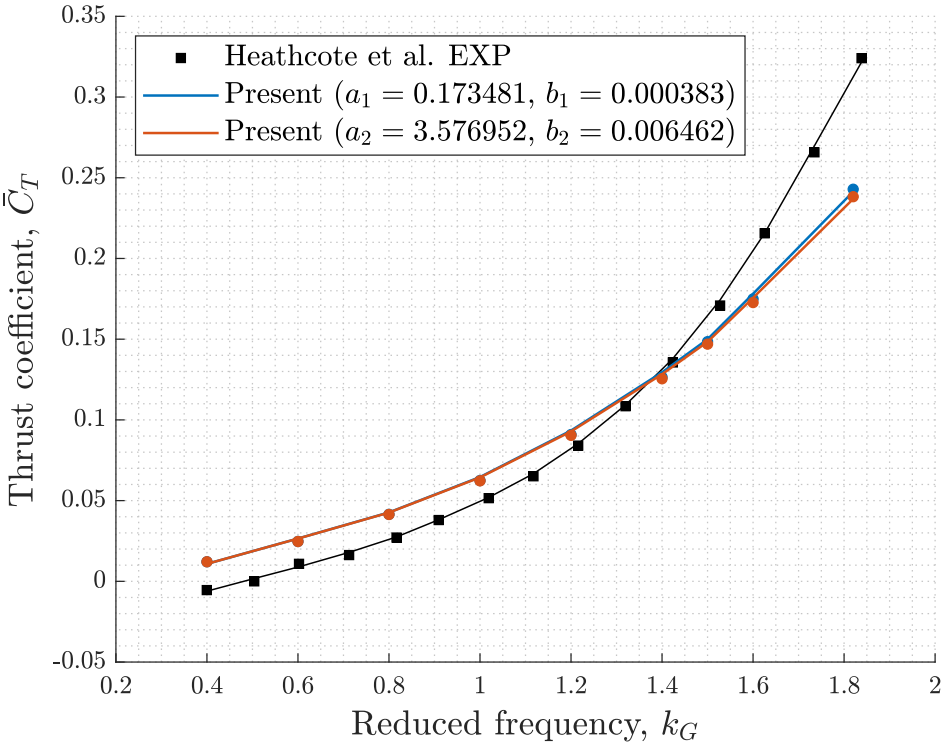

Figure 4.7: Thrust coefficient as a function of frequency and comparison with the experimental data in [75] for two sets of Rayleigh damping coefficients; (α_1, b_1) and (α_2, b_2).

of the wing modeled as a thin metal sheet of constant thickness and neglecting the effects of the PDMS material. It is possible that for higher frequencies, the PDMS material exhibits non-linear damping behavior that is not modeled in this benchmark study. Overall, the comparison suggests that *FlexWing3D* provides useful information for the physics behind flexible heaving plates submerged within a fluid medium, assuming that the flow around the wing is largely attached and forcing excitation lies within a range of low frequencies found in nature (i.e. $Str = \{0.2, 0.4\}$).

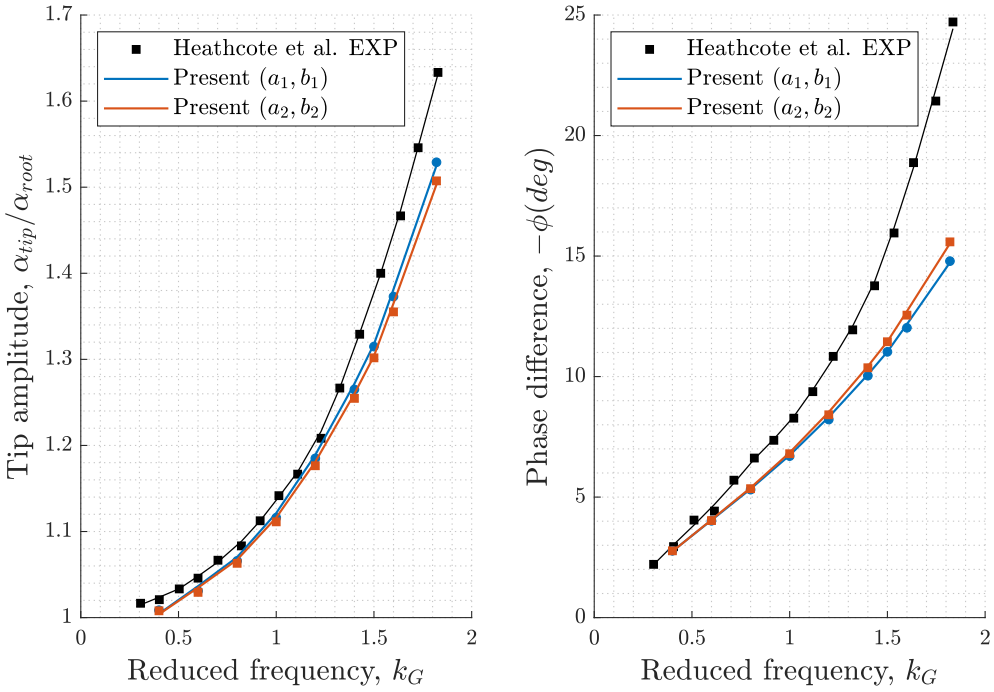

Figure 4.8: (a) Tip amplitude and (b) phase lag as a function of frequency and comparison with the experimental data in [75] for two sets of Rayleigh damping coefficients; (α_1, b_1) and (α_2, b_2).

In Figure 4.9, I compare the time history of tip-deformation for the inflexible and flexible wing at reduced frequency $k_G = 1.82$. The amplitude predictions are in good agreement, however, the phase lag is not predicted accurately. These observations suggest that strong coupling is considered necessary for accurate phase-lag and improved bending deflection predictions, which agrees with the discussion in Daniel et al. [96] and Zhu [63]. The red circles shown in the Figure denote selected time instances (during the last period of motion) for which instances of the deflected wing mid-surface are provided in Figure 4.10. On the latter, red circles

show the exact position on which the maximum tip-deflection is evaluated in Figure 4.9. The deflected shapes provide an indication that first bending mode is dominant in this scenario.

To provide additional information regarding the proposed scheme validity and probable reasons why this discrepancy occurs, I also include results obtained with the equivalent 2D version of the fluid-structure interaction tool and published in [177]. These comparisons are shown in Figures 4.11 and 4.12, where the trailing-edge response ratio, phase lag and thrust are shown. The results refer to a validation test case from the experimental work of [76], involving a flat plate submerged within a water tank and actuated from its leading edge to perform heaving motion within a flow of constant velocity. The plate's material properties are a flexural rigidity of $D = 0.018Nm$, material density $\rho_s = 1200kg/m^3$. The heaving amplitude is $h_0 = 0.033c$ and the forcing frequencies examine lie within the interval $\omega \in \{0.3, 8.0\}\, rad/s$ at Reynolds number $Re = 6,000$.

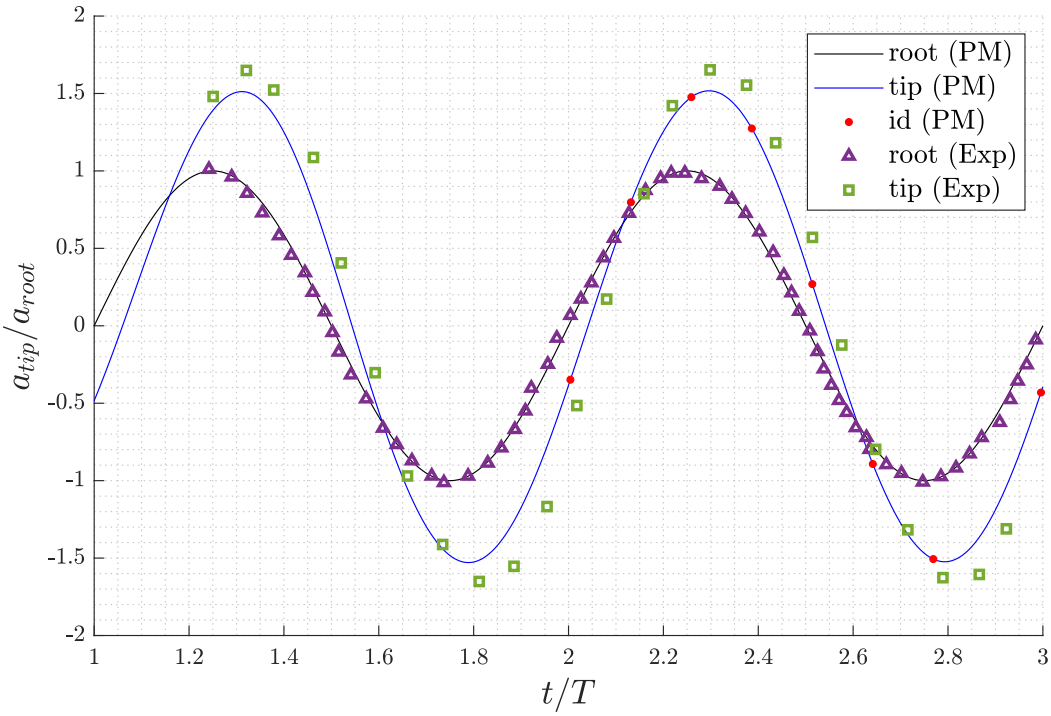

Figure 4.9: Time history of tip deflection during two periods of motion for reduced frequency $k_G = 1.82$. Red circles denote selected time instances (during the last period of motion) for which instances of the deflected wing mid-surface are provided in Figure 4.10.

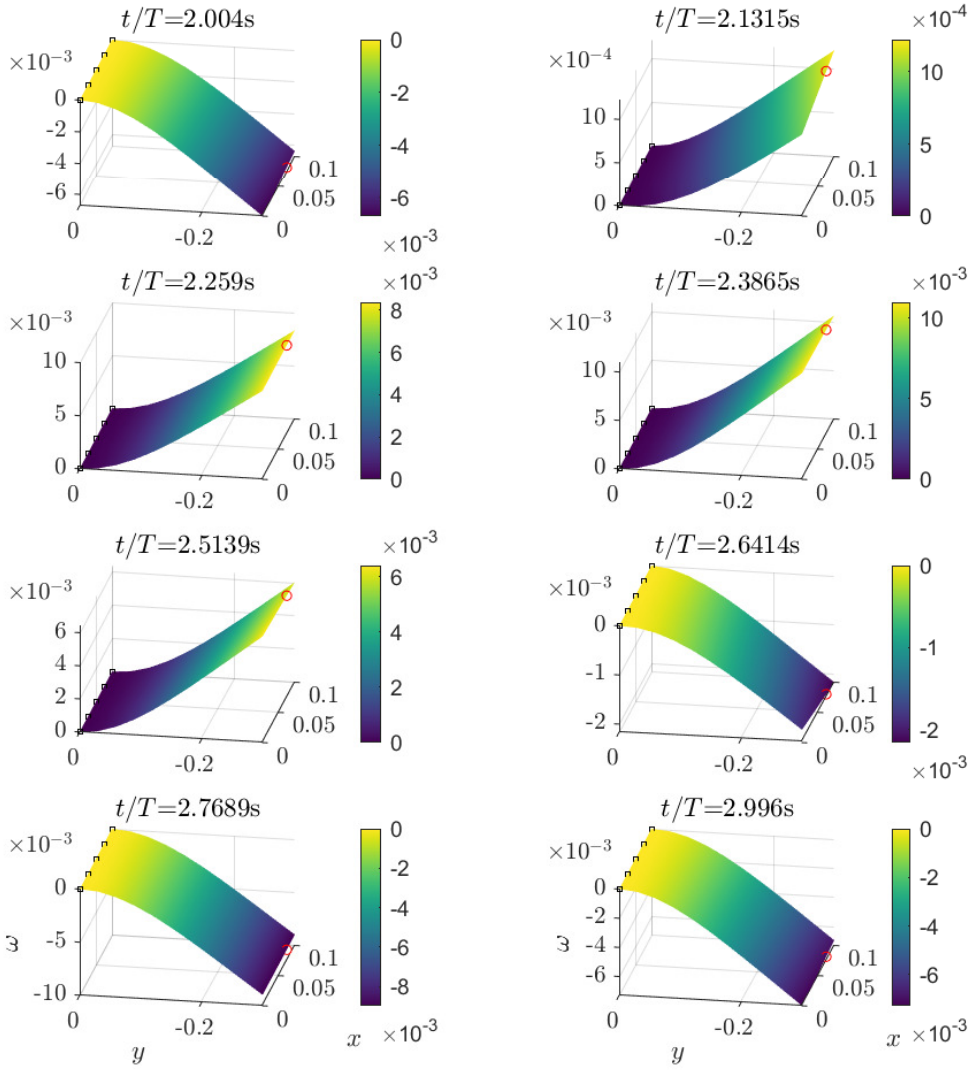

Figure 4.10: nstances of deformed wing with boundary conditions F-F-C-F for $k_G = 1.82$. Clamped nodes are denoted with black squares and red circles show the exact position on which the maximum tip-deflection is evaluated and shown in Figure 4.9.

In Figure 4.11, where the equivalent FSI BEM-FEM solver in 2D [177] is compared against Paraz et al. [76] experimental values, we can observe a second peak in the plate's response, revealing the second natural frequency of the coupled system. Similar parametric studies can be used to reveal the first and even the second natural frequency of the coupled system. It is important to note that calculation of eigenfrequencies for the flexible plate submerged in a fluid medium can be performed in a similar manner using the *FlexWing3D* by means of parametric studies, however the present method is not developed for that purpose. The ABM and NR legends in Figure 4.11 refer to two different solution schemes for the hydrodynamic problem; namely ABM stands for the Adams-Bashford-Moulton linear multi-step method and NR for the Newton Raphson method. More details regarding the FSI method in 2D can be found in Anevlavi et al. 2020 [177]. Essentially, the latter strongly coupled 2D BEM-FEM FSI scheme stands as the predecessor of *FlexWind3D* that is presented in this dissertation.

From our experience with the model in Anevlavi et al. 2020 [177], high values of stiffness proportional damping coefficient may lead to over-damping of the response, thus making the second peak unnoticeable. Reasonable damping yields proportional coefficients that correspond to $a > b$, therefore in the present comparison against Heathcote et al. 2008 [180] proportional damping coefficients satisfy this relation. Moreover, it is important to note that the present model (and the 2D version [177]) only considers proportional damping effects. The addition of viscous damping can improve predictions, especially at higher excitation frequencies. This direction is left for future work.

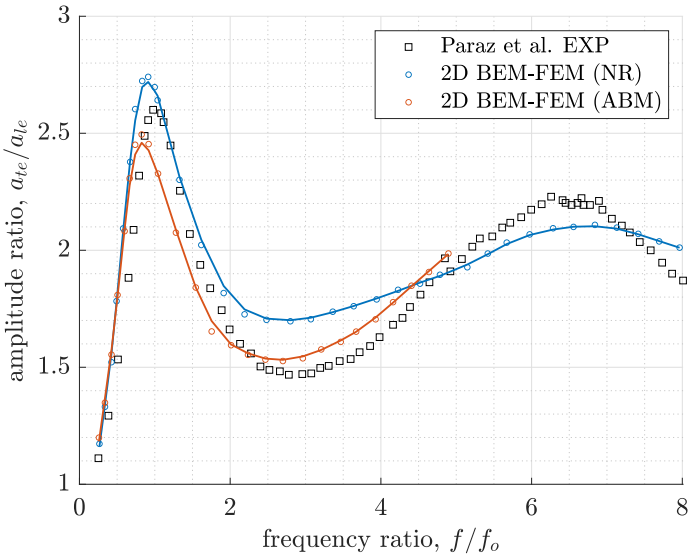

Figure 4.11: Trailing-edge response ratio comparison with experimental data (black squares) from [76] for the case of a heaving flexible flat plate with $D = 0.018Nm$, $h_0 = 0.004m$ at $Re = 6,000$.

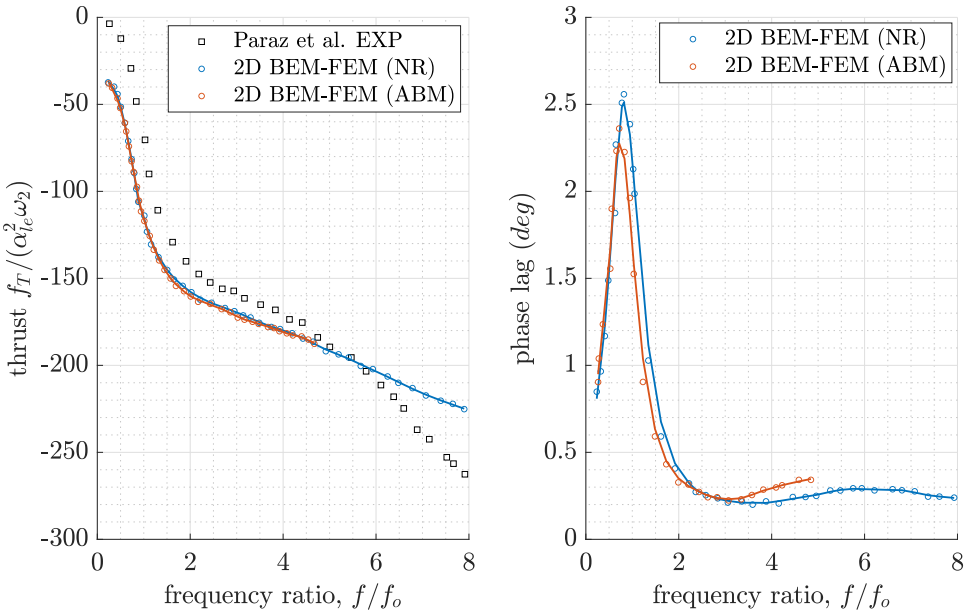

Figure 4.12: Thrust normalized by the characteristic elastic force $f_T/(a_{le}^2\omega^2)$ [left] and phase lag (deg) [right] as a function of frequency ratio. Comparison with experimental data (black squares) from [76].

4.3.2 Study 2. Flexible wing in steady flow. Mesh sensitivity

The experimental study in Zarruk et al. [207] addresses a steady fluid-structure interaction problem involving passively deformable wings made of different materials. The study is concerned with both metal and composite wings of an upright (unswept) tapered planform with NACA 0009 sections, i.e., thickness variability chordwise and spanwise. In their work, they conduct experimental modal analysis and then estimate the lift, moment, and drag coefficients for a wide range of effective angles, including past stall points. Out of the examined wings, I selected the Type-I prototype made of steel to compare against *FlexWing3D* for validation purposes. The experimental tests used a tailor-made support to ensure that the wing remains fully clamped at one edge; shown schematically in Figure 4.13.

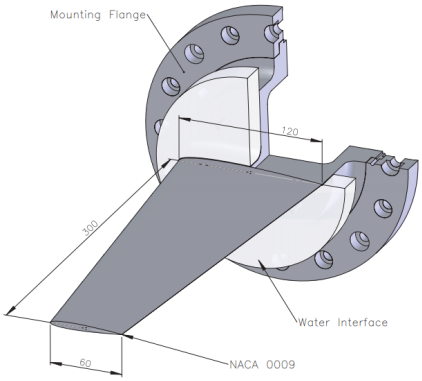

Figure 4.13: Arrangement, geometry and dimensions of model hydrofoils showing mounting flange and fairing disk where the models penetrate the tunnel wall (dimensions in mm); from [208].

FlexWing3D can treat steady fluid-structure interaction problems, assuming that a sufficient number of simulation periods allows convergence to a steady state. Our comparisons against the experiment refer to prediction of (1) the first natural frequency in air and (2) the maximum deflection, as observed at the wing-tip; assuming the flexible wing is placed into a flow at $a = 6deg$ angle of attack. The wing positioning corresponds to a 'nose-up' $a = 6deg$, and the reported maximum tip deflection is $4.9mm$. The first in-air natural frequency is calculated experimentally in [207] as $f_1 = 100Hz$.

The wing geometry is of unswept trapezoidal planform of $s_{fem} = 0.3m$ span, $c_r = 0.12m$ base (or root) chord and $c_t = 0.06m$ tip chord, i.e., with a taper ratio of $\lambda_r = 0.5$. The aspect ratio of the wing examined in the experiments is $AR = 3.33$. Because the wing in the experiments is clamped at the root section, from a

structural point of view, half the wing is modeled (i.e. exploiting symmetry) as a plate of variable thickness clamped at one edge. Following the boundary condition notation introduced in Chapter 3, this is labeled as F-C-F-F. The properties of stainless steel (316L) reported in [207] are Young's modulus of $E = 193MPa$ and density of $\rho_s = 7900kg/m^3$. Poisson's ratio for stainless steel is taken as $v = 0.265$, with typical values between $0.26 - 0.28$ assuming perfectly isotropic material. On the other hand, for the hydrodynamics I model the whole wing; corresponding to to a span of $s = 0.6m$ as shown in Figure 4.17.

Regarding the fluid-structure interaction simulations, for this particular test case additional information includes $Re = 1 \cdot 10^6$; corresponding to a velocity $11.11m/s$ based on kinematic viscosity $v = 10^{-6}m/s^2$ and mean chord $c_{mean} = 0.09m$, as discussed in [207].

Starting with the modal analysis, Tables 4.2-4.3 contain first natural in-air frequency predictions obtained using the *2dFEM* solver. Three meshes were tested for convergence and sensitivity. The coarse unstructured mesh consists of 106 DKT triangles and the fine mesh of 1696 elements, see Figure 4.16. Table 4.2 refers to the material properties reported in the experiment, whereas Table 4.3.2 contains results considering the mean value of Young's modulus for stainless steel.

Modal analysis is performed on wings with $s_{fem} = 0.3m$ and $s_{fem} = 0.29m$ span length, to account for mounting effects (i.e. the exact dimensions of the flange shown in Figure 4.13 are not provided in [207]) and with respect to the reported Young's modulus $E = 193GPa$ and a representative value for stainless steel in general, which is $E = 200GPa$. The latter is included to investigate effects of Young's modulus on the natural frequency. Especially, since in [207] material properties are based on data-sheet information and are not measured experimentally. The results suggest that the effects of Young's modulus on the natural frequency are small but rather non-negligible, whereas mounting effects (i.e. reduction of the effective span length) are substantial. The predictions converge as the mesh size increases as expected, suggesting that acceptable accuracy can be achieved even with the coarser mesh.

Deviations between our predictions and the data in Zarruk et al. [207] are expected, since the natural frequencies correspond to experimentally measured values and the reported material properties are based on reference data sheet for the stainless steel (316L) billet that was used to manufacture the wing prototype. However, deviations can also be attributed to mounting effects since the wing prototype has an extended length that is used to fully mount the structure. This type of support would be most accurately modeled by assuming an infinitely rigid boundary condition at the root.

Modeling an effective span length as $s_{fem} = 0.3m$ leads to large deviations (up to 6.9%) in terms of the first natural mode in air. However, by examining a wing

assuming smaller effective span $s_{fem} = 0.29m$ to account for mounting effects it is evident that are predictions lie closer to the reported results, suggesting that in the comparison this effective span should be used. This case study takes into consideration thickness variability in both directions, thus adds to the verification of our numerical scheme.

Table 4.2: First natural frequency (Hz) prediction for the wing in [207], where the reported value is $f_1 = 100Hz$. Stainless steel $E = 193GPa$, $\nu = 0.265$, $\rho = 7900kg/m^3$ and F-C-F-F boundary conditions.

id	span	DKT (106)	DKT (424)	DKT (1696)	Diff(%)
1	$s_{fem} = 0.30m$	92.2080	92.9969	93.0997	-6.9
2	$s_{fem} = 0.29m$	99.6464	100.5367	100.5669	+0.56

Table 4.3: First natural frequency (Hz) prediction for the wing in [207], where the reported value is $f_1 = 100Hz$. Stainless steel, $E = 200GPa$, $\nu = 0.265$, $\rho = 7900kg/m^3$ and F-C-F-F boundary conditions.

id	span	DKT (106)	DKT (424)	DKT (1696)	Diff(%)
1	$s_{fem} = 0.30m$	93.8652	94.6684	94.7730	-5.2
2	$s_{fem} = 0.29m$	101.4373	102.3437	102.3744	+2.37

Concerning maximum tip amplitude predictions, I performed simulations (linear wake) with parameters shown in Table 4.3.2 using the surface boundary element mesh shown in Figure 4.17. Selecting quantities related to the temporal discretization requires special care since $h_0 = 0$ and $Str = 0$. However, we can select a time-step based on the following period of motion using information related to the constant inflow $T_1 = c_r/U$. Temporal discretization is based on $t/T_1 = 0.35/100$ with ramp filter parameter $f_0 = 1.8$. Following the convention introduced in Sec. 2.2 phase difference is set to $\psi = 90^o$, in order to ensure that pitch angle has the desired value at the beginning of each simulation.

Simulations performed with the coarse finite element mesh of 106 DKT triangles required approximately $4.2hrs$ for $N_{per} = 5$ on our workstation. A denser mesh consisting of 426 DKT triangles is also tested in the context of sensitivity analysis. For our simulations calculation of the full Jacobian is performed during internal iterations when the following condition is true ($iter = 1 \,||\, iter > 3$), to save computational time.

Selection of damping ratio is important for steady state predictions using transient analysis. The simulations performed are based on different set of damp-

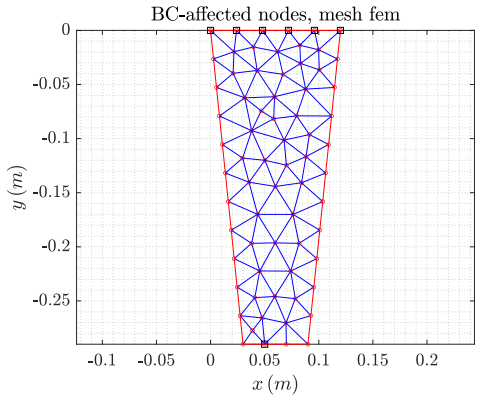

Figure 4.14: (a) DKT (106)

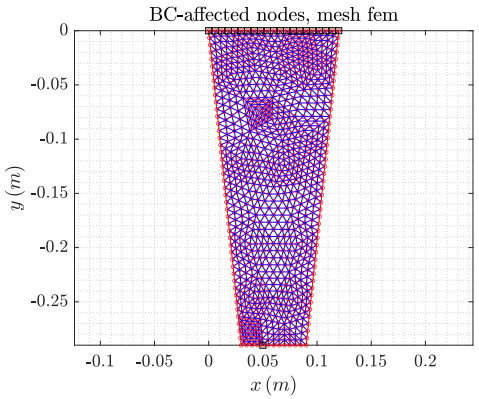

Figure 4.15: (b) DKT (1696)

Figure 4.16: Meshes used in the modal analysis benchmark study with Zarruk et al. [207]: (a) Coarse and (b) fine unstructured DKT FEM meshes for the half wing. Black squares at $y = 0$ denote the clamped nodes and on the opposite side tip deflection evaluation node location.

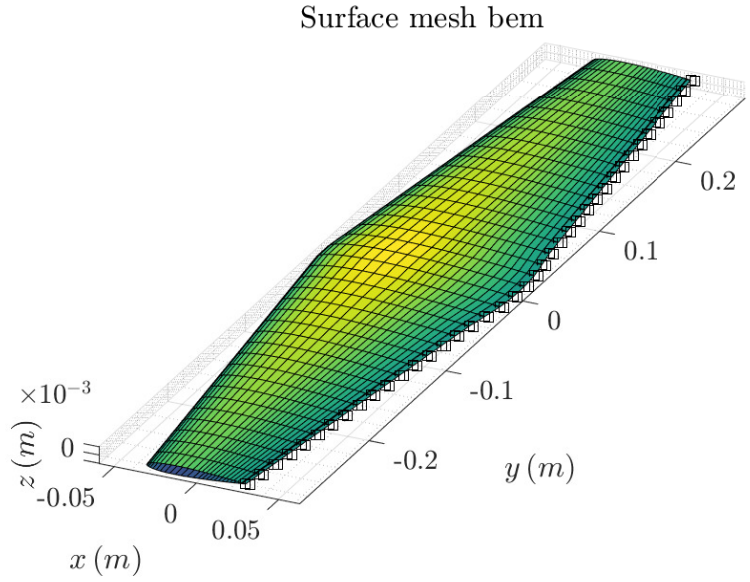

Figure 4.17: Structured quadrilateral *3dBEM* mesh ($NEC = 50$, $NEA = 6AR$) for the whole wing used in the validation study against Zarruk et al. [207]. Black squares indicate Kutta-strip nodes.

ing ratios to also investigate their effect on tip amplitude predictions, assuming $\zeta_1 = \zeta_2 = 0.5$ and $\zeta_1 = \zeta_2 = 1.0$ corresponding to critical damping. Figures 4.19 and 4.20 shows the difference in predicted response for the thrust coefficient and the tip deflection respectively, assuming $\zeta_1 = \zeta_2 = 0.1$ and $\zeta_1 = \zeta_2 = 0.5$. The latter selection is found to achieve convergence after $N_{per} > 3$. Minor numerical instabilities, of no importance to the final steady state we are seeking, occur in the time history of thrust coefficient in Figure 4.19. These instabilities, however, did not affect our tip deflection predictions. The spikes in Figure 4.19 can be eliminated by increasing the convergence threshold during each time step. However, because the benchmark study emphasizes the steady state, I avoided increasing the computational cost.

Table 4.3.2 summarizes the predicted values of tip deflection for the examined scenarios. Half-span is assumed equal to $s_{fem} = 0.29m$ to account for mounting effects by 'matching' the experimentally measured first natural frequency in-air with the *2dFEM* modal analysis predictions. Tip deflection for material of $E = 193GPa$ is over predicted by our method, whereas the deviation corresponding to a material of $E = 200GPa$ is the smallest. Figure 4.18 shows schematically the deformed wing shape for this scenario, where the circle indicates tip location at which the results are provided.

Viscous corrections are not implemented in the present fluid-structure interaction analysis, thus deviations can be partly attributed to an over prediction of hydrodynamic pressure due to the ideal-flow nature of the hydrodynamic solver; see also Sec. 4.3.1. Over prediction of the tip deflection is closely related to an over prediction of hydrodynamic loading, and since the wing is placed at a fixed angle of attack $a = 6^o$ viscous phenomena might be non-negligible. Other uncertainties related to the actual material rigidity of the wing and mounting effects can also be considered as contributor to the observed deviation. Regarding the boundary conditions examined, the F-C-F-F case was also found to be the most difficult one for the CPT model as shown in the verification studies of Chapter 3. Overall, this study showcases the capability of *FlexWing3D* to perform FSI steady-state analysis in the sense of converging in time. The solver behaves as exacted in terms of under/over damped scenarios highlighting the importance of tuning the proportional damping coefficients using natural frequency predictions and the desired set of damping ratios (ζ_1, ζ_2).

Table 4.4: Simulation parameters for comparison with [207]. The reported maximum tip deflection is $4.9mm$.

id	span $s(m)$	material $E(GPa)$	N_{per}	DKT	damping (z_1, z_2)	deflection $a_{tip}^{max}(mm)$	Diff. (%)
1	0.29	193	5	106	(1.0,1.0)	5.325	8.67
2	0.29	193	5	106	(0.5,0.5)	5.463	11.5
3	0.29	200	5	106	(1.0,1.0)	5.191	5.94
4	0.29	193	3	426	(1.0,1.0)	5.317	8.51

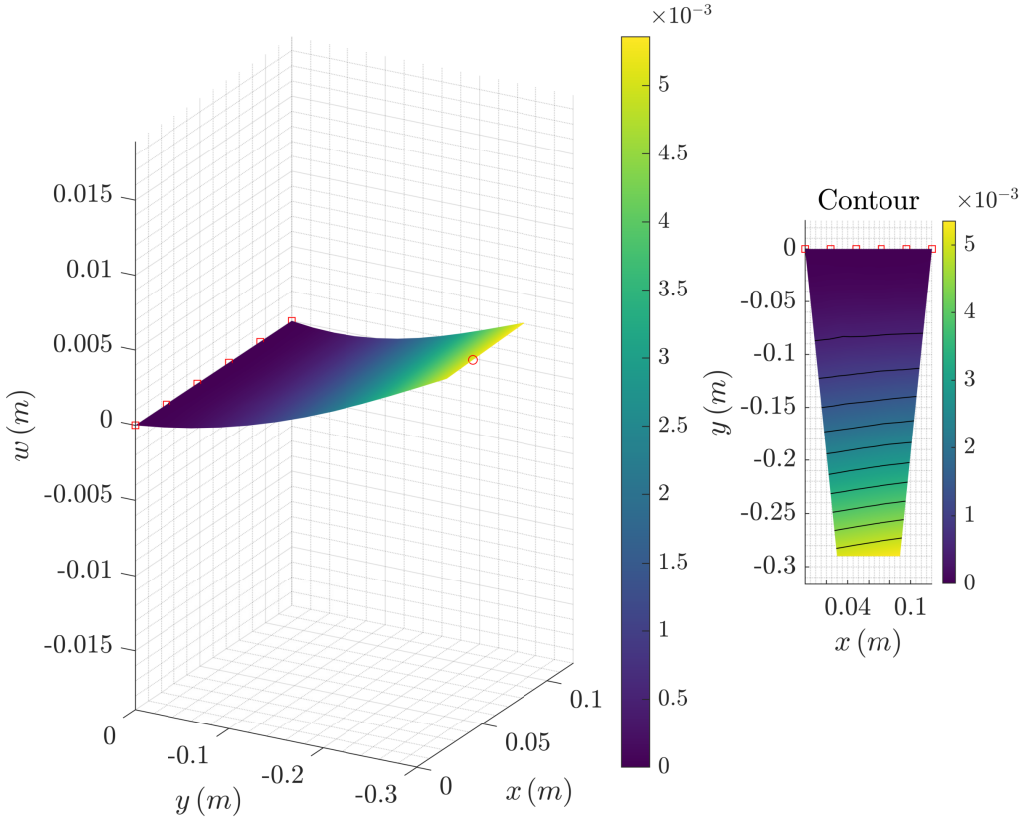

Figure 4.18: Bending deflection and contour plot for semi-span $s = 0.29m$, fixed support at the root section (i.e. $y = 0$) and Young modulus $E = 200GPa$. A selected tip deflection location is denoted with a circle. Comparison with [207].

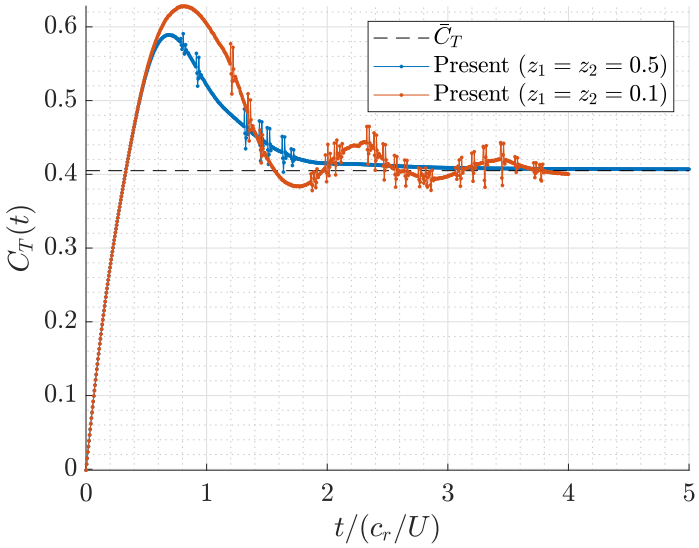

Figure 4.19: Steady-state simulations. Effect of damping ratio on the time history of thrust. Clamped wing of span $s = 0.58m$, Young's modulus $E = 193GPa$. Comparison with [207].

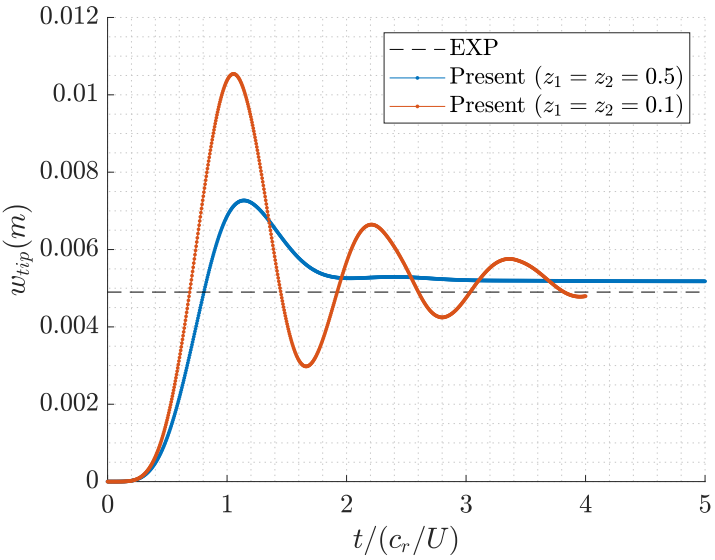

Figure 4.20: Steady-state simulations. Effect of damping ratio on the maximum tip amplitude. Clamped wing of span $s = 0.58m$, Young's modulus $E = 193GPa$. Comparison with [207].

4.3.3 Study 3. Flexible wing in flapping mode

To investigate effects of flexibility on the propulsive performance of a wing in flapping mode I examined a rectangular planform ($c = 0.33m$, $s = 1.0m$) of moderate aspect ratio with NACA 0009 profiles. The flapping parameters are provided in Table 4.5. Heaving amplitude and maximum effective angle are fixed, whereas the pitch motion amplitude is defined based on Strouhal number selection using Eq. (2.4). This process, described in Schouveiler et al. 2005 [52], ensures that flapping motion is within a range of effective angles potential theory can treat. The cruising speed is set to $U = 2.27m/s$ and Reynolds number is $Re = 7.5 \cdot 10^5$.

Table 4.5: Flapping kinematics of rectangular thruster.

Dimensions	$c = 0.33m$, $s = 1.0m$, $AR = 3$
Planform, sections	$\Lambda = 0^o$, $\lambda_r = 1.0$, NACA 0009
Inflow (i.e. forward motion)	$Re = 7.5 \cdot 10^5$, $U = 2.27m/s$
Heave motion, Phase lag.	$h_0/c = 0.75$, $\psi = -90^o$
Eff. angle, pivot point	$a_{eff} = 15^o$, $X_R = 1/3c$
Strouhal number	$Str = [0.2 - 0.35]$

This study is centered around chord-wise flexibility and therefore the wing is modeled as a plate fully clamped at the leading edge. On the contrary, a T-foil configuration where the root section of the wing is modeled as a fixed support is more appropriate for span-wise flexibility studies, see, e.g., Heathcote et al. [75] and the results of Studies 1-2. The plate's thickness variation in the chord-wise direction follows the NACA 0009 profile.

Regarding the discretization, I used $NEC = 60$, $NEA = 6AR$ panel elements for the *3dBEM* spatial discretization chordwise and spanwise respectively, for the finite element mesh $N_{elem} = 106$ DKT triangles and a shared time-discretization of $(dt/T_p)\% = 0.48$. Wake dynamics are linearized. The meshes used are depicted in Figure 4.23. The Jacobian size is $N = 204$ for the Newmark fsi, whereas for the Crank-Nicolson scheme it would be of size $N = 408$. The Rayleigh proportional damping coefficients used here are $a_1 = 2.5$, $a_2 = 0.01$.

Table 4.6 contains results of average thrust, efficiency and maximum TE deflection of the root section for different materials assuming a Strouhal number of $Str = 0.25$. The most flexible material labeled as $P1$ leads to an efficiency enhancement of 2.44% but the reduction of average thrust is substantial. The drop lowers as forcing frequency decreases, whereas efficiency enhancement is evident throughout the examined range of frequencies. This observation agrees with the findings of Zhu 2007 [63].

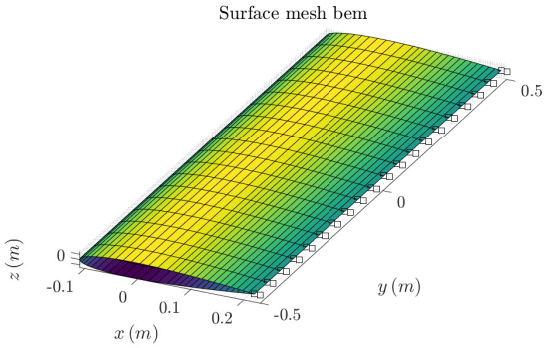

Figure 4.21: (a)

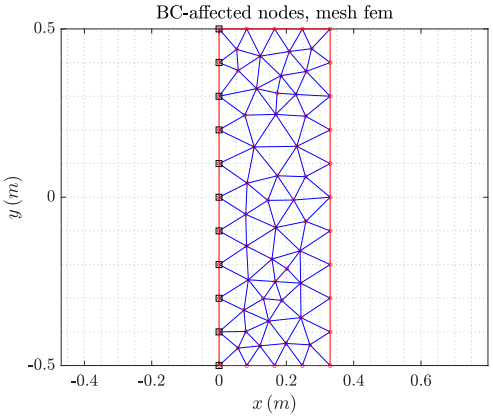

Figure 4.22: (b)

Figure 4.23: (a) *3dBEM* and (b) *2dFEM* meshes used in the chord-wise flexibility study referring to a NACA 0009 rectangular wing. Black squares denote fixed support in FEM simulations.

Table 4.6: Material selection for chord-wise flexibility study. NACA 0009 rectangular flapping thruster operating at $Str = 0.25$.

Materials	Rigid	$P1$	$P2$	AL	ST
$E(GPa)$	-	0.1	3.5	70	210
$\rho_s(kg/m^3)$	-	1200	1200	2710	7850
Poisson ratio ν	-	0.37	0.37	0.33	0.28
$w^{max}(m)$	-	0.0150	$7.61 \cdot 10^{-4}$	$3.37 \cdot 10^{-5}$	$3.47 \cdot 10^{-5}$
$E/\rho_s gc$	-	$2.6 \cdot 10^4$	$9.0 \cdot 10^5$	$8.0 \cdot 10^6$	$7.8 \cdot 10^6$
Thrust $\bar{C}_T$	0.2957	0.2411	0.2920	0.2946	0.2946
Efficiency η	0.7372	0.7550	0.7377	0.7371	0.7371

For the $P1$-material, I performed parametric runs to retrieve information on the wing's performance near the $Str = 0.25$ design point. The results are provided in Figure 4.24, where we can observe that efficiency enhancement is evident in the range of examined forcing frequencies. In Figure 4.25, I provide additional information regarding the maximum TE deflection at the root and predicted phase lag. The corresponding effective angle of attack profiles for $Str = \{0.2 - 0.4\}$ are provided in Figure 4.26 for completeness along with the selected pitch amplitudes.

A comparison between the time histories of lift, thrust and moment coefficients of the rigid and flexible wing thrusters operating in $Str = 0.25$ is provided in Figure 4.27. Chord-wise flexibility in this scenario reduces both thrust and lift coefficients, whereas leads to a small increase in the moment coefficient. Another important aspect, related to resonance effects, is the phase difference between the bending deflections and the enforced flapping frequency. A favorable phase difference results in larger bending deflections, leading to efficiency enhancement; see, e.g., [76]. In the examined scenario we can observe that, as Strouhal number increases, phase difference follows the trend resulting in greater bending deflections. Moreover, the ascending behavior of the tip amplitude curve in Figure 4.25 suggests that the first natural frequency of the coupled system does not lie within the examined range of Strouhal numbers.

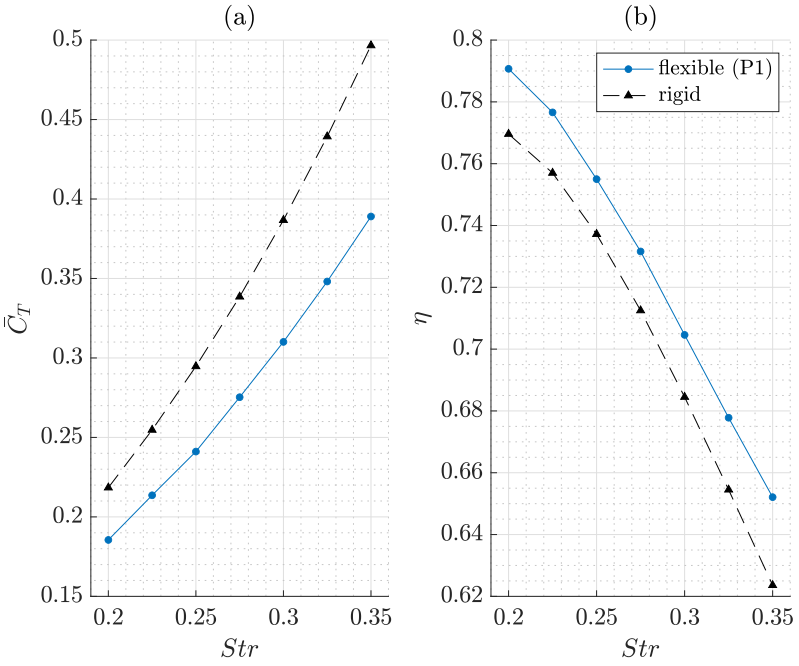

Figure 4.24: (a) Thrust and (b) propulsive efficiency as functions of Strouhal number for the rigid and flexible wing assuming $a_{eff}^{max} = 15^o$.

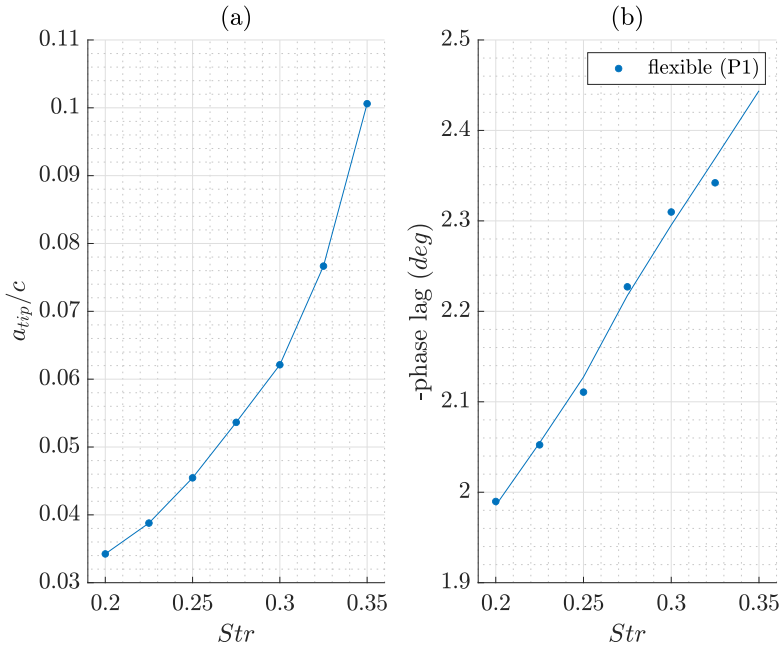

Figure 4.25: (a) Maximum TE tip amplitude at the root and (b) phase lag for the $P1$-flexible wing, assuming $a_{eff}^{max} = 15^o$.

Related to the structural solution, in Figures 4.28-4.29 I provide the time history of trailing edge deflection at the root section for $Str\{= 0.25, 0.35\}$ respectively. Instances of wing bending deflection during the last simulation period for operation at $Str = 0.25$ are shown schematically in Figure 4.30, where we can observe that chord-wise flexibility is dominant in this study case. The nodes affected by the fixed support boundary conditions are denoted with squares. An orange circle is used to denote the TE location for which the time history of deflections is provided in Figures 4.28-4.29. Deflection in the span-wise direction is observable, however chord-wise flexibility is dominant in this particular test case. It is also important to note that maximum pressure difference occurs closer to the leading edge where the thickness profile is fuller compared to the trailing edge region, therefore deflections in near the latter are very small as expected. Maximum deflection occurs at the root section in the trailing edge.

The diagram of tip amplitude and phase lag suggest that the first natural frequency of the coupled system does not lie within the examined range of forcing frequencies, otherwise a peak in terms of the tip amplitude would have been located based on the observations in Paraz et al. [76] experiments. Simulation of the wing's hydro-elastic behavior assuming homogeneous $P1$ material at higher frequencies lies outside the scope of thin plate theory, thus slightly stiffer material is used to simulate the response at higher forcing frequencies.

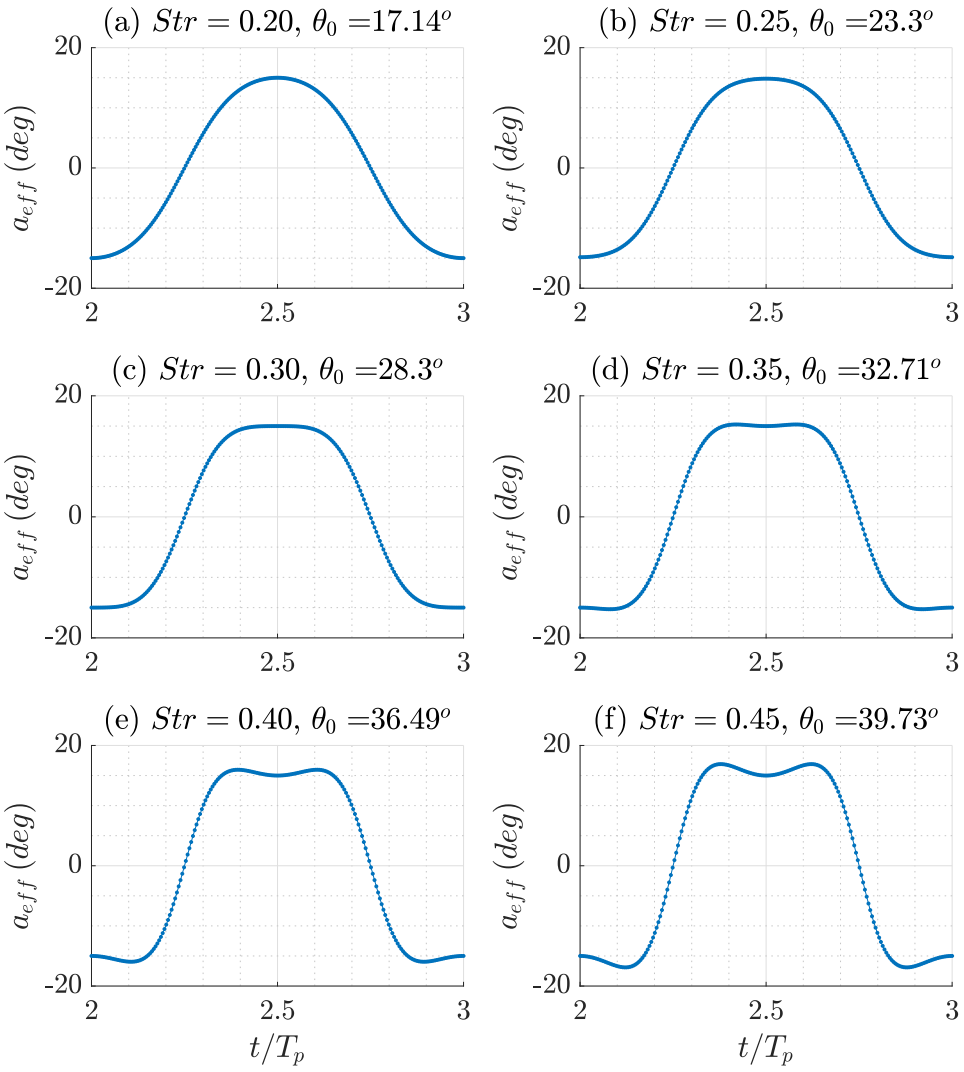

Figure 4.26: Effective angle of attack profiles in degrees under the $a_{eff}^{max} = 15^o$ constraint for various Strouhal numbers during the last cycle of simulations.

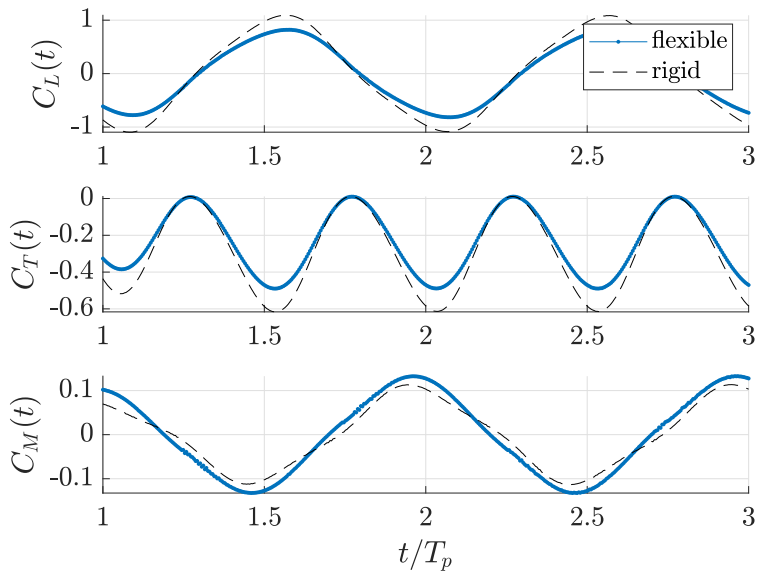

Figure 4.27: Instantaneous lift, thrust and moment coefficients for the rigid and flexible wing operating at $Str = 0.25$. Negative values of thrust denote force generated towards the direction of wing motion, i.e. negative $x-$axis.

It is evident that flexibility along the chord-line when significant yields an observable enhancement in terms of propulsive efficiency at the expense of thrust since it is reduced. These findings are compatible with 2D theory predictions and experimental works.

Useful guidelines for performing analysis using the developed numerical tools are also provided, since selection of material properties is important. Simulation of overly flexible wings might lead to numerical instabilities since it exceeds the prediction capabilities of the thin plate model used in our study. It is important to note that the *FlexWing3D* solver can be also used in a 'de-coupled' mode, where hydrodynamic pressure data from the *3dBEM* module are transferred to the finite element solver *2dFEM* at each time-step for independent structural analysis. These guidelines are summarized below,

1. Assuming a perfectly rigid wing thruster, begin by performing *3dBEM* simulations to obtain the reference propulsive performance metrics in the sense of $(\bar{C}_T - Str)$, $(\eta - Str)$ diagrams.

2. Select material properties, boundary conditions and a thickness profile for the wing-plate idealization. Perform decoupled (or one-way coupling) simulations with *FlexWing3D* to retrieve the time history of bending deflections. The *2dFEM* solver is numerically stable and may produce infeasible solutions

(i.e large bending deflections) might occur depending on the input parameters. Each 'de-coupled' simulation requires a few minutes of GPU/CPU computational time. Also, take into account that coupled *FlexWing3D* simulations yield lower deflections compared to the 'de-coupled' results for the same parameters.

3. Perform coupled *FlexWing3D* simulations to evaluate the effects of elasticity on the designed wing thruster.

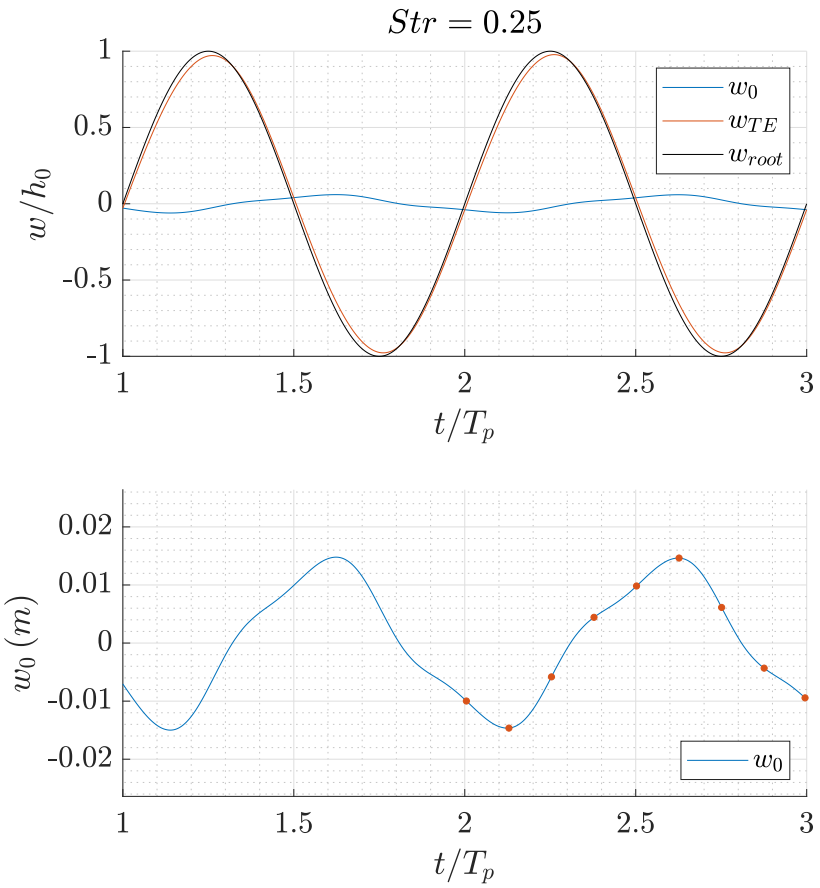

Figure 4.28: Time history of trailing edge deflection in the global [above] and local [below] systems during the last two periods of motion at $Str = 0.25$. The TE instances match the shapes provided in Figure 4.30 that follows.

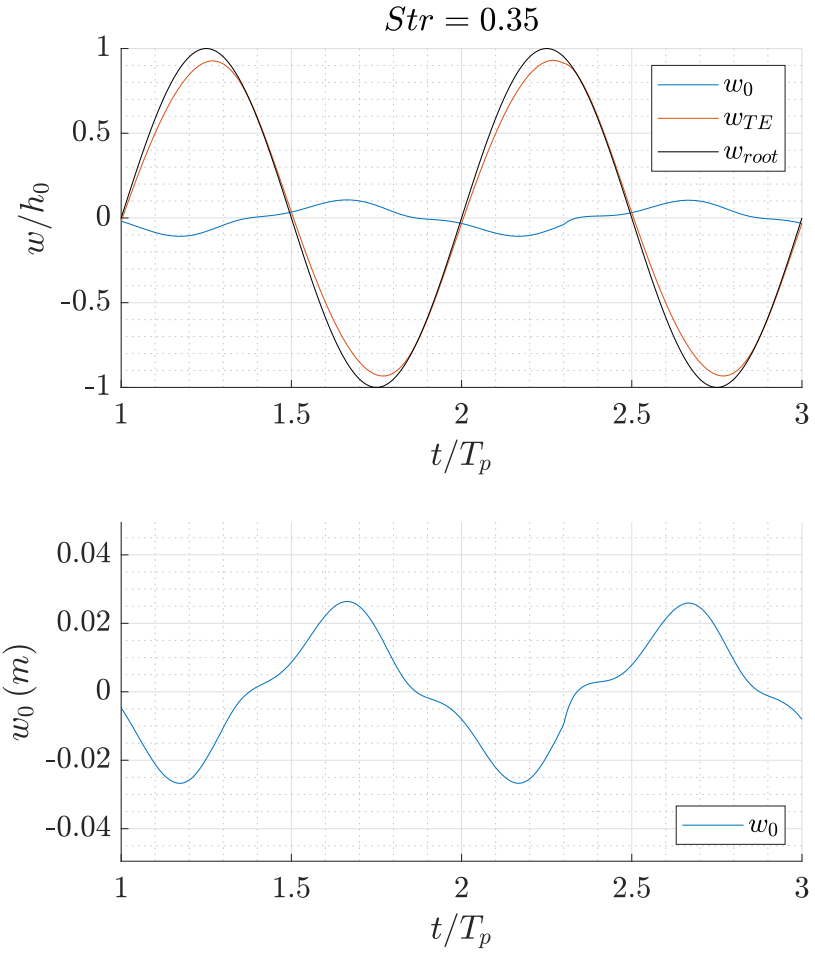

Figure 4.29: Time history of trailing edge deflection in the global [above] and local [below] systems during the last two periods of motion at $Str = 0.35$.

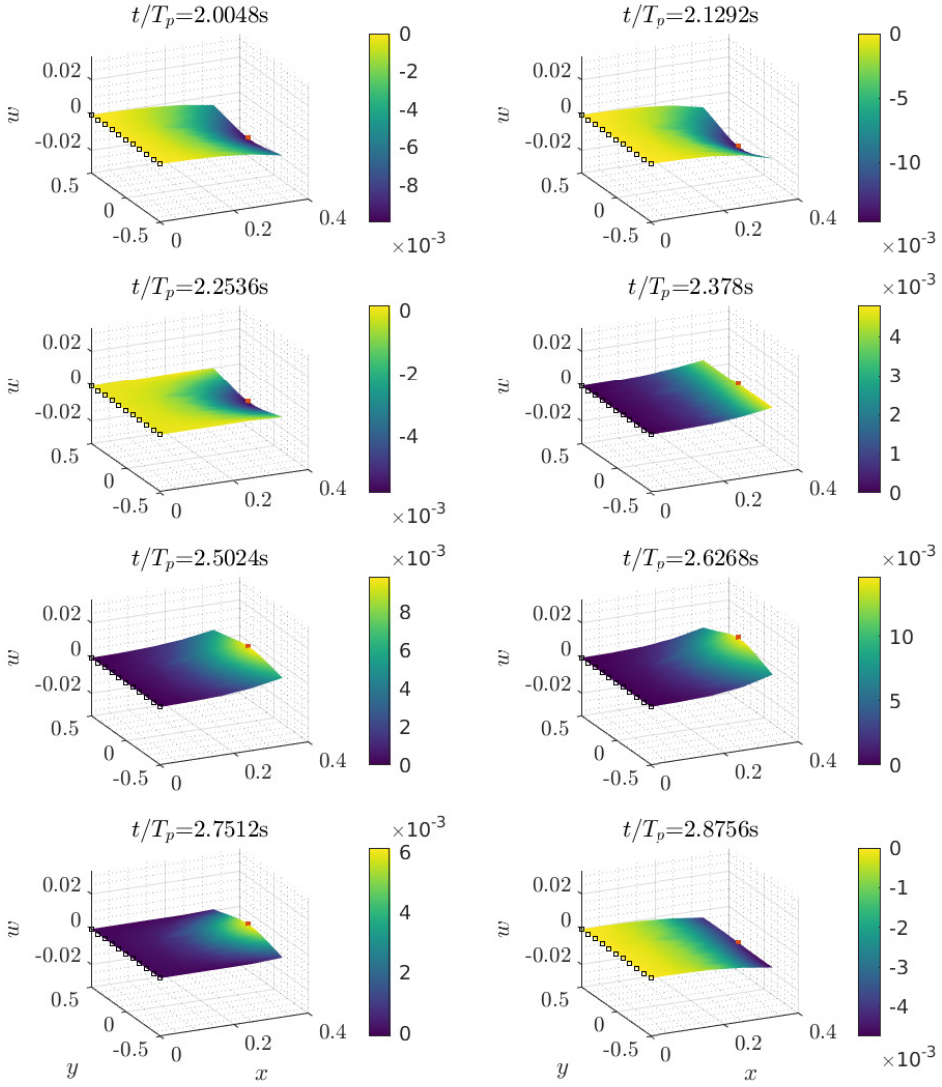

Figure 4.30: Instances of wing bending deflection during the last simulation period for operation at $Str = 0.25$. The wing is clamped at the leading edge and tip defections are provided for the TE location denoted with a circle.

4.4 Enhancing the performance of a passively morphing thruster via optimization

4.4.1 Case 1. Bio-inspired thickness profile

Riggs et al. 2010 [81] studied experimentally the effects of a bio-mimetic stiffness profile, mimicking that of a 'Pumpkinseed Sunfish' (Lepomis gibbosus), on the thrust generation capabilities of chord-wise flexible rectangular wings. Bioinspired sections outperformed the NACA 0012 wings in thrust production over the range of examined forcing frequencies. These profiles are shown schematically in Figure 4.31. Motivated by these findings, I performed an optimization study to determine an improved thickness profile for the chord-wise flexible wing thruster examined previously in Study 3 considering NACA 0012 profiles and material properties corresponding to $P1$ in Table 4.6.

Following a Direct Numerical Optimization (DNO) approach, I introduce a design variable vector containing geometric parameters that define the hydrofoil thickness profile. Efficiency maximization is the objective function under the thrust requirement formulated as a constraint. During the optimization process, modifications to the geometric shape of the hydrofoils, occurring locally, are handled using the PARSEC methodology. This method used widely in airfoil studies, introduces physically intuitive parameters to represent a hydrofoil, see Vecchia et al. 2014 [209].

PARSEC Parameterization

Modern airfoils have much more complex camber lines. Their shape is described not by explicit formulas, but by giving the coordinates of points on their surface. Local airfoil shape modification is usually obtained by smooth perturbations of the original airfoil coordinates through analytical function, such as Legendre, Chebyschev or Bernstein polynomials. These methods have the advantage of smooth local modifications, although they have no direct relation to geometry and this could lead to undulating curves. Therefore, the design of a new concept airfoils requires parameterization methods able to accommodate a wider range of new shapes. For instance B-splines and Bezier curves have been widely used to fit airfoil shapes via interpolation methods. They are very useful to reconstruct and optimize an airfoil (using several artifices on geometry curvature) but they give rise to some problems due to the difficulties related to managing control points' relative position. In Kostas et al. 2017 [145], an optimization procedure, based on an isogeometric BEM, is developed and used for hydrofoil shape optimization problems where airfoil shapes are represented by a closed B-spline curve defined by a set of eight parameters.

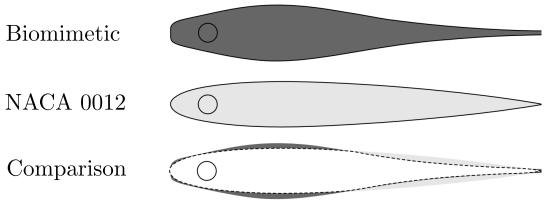

Figure 4.31: Bio-mimetic stiffness profile examined in Riggs et al. 2010 [81].

Physically intuitive methods enable the use of typical airfoil parameters for shape definition such as the leading edge radius, airfoil thickness or trailing edge angle. A methodology of this type, known as PARSEC, was developed by Sobieczky in 1999. PARSEC uses the 11 parameters shown in Figure 4.32 to represent an airfoil and these are directly linked to the geometry (thickness, curvature, maximum thickness abscissa, etc.) [209]. A description of the parameters is summarized in Table 4.7. This parameterization is well-known to the aerodynamics community and its physically intuitive parameters facilitate the optimization process by directly providing information about the current airfoil shape. PARSEC analytical formulation is given by,

$$z_{up} = \sum_{i=1}^{n=6} a_{up}^{i} \cdot x^{i-1/2}, \quad z_{lo} = \sum_{i=1}^{n=6} a_{lo}^{i} \cdot x^{i-1/2}, \tag{4.30}$$

where z_{up}, z_{lo} are the vertical coordinate of the upper and lower side respectively, x is the horizontal, or chord-wise coordinate normalized in $[0, 1]$. The coefficients a_{up}, a_{lo} have to be computed by using the 11 given parameters as follows,

$$C_{up} \times a_{up} = b_{up}, \quad C_{lo} \times a_{lo} = b_{lo}, \tag{4.31}$$

where both coefficient matrices (C_{up}, C_{lo}) and right hand sides (b_{up}, b_{lo}) are defined as shown in the matrices,

$$C_{up} = \begin{bmatrix} 1 & 1 & 1 & 1 & 1 & 1 \\ p_2^{1/2} & p_2^{3/2} & p_2^{5/2} & p_2^{7/2} & p_2^{9/2} & p_2^{11/2} \\ 1/2 & 3/2 & 5/2 & 7/2 & 9/2 & 11/2 \\ \frac{1}{2}p_2^{-1/2} & \frac{3}{2}p_2^{1/2} & \frac{5}{2}p_2^{3/2} & \frac{7}{2}p_2^{5/2} & \frac{9}{2}p_2^{7/2} & \frac{11}{2}p_2^{9/2} \\ \frac{-1}{4}p_2^{-3/2} & \frac{3}{4}p_2^{-1/2} & \frac{15}{4}p_2^{1/2} & \frac{15}{4}p_2^{1/2} & \frac{63}{4}p_2^{5/2} & \frac{99}{4}p_2^{7/2} \\ 1 & 0 & 0 & 0 & 0 & 0 \end{bmatrix}, \tag{4.32}$$

$$C_{lo} = \begin{bmatrix} 1 & 1 & 1 & 1 & 1 & 1 \\ p_5^{1/2} & p_5^{3/2} & p_5^{5/2} & p_5^{7/2} & p_5^{9/2} & p_5^{11/2} \\ 1/2 & 3/2 & 5/2 & 7/2 & 9/2 & 11/2 \\ \frac{1}{2}p_5^{-1/2} & \frac{3}{2}p_5^{1/2} & \frac{5}{2}p_5^{3/2} & \frac{7}{2}p_5^{5/2} & \frac{9}{2}p_5^{7/2} & \frac{11}{2}p_5^{9/2} \\ \frac{-1}{4}p_5^{-3/2} & \frac{3}{4}p_5^{-1/2} & \frac{15}{4}p_5^{1/2} & \frac{15}{4}p_5^{1/2} & \frac{63}{4}p_5^{5/2} & \frac{99}{4}p_5^{7/2} \\ 1 & 0 & 0 & 0 & 0 & 0 \end{bmatrix}, \tag{4.33}$$

$$b_{up} = \begin{bmatrix} p_8 + p_9/2 \\ p_3 \\ tan(p_{10} - p_{11}/2) \\ 0 \\ p_4 \\ \sqrt{2p_1} \end{bmatrix}, \qquad b_{lo} = \begin{bmatrix} p_8 - p_9/2 \\ p_6 \\ tan(p_{10} + p_{11}/2) \\ 0 \\ p_4 \\ \sqrt{2p_1} \end{bmatrix}. \tag{4.34}$$

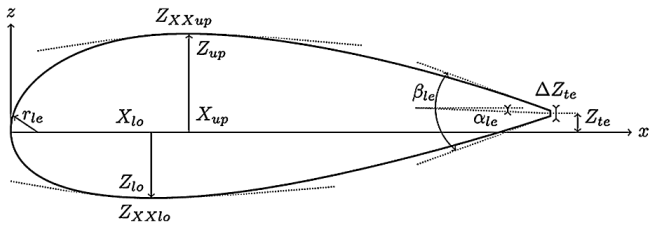

Figure 4.32: PARSEC variable definition in Vecchia et al. [209].

Problem formulation and solution

For simplicity, hydrofoil sections are assumed uniform in the direction of span and, since only symmetric profiles are examined, PARSEC parameterization is based on five independent parameters (r_{le},X_{up},Z_{up},$Z_{XX_{up}}$,α_{te}), whereas the others are be

Table 4.7: PARSEC parameter definition.

Parameter	Symbol	Definition
p1	r_{le}	leading edge radius
p2	X_{up}	upper crest position in horizontal coordinates
p3	Z_{up}	upper crest position in vertical coordinates
p4	$Z_{XX_{up}}$	upper crest curvature
p5	X_{lo}	lower crest position in horizontal coordinates
p6	Z_{lo}	lower crest position in vertical coordinates
p7	$Z_{XX_{lo}}$	lower crest curvature
p8	Z_{te}	trailing edge offset in vertical sense
p9	ΔZ_{te}	trailing edge thickness
p10	α_{te}	trailing edge direction
p11	β_{te}	trailing edge wedge angle

defined as,

$$X_{lo} = X_{up}, \quad Z_{lo} = -Z_{up}, \quad Z_{XX_{lo}} = Z_{XX_{up}},$$
$$Z_{te} = \Delta Z_{te} = b_{te} = 0. \tag{4.35}$$

Regarding the kinematics, I assume that the wing follows a flapping trajectory examined previously in Study 3 and exhibits passive morphing mainly due to the hydrodynamic loads leading to dominant deflection in the chord-wise direction. Design variable vector comprises of $b_n = \{p1, p2, p3, p4, p5\}$ based on parameter definition shown in Table 4.7. Optimal tuning of geometric parameters is accomplished via the solution of an optimization problem on efficiency maximization under a thrust constraint. Pitch amplitude is defined based on Strouhal number so that the effective angle of attack is $\alpha_{eff} = 15^o$.

Propulsive efficiency maximization (or minimization of $1/\eta$) is selected as the objective function,

$$\eta = U\overline{T}/P_{in}, \tag{4.36}$$

where $\overline{T}$ is the mean thrust force and P_{in} the input power required to sustain the wing's prescribed motions (flapping, morphing) under the resulting hydrodynamic loads. Taking into consideration that thrust losses due to flexibility are greater for finite wing cases, compared to two-dimensional simulations as discussed in Zhu 2007 [63] I assume a tolerance parameter of $p = 21\%$[3],

$$(1-p)C_{Treq} \leq \overline{C}_T \leq (1+p)C_{Treq}, \tag{4.37}$$

[3]Smaller values of parameters p did not yield noticeable propulsive performance enhancement, thus it was decided that a higher value is to be selected; which yielded $p = 21\%$.

where C_{Treq} is the thrust generated by the rigid thruster at design point $Str = 025$. Mean thrust is calculated using time history data from the last flapping-cycle of motion, and the constraint is valid for the inviscid value. However, viscous-corrected mean thrust and efficiency are included in the results assuming coefficients $C_F = 0.0039$ and $C_a = 0.13$, see also Section 2.5.3 for details regarding coefficient calibration. Proportional damping coefficients are assumed $a = 2.5$ (mass), $b = 0.01$ (stiffness).

All optimization studies are run using the Matlab sequential quadratic programming algorithm *fmincon* that is suitable for handling nonlinear constraints. Sensitivity and Hessian computations are based on forward differences; using default options. A typical three flapping-cycle simulation based on the linear wake model and a coarse discretization ($NEA = 6AR$, $NEC = 50$, $N_{elem} = 106$ and $dt/T_p = 0.4\%$) requires $210min$ on the AMD Ryzen 9 3900XT workstation equipped with an NVIDIA GeForce RTX 3080 (10GB VRAM). Thus for a few optimization cycles the optimization problem required roughly 9 days simulation time.

Table 4.8 contains the optimal and reference designs along with the upper/lower bounds required by the 'fmincon' solver. Sequential quadratic programming algorithms, during the search for an optimal solution that also satisfied the constraints, may favor the user-defined, preselected, upper and lower design-variable bounds.

Table 4.8: Optimal thickness profile.

		naca0012	lb	optimal	ub
p1	r_{le}	0.0152	0.0114	0.0130	0.0175
p2	X_{up}	0.2966	0.2521	0.2400	0.3411
p3	Z_{up}	0.0588	0.0500	0.0605	0.0617
p4	$Z_{XX_{up}}$	-0.4515	-0.4741	-0.4741	-0.000
p10	α_{te}	-9.0000	-11.250	-7.6500	-7.000

Figure 4.33 depicts the optimal thickness profile deduced from our simulations, where similarity with the bio-mimetic stiffness profile in Riggs et al. [81] is evident. In their designs, the bio-mimetic profile is more slender towards the trailing edge and near the hydrodynamic center it becomes thicker compared to the NACA 0012 profile. Optimal shape, in our case, is slenderer near the trailing edge; however, the increase in thickness near the pitch axis X_R is more subtle, but evident. This is shown in Figure 4.34 containing a 'close up' to the leading edge region. The PARSEC parameter affecting the leading-edge radius for the optimal geometry is greater than the NACA 0012.

Regarding the propulsive performance of the optimal shape, results show that

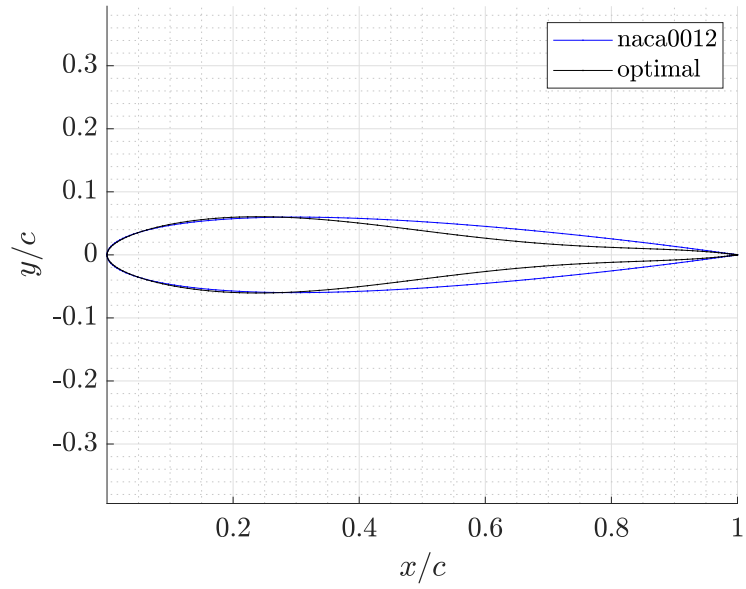

Figure 4.33: Reference and optimal hydrofoil thickness profiles.

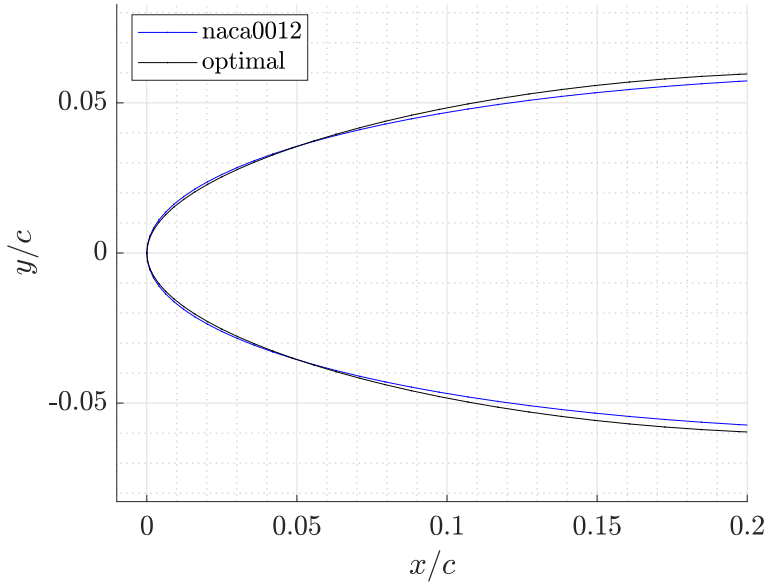

Figure 4.34: Close up on leading edge region for the reference and optimal hydrofoil thickness profiles.

slenderness towards the trailing edge region gives rise to higher bending deflections which increase the efficiency η. Table 4.9 summarizes the propulsive performance metrics, in the sense of Strouhal number, mean thrust coefficient and efficiency (i.e. without viscous corrections), corresponding to the reference and optimal thrusters. An enhancement of 3.1% is be obtained due to the bio-inspired selection of thickness profile at a thrust reduction of 21%. The latter is considerable, thus further investigation is needed for thrust compensation.

Table 4.9: Propulsive performance metrics (Str, $\overline{C}_T$, η) for the optimal and reference thruster.

id	Material	Profile	Strouhal	Mean thrust $\overline{C}_T$	Diff. (%)	Efficiency η	Diff. (%)	Max. $w\,(m)$
0	Rigid	0012	0.250	0.2926	-	0.7308	-	-
1	Flex. $P1$	optimal	0.250	0.2309	-21.08	0.7532	3.1	0.0173
2	Flex. $P1$	optimal	0.265	0.2482	-19.93	0.7389	1.2	0.0187
3	Flex. $P1$	0012	0.250	0.2612	-10.70	0.7350	0.6	0.0079

Figure 4.35 contains the time histories of thrust, lift and moment coefficients for the reference and optimal thruster at design point, where the loss of thrust is evident. The efficiency enhancement is also attributed to the phase difference between the force coefficients. Instantaneous bending deflection at the trailing edge at root section is presented in Figure 4.36, highlighting that deflections are observable with respect to the wing's dimensions. Finally, I provide a snapshot of the flexible wing shape at maximum deflection in Figure 4.37 where chord-line flexibility is dominant. Span-wise effects are still visible since variability along the trailing edge deflection is visible. This effect may contribute to thrust reduction and it needs to be addressed in future investigations.

For completeness, I also include results referring to the optimal thruster operating at a higher frequency $Str = 0.265$ ($id = 2$), where efficiency enhancement is still evident. Moreover, the performance metrics of the flexible NACA 0012 thruster ($id = 3$) are included for the design point under study.

Loss of thrust is significant in this example, however for applications involving AUVs for oceanic exploration running on limit battery capacity even the slightest improvement in the propulsive efficiency corresponds to valuable extension of the vehicle's range. Further investigations need to be conducted in order to reveal potential mechanisms for thrust compensation in cases of flexible thrusters.

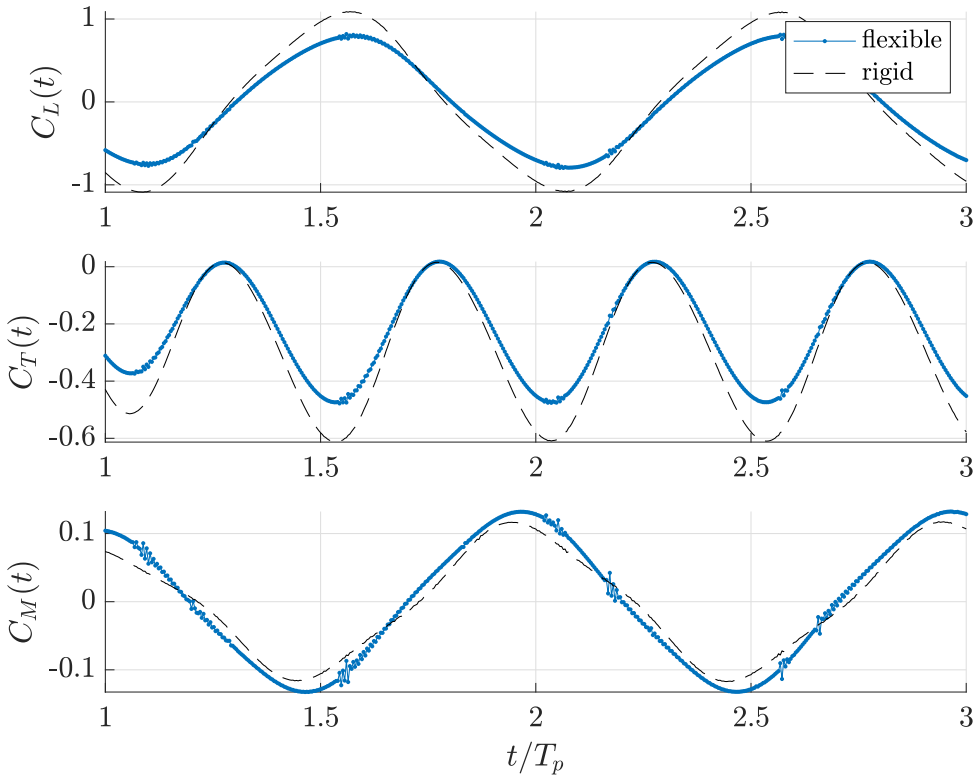

Figure 4.35: Instantaneous lift ($\overline{C}_L$), thrust ($\overline{C}_T$) and moment ($\overline{C}_M$) coefficients for the rigid (reference) and flexible (optimal) wing thruster deduced from the optimization study at design point $Str = 0.25$.

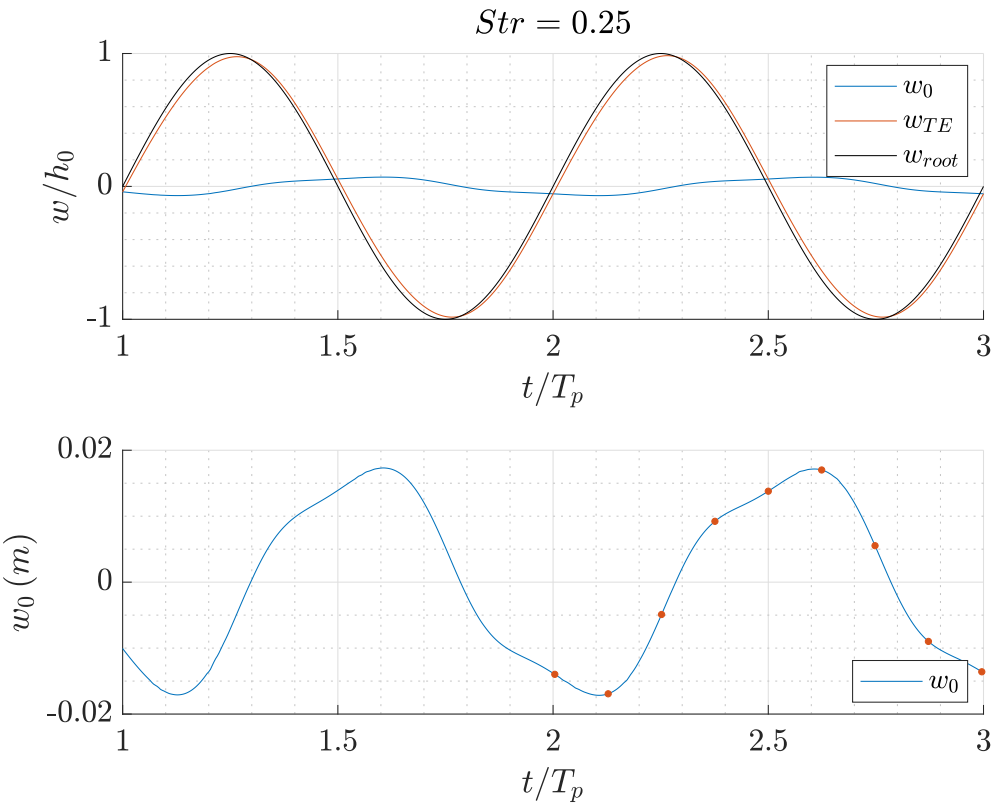

Figure 4.36: Time history of global and local displacement for the flexible thruster with optimal thickness profile at design point $Str = 0.25$.

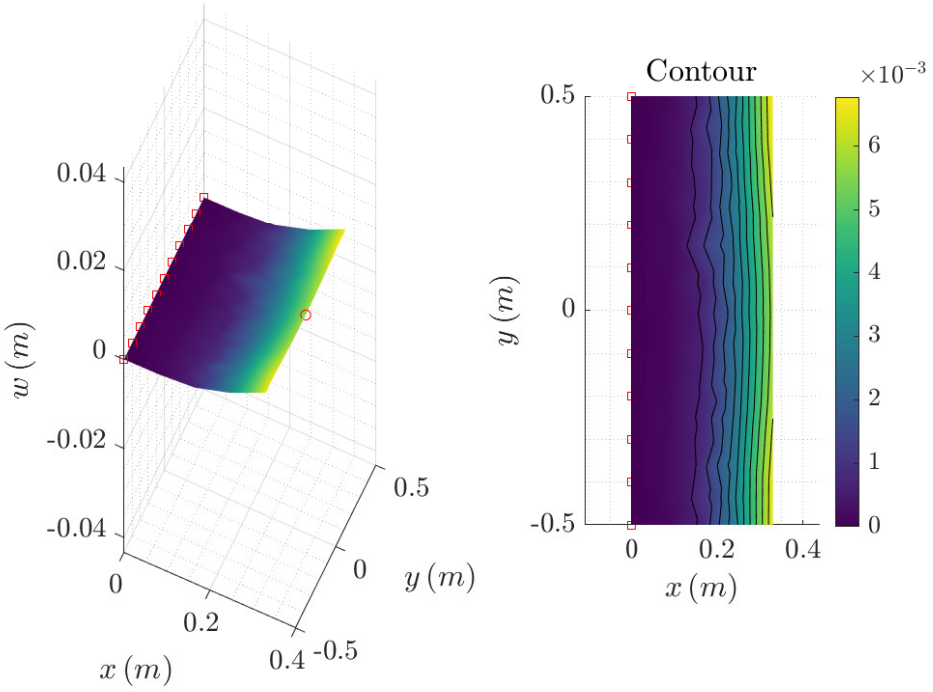

Figure 4.37: Flexible wing thruster shape at maximum deflection referring to design point $Str = 0.25$ in the local coordinate system.

4.5 Future extensions

Examination of various different support options and thruster planform shapes over a range of flapping parameters and thickness profiles is left for future work. Direct extensions referring to each sub-solver are also valuable for the coupled computational tool. Further validation via comparisons against other works is beneficial to the process of developing the present fluid-structure interaction tool by means of showcasing its strengths and limitations.

For example, comparison with the numerical work of Zhu 2007 [63], where very thin rectangular plates of constant thickness are tested can only be accomplished by considering an extremely thin hydrofoil profile with our numerical tool as is. The computational tool introduced in [63] is also based on potential flow formulation for the hydrodynamics and since rigidity is varied from very stiff to flexible cases, comparison against this work has some merit in terms of verification. Comparisons require a very fine time-step (e.g. $0.05\%T_p$) to achieve convergence during internal iteration and the overall computational time becomes extremely high.

To reduce the overall computational time for such cases in just a few hours

requires further code development, exploitation of parallel computation techniques on graphics cards and approximation of the Jacobian instead of direct calculation. As the finite element mesh gets denser, the Jacobian size increases; resulting in a significant increase of the overall simulation time. This translates as a 'bottle-neck' in terms of scaling to finer grids with the algorithm for strong coupling as is. A direct extension related to this is the following,

- **Approximate Jacobian.** One way to alleviate these effects can be accomplished by implementing methodologies that do not require evaluation of the full Jacobian, in order to save computational time. Spenke et al. 2020 [210] introduce a methodology that produces estimates of the Jacobian using information from previous time steps, which significantly reduces the overall computational time. This approach was successfully implemented by Lauber et al. 2023 [211], to the numerical scheme developed for tackling the FSI problem of flexible membranes.

- **Optimization algorithms.** The above extensions will enable optimization studies involving a greater number of design variables. In addition, the use of more sophisticated optimization algorithms, hybrid methods and evolutionary approaches is left as an interesting future work extension. The solution of MDO problems can also be pursued.

Other extensions referring to investigation of flexibility effects on flapping-foil configurations include,

- **Boundary conditions.** Perform simulations on flapping wing thrusters assuming T-foil configurations (see, e.g., Figure 1.6), or more sophisticated support options, to quantify effects on the propulsive performance.

- **Planform shape parameterization.** Curved boundaries and more complex wing geometries. This requires extension of the mesh generation modules in the *3dBEM*, *2dFEM* tools. Alternatively, external modelers could be used to generate the meshes.

- **Non-uniform stiffness.** Investigate effects of variability in material stiffness, i.e. $D(x, y)$, on the elastic response of wing thrusters. This includes non-uniform material properties in the context of functionally graded materials, for instance Young's modulus $E = E(x, y)$.

- **Friction-drag corrections.** The friction drag coefficients that were introduced in the post-processing phase of *3dBEM* simulations, can be introduced before mapping of hydrodynamic load to the finite element mesh so that they are included in the fsi simulations.

- **Technological applications.** The bio-inspired wings examined in the present work, apart from small-scale AUV propulsion solution, are also studied in the literature as wave/current energy extraction devices. Extension of the developed scheme to address problems of semi-active or fully active flexible flapping-foil energy harvesting devices is also possible; see, e.g. [40], [41] and [9].

Part II

Partial-cavitation model based on inverse design

Chapter 5

Adjoint BEM-based method for partially cavitating hydrofoils beneath the free surface

In the present work, the problem of partial cavitation prediction for hydrofoils steadily operating at finite submergence depths is addressed. Results regarding the case of partially cavitating hydrofoils in an unbounded domain have been published in Anevlavi & Belibassakis 2021 [212]. Ideal flow models are suitable for predictions away from the wave-breaking regime, and therefore the present method is suitable for cases of moderate submergence depths. The mathematical formulation is for steady-state modeling of partially cavitating hydrofoils, and transient phenomena are not part of the simulations. However, this method is extensible to the case of unsteady partially cavitating hydrofoils where the length and shape of the attached cavity must be modified accordingly; see the work of Behbahani-Nejad and Changizian [213] for ideal-flow based unsteady partial cavitation modeling. The sensitivities required for the gradient-based optimization algorithm are derived using the adjoint method.

The adjoint method is extremely cost-effective for large numbers of design variables compared to the number of objective functions as it requires only two solver evaluations per optimization cycle to produce the sensitivity derivative estimates for every design variable. The objective function follows the assumption of constant pressure on the cavity boundary, which is typical for cavitation prediction ideal-flow solvers. The primary and adjoint boundary value problems are solved numerically at each optimization cycle using the source/vorticity BEM solver, see, e.g. [58], [59]. The hydrofoil/cavity boundary parameterization tool uses B-splines and the coordinates of control points included in the design variable vector [137].

The inverse problem solution yields the initially unknown cavitation number and the attached cavity shape for given cavity extent, see, e.g. Uhlman [214],

Kinnas & Fine [62]. The cavity termination model introduced in the proposed method consists of two modeling components. This model has a transition region with the user-defined length between the rear part of the cavity, where a constant-pressure condition needs to be satisfied, and the wet portion of the boundary where a flow tangency condition holds. In the transition region, a flow tangency condition on the cavity surface is also satisfied. Certain geometric constraints act on the B-spline control points affecting the transition region. A comparison between the present method and a standard finite difference scheme highlights the benefits of using the adjoint method to produce sensitivity estimates for each design variable.

Alternative methodologies exist, such as the non-iterative algorithm of [213] for unsteady partial cavitation of hydrofoils without free surface effects, where the spatial-iterative scheme is removed by means of a new approach in determining the instantaneous cavity length. Moreover, in the work of Choi et al. 2005 [215] a shape-optimization model based on the continuous adjoint method was employed to determine the optimum (minimum-drag) shape of a super-cavitating torpedo given certain operating conditions and the cavitation phenomenon concurrently as part of the solution. In Lemonnier &. Rowe 1998 [216], the authors introduce a simple and adjustable minimization principle for cavity modeling and discuss its effects on the predicted pressure profiles.

Results obtained using the proposed method are compared against the PC-PAN solver from Kinnas & Fine [62], in the case of NACA 16006 hydrofoil at various Froude numbers. The comparison targets wave elevation profile results, the pressure coefficient distribution and the attached cavity shape. Additional comparisons between the present method and experimental data illustrate that the solver shows similar trends with other potential-based methods in terms of the cavity length/cavitation number curve. Moreover, this work contains simulations that detail angle of attack and submergence depth effects on the cavitation number and cavity volume.

Chapter 5 is structured as follows. Following this short introduction, the mathematical formulation of the proposed inverse model for partially cavitating hydrofoils operating beneath the free surface at a constant speed is provided. Then, information regarding the numerical implementation of the method and the geometric representation of the attached cavity, using B-splines, are given. Our method is verified via comparisons against other works, including the famous PC-PAN method [62], and experimental data. Then, results concerning simulations for the NACA 16006 hydrofoil at various angles of attack and submergence depths is included. Interpretation and discussion on the results is provided in relation to the predicted wave elevation profile, the pressure distribution on the hydrofoil surface, and the attached cavity shape for a given cavity extent. Summary of the findings are given in the conclusion section along with highlights. Exploitation of

the present method is possible for the preliminary design of partially cavitating lifting flow systems and applications of ship and marine hydrodynamics.

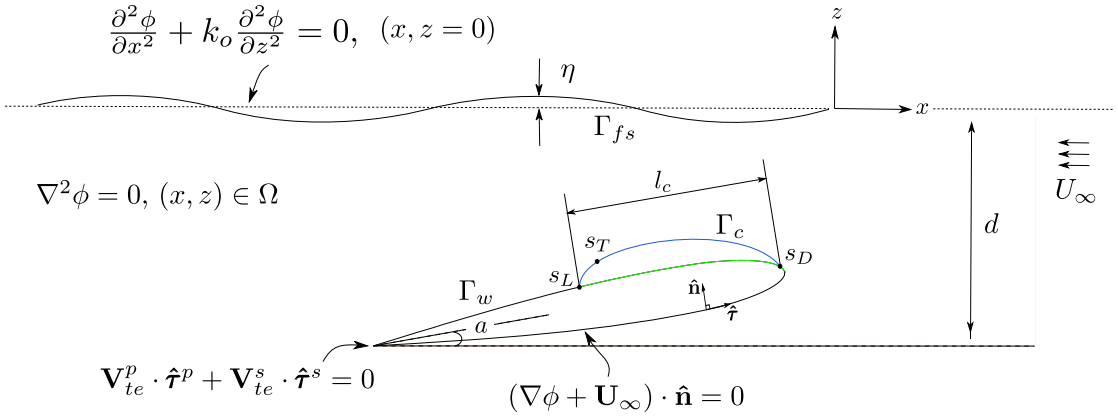

Figure 5.1: Problem definition for a partially cavitating hydrofoil steadily moving beneath the free surface.

5.1 Mathematical formulation

This section presents first the governing partial differential equations for the lifting flow problem of a hydrofoil steadily moving beneath the free surface under the assumptions of ideal fluid flow, namely the primal problem. Various numerical methods address non-cavitating hydrofoils submerged beneath the free surface, such as [121], [136] and [217], under the assumptions of a linearized free surface boundary and [218] for a more detailed overview.

The present work addresses the problem of a hydrofoil moving beneath the free surface at constant velocity with the effects of finite submergence depth via a steady formulation by introducing a body-fixed coordinate system, see Bal et al. [121]. The steady formulation is shown schematically in Figure 5.1, where the constant forward motion of the hydrofoil becomes equivalent to a uniform inflow velocity profile denoted as $\mathbf{U}_\infty = (-U_\infty, 0)$. The $x-$axis is negative in the direction of uniform inflow, the $z-$axis is positive upwards, and the linearized free surface at $z = 0$.

The domain boundary consists of the wetted part of the hydrofoil Γ_w (highlighted with gray), the attached cavity Γ_c (shown in blue) that has an initially unknown shape in the context of free-streamlines, and the free surface boundary Γ_{fs}. The hydrofoil of chord length c, is positioned at submergence depth d with respect to its trailing edge (TE), facing the inflow at an angle of attack α. The unit

normal vector denoted as $\hat{\mathbf{n}}$, faces the exterior of domain Ω and the unit tangential vector at each position along the boundaries denoted as $\hat{\boldsymbol{\tau}}$, shown in Figure 5.1.

Under ideal-flow assumptions the total velocity potential $\Phi = -U_\infty x + \phi$, an expression that arises from the superposition of inflow and perturbation potential. The primary unknown for the boundary value problem (BVP) presented in this section is the perturbation velocity field. The governing equation is the Laplace,

$$\nabla^2 \Phi = 0, \quad (x, z) \in \Omega \tag{5.1}$$

The body boundary, comprising of the wetted part and the attached cavity, is modeled as a stream line and therefore a flow tangency condition must hold,

$$(\nabla\phi + \mathbf{U}_\infty) \cdot \hat{\mathbf{n}} = 0, \quad (x, z) \in \Gamma_c \cup \Gamma_w. \tag{5.2}$$

A pressure-type Kutta condition is enforced to ensure that the total velocity, defined as $\mathbf{V} = \nabla\phi + \mathbf{U}_\infty$, remains finite in the TE vicinity, which in the case of a steady problem reads equivalently,

$$\mathbf{V}^p_{te} \cdot \hat{\boldsymbol{\tau}}^p_{te} + \mathbf{V}^s_{te} \cdot \hat{\boldsymbol{\tau}}^p_{te} = 0, \tag{5.3}$$

where $\mathbf{V}^p_{te}$, $\mathbf{V}^s_{te}$ denote the total velocity on the pressure and suction sides of the hydrofoil, respectively, in the TE vicinity. Under the assumption of moderate submergence depths, a linearized free surface condition holds on $z = 0$,

$$\frac{\partial^2 \phi}{\partial x^2} + k_o \frac{\partial \phi}{\partial z} = 0, \quad (x, z = 0) \in \Gamma_{fs}, \tag{5.4}$$

where $k_o = g/U^2_\infty$ is the wave number for infinite water depth and g the gravitational acceleration. The wavelength for infinite water depth can be calculated as $\lambda = 2\pi/k_o$. This linearization allows for the velocity potential and the free surface elevation fields to be decoupled. The BVP in Eqs. (5.1)-(5.4) can be solved when the inflow conditions and the hydrofoil/cavity boundary are known. An integral formulation, based on a distribution of fundamental solutions of the Laplace equation on the boundaries, is used to represent the perturbation (or disturbance) potential in the following section. The solution representation satisfies by definition the condition at infinity that holds as,

$$lim_{z\to\infty} \nabla\phi \to 0. \tag{5.5}$$

The infinity condition expresses the physical assumption that the disturbances caused to the local fluid flow by the submerged lifting hydrofoil will decay at large distances, and the constant inflow velocity profile with be dominant at infinity. The standard ideal-flow models lack a mechanism that yields the decay of vortex formation at large distances due to the inviscid assumption. Therefore, the very

definition of the admissible solutions satisfies an infinity condition that holds for the potential field representation.

The solution of the BVP yields the velocity distribution on the hydrofoil, and Bernoulli's theorem for steady potential flow provides estimates for the pressure distribution from the velocity information,

$$p + 0.5\rho V^2 = p_\infty + 0.5\rho U_\infty^2, \tag{5.6}$$

with ρ denoting the fluid density. The free surface elevation is derived from,

$$\eta = -\frac{U_\infty}{g}\frac{\partial \phi}{\partial x}, \quad (x, z = 0) \in \Gamma_{fs}. \tag{5.7}$$

In the case of non-cavitating hydrofoils, the above formulation is suitable to treat the wave resistance problem and provide predictions for the free surface elevation at moderate hydrofoil submergence depths. In the case of near or wave-breaking regimes, where non-linearities dominate, they need to be taken into count as in [219]. In Section 5.1.3, a discussion about the representation of the velocity potential and the solution of the BVP using Boundary Integral Equations provides additional details on the matter. Predicting the effects of free surface on a hydrofoil operating in the partial cavitation regime requires information about the shape of the free-streamline that coincides with the attached cavity boundary for given inflow conditions. The latter is an unknown boundary, which introduces non-linearity to the problem under consideration.

A new formulation is proposed in this work to address free surface effects on partial cavitation at moderate submergence depths and angles of attack. The free-streamline problem for a given cavity length is treated in the context of inverse problems. Regarding the problem statement, the following variation is considered: Determine the cavity shape and cavitation number, following a constant-pressure assumption on the cavity, for given cavity length and inflow conditions. The fixed-cavity-length simplification facilitates the verification of the proposed numerical scheme through comparisons against other methods that follow the same assumptions, i.e. [214]. However, the fixed cavity length assumption can be waived via an iterative scheme, as shown in [121], thus allowing the present method to consider more realistic applications in future work. The proposed method consists of implementing a gradient-based optimization scheme to produce cavity shape and cavitation number predictions at each optimization cycle, until the boundary conditions are satisfied. The sensitivities required by the gradient-based optimizer are derived analytically using the continuous adjoint method.

5.1.1 Cavity termination model

For the parametric representation of the hydrofoil/cavity using B-splines a clockwise convention is adopted,

$$\mathbf{r}(t) = \{(x, z) \in R^2 : x = x(t), z = z(t), t \in I = [0, 1]\}, \tag{5.8}$$

with $x^p_{te} = (x(t_o), z(t_o))$, $x^s_{te} = (x(t_1), z(t_1))$ denoting TE on the pressure and suction sides respectively. The hydro- foil/cavity outline can then be remodeled for any given set of nodal coordinates using interpolation [137]. The detachment point is placed at the leading edge in the case of hydrofoils with a sharp nose, however for a smoother leading edge, the cavity would detach at a point downstream of the at a point downstream the leading edge laminar boundary, see Celik et al. [122]. The detachment point position is user-defined and measured as l_D in SI units with respect to the $x-$axis of the hydrofoil body-fixed coordinate system, whereas for the case of leading-edge detachment point $l_D = 0$.

After the cavity geometry has been parameterized a termination model must be implemented alongside the parametric representation. Cavity termination modeling is an essential tool that brings numerical results closer to experimental data, since in reality, the cavity closure region consists of a two-phase turbulent zone where a very complex flow occurs. In the context of potential-based methods using a cavity, the termination model allows overcoming the difficulties in obtaining information about the pressure distribution around the hydrofoil and a more realistic cavity shape. There are various termination models, such as the end-plate Riabouchinsky (or wall termination model) implemented in Uhlman [214], the reentrant jet model, and a more sophisticated approach in Yoon & Semenov [220] based on viscid-inviscid formulations.

In the $(s_D - s_L)$ region, which is confined by the detachment s_D and termination s_T positions, following a curvilinear parameterization as shown in Figure 5.1, a constant pressure condition must hold. The transition region $(s_T - s_L)$ of length l_{TL}, defined by the termination s_T and the reattachment point s_L, belongs to the wetted portion of the boundary where the flow-tangency condition is to be satisfied. The proposed pressure recovery model is inspired from Celik et al. [122] and assumes that pressure on the transition zone $(s_T - s_L)$ of the attached cavity surface is defined upon solution of the boundary value problem; thus a criterion for constant pressure only holds for the $(s_D - s_T)$ region. The parametric representation of the attached cavity using B-splines allows for certain constraints to be enforced on the control points affecting the shape of $(s_T - s_L)$ region to ensure that the cavity either reattaches smoothly onto the wetted boundary of the hydrofoil or a stagnation point occurs at the reattachment point, see Section 5.2.1 for details.

Following [122], two user-defined parameters are required to deduce a dynamic boundary condition that holds along the attached cavity boundary. Moreover, its

shape changes at each iteration by shifting the panels to form the new shape of the discretized cavity boundary. The cavity termination model proposed in this paper alleviates the need for a dynamic boundary condition formula based on user-defined parameters. The proposed cavity model implements B-spline parameterization for the attached cavity shape, which allows for a more intuitive tuning of the changes in geometry in the reattachment region.

It is important to note that the B-spline parameterization of the boundary is compatible with cavity termination models based on geometric criteria, such as the wall termination model, which imposes a stagnation point at the reattachment point, or the more realistic re-entrant jet model. Comparisons with other potential-based models and experimental data have shown that the proposed cavity termination model yields results and pressure coefficient profiles that agree well with the literature, see Section 5.3 for additional details.

5.1.2 Inverse problem definition

For certain flow configurations, where the region near cavity termination is only moderately perturbed, and therefore and steady solution is attainable. The present work is based on the above assumption and particularly for the case of partially cavitating hydrofoils operating beneath the free surface. This model can be extended to treat the corresponding unsteady problem providing information concerning transient effects, however this is left for future work. The minimization function expresses the assumption of constant-pressure on the $(s_D - s_T)$ region, between detachment and termination points, of the cavity boundary,

$$F = \int_{\Gamma_c} g ds = \int_{\Gamma_c} \frac{1}{2}(p - p_v)^2 ds, \tag{5.9}$$

with p_u denoting the initially unknown saturated vapor pressure. An optimum has obtained when the predicted pressure on the cavity boundary is constant and equal to the saturated vapor pressure. The cavitation number is defined as,

$$\sigma = \frac{p_\infty - p_v(T)}{0.5\rho U_\infty^2}, \tag{5.10}$$

where U_∞, p_∞ and T_∞ are, respectively the ambient velocity, pressure and temperature in the flow field. In Eq. (5.9) the kernel can also be expressed in terms of the non-dimensional pressure coefficient as follows,

$$p - p_v = 0.5\rho U_\infty^2 (C_p - \sigma). \tag{5.11}$$

The design variables, denoted as b_n, $n = \{1, ..., N\}$ for the inverse problem presented in this section, refer to the target cavity pressure (or cavitation number) and

B-spline control points used for the attached cavity shape parameterization. To sum up, the design variable vector takes the form $\mathbf{b} = [\sigma, x_1, y_1, ..., x_m, y_m]$, where $m = (N-1)/2$, assuming that N denotes the total number of design variables. Notably, admissible solutions must comply with the requirements of 2D incompressible, inviscid, and irrotational fluid flow in the region. Our primal boundary value problem (BVP) serves as a constraint for the optimization problem,

$$\Delta\phi = 0, \quad (x, z) \in \Omega, \tag{5.12}$$

$$(\nabla\phi + \mathbf{U}_\infty) \cdot \hat{\boldsymbol{\tau}}|_{t_0} + (\nabla\phi + \mathbf{U}_\infty) \cdot \hat{\boldsymbol{\tau}}|_{t_1} = 0, \tag{5.13}$$

$$(\nabla\phi + \mathbf{U}_\infty) \cdot \hat{\boldsymbol{n}} = 0, \quad (x, z) \in \Gamma_c \cup \Gamma_w, \tag{5.14}$$

$$\frac{\partial^2\phi}{\partial x^2} + k_o \frac{\partial\phi}{\partial z} = 0, \quad (x, z = 0) \in \Gamma_{fs}. \tag{5.15}$$

The perturbation potential which is selected as the primal variable in our formulation is implicitly dependent on the design variables $\phi = \phi(x, z; b_n)$.

A typical approach to sensitivity derivative estimates concerning each design variable is via finite differences. For example, a central scheme would require $2N$ evaluations of the primal solver, with N denoting the total number of design variables. On the contrary, with the adjoint method we can produce estimates based on two evaluations of the fluid flow solver per optimization cycle. It is important to note that the adjoint method implemented here is part of a cavitation prediction tool used to investigate free surface effects on the performance of partially cavitating hydrofoils.

Examples of CFD-based adjoint optimization methods that serve as a direct link between numerical models for cavitation prediction and design improvement, in the sense of cavitation suppression, are notably the works of Boger & Paterson 2014 [221] and Vrionis et al. 2021 [222]. These works show that cavitation suppression and lift maximization can be achieved concurrently using single-fluid solvers based on conservation equations governing the homogeneous mixture with averaged properties. A similar extension that could be used for cavitation prediction and design optimization of hydrofoils beneath the free surface using the present numerical tool is left for future work.

The derivation of sensitivities, based on the continuous adjoint method, occurs at the level of partial differential equations. Alternatively, symbolic mathematics can be exploited to facilitate the derivation process; see, e.g., [223] on a similar problem. Following the methodology presented in Papadimitriou & Giannakoglou 2007 [224], at first we introduce the adjoint velocity potential; a continuous and twice differentiable Lagrange multiplier denoted as ψ. This is essential for the derivation of adjoint-state equations. Then, the augmented minimization cost function is introduced based on Eq. (5.9) and Eqs. (5.12)-(5.13) of the primal boundary value problem.

The augmented minimization function[1] reads as,

$$L = F + \int\int_{\Omega} \psi \nabla^2 \phi \, dV + \int_{\Gamma} \psi \delta(s - s_0) \Big[(\nabla\phi + \mathbf{U}_\infty) \cdot \hat{\boldsymbol{\tau}}|_{t_0} + (\nabla\phi + \mathbf{U}_\infty) \cdot \hat{\boldsymbol{\tau}}|_{t_1} \Big] \, ds \tag{5.16}$$

where $\delta(s - s_0)$ is the Dirac delta function. The first variation of the above Eq. (5.16) obtained analytically with respect to each design variable holds as,

$$\begin{aligned} \frac{\delta L}{\delta b_n} = SD &- \int\int_{\Omega} \frac{\delta \phi}{\delta b_n} \Delta \psi \, d\Omega - \int_{\Gamma_{fs}} \frac{\delta \phi}{\delta b_n} \Big[\frac{1}{k_o} \frac{\partial^2 \psi}{\partial x^2} + \frac{\partial \psi}{\partial z} \Big] dx \\ &+ \int_{\Gamma_w} \frac{\delta \phi}{\delta b_n} \Big[\nabla\phi \cdot \hat{\mathbf{n}} \Big] ds + \int_{\Gamma_c} \frac{\delta \phi}{\delta b_n} \Big[-\nabla\psi \cdot \hat{\mathbf{n}} + \rho \nabla_s \big(V_t (p - p_v) \big) \Big] \, ds \\ &- \Big[\rho V_t (p - p_v) \frac{\partial \phi}{\partial b_n} \Big]_{s_D}^{s_T} + \psi(s_0) \frac{\delta (\nabla\phi)|_{s_0}}{\delta b_n} + \psi(s_1) \frac{\delta (\nabla\phi)|_{s_1}}{\delta b_n}, \end{aligned} \tag{5.17}$$

with

$$\begin{aligned} SD = &- \int_{s_D}^{s_T} (p - p_v) \frac{\delta p_v}{\delta b_n} \, ds + g(s_T) \frac{\delta s_T}{\delta b_n} - g(s_D) \frac{\delta s_D}{\delta b_n} \\ &+ \int_{t_D}^{t_T} g \frac{\delta ||\dot{\mathbf{r}}||}{\delta b_n} \, dt - \int_{t_D}^{t_T} \rho V_t (p - p_v) (\nabla\phi + \mathbf{U}_\infty) \cdot \frac{\delta \hat{\boldsymbol{\tau}}}{\delta b_n} \, dt \\ &- \int_{\Gamma_c} \psi (\nabla\phi + \mathbf{U}_\infty) \cdot \frac{\delta \hat{\boldsymbol{n}}}{\delta b_n} \, ds, \end{aligned} \tag{5.18}$$

where $s_D = \int_{t_0}^{t_D} ||\dot{\mathbf{r}}|| \, ds$, $s_T = \int_{t_0}^{t_T} ||\dot{\mathbf{r}}|| \, ds$ with $\{t_0, t_D, t_T\} \in I = [0, 1]$ and the formula in Eq. (5.18) represents and approximation for the sensitivity derivatives SD. Additional details regarding the derivation are contained in Appendix D.

Following the adjoint method, sensitivities in the above formula are by definition independent of the term $\partial\phi/\partial b_n$, i.e. partial derivatives of potential with respect to the design variables.

Regarding Eq. (5.17), additional assumptions are made to ease numerical computations. Particularly, since admissible cavity shapes are such that both s_D and s_L points on the boundary are fixed, the corresponding variation of each $\delta\phi/\delta b_n$ on these points are set to zero. The only problem arises regarding the extent of pressure attenuation (or transition) region $(s_T - s_L)$. In our formulation the position of s_T should be such that $V_t = U_\infty \sqrt{\sigma + 1}$, equivalently $p = p_v$. For

[1] At first glance it may seem odd that the expression in Eq. (5.16) only considers Eqs. (5.12) and (5.13); considering that the primal boundary value problem serves as a constraint to the minimization process. However, the remaining Eqs. (5.14)-(5.15) are to be exploited during the first variation of the augmented cost function, since they are 'labeled' as boundary conditions.

that reason, it is assumed that terms associated with s_T can also be neglected. The extent of pressure transition region, i.e. $t \in (t_T, t_L)$, is thus defined by numerical experimentation, and the corresponding values, as it will be shown later on, are compatible with the findings in Kinnas & Fine [62].

The adjoint boundary value problem presented below is introduced so that sensitivity calculation becomes independent of $\delta\phi/\delta b_n$ and equivalently Eq. (5.17) reads as $\delta L/\delta b_n = SD$. Thus,

$$\Delta\psi = 0, \quad (x,z) \in \Omega, \tag{5.19}$$

$$\nabla\psi \cdot \hat{\boldsymbol{n}} = 0, \quad (x,z) \in \Gamma_w, \tag{5.20}$$

$$\nabla\psi \cdot \hat{\boldsymbol{n}} = \rho\nabla_s\big(V_t(p-p_v)\big) = 0, \quad (x,z) \in \Gamma_c, \tag{5.21}$$

$$\frac{\partial^2\psi}{\partial x^2} + k_o\frac{\partial\psi}{\partial z} = 0, \quad (x, z=0) \in \Gamma_{fs}. \tag{5.22}$$

Finally, it is important to note that the $\delta\phi/\delta b_n$ terms are computationally expensive to calculate explicitly via finite differences, as additional calls to the primal BEM solver are required. Via the adjoint method this is circumvented and the overall computational cost reduced significantly.

The adjoint boundary value problem is very similar to the primal, however, on the cavity boundary, a non-homogeneous Neumann condition has to be satisfied. The undefined constant $\psi(t_o)$ associated with the exterior Neumann boundary value problem Eqs. (5.19)-(5.22) is resolved, in the present work, by assuming $\psi(t_0) = 0$. The latter is used in conjunction with continuity assumption of the adjoint potential ψ, thus dropping the last two terms in the right hand-side of Eq.(5.17). It is worth mentioning here that the numerical solution of the primal and adjoint BVPs is obtained in the sense of BIE.

The present method can be directly extended to three-dimensions for the case of a finite wing steadily moving at moderate submergence depths near a free surface. The primal boundary value problem for the case of finite wings can be formulated based on the work of Bal et al. [121], whereas the attached sheet can be parameterized using a NURBS surface, see Hughes et al. [225] on this topic. Regarding the cavity termination model, for the 3D case the transition zone extent should be defined at each hydrofoil section along the wing span. Particularly, for the case of sheet cavitation without free surface effects, the present method as is could be implemented in selected positions along the span (in a strip-wise manner) to produce estimates for the cavitation number and attached cavity sheet shape.

5.1.3 Solution representation based on BIE

The potential ϕ and velocity field $V = \nabla\phi$ corresponding to the fluid flow problem, are solutions to the BVP presented in Eqs. (5.12)-(5.15). This solution must

also satisfy the equivalent weak form of the BVP in terms of Boundary Integral Equations (BIE). The adopted formulation is based on a perturbation velocity field representation using a superimposing of the governing equation solutions, i.e. source and vortex [59]. The perturbation potential $\forall r = (x, z) \in \Omega$ that results from changes in the flow field due to the existence of a submerged hydrofoil, is represented as follows,

$$\phi = \int_{\Gamma} G_1(\mathbf{r}, \mathbf{r}_o)\sigma(\mathbf{r}_o)\, ds(\mathbf{r}_o) + \gamma \int_{\Gamma} G_2(\mathbf{r}, \mathbf{r}_o)\, ds(\mathbf{r}_o), \tag{5.23}$$

$$G_1(\mathbf{r}, \mathbf{r}_o) = \frac{ln(\mathbf{r}, \mathbf{r}_o)}{2\pi}, \quad r \in \Omega - \{\mathbf{r}_o\}, \tag{5.24}$$

$$G_2(\mathbf{r}, \mathbf{r}_o) = \frac{1}{2\pi} tan^{-1}\Big(\frac{z - z_o}{x - x_o}\Big), \quad r \in \Omega - \{\mathbf{r}_o\}, \tag{5.25}$$

where $G_1(\mathbf{r}, \mathbf{r}_o)$, $G_2(\mathbf{r}, \mathbf{r}_o)$ denote the point source- and vortex-type singularities, solutions to the Laplace equation that also satisfy by definition the required condition at infinity in Eq. (5.5). The total velocity potential in that sense becomes,

$$\Phi = \phi_\infty + \phi, \tag{5.26}$$

where ϕ_∞ denotes the velocity potential of the uniform inflow background field. By differentiating Eq. (5.26) under the integral sign and using a limiting process the new form of the integral equation is valid for each point on the boundary $\mathbf{r} = (x, z) \in \Gamma$ the following representation for the total velocity field is derived,

$$\begin{aligned} \mathbf{V} = \mathbf{U}_\infty - \frac{\sigma(\mathbf{r})}{2} \cdot \hat{\mathbf{n}}(\mathbf{r}) + \int_{\Gamma} \nabla_r G_1(\mathbf{r}, \mathbf{r}_o)\sigma(\mathbf{r}_o)\, ds(\mathbf{r}_o) \\ - \frac{\gamma(\mathbf{r})}{2} \cdot \hat{\boldsymbol{\tau}}(\mathbf{r}) + \int_{\Gamma_c \cup \Gamma_w} \nabla_r G_2(\mathbf{r}, \mathbf{r}_o)\, ds(\mathbf{r}_o), \end{aligned} \tag{5.27}$$

with unknowns the source strength distribution $\sigma(\mathbf{r}_o)$ and vorticity γ, see also [59].

We shall distinguish by indices + and – the limits obtained by approaching the boundary $\partial\Omega$ from inside $R^2 \backslash \bar{\Omega}$ (exterior) and Ω (interior), respectively. Particularly Eq. (5.27) used express the boundary conditions of the BVP, thus forming a system of equations with the strength of vortices and source singularities as the unknowns. A distribution of vortices, that is associated with the circulation and lift around the foil, is used only on the foil and cavity surface. In the discrete version it is assumed constant along the foil, i.e. $\gamma(s) = \gamma$. The above Boundary Integral Equation (BIE) formulation leads to a significant size reduction of the numerical procedure, since the unknown velocity field solely dependents on the boundary singularities $\sigma(s)$ and γ.

5.2 Numerical model

5.2.1 Mesh generation

Free surface

The discretized, linearized free surface is defined by the forward (upstream) and aft (downstream) truncation points; denoted as x_F and x_A, respectively. Typical values include $x_F = 3\lambda$ and $x_A = -5\lambda$, assuming a wave length λ. To ensure that unrealistic upstream waves are suppressed, the upstream-region is discretized using an exponential distribution of panel elements with user-defined sparsity, so that the final mesh is coarser in the upstream region.

$$x_{fs} = -w_d\, c - (x_A - w_d\, c)\, x_k^{n_p}, \quad x_k \in [0,1],\, k = \{0, ..N_{ss}\}, \tag{5.28}$$

with c denoting the hydrofoil chord length and assuming $w_d = -2$, $n_p = 2$ and $N_{ss} = 25$ as typical values for the above parameters. Particularly, w_d defines the upstream region length, n_p denotes a power coefficient related to the mesh sparsity and N_{ss} is the number of panel elements in the upstream region. Downstream iso-spacing is used; see also Figure 5.2 containing a free surface mesh example.

Hydrofoil with attached cavity

The hydrofoil section is defined using two concatenated cubic Bezier curves as (x_{foil}, y_{foil}) based on the parametric representation found in [226]. To generate an initial guess for the attached cavity a parabolic function with one free parameter $\beta \in R+$ that controls the cavity volume is used,

$$z = z_{foil} - \beta x_{foil}(x_{foil} - x_{foil}(t_L)). \tag{5.29}$$

The hydrofoil/cavity outline described in (5.8) consists of the original geometry of the hydrofoil superimposed with the attached cavity generated using (5.8) above. The attached cavity is then represented using B-spline interpolation of the fourth order. B-splines are popular for their characteristic locality property [225], while the control points of a Bezier curve affect the entire shape of the curve. B-spline control points are include into the set of design variables b_n, $n = \{1, ..., N\}$ along with the unknown cavitation number, denoted as σ.

The initial guess significantly affects the convergence rate of the optimization method; see, also the discussion in Section 5.3. Additional results can be found in Anevlavi & Belibassakis 2022 [158]. Starting from a parabolic shape does not guarantee smooth transition near the cavity closure, and therefore the slope of B-spline at the vicinity of cavity termination region should be adjusted, as shown in Figure 5.3 for compliance with the selected cavity termination criteria. The

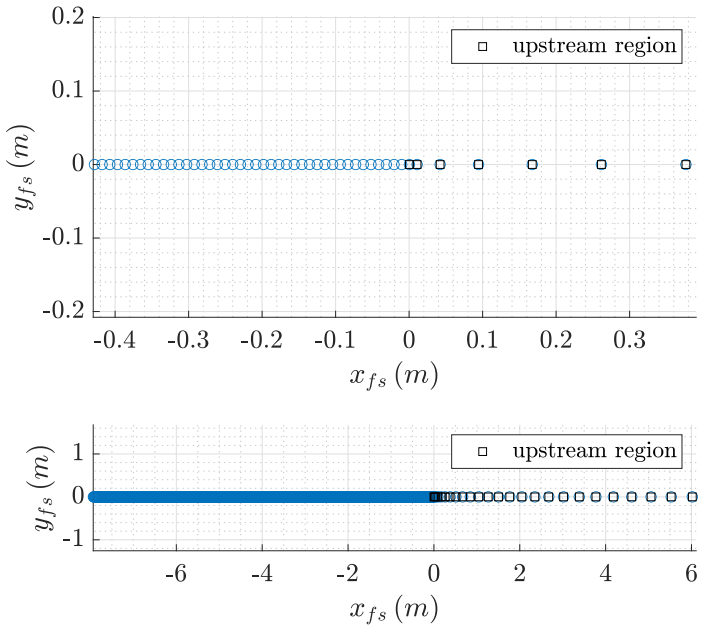

Figure 5.2: Discretized free surface comprising of an upstream region ($w_d = -2$, $n_p = 2$ and $N_{ss} = 25$) with exponential spacing and a downstream region with isospacing. The example domain [below] and a close up of the transition between upstream/downstream regions [above].

same holds for the attached cavity near the leading edge (LE), to ensure that intersection between the cavity and reference hydrofoil geometry occur only at the detachment point; for each optimization cycle.

In some cases, it is experimentally observed that the cavity detaches from a position different from the leading edge. According to nonlinear cavity theory the cavity slope equals the foil geometry slope at detachment point. The proposed cavity representation can be used to model an attached cavity that detaches smoothly from a selected position downstream the leading edge. Particularly, in Section 5.3.2 where the present method is compared against experimental data the detachment point is positioned at $l_D = 2 - 4mm$ downstream the leading edge to comply with the observations mentioned in [120]. Control points near detachment are positioned accordingly, in order to ensure that the cavity detaches smoothly from the hydrofoil; thus satisfying the slope requirement.

As previously discussed, the pressure transition region extent l_{TL} is an input parameter for the proposed cavity termination model, similar to the approach followed in Bal et al. [121]. Since the aforementioned optimization problem is

subjected to no constraints, it is essential to verify during the optimization process that the attached cavity remains compatible with the physical assumption of the free-streamline problem, i.e., the attached cavity boundary does not intersect with the original hydrofoil geometry. The only intersections allowed are the detachment and reattachment points of the cavity. Particularly, the first and last two control points, see Figure 5.3, are not included in the design variable vector. The cavity shape in re-attachment region depends solely on the cavity geometric model constraints. It is important to note here, that the B-spline representation is capable of reproducing other cavity termination models as well, such as the classic wall termination model or the more sophisticated re-entrant jet, see e.g., [119] for more details about these termination models. This can be achieved by introducing more control points in the re-attachment region of the cavity and imposing certain constraints on them to re-create the desired shape of the cavity over the re-attachment region, see Figure 5.4.

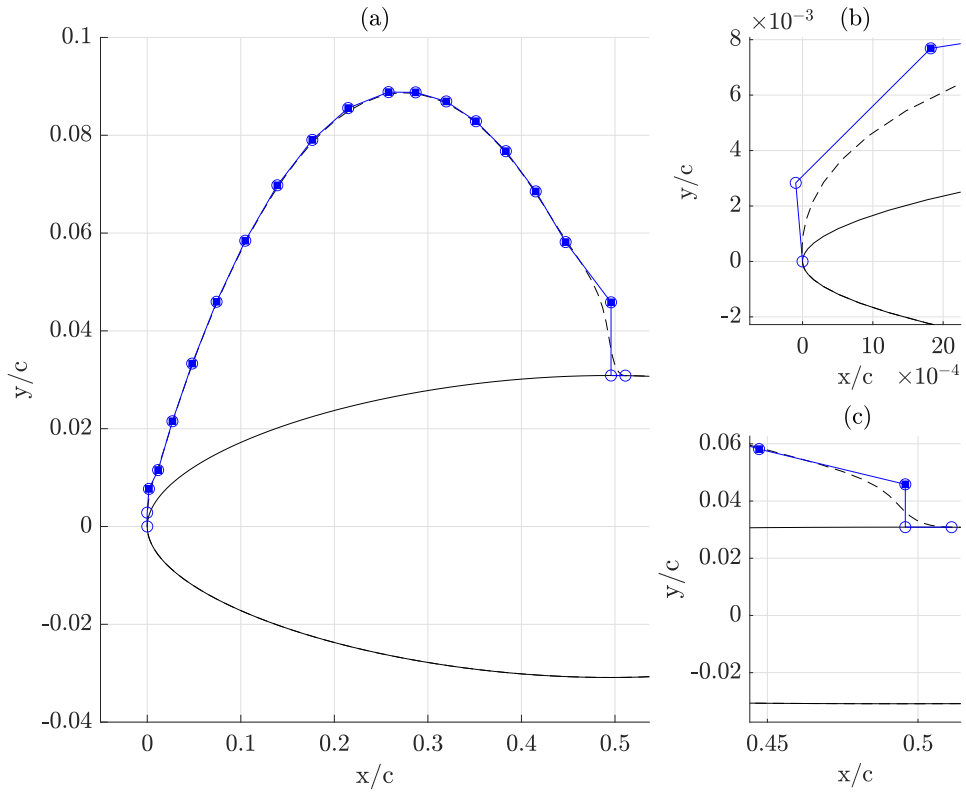

Figure 5.3: (a) Attached cavity parametrization using B–splines, with details about (b) the cavity detachment position at the LE and (c) the cavity closure region.

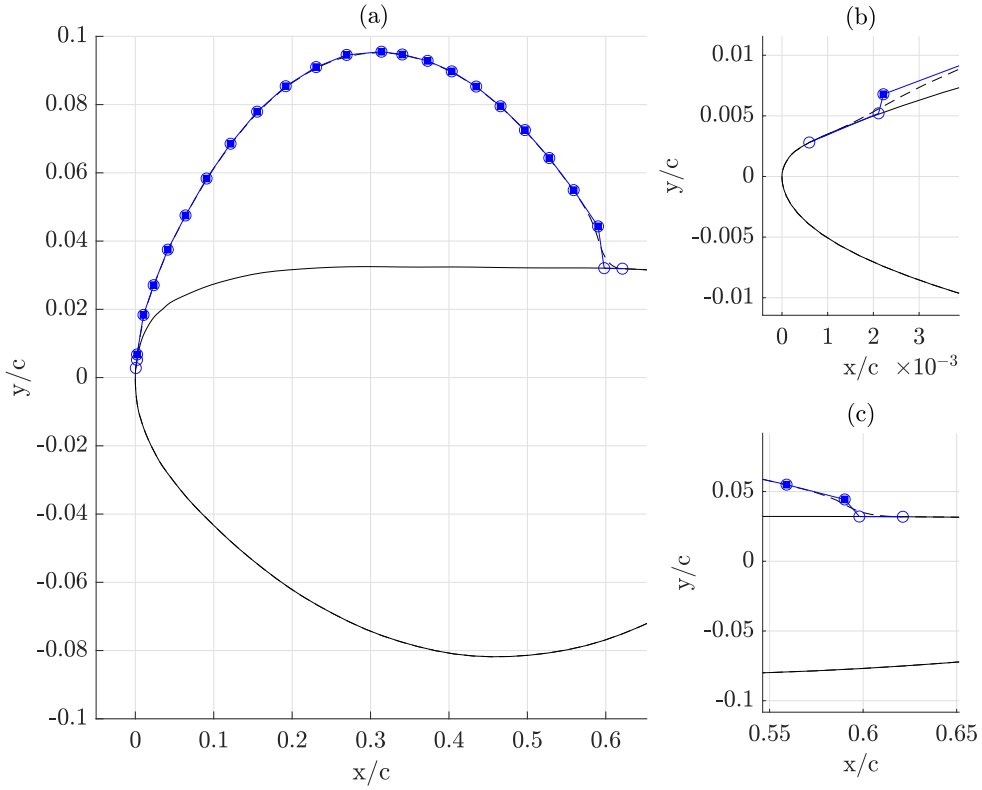

Figure 5.4: (a) Attached cavity parametrization using B–splines for the cambered Foil A from [120], with details about (b) the cavity detachment position 0.5mm from the LE and (c) the cavity closure region.

5.2.2 Minimization algorithm

Amongst optimization methods, gradient-based ones can be more efficient when the optimum is nearby. Particularly, adjoint methods, following either continuous [148] or discrete formulations [227], are of great interest due to their ability of efficiently handling large numbers of design variables. Notable is the introduction of continuous adjoint methods for design problems in fluid dynamics, typically attributed to [147] who studied drag minimization for two-dimensional shapes in Stokes and Low-Reynolds number flows. In the present work, the simple steepest-descend method is implemented to treat numerically the deterministic optimization problem based on the continuous adjoint method as a means for sensitivity derivative approximation.

Our analysis leads to the algorithm described below, namely the *PCavPreMod*. Rate of convergence is strongly dependent on the selection of steepest-descend

parameter vector $\mathbf{B}$, as well as the initial guess for the design variable vector. It is important to note that since the steepest-descend parameters, denoted as $B_n\, n = \{1, ...N\}$, are dimensional, the convergence thresholds must be properly tuned beforehand. A local optimum is reached as the design cycles progress, assuming that the parameter vector selected for the steepest-descend scheme are sufficiently small. The optimization process continues until the solution has converged, i.e., the values of sensitivities and cost function are below a certain threshold, or the number of maximum evaluations M max has been reached. The convergence metric, denoted as $|F/F_o|$, introduced in this work is defined as the absolute value of the ratio between current and initial values of the minimization function in Eq. (5.9). One way to explore further the design space within the capabilities of a gradient-based method is to search for the optimal solution starting from different initial cavity shapes.

Algorithm 1 *PCavPreMod*

Initialize $b_n^0 = \{1, ..., N\}$, set $\mathbf{B} > 0$, set M_{max}
while ($M_{OPTIM} < M_{max}$ or Convergence) **do**
  Solve primal problem for ϕ
  Solve adjoint problem for ψ
  Calculate sensitivity derivatives $SD = \delta L/\delta b_n$
  Update $b_n^{k+1} = b_n^k - B_n \cdot SD$
  Update $k = k + 1$
  Update $M_{OPTIM} = M_{OPTIM} + 1$
end while
return b_n^{k+1}

5.2.3 Solution of the primal problem

For the solution of the primal BVP in Eqs. (5.12)-(5.15) a low-order panel (BEM) solver based on piece-wise constant source and vortex distributions is implemented. The boundary is approximated with $(M_1 + M_2)$ straight-line segments, namely the panel elements,

$$\sigma(s) = \sigma_j, \quad j = \{1, ..., M_1 + M_2\}, \tag{5.30}$$

$$\gamma(s) = \gamma, \quad j = \{M_1 + 1, ..., M_1 + M_2\}, \tag{5.31}$$

with M_1 source panel elements on the linearized free surface and M_2 source, vortex panel elements distributed on the hydrofoil boundary. Particularly, cosine spacing near the leading/trailing edge of the hydrofoil is implemented and the same holds for the cavity termination region. The total velocity induced at the midpoint of

$i-th$ panel from the source- and vortex distributions is given by,

$$\mathbf{V}_i = \mathbf{U}_\infty + \sum_{j=1}^{M_1+M_2} \sigma_j \mathbf{u}_{\sigma,ij} + \gamma \sum_{j=M_1+1}^{M_1+M_2} \mathbf{u}_{\gamma,ij}, \tag{5.32}$$

$$\mathbf{u}_{\sigma,ij} = \int_{panel\, j} \frac{(x_{s,i}, z_{s,i})}{2\pi r_{r,i}^2} ds, \quad \mathbf{u}_{\gamma,ij} = \int_{panel\, j} \frac{(-z_{s,i}, x_{s,i})}{2\pi r_{r,i}^2} ds, \tag{5.33}$$

where $\mathbf{r}_{s,i} = (x_{s,i}, z_{s,i})$ is the relative position of the control point $(\bar{x}_i, \bar{z}_i)$ to the point of integration. Particularly, $x_{s,i} = \bar{x}_i - x_s$ and $z_{s,i} = \bar{z}_i - z_s$. The discretized form of the boundary conditions is as follows,

$$\partial_x(\mathbf{V}_j \cdot \hat{\boldsymbol{\tau}}_j) + k_o \mathbf{V}_j \cdot \hat{\mathbf{n}}_j = 0, \quad j = \{1, ..., M_1\}, \tag{5.34}$$

$$\mathbf{V}_j \cdot \hat{\boldsymbol{n}}_j = 0 \quad j = \{M_1 + 1, ...M_1 + M_2\}, \tag{5.35}$$

$$\mathbf{V}_{M_1+1} \cdot \hat{\boldsymbol{\tau}}_{M_1+1} + \mathbf{V}_{M_1+M_2} \cdot \hat{\boldsymbol{\tau}}_{M_1+M_2} = 0. \tag{5.36}$$

The x-derivative operator that appears above is numerically calculated using an upstream fourth order finite difference scheme, or the Dawson's operator [228]. Particularly,

$$\frac{\partial u}{\partial x}|_k \simeq A_k u_k + B_k u_{k-1} + C_k u_{k-2} + D_k u_{k-3}, \tag{5.37}$$

with

$$A_k = -(B_k + C_k + D_k),$$

$$B_k = \frac{1}{E_k}(x_{k-2} - x_k)^2(x_{k-3} - x_k)^2(x_{k-3} - x_{k-2})(x_{k-3} + x_{k-2} - 2x_k),$$

$$C_k = -\frac{1}{E_k}(x_{k-1} - x_k)^2(x_{k-3} - x_k)^2(x_{k-3} - x_{k-1})(x_{k-3} + x_{k-1} - 2x_k),$$

$$D_k = \frac{1}{E_k}(x_{k-1} - x_k)^2(x_{k-2} - x_k)^2(x_{k-2} - x_{k-1})(x_{k-2} + x_{k-1} - 2x_k),$$

$$E_k = (x_{k-1} - x_k)(x_{k-2} - x_k)(x_{k-3} - x_k)(x_{k-3} - x_{k-1}) \cdot (x_{k-2} - x_{k-1})(x_{k-3} - x_{k-2})(x_{k-3} - x_{k-2} - x_{k-1} - 3x_k),$$

where x_k, $k = \{1, 2, ..., M_1\}$ denotes the control points on the free surface. Based on the above, we derive the discrete form of the $x-$derivative of the horizontal velocity on the free surface boundary as follows,

$$\partial u_{k,j} = A_k u_{k,j} + B_k u_{k-1,j} + C_k u_{k-2,j} + D_k u_{k-3,j}, \tag{5.38}$$

that represents the contribution of $j-ith$ element in terms of $\partial_x()$ velocity on the $k-th$ control point on the free surface boundary.

Based Eqs. (5.34)-(5.36), we form a linear system of $(M_1 + M_2 + 1)$ equations with $(M_1 + M_2 + 1)$ unknowns with respect to the strengths of source and vortex distributions. The pressure coefficient at the midpoint of each panel can be calculated using

$$C_p(\bar{x}_j, \bar{z}_j) = 1 - V_t^2/U_\infty^2. \tag{5.39}$$

After the solution has been obtained the lift and moment coefficients C_L, C_M be calculated via numerical integration, see also [59]. The wave making resistance C_W of the hydrofoil can also be estimated by numerically integrating pressure on the hydrofoil and projecting in the direction of inflow velocity.

5.2.4 Solution of the adjoint problem

The adjoint field equation accompanied with a Neumann-type boundary condition can also be treated in the sense of BIE. However, the numerical solution of this problem is much simpler than the primal problem. The same discretization scheme is used to approximate the boundary of the hydrofoil/cavity. Since this problem does not have circulation, vortex elements are not used in the representation. The total adjoint velocity $\mathbf{V}_{a,i}$ at the midpoint of $i-th$ panel is given by,

$$\mathbf{V}_{a,i} = \mathbf{U}_\infty + \sum_{j=1}^{M_1+M_2} q_{a,j}\mathbf{u}_{\sigma,ij}, \tag{5.40}$$

with induced velocities $\mathbf{u}_{\sigma,ij}$ defined in (5.33). The corresponding boundary conditions in discretized form are,

$$\partial_x(\mathbf{V}_{a,j} \cdot \hat{\boldsymbol{\tau}}_j) + k_o \mathbf{V}_{a,j} \cdot \hat{\mathbf{n}}_j = 0, \quad j = \{1, ..., M_1\}, \tag{5.41}$$

$$\mathbf{V}_{a,j} \cdot \hat{\boldsymbol{n}}_j = \rho\partial_s\big(V_{t,j}(p - p_v)\big), \quad j = \{M_1 + 1, ...M_1 + M_2\} \cap \Gamma_c, \tag{5.42}$$

$$\mathbf{V}_{a,j} \cdot \hat{\boldsymbol{n}}_j = 0, \quad j = \{M_1 + 1, ...M_1 + M_2\} \cap \Gamma_w. \tag{5.43}$$

The above Eqs. (5.41)-(5.43) form a system of $(M_1 + M_2)$ equations with the same number of unknowns, with respect to the strengths $q_{a,j}$ of the piece-wise constant source distributions.

5.2.5 Calculation of sensitivity derivatives

The formula in Eq. (5.18) can be used to produce estimates of the sensitivities $\delta L/\delta b_n$ after the solutions of both the primal and adjoint problems are obtained. The integrals are evaluated by means of standard numerical integration, and the derivatives of geometric quantities with respect to the design variables are approximated via central finite differences. These quantities include the normal and tangential vectors $\hat{\mathbf{n}}$, $\hat{\boldsymbol{\tau}}$ vectors, and the Jacobian of the curve representation $||\dot{\mathbf{r}}||$.

In order to verify the validity of Eq. (5.18), the sensitivities are compared against results obtained via a direct implementation of a central difference scheme on the cost function $\delta F/\delta b_n$ in Eq. (5.8) for various study cases, with one example provided in Section 5.3 that follows. It is important to note that an estimate for the sensitivities obtained with central differences, requires $2N$ evaluations of the BEM solver, with N denoting the total number of design variables. On the other hand, the approximation based on the continuous adjoint method requires only two solver evaluations, i.e., namely one solution for the primal and one for adjoint problem. Thus, reducing significantly the computational cost, since this approach remains independent of the total number of design variables(i.e degrees of freedom).

5.3 Results and discussion

5.3.1 Primal solver verification for non-cavitating hydrofoils

Wave elevation due to a submerged point-vortex

A common abstraction in the sense of mathematical modeling, involving analytic solutions based on complex theory, is to represent a hydrofoil section with a point vortex-type singularity of the same circulation strength, denoted as Γ. Following this approach with an aim to verify the potential-based solver, wave elevation profile results that were obtained from a modified version of the primal BEM solver are compared against the complex-variable method asymptotic solution in [229] for the case of a point vortex of constant strength submerged within a fluid in uniform velocity profile. Additional details about the asymptotic solution derived with the complex-variable method for this problem can be found in Appendix E.

The comparison in Figure 5.5 refers to the case of a point vortex with unit strength. The singularity is assumed to be submerged into a uniform inflow $U_\infty = 1.77m/s$ at submergence $d = 0.15\lambda$, where λ denotes the corresponding wave length. A number of $N_{fs} = 1290$ non-uniformly spaced panels is used on the free surface, whereas mesh spacing is increased in the upstream part to improve the quality of numerical results. The predicted wave profile agrees well with the asymptotic solution downstream the singularity. Our model slightly over predicts wave elevation peaks downstream. This behavior can be attributed to effects of domain truncation; which are treated by Dawson's discrete scheme up to a degree. The non-trivial deviation between the predicted wave elevation profile and [229], occurring at the location of singularity in the $x - axis$, is attributed to the asymptotic nature of the analytic solution expression; see also Appendix E.

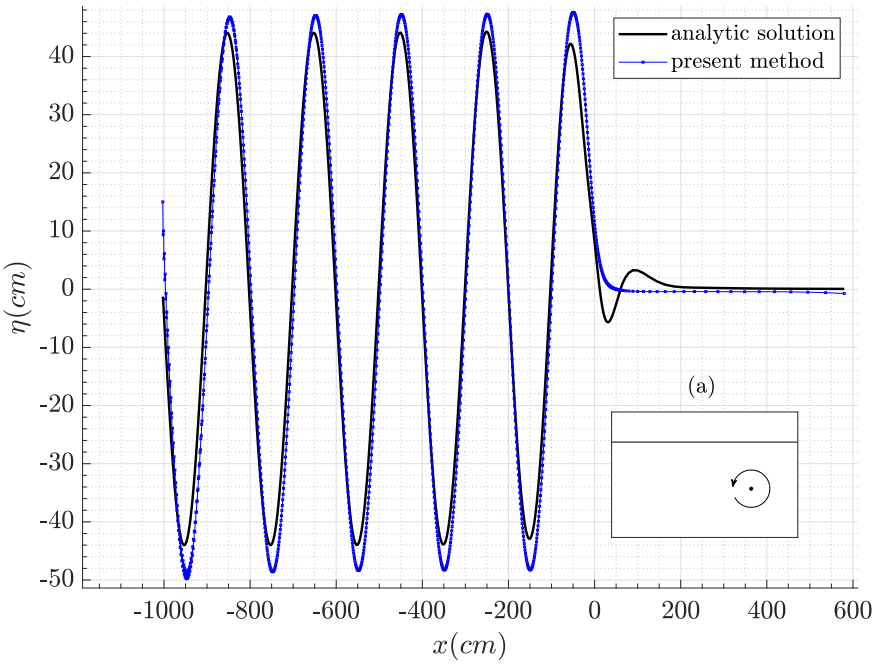

Figure 5.5: Wave elevation comparison between the asymptotic solution from Kuznetsov et al. [229] and the present BEM for a point vortex singularity; submerged in uniform inflow. Sub-figure (a) shows the vortex direction for visualization purposes.

Pressure coefficient and wave elevation for a NACA 4412

Additional comparisons between the present method and the work of Yeung & Bouger [230] are performed. The first study case refers to a NACA 4412 hydrofoil at $a = 5deg$ moving steadily beneath the free surface at $Fr(c) = U_\infty/\sqrt{(gc)} = 1$ including bottom effects, with $Fr(c) = U_\infty/\sqrt{(gh)} = 0.447$, with h denoting the vertical distance of the flat-bottom boundary. Non-dimensional submergence depth is taken as $d/c = 1$, whereas $h/c = 5$. The method of images, see, e.g. [59], is employed to include flat bottom effects in the modeling.

The comparisons in Figure 5.6 suggest that the primal solver is capable of accurately predicting, within the limits of potential flow, the pressure profile when free surface effects are present. Particularly, the C_p profiles at $\alpha = 5deg$ compare well with the numerical results in Giesing & Smith [231]. For this scenario the predicted lift and wave resistance coefficients $C_L = 0.74$, $C_R = 0.065$ also compare well with the values reported in [230]. Regarding comparisons against available experimental data, it is observed that the measured data lie below the calculated

values for $\alpha = 5deg$. However, as reported in [231] this phenomenon can be attributed to boundary layer displacement effects; that lower the circulation. A comparison against equal lift coefficients, for instance $C_L = 0.48$, reveals that the present method is indeed in excellent agreement with the numerical tool presented in [231]; assuming that the angle of attack for the potential model is adjusted to $\alpha = 3.5deg$.

Concerning results for wave elevation, in Figure 5.7 primal solver predictions are compared against those in [230] for the case of a NACA 4412 at the same angle of attack, submergence depth ratio $d/c = 1$ and at various Froude numbers $Fr(c) = \{0.35, 0.45, 0.6, 1.8\}$. For the computations $N_b = 240$ panels are used for the foil boundary and $N_{fs} = 1000$ on the free surface, assuming non-uniform spacing. It was found that for $Fr(h) = 1.0$, uniform spacing with $Nfs = 3600$ panels on the free surface produced the best results, and these are shown in Figure 5.7 (d).

5.3.2 Verification of the adjoint prediction method for cavitating hydrofoils

The proposed model has been compared against other works, both numerical and experimental, for cases of partially cavitating hydrofoils at deep submergence with results presented in Anevlavi & Belibassakis 2021 [212]. The benchmarks, targeting cavitation number and cavity volume predictions, suggest that *PCavPreMod* performs satisfactorily for cases of deep submergence.

In this Section we emphasize on indicative results supporting the validity of Eq. (5.18), which yields approximations for the sensitivity derivatives. These results refer to the case of a NACA 16006 hydrofoil at $a = 5deg$ with cavity length $l_c = 0.5c$ at deep submergence. Results for the same hydrofoil at finite submerge of $d/c = 0.6$ and various Froude numbers are included and compared against the PCPAN solver from the work of Bal et al. [121], which is also based on potential theory.

In order to illustrate the capabilities of our method with respect to cavitation number and cavity shape prediction, I analyzed cases of varying effective angle and submergence. The initial guesses for the cavity boundary in all simulations are based on Eq. (5.29) and the detachment point s_D is placed at the LE. In addition, the $(s_T - s_L)$ transition region was tuned to $l_{TL} = 0.10l_c$, which lies within the reported values found in Kinnas & Fine [62].

Cavitating hydrofoils at deep submergence

The extended method presented here can also treat the problem of partially cavitating hydrofoils without free surface effects, assuming that submergence depth

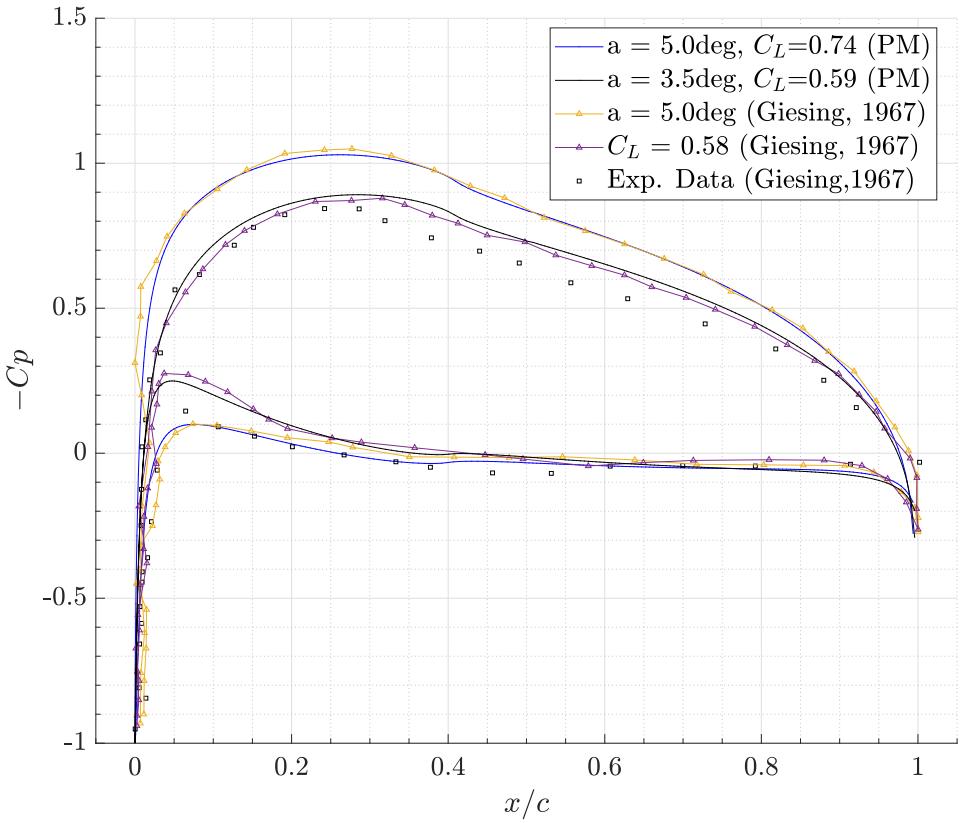

Figure 5.6: Comparison of calculated and experimental pressure distributions from Giesing & Smith [231] on a NACA 4412 hydrofoil at equal angles of attack and at equal lift coefficients at $Fr(c) = 1$, $Fr(h) = 0.447$, $d/c = 1$ including bottom effects $h/c = 5$.

is large enough. To demonstrate this, detailed results concerning a NACA 16006 hydrofoil at $a = 5deg$ angle of attack, cavity length $l_c = 0.5c$ and submergence depth $d/c = 10$ without bottom effects are presented in this section. Particularly, the $(s_T - s_L)$ transition region was tuned to $l_{TL} = 0.10l_c$. Upon solution of the inverse problem, the cavitation number and cavity shape are determined. Figure 5.8 contains the comparison between sensitivities based on SD formula in Eq. (5.18) and estimated values obtained via direct numerical differentiation of the objective function using central differences. The design variables consist of the cavitation number and the B-spline control point coordinates of the attached cavity, yielding a total of $N = 38$ design variables (or degrees-of-freedom). The optimization algorithm, as presented in Section 5.2.2 requires information about

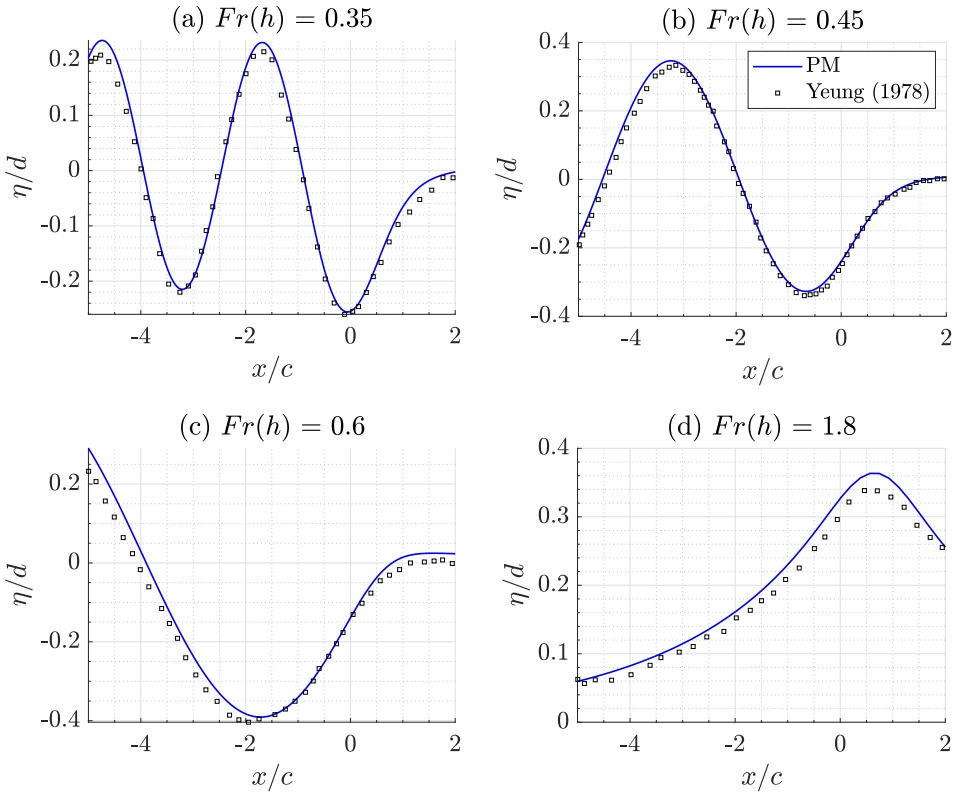

Figure 5.7: Wave elevation profiles for the case of a submerged NACA 4412 at $\alpha = 5deg$, $d/c = 1$, including bottom effects $h/c = 4$ at various Froude numbers. Comparison between the present method and Yeung & Bouger [230].

the steepest-descend parameter vector (i.e. of the same size as the design-variables. It is important to note, that it is possible to restrict the x_i-coordinates of the B-spline control points affecting the cavity shape by simply setting the corresponding steepest-descend parameters equal to zero. Figure 5.8 shows that the results are in good agreement, considering that our method for SD yields an approximation of the sensitivities; see Appendix D for more details on the terms that are omitted from the final SD expression.

Additionally, in Figure 5.9(a) contains the comparison between Bal et al. [121] and our prediction for the pressure profile. Regarding the foil boundary discretization, a number of $N_b = 290$ panels was used, with cosine spacing to achieve a denser mesh near the trailing/leading edge and detachment/re-attachment regions of the cavity. A non-uniform mesh of $N_{fs} = 700$ panels was used on the free surface. Our method yielded a cavitation number $\sigma = 1.11$ after $M_{OPTIM} = 500$ cycles. This

agrees with the findings in Bal et al. [121]. Also, the predicted sectional area of the cavity is $Vol/c^2 = 0.0206$ and the maximum cavity height $h_{MAX} = 0.082m$.

The wave-like behavior of the pressure profile observed near cavity detachment and reattachment points is attributed to the way our objective function in Eq. (5.9) is defined. To suppress the wave-like behavior of the optimal solution, we could reformulate the cost function so that it requires the first derivative of the pressure profile on the attached cavity to be a constant. However, since these fluctuations do not significantly affect the accuracy of our predictions, in terms cavitation number or cavity sectional area, it is assumed that the cost function expression in Eq. (5.9) suffices.

The cavity shape is shown in Figure 5.9(b). A close-up in the final geometry of the attached cavity shape is provided in Figure 5.10, where *active* B-spline control points are marked with squares. The dashed line corresponds to the initial guess for the attached cavity shape. Finally, the convergence history as a function of optimization cycle number is provided in Figure 5.11. It is shown that for values of the ratio F/F_o that lie below two orders of magnitude, we assume that convergence has been achieved. An extensive discussion regarding this matter, particularly for cases of partially cavitating hydrofoils in unbounded flow can be found in Anevlavi & Belibassakis [212].

Validation with experimental data

To investigate whether the present numerical scheme is capable of predicting cavitation number as a function of cavity length, I compared our results against experimental measurement data from a small hydrodynamic tunnel at the Bassin d'Essais des Carène in France, which were published by Pellone & Maitre [120]. The outline of Foil-A, as stated in the publication, is given in the form of tabulated data, which were then interpolated using B-splines for our numerical simulations. This hydrofoil section has a maximum thickness of 11%, presents a negative camber, and is the solution of an inverse two-dimensional potential calculation to provide a target pressure profile. The work by Pellone & Maitre [120] also contains a numerical model for the analysis of partially cavitating hydrofoils using a viscid-inviscid method. Their numerical results are also included in the comparisons presented in Figures 5.12 and 5.13 that follow.

All simulations are performed using $N_b = 260$ panels on the foil and by assuming that submergence depth is large enough $d/c = 15$, thus interactions between the free surface boundary and the hydrofoil are considered negligible. The study case refers to $\alpha = 4deg$ angle of attack and uniform inflow velocity $U_\infty = 1.6m/s$. The experimental findings suggest that the detachment point occurs at $l_D = 0.5 - 4mm$ downstream the leading edge.

Additional details regarding the numerical parameters, and the predicted cav-

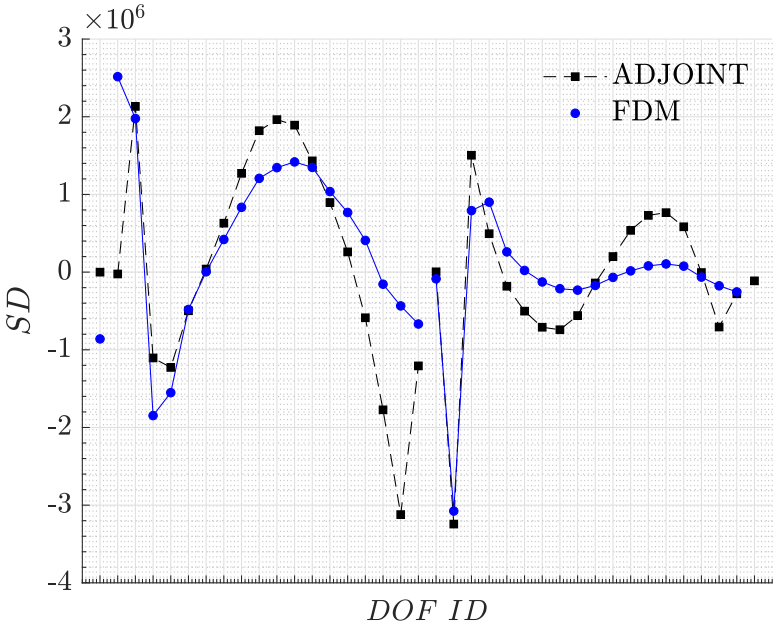

Figure 5.8: Sensitivity derivatives for each design variable after the first iteration. Comparison between the present method and direct calculation via finite differences.

itation number σ and lift coeffcient C_L as functions of cavity length l_c/c, are provided in Table 5.1 that follows. The cavity detachment position and transition region $(s_T - s_L)$ extent are user-defined parameters along with the number of design variables. Figure 5.12 contains the comparison between our method and the experimental data. Convergence was achieved after 100–250 optimization cycles; depending on the selection of an appropriate steepest-descend parameter vector. The convergence metric used here, suggests that if $F/F_o < 0.006$ the solution has converged.

The results indicate that the present method is capable of capturing the same trend in terms of cavitation number prediction as a function of the cavity length as the other numerical method. It is typical for potential based methods to overestimate the cavity length for a given cavitation number, as illustrated in Celik et al. [122] though comparisons of potential based results and CFD simulations. In terms of the lift coefficient, experimental data were not available, however the present method agrees well with the viscid-inviscid model from Pellone & Maitre [120] as shown in Figure 5.13, although the present method underestimates the predicted values for the lift.

For attached cavity lengths up to $l_c/c = 0.3$ our prediction curve has a slope

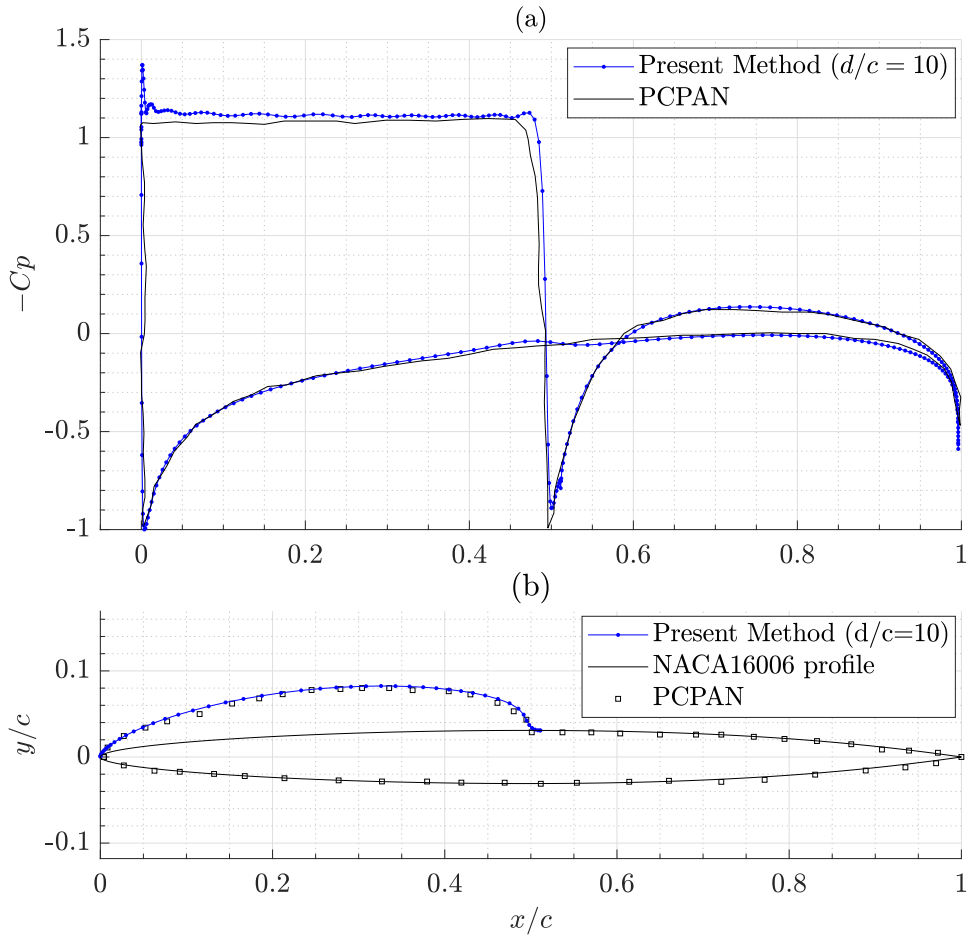

Figure 5.9: Comparison between (a) the pressure coefficient and (b) the cavity profile, as obtained with present method and numerical results found in [121] for a NACA 16006 at $a = 5deg$, $d/c = 10$.

that agrees well with the data from Pellone & Maitre [120]. However for higher values of cavity length the deviation of our predictions from the numerical data from Pellone & Maitre [120] reduces. Overall the comparison is good, taking into consideration that a full agreement between the present purely potential-based method and either the numerical model (that includes boundary-layer thickness into the formulation) or the experimental data from Pellone & Maitre [120] would not be possible.

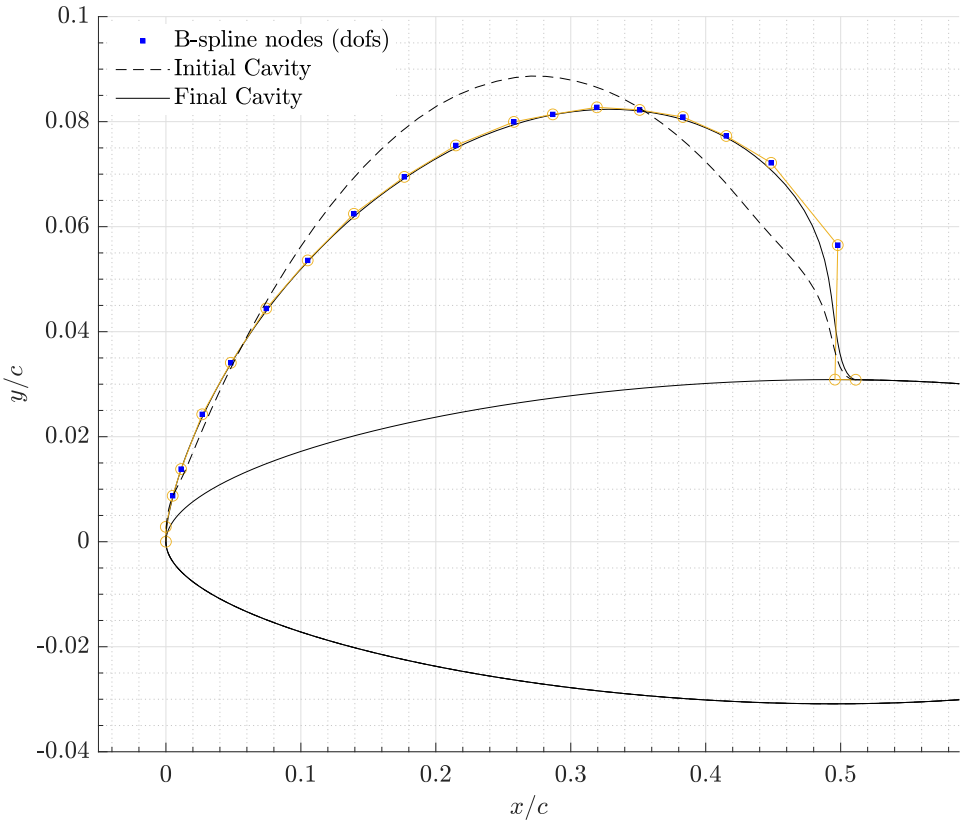

Figure 5.10: Cavity profile of a NACA 16006 hydrofoil at $5deg$ in deep submergence $d/c = 10$. The B-spline control points included in the design variable vector are illustrated in squares. The dashed line corresponds to the initial guess for the attached cavity shape.

Cavitating hydrofoils with free surface effects

Verification of the present method for cases including fre surface effects on partially cavitating hydrofoils is performed via comparisons against the work by Bal et al. [121], where finite submergence depths are considered. However, in our method the two problems 1-hydrofoil beneath the free surface, 2-partially cavitating foil at deep submergence) are treated via a monolithic approach. In order to avoid numerical instabilities, especially as the submergence decreases, a filter-function is used to eliminate strong interactions between the free surface and the foil; affecting mainly the enforcement of flow-tangency condition on the hydrofoil boundary.

The first case study refers to a NACA 16006 hydrofoil at angle of attack $\alpha =$

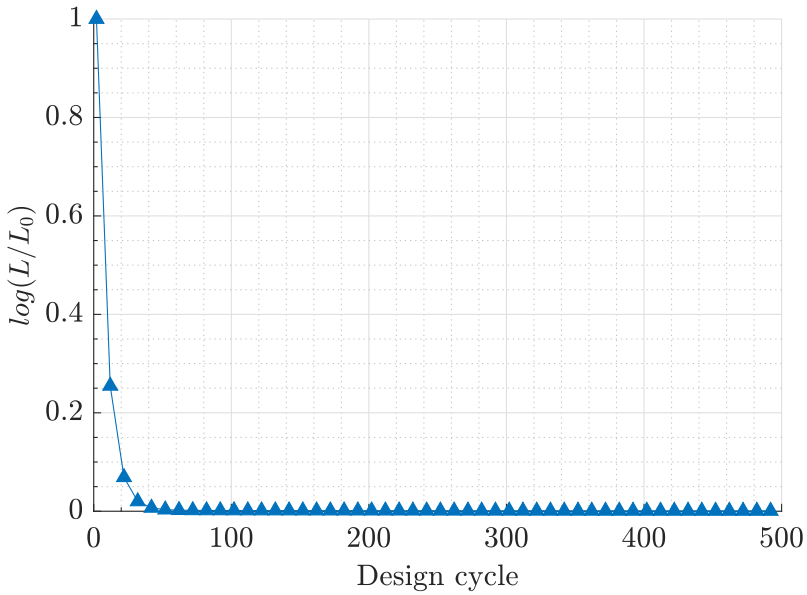

Figure 5.11: Convergence history in terms of objective function with respect to its value at initialization.

Table 5.1: Partially cavitating Foil-A: results and parameters.

			Cavity				
l_c/c	σ	C_L	Vol/c^2	$l_D(m)$	$l_{TL}(m)$	$h_{MAX}(m)$	N
0.10	1.3669	0.2008	0.0004	0.0035	0.0135	0.033	38
0.18	1.1501	0.2064	0.0017	0.0040	0.0243	0.043	42
0.30	1.0054	0.2179	0.0049	0.0020	0.0405	0.055	46
0.40	0.9090	0.2339	0.0091	0.0015	0.0460	0.066	46
0.50	0.8470	0.2500	0.0133	0.0010	0.0500	0.072	46
0.60	0.7967	0.2956	0.0227	0.0005	0.0600	0.085	46

$5deg$, chord length $c = 1$, submergence $d/c = 0.6$ and Froude number $Fr(c) = 0.5$. Figure 5.14 contains the predicted pressure profile and wave elevation, which are compared against the PCPAN method from Bal et al. 2001 [121]; with data denoted as black squares. It is evident that results for cavitation number and cavity volume are in good agreement. The wave-like behavior of the pressure profile on the region corresponding to the attached cavity, does not affect the final predictions, and is attributed to the nature of cost function definition. Follow Anevlavi & Belibassakis 2021 [212] for additional details on this topic.

All simulations were performed using $N_b = 240$ on the hydrofoil and $N_{fs} = 700$

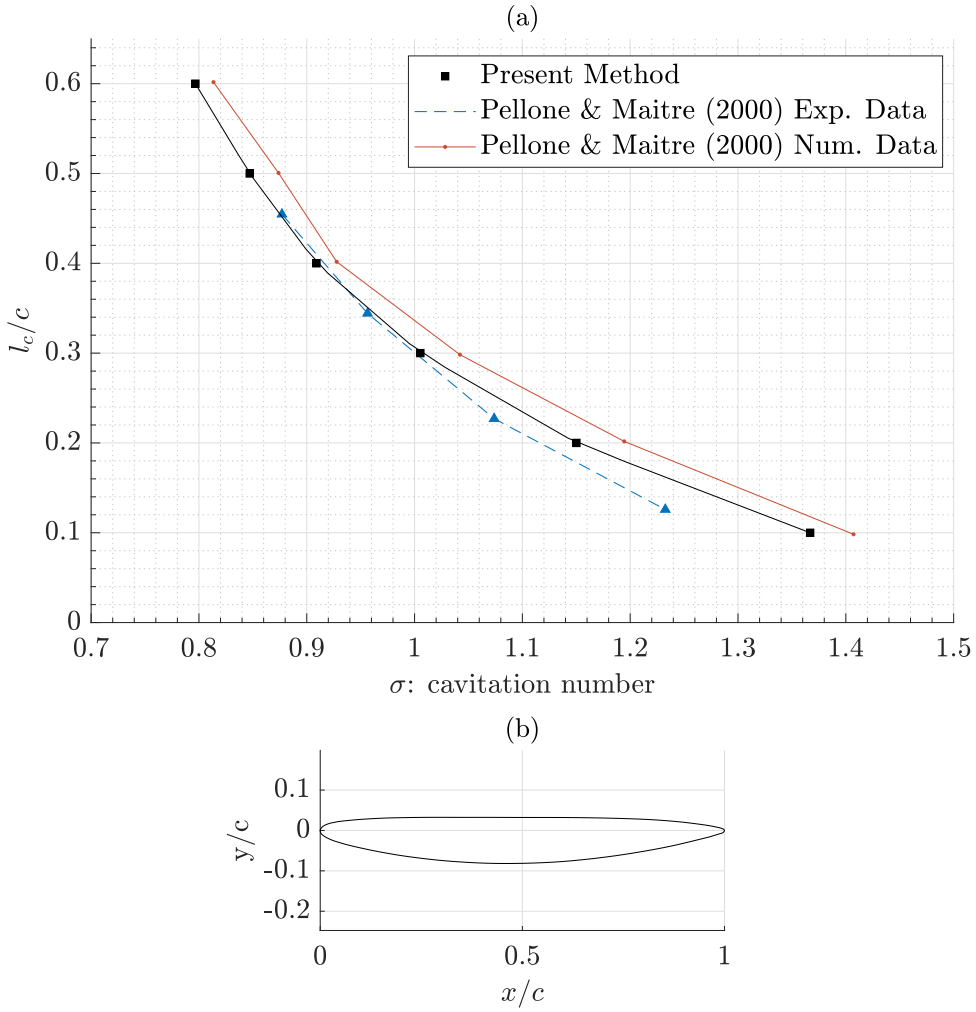

Figure 5.12: (a) Cavity length predictions as a function of cavitation number σ obtained with the present method and results from [120]. (b) Geometry of the examined cambered Foil-A at 4_o angle of attack at deep submergence.

on the free surface. Discrepancy regarding the cavitation number is attributed to the implementation of cavitation modeling that is embedded in the geometric model. To improve predictions, the attached cavity extent, including the transition zone, can be slightly adjusted to bring the numerical results closer to Bal et al. [121] predictions. Proper tuning of the steepest-descend parameter vector **B** significantly improves the convergence rate. In these simulations an optimal is

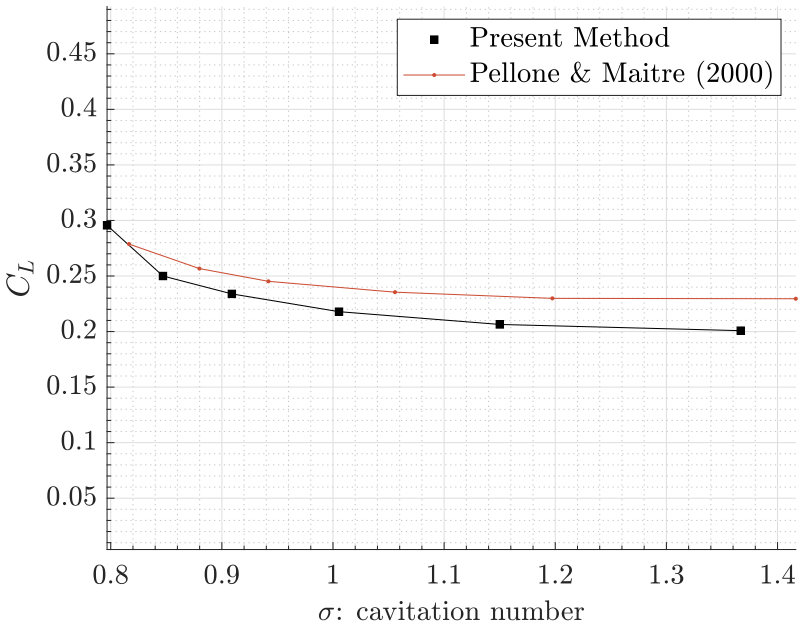

Figure 5.13: Comparison of lift coefficient prediction as a function of cavitation number σ obtained with the present method and the viscid-inviscid cavitation model [120] for Foil-A at $4deg$.

achieved after $M_{OPTIM} = 120$ optimization cycles.

The second case study considered differs only in terms of the Froude number, which is $Fr(c) = 0.75$ with results provided in Figure 5.15. Again, PCPAN predictions are denoted as black squares. Table 5.2 contains additional information regarding the predicted results and other parameters for the examined Froude numbers. It is shown that for an attached cavity of fixed length, cavitation number and lift coefficient decrease at higher Froude numbers at this submergence depth. The same holds for the predicted cavity volume and maximum height. However, the wave profile has higher wave length and amplitude as Froude number increases.

5.3.3 Analysis of partially cavitating hydrofoils with free surface effects

Angle of attack and submergence depth are two parameters that significantly affect the behavior of partially cavitating hydrofoils. To further investigate the matter,

Table 5.2: Froude number effects on a partially cavitating NACA 16006 at angle of attack $a = 5deg$ with $l_c = 0.5c$ and submergence $d/c = 0.6$.

			Cavity			Wave	
$Fr(c)$	σ	C_L	Vol/c^2	$l_{TL}(m)$	$h_{MAX}(m)$	λ	$max(\eta/c)$
0.50	1.252	0.781	0.0202	0.0525	0.081	1.63	0.1060
0.75	1.027	0.649	0.0166	0.0525	0.072	3.38	0.2915
1.00	0.871	0.531	0.0158	0.0550	0.070	6.15	0.3941

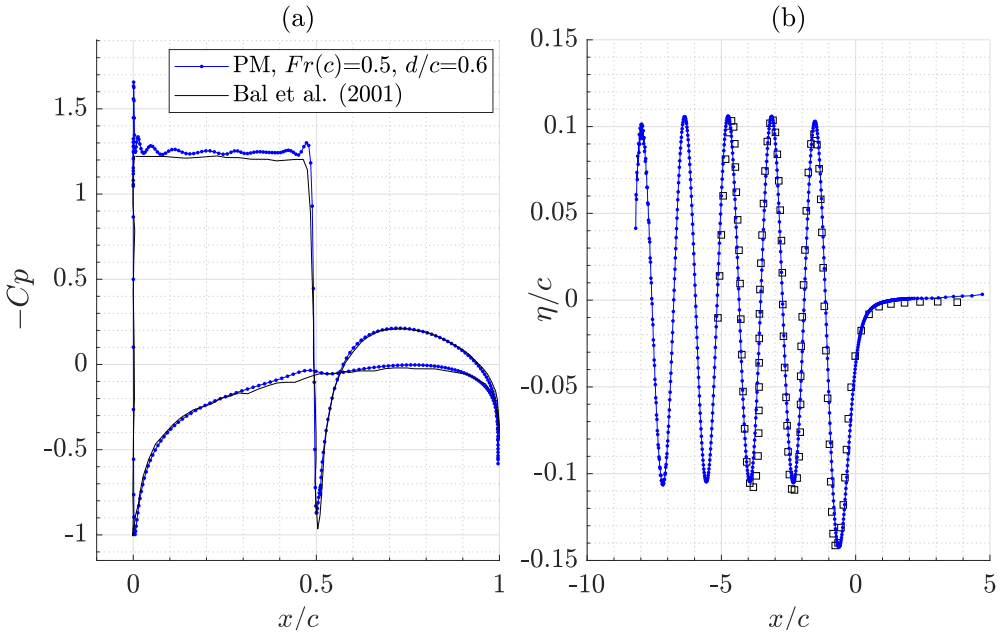

Figure 5.14: Comparison between the present method and PCPAN [121] predictions (black squares); for a NACA 16006 at $\alpha = 5deg$, $c = 1m$, $d/c = 0.6$ and $Fr(c) = 0.5$: (a) Pressure profile ($\sigma = 1.25$), (b) Wave elevation.

I performed a series of simulations, with results shown in Figure 5.16 referring to a NACA 16006 hydrofoil at $d/c = 1.0$ submergence depth with $Fr(c) = 0.5$. The angles of attack tested were $\alpha = \{2, 4, 6\}deg$. The total number of design variables is $N = 34$. All simulations are based on the $l_c = 0.4c$ cavity length assumption with the transition zone $(s_T - s_L)$ extent provided in Table 5.3 that follows. It also contains other quantities of interest including the predicted cavitation number σ, the cavity volume Vol/c^2, maximum height h_{max} of attached cavity, wave length λ and greatest wave height η/c. For these simulations, $\lambda = 2\pi U_\infty^2/g$ is the kept same, as it depends on the inflow velocity. Results that correspond to the deep

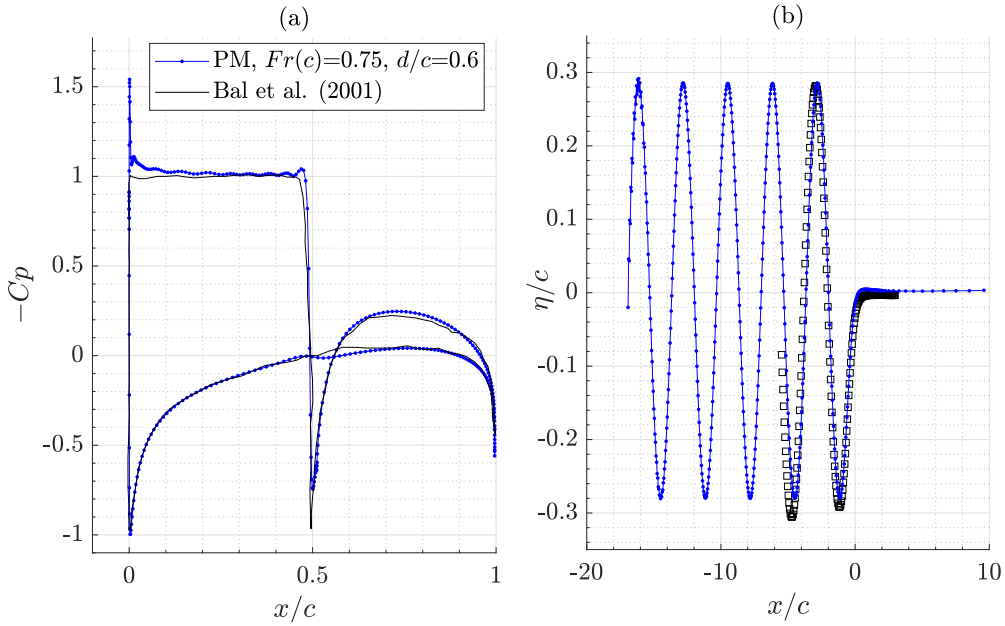

Figure 5.15: Comparison between the present method and PCPAN [121] predictions (black squares); for a NACA 16006 at $\alpha = 5deg$, $c = 1m$, $d/c = 0.6$ and $Fr(c) = 0.75$: (a) Pressure profile ($\sigma = 1.02$), (b) Wave elevation.

submergence case are also included for comparative purposes. The results suggest that as the angle of attack increases so does the cavitation number, attached cavity volume and wave elevation amplitude within the examined range of parameters.

The second series of parametric runs addresses the effects of finite submergence depth on the predicted cavitation number and cavity shape. The present method is capable of producing acceptable results for moderate submergence depths as it has been shown in a previous section. In Figure 5.17, results concerning the pressure coefficient, wave elevation profile and cavity shape as obtained with the extended *PCavPreMod* algorithm are provided for a NACA 16006 hydrofoil at $Fr(c) = 1.0$, cavity length $l_c = 0.5c$, angle of attack $\alpha = 5deg$ and submergence depths $d/c = \{0.6, 0.8, 1.0\}$.

To ensure that the present method performs well at the smallest submergence depth which is $d/c = 0.6$, results obtained with the PCPAN solver [121] are also included. The quantities of interest, namely the cavitation number, cavity volume and minimum wave elevation are provided in Table 5.4. The results indicate that for cases where the cavity length is kept the same, cavitation number decreases for higher values of submergence depth and the same holds for the cavity volume. On the other hand, the wave amplitude increases as the hydrofoil comes closer to the free surface. These simulations illustrate that hydrofoils operating at submergence

depths, smaller than $d/c = 1$, will have more strict requirements; to avoid or suppress cavitation, and that it would be beneficial to include such cost-effective, low-fidelity models to the preliminary phase of hydrofoil design.

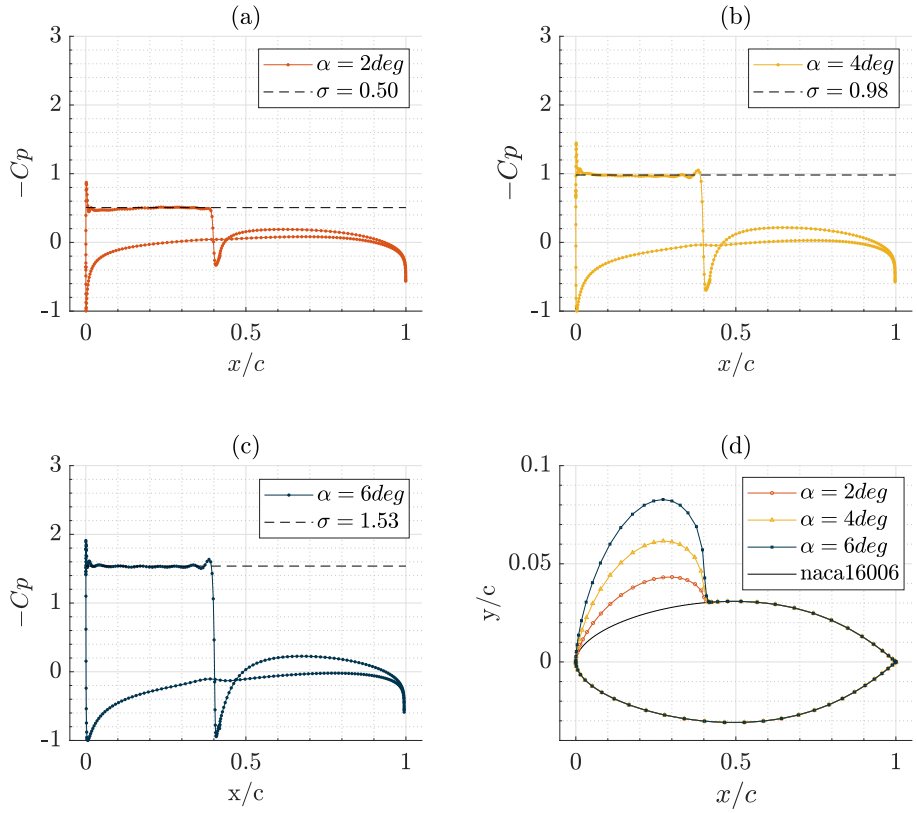

Figure 5.16: Pressure profiles for NACA 16006 at $Fr(c) = 0.5$, $d/c = 1.0$ at angle of attack (a) $\alpha = 2deg$, (b) $\alpha = 4deg$, (c) $\alpha = 6deg$ and the corresponding cavity profiles in (d).

5.4 Discussion and future work

In this work, a new adjoint BEM-based prediction model for partially cavitating two-dimensional hydrofoils that move at a constant speed beneath the free surface is proposed. Following an inverse problem formulation, the optimal solution for the steady state phenomenon, is determined using a gradient-based algorithm with sensitivities derived via the continuous adjoint method. The saturated vapor

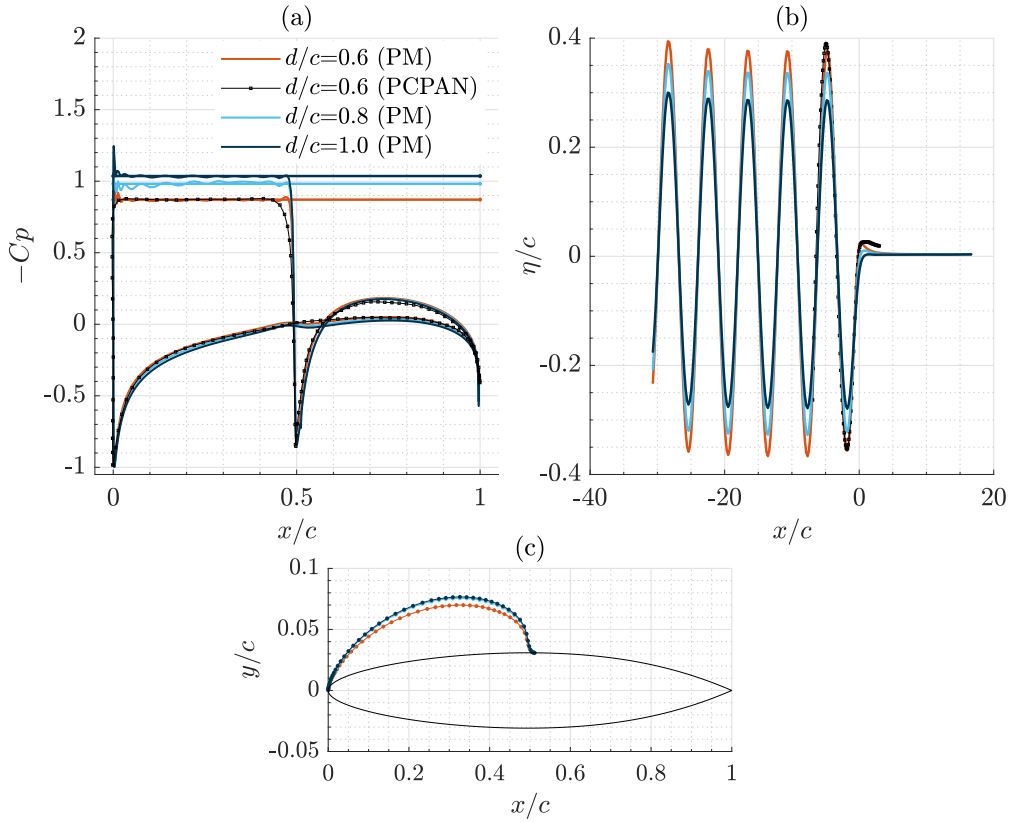

Figure 5.17: (a) Pressure profiles, (b) wave elevation and (c) cavity profile, for a NACA 16006 at $Fr(c) = 1.0$, cavity length $l_c = 0.5c$, angle of attack $\alpha = 5deg$ at submergence depths $d/c = \{0.6, 0.8, 1.0\}$.

Table 5.3: Angle of attack effects on a partially cavitating NACA 16006 at $Fr(c) = 0.5$ with $l_c = 0.4c$ and submergence $d/c = 1.0$.

				cavity			numerics	wave	
α	σ_o	σ	C_L	Vol/c^2	l_{TL}	h_{max}	M_{OPTIM}	λ	max
(deg)	$(d/c = 10)$				(m)	(m)			(η/c)
2	0.4730	0.5060	0.2634	0.0049	0.041	0.043	200	1.63	0.0081
4	0.9440	0.9810	0.5362	0.0108	0.041	0.062	201	1.63	0.0155
6	1.4731	1.5380	0.8277	0.0176	0.041	0.078	350	1.63	0.0262

pressure (cavitation number) and the cavity shape are included in the problem unknowns, whereas the detachment and termination points are considered given quantities. The objective function expresses a constant-pressure assumption on

Table 5.4: Submergence effects on a partially cavitating NACA 16006 with $l_c = 0.5c$ at angle of attack $a = 5deg$.

	$Fr(c) = 1.0$		
d/c	0.6	0.8	1.0
σ	0.87	0.98	1.03
Vol/c^2	0.0158	0.0179	0.0183
η_{min}	0.3941	0.3525	0.3001

the cavity boundary apart from the transition region $(s_T - s_L)$ which is included in the wetted portion of the boundary where a flow-tangency condition holds based on the implemented cavity termination model. Candidate solutions are evaluated at each optimization cycle using a source-vorticity BEM solver. The cavity boundary is parametrized as a B-spline and the control points are included in the design variable vector along with the initially unknown cavitation number.

The proposed method is validated against experimental data and a viscid-inviscid model for the case of steady cavitating hydrofoils without free surface effects, and provides predictions for the cavitation number and lift coefficient as functions of cavity length with good accuracy. These simulations correspond to cambered hydrofoil at $4deg$ angle of attack and a $U = 1.6m/s$ uniform inflow, with the detachment point placed downstream the leading edge to comply with experimental findings. Additional comparisons against the potential-based PC-PAN method with free surface interaction, for the case of partially cavitating hydrofoils moving at a constant speed, illustrate that the proposed scheme with the selected cavity termination model agrees well with the reported shapes of the attached cavity, cavitation numbers and wave elevation.

Two parametric studies with indicative results for the NACA 16006 hydrofoil are also performed to investigate angle of attack and submergence depth effects. The first case study yields that an increase in the angle of attack results in a higher cavitation number, attached cavity volume and wave elevation amplitude, for fixed cavity length and submergence depth. Results corresponding to the same scenario at deep submergence-depth are shown to highlight the importance of including free surface effects in cavitation prediction models. The second case study consists of three simulations at $d/c = \{0.6, 0.8, 1.0\}$ submergence depth, illustrating that as submergence-depth increases the cavitation number decreases and the same holds for the cavity volume. To conclude, cavitation imposes is more severe when the submergence depth is small, and therefore it is essential to be included in the preliminary design phase.

The developed numerical tool, being computationally inexpensive compared

to high-fidelity multi-phase methods, can be exploited in systematic applications required for the preliminary design of lifting surfaces with, or without, free surface effects to predict the cavitation number and cavity shape as functions of cavity length.

The extension of *PCavPreMod* to non-linear free surface models for on partially cavitating hydrofoils, would allow simulating foils at smaller submergence. Future work is also directed towards extending our method to 3D, in order to tackle problems of attached sheet cavitation for bio-mimetic wings operating at close proximity to the free surface. Extensions addressing the unsteady problem would provide valuable information on transient effects. Finally, cavitation predictions on propeller blade geometries is also of interest.

Part III

Concluding remarks

Chapter 6

Summary and suggestions future work

6.1 Hydrodynamics of morphing thrusters

To enable fast and efficient optimization studies, targeting quantities related to hydrodynamic loading and performance metrics associated with actively morphing flapping-foil thrusters, I developed the *3dBEM* solver as an extension to the GPU-BEM method introduced in Filippas & Belibassakis 2022 [12] exploiting the capabilities of parallel computation using CUDA API. The unsteady hydrodynamic problem formulation considers a non-linear pressure type Kutta condition and also includes a free-wake dynamics model to improve predictions in cases of high unsteadiness.

6.1.1 Summary

The optimization studies conducted using the aforementioned solver for candidate thruster evaluation revealed certain trends concerning the effects of planform shape, flapping, and active morphing parameters in thruster performance. The findings, which are summarized below, can be useful to the design of efficient bio-inspired thrusters; especially those related to autonomous underwater vehicle (AUV) propulsion applications.

The first thruster concept (Case 1) refers to a flapping foil with active chordline morphing. The optimal planform shape has a $\lambda_r = 1.0$ taper ratio and $\Lambda = 18^o$ backward sweep angle. Optimal tuning of the design variables consisting of $b_n = \{\Lambda, \lambda_r, A_c, \psi_c, Str\}$ yields an impressive +25.3% propulsive performance enhancement. This result can inspire continuously morphing designs or simpler solutions based on multi-component concepts with rigid parts. Technological ap-

plications of continuously morphing wings with hydrofoil-section adjustment (i.e., chord-line morphing) require the use of smart materials, compliant structures, and advanced actuation, see, also [8], [164]. A simple technical solution that has the potential of enhancing the propulsive performance can be the rigid wing with a trailing edge flap. Following the trends revealed from the optimization studies, it is beneficial to the efficiency that flap displacement follows or is aligned with, the flapping trajectory.

The second thruster concept (Case 2) refers to a flapping foil able to perform active spanwise bending and twisting morphing in a continuous manner. The design parameters examined correspond to $b_n = \{\lambda_r, A_b, \psi_b, A_\gamma, \psi_\gamma, h_0/c, \theta_0, Str\}$ vector of design variables. It performs a combination of prescribed out-of-phase heave/pitch motions and continuous spanwise bend/twist morphing. The optimal planform is crescent-like (i.e. resembling a whale-tail) with a taper ratio of $\lambda_r = 0.55$ and a backward sweep angle of $\Lambda = 18^o$. Optimal tuning of the parameters deduced from our optimization studies yields $+7.5\%$ propulsive performance enhancement in this case. The above morphing scenario can be implemented technologically using an internal mechanism that would be responsible for the active bend/twist coupling motion, similar to micro-aerial vehicles (MAV), see [6]. For marine applications and especially AUV propulsion, such mechanisms can be used to improve both propulsive efficiency and maneuverability.

6.1.2 Future work

Morphing wings have a wide range of technological applications for the marine industry. Bio-mimetic flapping-foil propulsion systems for AUVs with increased stealth and energy range pose as one future application, see [31]. Moreover, morphing dynamic wings can also be considered as ship thrust-augmentation devices that extract energy from the waves during the voyage, see [39] and [34]. In general, wings are being used in ship-stabilization systems (fin stabilizers, T-foil, etc.) for conventional ocean-going vessels and also for modern sailing yachts inspired by the America's Cup flying race boats [168]. Thus, morphing wing prototypes can be exploited in all the above cases, since the control of wing shape can be tuned to improve maneuverability and stability of vessels equipped with such devices.

Regarding future work directions associated with the unsteady hydrodynamic model for wing operating as marine thrusters and the *3dBEM* numerical tool, the following extensions are proposed:

- **Free surface effects.** The mathematical model introduced in [12], upon which the present computational tool is based, considers interactions between the wing thruster and the wavy free surface for regimes where wake-breaking does not occur. Including the free surface boundary in the mod-

eling will enrich our model by accounting for inflow velocity profile variations, similar to gusts, thus improving predictions for cases where the morphing thrusters operate submerged but at close proximity to the wavy free surface. This extension is useful for applications involving wings operating as thrust-augmentation devices for ships, and also for evaluating the performance of bio-inspired AUV thrusters operating at small submergence depths. Moreover, these extensions open the field to applications that address wave/current energy harvesting devices based on bio-mimetic wings; see, e.g. [40] and [9].

- **Viscous-inviscid interaction.** The adoption of boundary-layer corrections to potential flow solvers enriches the obtained solutions from the physical point of view, [145]. In addition, separation effects are also modeled by introducing a second wake originating, namely a 'double-wake' model, from the separation point that is provided as part of the boundary layer solution, see, e.g., Riziotis & Voutsinas 2008 [185]. These models could be implemented, for instance, in a strip-wise manner to improve predictions at off-design points where separation and viscous phenomena are dominant.

6.2 Hydro-mechanics of thin plates

To address the problem of elastic response for wings under hydrodynamic and inertial force excitation, a thin plate model (CPT) is formulated. Stiffness variation, involving thickness and material properties (i.e. Young's modulus) is included in the modeling. I developed the finite element method *2dFEM* based on the low-cost 3-node Discrete Kirchhoff Triangles (DKT) to obtain predictions on the elastic response of wings modeled as plates. The source code of *2dFEM* is written in C/C++ and allows for parallel computation on an NVIDIA graphics cards through the CUDA API. Extensive validation of the finite element solver, including eigenvalue problems and static analysis confirms its applicability for the category of engineering problems examined in the present dissertation; mainly involving bio-mimetic flapping thrusters for AUV propulsion.

6.2.1 Future work

Direct extensions, related to the hydro-mechanics of wings modeled as plates, include:

- **Modeling moderate or large displacements/rotation.** Enriching the thin plate model by retaining non-linear terms to address problems of mod-

erate rotations, or large deflections using the Föppl–von Kármán equations, allows for accurate predictions when non-linear effects are dominant.

- **Higher-fidelity FSI.** Coupling the developed solver with a viscous CFD solver gives rise to a series of studies associated with viscous effects on the elastic response of flexible wings, including resonance effects and flatter-type instabilities. Other applications include small-scale autonomous underwater vehicle appendages, maneuvering studies, self-propulsion applications [182], or even wave/current source energy harvesting devices [40], [9]. Moreover, coupling the present plate model (or its extension including non-linear terms) with a viscous solver is also useful for studies on the aero-elastic response of wings in gust conditions.

6.3 Fluid-structure interaction model

All the above extensions can be beneficial to the proposed fluid-structure interaction model and the corresponding *FlexWing3D* computational tool, comprising of the unsteady hydrodynamic boundary element solver *3dBEM* and the thin plate solver for plates with stiffness variation based on DKT elements *2dFEM*. The strong coupling scheme that is developed treats the implicit non-linearity arising from the fact that hydrodynamic pressure affects bending displacement field (thus the deformed shape of the wing under study that is modeled as a plate) and vice-versa.

6.3.1 Summary

Validation of the proposed model is based on comparisons against experimental works found in the literature involving a rectangular plate under prescribed heaving excitation submerged within a constant inflow and the steady response of a tapered wing at an angle of attack also submerged within a fluid medium. *FlexWing3D* simulations also exploit the parallel computation capabilities of graphics cards, thus requiring a few hours on a typical desktop for a three-period simulation on passively deforming wings operating as marine thrusters.

Moreover, an optimization study is performed to define an improved thickness profile for the case of a flexible flapping-wing thruster, assumed to be clamped at the trailing edge, thus ensuring that chord-wise flexibility effects are dominant. Results revealed that wings with a more slender shape near the trailing edge (i.e. with a smaller thickness profile), compared to the NACA series, yield a performance enhancement with a significant reduction in thrust. The final shape is similar to the bio-mimetic stiffness profiles extracted from the analysis of fish fins.

Overall, the findings agree with relevant works from the literature and contribute to the field of bio-mimetic applications for flexible wing thrusters by introducing a new cost-effective computational tool that is able to capture non-linear loading effects and gives useful predictions related to both the elastic response of the wing and its propulsive performance.

6.3.2 Future work

I propose the following directions for future work:

- **Reducing computational time.** One way to further reduce the computation time is to implement approximate methods for Jacobian evaluation based on information related to the residual equation and previous changes to the vector of unknowns. This type of methodology is introduced in Spenke et al. (2020) [210] and successfully implemented in the numerical scheme developed for the fluid-structure interaction problem of flexible membranes presented in Lauber et al. (2023) [211]. These extensions will enable optimization studies involving a greater number of design variables and allow for the use of more sophisticated optimization algorithms, such as hybrid methods or evolutionary approaches.

- **Complex shapes and non-uniform stiffness.** Investigations related to the effects of boundary conditions on the performance of wing thrusters, for instance, exploring T-foil configurations; see, e.g. the wing support shown in Figure 1.6 and studied in [34]. Performing simulations involving more realistic planform shapes with curved leading edges, large taper/sweep, and hydrofoil section variation along the span. In addition, the effects of variability in material stiffness, i.e., $D(x, y)$, on the elastic response of wing thrusters are also of interest. This might also refer to non-uniform material properties in the context of functionally graded materials.

6.4 Partial cavitation model

Within the context of this thesis, a new adjoint BEM-based partial cavitation prediction model for hydrofoils operating at constant speed beneath the free surface is introduced. The developed computational tool *PCavPreMod* written in Matlab is compared against other methods and found to predict well the cavitation number and cavity shape under the fixed-length attached cavity assumption. The proposed method is computationally inexpensive compared to higher-fidelity multi-phase solvers and thus can facilitate the preliminary design phase of lifting surfaces.

6.4.1 Future work

Regarding future work extensions, I propose:

- **Given cavitation number.** Addressing optimization problems where the cavitation number is given and the attached cavity length is included in the design variable vector.
- **Sheet cavitation.** Extension of the present model to three-dimensional problem for sheet cavitation prediction on bio-mimetic wings or propeller blades; including free-surface effects. As a first approach, the present 2D model can be implemented strip-wise to obtain predictions of the shape of the sheet cavity; see, e.g., Kinnas & Fine 1993 [62].
- **Unsteady cavitation.** Consideration of a time-varying attached cavity length leads to transient models.
- **Non-linear free surface.** Hydrofoils moving at close proximity to the free surface give rise to non-linear wave phenomena, thus consideration of non-linear free surface dynamics will improve the accuracy of the present model in cases where $d/c < 1$.

Bibliography

[1] IMO, "Marine environmental protection committee. Revised IMO strategy on reduction of GHG emissions from ships, resolution MEPC.377 (80). MEPC 80/WP.12 annex 11 International Maritime Organization", 2023. [Online]. Available: https://www.imo.org/en/MediaCentre/PressBriefings/pages/Revised-GHG-reduction-strategy-for-global-shipping-adopted-.aspx.

[2] J. Faber and S. H. et al., "Fourth IMO greenhouse gas study", *International Maritime Organization*, 2020. [Online]. Available: https://www.imo.org/en/ourwork/Environment/Pages/Fourth-IMO-Greenhouse-Gas-Study-2020.aspx.

[3] S. Lagouvardou, B. Lagemann, H. Psaraftis, E. Lindstadt, and S. O. Erikstad, "Marginal abatement cost of alternative marine fuels and the role of market-based measures", *Nature Energy*, 2023. DOI: https://doi.org/10.1038/s41560-023-01334-4.

[4] K. V. Rozhdestvensky and V. A. Ryzov, "Aerodynamics of flapping-wing propulsors", *Progress in Aerospace Sciences*, vol. 39, pp. 585–633, 2003. DOI: https://doi.org/10.1016/S0376-0421(03)00077-0.

[5] A. J. Smits, "Undulatory and oscillatory swimming", *Journal of Fluids Mechanics*, vol. 874, 2019. DOI: https://doi.org/10.1017/jfm.2019.284.

[6] W. Shyy, H. Aono, S. Chimakurthi, *et al.*, "Recent progress in flapping wing aerodynamics and aeroelasticity", *Engineering Analysis with Boundary Elements*, vol. 46, pp. 284–327, 7 2014. DOI: https://doi.org/10.1016/j.paerosci.2010.01.001.

[7] R. K. Katzschmann, A. D. Marchese, and D. Rus, "Hydraulic autonomous soft robotic fish for 3d swimming", in *Experimental Robotics: The 14th International Symposium on Experimental Robotics*. Springer International Publishing, 2016, pp. 405–420, ISBN: 978-3-319-23778-7. DOI: 10.1007/978-3-319-23778-7_27. [Online]. Available: https://doi.org/10.1007/978-3-319-23778-7_27.

[8] R. K. Katzschmann, "Building and controlling fluidically actuated soft robots: From open loop to model-based control", Ph.D. dissertation, Department of Mechanical Engineering MIT, 2018. [Online]. Available: https://dspace.mit.edu/handle/1721.1/119278.

[9] J. Xing and L. Yang, "Wave devouring propulsion: An overview of flapping foil propulsion technology", *Renewable and Sustainable Energy Reviews*, vol. 184, p. 113 589, 2023. DOI: https://doi.org/10.1016/j.rser.2023.113589.

[10] K. Belibassakis, E. Filippas, and G. Papadakis, "Numerical and experimental investigation of the performance of dynamic wing for augmenting ship propulsion in head and quartering seas", *Journal of Marine Science and Engineering*, vol. 10, no. 1, 2022. DOI: https://doi.org/10.3390/jmse10010024.

[11] D. Ntouras, G. Papadakis, and K. Belibassakis, "Ship bow wings with application to trim and resistance control in calm water and in waves", *Journal of Marine Science and Engineering*, vol. 10, no. 4, 2022. DOI: https://doi.org/10.3390/jmse10040492.

[12] E. Filippas and K. Belibassakis, "A nonlinear time-domain bem for the performance of 3d flapping-wing thrusters in directional waves", *Ocean Engineering*, vol. 245, p. 110 157, 2022. DOI: https://doi.org/10.1016/j.oceaneng.2021.109332.

[13] J. Barreiro, S. Zaragoza, and V. Diaz-Casa, "Review of ship energy efficiency", *Ocean Engineering*, vol. 257, p. 111 594, DOI: 10.1016/j.oceaneng.2022.111594.

[14] F. Spinelli, S. Mancini, L. Vitiello, R. N. Bilandi, and M. D. Carlini, "Shipping decarbonization: An overview of the different stern hydrodynamic energy saving devices", *Journal of Marine Science and Engineering*, vol. 10, p. 574, 5 2022. DOI: https://doi.org/10.3390/jmse10050574.

[15] IMO, *Energy efficiency design index improving the technical performance of new build ships*. [Online]. Available: https://www.imo.org/en/MediaCentre/HotTopics/Pages/EEXI-CII-FAQ.aspx.

[16] V.-T. Nguyen and D. Chandar, "Ship specific optimization of pre-duct energy saving devices using reduced order models", *Applied Ocean Research*, vol. 131, p. 103 449, 2023. DOI: https://doi.org/10.1016/j.apor.2022.103449.

[17] P. Anschau, N. Kornev, and S. Samarbakhsh, "Unsteady hydrodynamic loads on energy saving ducts", *Ocean Engineering*, vol. 269, p. 113 431, 2023. DOI: https://doi.org/10.1016/j.oceaneng.2022.113431.

[18] W.-S. Jin, M.-C. Kim, J.-G. Kang, Y.-J. Shin, and K.-W. Lee, "Optimization of blade position on an asymmetric pre-swirl stator used in container ships", *Journal of Marine Science and Engineering*, vol. 11, no. 1, 2023. DOI: https://doi.org/10.3390/jmse11010050.

[19] F. Furcas and S. Gaggero, "Pre-swirl stator design using a coupled BEM-RANSE approach", *Ocean Engineering*, vol. 222, p. 108 579, 2021. DOI: https://doi.org/10.1016/j.oceaneng.2021.108579.

[20] H. Prins, M. Flikkema, B. Schuiling, *et al.*, "Green retrofitting through pptimisation of hull-propulsion interaction – GRIP", *Transportation Research Procedia*, vol. 14, pp. 1591–1600, 2016, Transport Research Arena TRA2016, ISSN: 2352-1465. DOI: https://doi.org/10.1016/j.trpro.2016.05.124.

[21] E. O. Obwogi, H. long Shen, and Y. min Su, "The design and energy saving effect prediction of rudder-bulb-fin device based on cfd and model test", *Applied Ocean Research*, vol. 114, p. 102 814, 2021. DOI: https://doi.org/10.1016/j.apor.2021.102814.

[22] E. O. Obwogi, H. long Shen, and Y. min Su, "Study on the design procedure of rudder attached thrust fin for merchant ship based on computational fluid dynamics", *Ocean Engineering*, vol. 234, p. 109 263, 2021. DOI: https://doi.org/10.1016/j.oceaneng.2021.109263.

[23] K. Mizzi, Y. K. Demirel, C. Banks, O. Turan, P. Kaklis, and M. Atlar, "Design optimization of Propeller Boss Cap Fins for enhanced propeller performance", *Applied Ocean Research*, vol. 62, pp. 210–222, 2017. DOI: https://doi.org/10.1016/j.apor.2016.12.006.

[24] F. Spinelli, S. Mancini, L. Vitiello, R. N. Bilandi, and M. D. Carlini, "Shipping decarbonization: An overview of the different stern hydrodynamic energy saving devices", *Journal of Marine Science and Engineering*, vol. 10, no. 5, 2022. DOI: https://doi.org/10.3390/jmse10050574.

[25] J. Carlton, *Marine Propellers and Propulsion*. (Imprint) Butterworth-Heinemann, 2017, ISBN: 978-0-7506-8150-6. DOI: https://doi.org/10.1016/B978-0-7506-8150-6.X5000-1.

[26] S. Gaggero, J. GOnzalez-Adalid, and M. P. Sobrino, "Design of contracted and tip loaded propellers by using boundary element methods and optimization algorithms", *Applied Ocean Research*, vol. 55, pp. 109–129, 2016. DOI: https://doi.org/10.1016/j.apor.2015.12.004.

[27] P. Andersen, J. Friesch, J. J. Kappel, L. Lundegaard, and G. Patience, "Development of a marine propeller with nonplanar lifting surfaces", *Mar Technol SNAME N 42 (03)*, 144–158, 2005. DOI: https://doi.org/10.5957/mt1.2005.42.3.144.

[28] D. Bertetta, S. Brizzolara, E. Canepa, S. Gaggero, and M. Viviani, "Efd and cfd characterization of a clt propeller", *International Journal of Rotational Machinery*, vol. 2012, 2012. DOI: https://doi.org/10.1155/2012/348939.

[29] C.-W. Chen, X.-P. Chen, Z.-Y. Zhou, *et al.*, "Effect of tip rake distribution on the hydrodynamic performance of non-planar kappel propeller", *Journal of Marine Science and Engineering*, vol. 11, no. 4, 2023, ISSN: 2077-1312. DOI: https://doi.org/10.3390/jmse11040748.

[30] M. J. Lighthill, "Hydromechanics of aquatic animal propulsion", *Annual Review of Fluid Mechanics*, vol. 1, pp. 413–446, 1969. DOI: https://doi.org/10.1146/annurev.fl.01.010169.002213.

[31] R. Salazar, V. Fuentes, and A. Abdelkefi, "Classification of biological and bioinspired aquatic systems: A review", *Ocean Engineering*, vol. 148, pp. 75–114, 2018. DOI: https://doi.org/10.1016/j.oceaneng.2017.11.012.

[32] W. Shyy, H. Aono, C. kwon Kang, and H. Liu, *An Introduction to Flapping Wing Aerodynamics*. Cambridge University Press, 2013, ISBN: 978-1-107-03726-7.

[33] E. Bøckmann and S. Steen, "Experiments with actively pitch-controlled and spring-loaded oscillating foils", *Applied Ocean Research*, vol. 48, pp. 227–235, 2014. DOI: https://doi.org/10.1016/j.apor.2014.09.004.

[34] J. Bowker and N. Townsend, "A probabilistic method to evaluate bow foils for realistic seas and shipping routes", *Applied Ocean Research*, vol. 129, p. 103 374, 2022. DOI: https://doi.org/10.1016/j.apor.2022.103374.

[35] Y. Zhang, L. Xu, and Y. Zhou, "A wave foil with passive angle of attack adjustment for wave energy extraction for ships", *Ocean Engineering*, vol. 246, p. 110 627, 2022. DOI: https://doi.org/10.1016/j.oceaneng.2022.110627.

[36] L. Mei, W. Yan, J. Zhou, and W. Shi, "Thrust enhancement of dtmb 5415 with elastic flapping foil in regular head waves", *Journal of Marine Science and Engineering*, vol. 11, no. 3, 2023. DOI: https://doi.org/10.3390/jmse11030632.

[37] E. Filippas, *Hydrodynamic analysis of ship and marine biomimetic systems in waves using GPGPU programming, PhD Thesis*. NTUA, 2019.

[38] J. Vermeiden, T. Terwisga, K. Kooiker, and F. H. Lafeber, "A systematic experimental study on powering performance of flapping foil propulsors", Aug. 2012.

[39] K. Belibassakis, E. Filippas, and G. Papadakis, "Numerical and experimental investigation of the performance of dynamic wing for augmenting ship propulsion in head and quartering seas", *Journal of Marine Science and Engineering*, vol. 10, p. 24, 1 2021. DOI: https://doi.org/10.3390/jmse10010024.

[40] Q. Xiao and Q. Zhu, "A review on flow energy harvesters based on flapping foils", *Journal of Fluids and Structures*, vol. 46, pp. 174–191, 2014. DOI: https://doi.org/10.1016/j.jfluidstructs.2014.01.002.

[41] E. S. Filippas, T. P. Gerostathis, and K. A. Belibassakis, "Semi-activated oscillating hydrofoil as a nearshore biomimetic energy system in waves and currents", *Ocean Engineering*, vol. 154, pp. 396–415, 2018. DOI: https://doi.org/10.1016/j.oceaneng.2018.02.028.

[42] M. Sfakiotakis, D. M. Lane, and J. B. C. Davies, "Review of fish swimming modes for aquatic locomotion", *IEEE Journal of Oceanic Engineering*, vol. 24, no. 2, pp. 237–252, 1999. DOI: https://doi.org/10.1109/48.757275.

[43] D. S. Barrett, "The design of a flexible hull undersea vehicle propelled by an oscillating foil", M.S. thesis, Department of Ocean Engineering MIT, 1994. [Online]. Available: https://dspace.mit.edu/handle/1721.1/12109.

[44] D. S. Barrett, "Propulsive efficiency of a flexible hull underwater vehicle", Ph.D. dissertation, Department of Ocean Engineering MIT, 1996. [Online]. Available: https://dspace.mit.edu/handle/1721.1/10559.

[45] F. E. Fish, "Biomechanical perspective on the origin of cetacean flukes", in *The Emergence of Whales. Advances in Vertebrate Paleobiology.* Vol. 1, Boston MA: Springer, 1998, 303–324. DOI: https://doi.org/10.1007/978-1-4899-0159-0_10.

[46] J. Esfahani, E. Barati, and H. R. Karbasian, "Fluid structures of flapping airfoil with elliptical motion trajectory", *Computers & Fluids*, vol. 108, pp. 142–155, 2015. DOI: https://doi.org/10.1016/j.compfluid.2014.12.002.

[47] H. R. Karbasian and J. A. Esfahani, "Enhancement of propulsive performance of flapping foil by fish-like motion pattern", *Computers & Fluids*, vol. 156, pp. 305–316, 2017. DOI: https://doi.org/10.1016/j.compfluid.2017.07.016.

[48] M. S. Triantafyllou, G. S. Triantafyllou, and R. Gopalkrishnan, "Wake mechanics for thrust generation in oscillating foils", *Physics of Fluids*, vol. 3, pp. 2835–2837, 1 1991. DOI: https://doi.org/10.1063/1.858173.

[49] G. K. Taylor, R. L. Nudds, and A. L. R. Thomas, "Flying and swimming animals cruise at a strouhal number tuned for high power efficiency", *Nature*, vol. 425, pp. 707–711, 2003. DOI: https://doi.org/10.1038/nature02000.

[50] D. A. Read, F. S. Hover, and M. S. Triantafyllou, "Forces on oscillating foils for propulsion and maneuvering", *Journal of Fluids and Structures*, vol. 17, pp. 163–183, 2003. DOI: https://doi.org/10.1016/S0889-9746(02)00115-9.

[51] F. S. Hover, O. Haugsdal, and M. S. Triantafyllou, "Effect of angle of attack profiles in flapping foil propulsion", *Journal of Fluids and Structures*, vol. 19, pp. 37–47, 2004. DOI: https://doi.org/10.1016/j.jfluidstructs.2003.10.003.

[52] L. Schouveiler, F. S. Hover, and M. S. Triantafyllou, "Performance of flapping foil propulsion", *Journal of Fluids and Structures*, vol. 20, pp. 949–959, 2004. DOI: https://doi.org/10.1016/j.jfluidstructs.2005.05.009.

[53] M. S. Triantafyllou, F. S. Hover, A. H. Techet, and D. K. P. Yue, "Review of hydrodynamic scaling laws in aquatic locomotion and fishlike swimming", *Appl. Mech. Rev.*, vol. 58, 4 2005. DOI: https://doi.org/10.1115/1.1943433.

[54] B. M. Boschitsch, P. A. Dewey, and A. J. Smits, "Propulsive performance of unsteady tandem hydrofoils in an in-line configuration", *Physics of Fluids*, vol. 26, p. 051 901, 2014. DOI: https://doi.org/10.1063/1.4872308.

[55] H. J. A. Bird and K. Ramesh, "Unsteady lifting-line thoery and the influence of wake vorticity on aerodynamic loads", *Theor. Comput. Fluid Dyn.*, vol. 35, pp. 609–631, 2021. DOI: https://doi.org/10.1007/s00162-021-00578-8.

[56] J. T. Reid, *A general approach to lifting-line theory, applied to wings with sweep*. Utah State University, 2020. DOI: https://digitalcommons.usu.edu/etd/7842.

[57] H. J. A. Bird, K. Ramesh, S. Ōtomo, and I. M. Viola, "Usefulness of inviscid linear unsteady lifting-line theory for viscous large-amplitude problems", *AAIA Journal*, vol. 60, 2 2021. DOI: https://doi.org/10.2514/1.J060808.

[58] A. S. J. Hess, "Calculation of potential flow around arbitrary bodies", *Prog. Aeronaut. Sci.*, vol. 8, 1–138, 1966. DOI: https://doi.org/10.1016/0376-0421(67)90003-6.

[59] J. Moran, *An Introduction to Theoretical and Computational Aerodynamics*. John Wiley & Sons, 1984, ISBN: 0-471-87491-4.

[60] A. P. J. Katz, *Low-Speed Aerodynamics*. Cambridge University Press, 2001, ISBN: 9780511810329. DOI: https://doi.org/10.1017/CBO9780511810329.

[61] K. Belibassakis, T. Gerostathis, K. Kostas, *et al.*, "A bem-isogeometric method for the ship wave-resistance problem", *Ocean Engineering*, vol. 60, pp. 53–67, 2013. DOI: https://doi.org/10.1016/j.oceaneng.2012.12.030.

[62] N. F. S.A. Kinnas, "A numerical nonlinear analysis of the flow aoround two- and three-dimensional partially cavitating hydrofoils", *J. Fluid Mech.*, vol. 254, 151–181, 1993. DOI: https://doi.org/10.1017/S0022112093002071.

[63] Q. Zhu, "Numerical simulation of a flapping foil with chordwise or spanwise flexibility", *AIAA*, vol. 45, pp. 2448–2457, 10 2007. DOI: https://doi.org/10.2514/1.28565.

[64] F. Fish and J. Battle, "Hydrodynamic design of the humpback whale flipper", *Journal of Morphology*, vol. 225, 1 1995. DOI: https://doi.org/10.1002/jmor.1052250105.

[65] S. Aftab, N. Razak, A. M. Rafie, and K. Ahmad, "Mimicking the humpback whale: An aerodynamic perspective", *Progress in Aerospace Sciences*, vol. 84, pp. 48–69, 2016. DOI: https://doi.org/10.1016/j.paerosci.2016.03.002.

[66] N. Rostamzadeh, K. Hansen, and R. Kelso, "Tubercled wing flow physics and performance", in *Flow Control Through Bio-inspired Leading-Edge Tubercles: Morphology, Aerodynamics, Hydrodynamics and Applications*. Springer International Publishing, 2020. DOI: https://doi.org/10.1007/978-3-030-23792-9_2.

[67] Z. Wei, J. Toh, I. Ibrahim, and Y. Zhang, "Aerodynamic characteristics and surface flow structures of moderate aspect-ratio leading-edge tubercled wings", *European Journal of Mechanics /B Fluids*, vol. 75, pp. 143–152, 2019. DOI: https://doi.org/10.1016/j.euromechflu.2019.01.001.

[68] G. Moscato, J. Mohamed, and G. P. Romano, "Improving performances of biomimetic wings with leading-edge turbecles", *Experiments in Fluids*, vol. 63, p. 146, 2022. DOI: https://doi.org/10.1007/s00348-022-03493-8.

[69] Z. Wei, T. New, and Y. Cui, "An experimental study on flow separation control of hydrofoils with leading edge tubercles at low reynolds numbers", *Ocean Engineering*, vol. 108, pp. 336–346, 2015. DOI: https://doi.org/10.1016/j.oceaneng.2015.08.004.

[70] W. Shi, R. Rosli, M. Atlar, R. Norman, D. Wang, and W. Yang, "Hydrodynamic performance evaluation of a tidal turbine with leading-edge tubercles", *Ocean Engineering*, vol. 117, pp. 246–253, 2016. DOI: https://doi.org/10.1016/j.oceaneng.2016.03.044.

[71] BlueNav, *Bluenav's hubless drive propulsion system specifically tailored for the yachting sector*, https://bluenav.com/bluenav-whale-design/, Online; accessed 4 April 2024, 2024.

[72] Y. Zhang, X. Zhang, Y. Li, M. Chang, and J. Xu, "Aerodynamic performance of a low-reynolds uav with leading edge protuberances inspired by humpback whale flippers", *Chinese Journal of Aeronautics*, vol. 34, pp. 415–424, 2021. DOI: https://doi.org/10.1016/j.cja.2020.11.004.

[73] P. Prempraneerach, F. S. Hover, and M. S. Triantafyllou, "The effect of chordwise flexibility on the thrust and efficiency of a flapping foil", 2003. [Online]. Available: https://api.semanticscholar.org/CorpusID:705359.

[74] S. Heathcote, D. Martin, and I. Gursul, "Flexible flapping airfoil propulsion at zero freestream velocity", *AIAA Journal*, vol. 42, 11 2004. DOI: https://doi.org/10.2514/1.5299.

[75] S. Heathcote, Z. Wang, and I. Gursul, "Effect of spanwise flexibility on flapping wing propulsion", *Journal of Fluids and Structures*, vol. 24, pp. 183–199, 2 2008. DOI: https://doi.org/10.1016/j.jfluidstructs.2007.08.003.

[76] F. Paraz, C. Eloy, and L. Schouveiler, "Experimental study of the response of a flexible plate to a harmonic forcing in a flow", *Comptes Rendus Mèchanique*, vol. 342, no. 9, pp. 532–538, 2014. DOI: https://doi.org/10.1016/j.crme.2014.06.004.

[77] A. Richards and P. Oshkai, "Effect of the stiffness, inertia and oscillation kinematics on the thrust generation and efficiency of an oscillating-foil propulsion system", *Journal of Fluids and Structures*, vol. 57, pp. 357–374, 2015. DOI: https://doi.org/10.1016/j.jfluidstructs.2015.07.003.

[78] A. Kancharala and K. Philen, "Optimal chordwise stiffness profiles of self-propelled flapping fins", *Bioinspiration & Biomimetics*, vol. 11, p. 056 016, 5 2016. DOI: https://doi.org/10.1088/1748-3190/11/5/056016.

[79] D. Quinn, G. Lauder, and A. Smits, "Maximizing the efficiency of a flexible propulsor using experimental optimization", *Journal of Fluids Mechanics*, vol. 767, pp. 430–448, 2015. DOI: https://doi.org/10.1017/jfm.2015.35.

[80] S. Heathcote and I. Gursul, "Flexible flapping airfoil propulsion at low Reynolds numbers", *AIAA Journal*, vol. 45, 5 2007. DOI: https://doi.org/10.2514/1.25431.

[81] P. Riggs, A. Bowyer, and J. Vincent, "Advantages of a biomimetic stiffness profile in pitching flexible fin propulsion", *Journal of Bionic Engineering*, vol. 7, pp. 113–119, 2 2010. DOI: https://doi.org/10.1016/S1672-6529(09)60203-1.

[82] O. Barannyk, B. Buckham, and P. Oskai, "On performance of an oscillating plate underwater propulsion system with variable chordwise flexibility at different depths of submergence", *Journal of Fluids and Structures*, vol. 28, pp. 152–166, 2012. DOI: https://doi.org/10.1016/j.jfluidstructs.2011.10.005.

[83] D. Quinn, G. Lauder, and A. Smits, "Scaling the propulsive performance of heaving flexible panels", *Journal of Fluids Mechanics*, vol. 738, pp. 250–267, 2013. DOI: https://doi.org/10.1017/jfm.2013.597.

[84] K. W. Moored, P. A. Dewey, B. M. Boschitsch, A. J. Smith, and H. Haj-Hariri, "Linear instability mechanisms leading to optimally efficient locomotion with flexible propulsors", *Physics of Fluids*, vol. 26, 4 2014. DOI: https://doi.org/10.1063/1.4872221.

[85] D. J. Cleaver, I. Gursul, D. E. Calderon, and Z. Wang, "Thrust enhancement due to flexible trailing-edge of plunging foils", *Journal of Fluids and Structures*, vol. 51, pp. 401–412, 2014. DOI: https://doi.org/10.1016/j.jfluidstructs.2014.09.006.

[86] D. Iverson, M. Rahimpour, W. Lee, T. Kiwata, and P. Oshkai, "Effect of chordwise flexibility on propulsive performance of high inertia oscillating-foils", *Journal of Fluids and Structures*, vol. 91, p. 102 750, 2019. DOI: https://doi.org/10.1016/j.jfluidstructs.2019.102750.

[87] K. Lucas, P. Thornycroft, B. Gemmell, S. Colin, J. Costello, and G. Lauder, "Effect of chordwise flexibility on propulsive performance of high inertia oscillating-foils", *Bioinspiration & Biomimetics*, vol. 10, p. 056 019, 5 2015. DOI: https://doi.org/10.1088/1748-3190/10/5/056019.

[88] R. Fernandez-Pratz, "Effect of chordwise flexibility on pitching foil propulsion in a uniform current", *Ocean Engineering*, vol. 145, pp. 24–33, 2017. DOI: https://doi.org/10.1016/j.oceaneng.2017.08.055.

[89] S. Alben, C. Witt, T. Baker, E. Anderson, and G. Lauder, "Dynamics of freely flexible foils", *Physics of Fluids*, vol. 24, p. 051 901, 2012. DOI: https://doi.org/10.1063/1.4709477.

[90] F. Paraz, L. Schouveiler, and C. Eloy, "Thrust generation by a heaving flexible foil: Resonance, nonlinearities, and optimality", *Physics of Fluids*, vol. 28, p. 011 903, 2016. DOI: https://doi.org/10.1063/1.4939499.

[91] R. F. Feria and J. Alaminos-Quesada, "Analytical results for the propulsion performance of a flexible foil with prescribed pitching and heaving motions and passive small deflection", *Journal of Fluid Mechanics*, vol. 910, 2021. DOI: https://doi.org/10.1017/jfm.2020.1015.

[92] E. Sanmiguel-Rojas and R. F. Feria, "Propulsion enhancement of flexible plunging foils: Comparing linear theory predictions with high-fidelity cfd results", *Ocean Engineering*, vol. 235, 2021. DOI: https://doi.org/10.1016/j.oceaneng.2021.109331.

[93] Q. Zhu and K. Shoele, "Propulsion performance of a skeleton-stregthened fin", *Journal of Experimental Biology*, vol. 211, pp. 2087–2100, 10 2008. DOI: https://doi.org/10.1242/jeb.016279.

[94] Y. Luo, Q. Xiao, G. Shi, L. Wen, D. Chen, and G. Pan, "A fluid-structure interaction solver for the study on a passively deformed fish fin with non-uniformly distributed stiffness", *Journal of Fluids and Structures*, vol. 92, p. 102 778, 2020. DOI: https://doi.org/10.1016/j.jfluidstructs.2019.102778.

[95] A. Ducoin and Y. L. Young, "Hydroelastic response and stability of a hydrofoil in viscous flow", *Journal of Fluids and Structures*, vol. 38, pp. 40–57, 2013. DOI: https://doi.org/10.1016/j.jfluidstructs.2012.12.011.

[96] T. L. Daniel and S. A. Combes, "Flexible wings and fins: Bending by inertial or fluid-dynamic forces?", *Integr. Comp. Biol.*, vol. 42, pp. 1044–1049, 2002. DOI: https://doi.org/10.1093/icb/42.5.1044.

[97] H. Dai, H. Luo, P. J. S. A. F. de Sousa, and J. F. Doyle, "Thrust performance of a flexible low-aspect-ratio pitching plate", *Physics of Fluids*, vol. 24, p. 101 903, 2012. DOI: https://doi.org/10.1063/1.4764047.

[98] Y. Liao, N. Garg, J. R. Martins, and Y. L. Young, "Viscous fluid-structure interaction response of composite hydrofoils", *Composite structures*, vol. 212, pp. 571–585, 2019. DOI: https://doi.org/10.1016/j.compstruct.2019.01.043.

[99] L. Wang, Z. Fang, R.-N. Hua, and Z.-R. Peng, "Numerical simulations of an inverted flexible plate in linear shear flow", *Physics of Fluids*, vol. 32, p. 043 104, 2020. DOI: https://doi.org/10.1063/1.5144982.

[100] D. J. Willis, E. R. Israeli, P.-O. Persson, M. D. J. Peraire, S. M. Swartzk, and K. S. Breuer, "A computational framework for fluid structure interaction in biologically inspired flapping flight", *Session: APA-1: Aerodynamics and Structural Dynamics Interaction*, 2007. DOI: https://doi.org/10.2514/6.2007-3803.

[101] N. Garg, G. K. Kenway, J. R. Martins, and Y. L. Young, "High-fidelity multipoint hydrostructural optimization of a 3-d hydrofoil", *Journal of Fluids and Structures*, vol. 71, pp. 15–39, 2017. DOI: https://doi.org/10.1016/j.jfluidstructs.2017.02.001.

[102] N. Garg, B. W. Pearce, P. A. Brandner, A. W. Phillips, J. R. Martins, and Y. L. Young, "Experimental investigation of a hydrofoil designed via hydrostructural optimization", *Journal of Fluids and Structures*, vol. 84, pp. 243–262, 2019. DOI: https://doi.org/10.1016/j.jfluidstructs.2018.10.010.

[103] Y. Liao, J. R. Martins, and Y. L. Young, "3-d high-fidelity hydrostructural optimization of cavitation-free composite lifting surfaces", *Journal of Fluids and Structures*, vol. 268, p. 113 937, 2021. DOI: https://doi.org/10.1016/j.compstruct.2021.113937.

[104] J. Franc and J. Michel, *Fundamentals of Cavitation*. Springer, Dordrecht, 2006, ISBN: 978-1-4020-2233-3. DOI: https://doi.org/10.1007/1-4020-2233-6.

[105] J. Carlton, *Marine Propellers and Propulsion*. Butterworth-Heinemann, 2018, ISBN: 9780081003664.

[106] E. Foeth, C. v. Doorne, T. v. Terwisga, and B. Wieneke, "Time resolved piv and flow visualization of 3d sheet cavitation", *Exp. Fluids*, vol. 40, 503–513, 2006. DOI: https://doi.org/10.1007/s00348-005-0082-9.

[107] J. Leroux, O. Coutier-Delgosha, and J. Astolfi, "A joint experimental and numerical study of mechanisms associated to instability of partial cavitation on two-dimensional hydrofoil", *Phys. Fluids*, vol. 17, p. 052 101, 2005. DOI: https://doi.org/10.1063/1.1865692.

[108] S. Seyfi and N. Nouri, "Experimental studies of hysteresis behavior of partial cavitation around naca0015 hydrofoil", *Ocean Eng.*, vol. 217, p. 107 482, 2020. DOI: https://doi.org/10.1016/j.oceaneng.2020.107482.

[109] Z. Mengjie, H. Biao, Q. Zhongdong, *et al.*, "Cavitating flow structures and corresponding hydrodynamics of a transient pitching hydrofoil in different cavitation regimes", *Int. J. Multiph. Flow*, vol. 132, p. 103 408, 2020. DOI: https://doi.org/10.1016/j.ijmultiphaseflow.2020.103408.

[110] S. Phoemsapthaweea, J. Leroux, S. Kerampranb, and J. Laurens, "Implementation of a transpiration velocity based cavitation model within a ranse solver", *Eur. J. Mech. B Fluids*, vol. 32, 45–51, 2011. DOI: https://doi.org/10.1016/j.euromechflu.2011.11.001.

[111] E. Kadivar, O. Moctar, and K. Javadi, "Investigation of the effect of cavitation passive control on the dynamics of unsteady cloud cavitation", *Appl. Math. Model.*, vol. 64, 333–356, 2018. DOI: https://doi.org/10.1016/j.apm.2018.07.015.

[112] A. Movahedian, M. Pasandidehfard, and E. Roohi, "Les investigation of sheet-cloud cavitation around a 3-d twisted wing with a naca 16012 hydrofoil", *Ocean Eng.*, vol. 192, p. 106 547, 2019. DOI: https://doi.org/10.1016/j.oceaneng.2019.106547.

[113] J. Liu, J. Yu, Z. Yang, *et al.*, "Numerical investigation of shedding dynamics of cloud cavitation around 3d hydrofoil using different turbulence models", *Eur. J. Mech. B Fluids*, vol. 85, 232–244, 2021. DOI: https://doi.org/10.1016/j.euromechflu.2020.09.016.

[114] L. Bonfiglioa, P. Perdikaris, S. Brizzolara, and G. Karniadakis, "Multi-fidelity optimization of super-cavitating hydrofoils", *Comput. Methods Appl. Mech. Eng.*, vol. 332, 63–85, 2017. DOI: https://doi.org/10.1016/j.cma.2017.12.009.

[115] S. Kim and S. Kinnas, "Prediction of unsteady developed tip vortex cavitation and its effects on the induced hull pressures", *J. Mar. Sci. Eng.*, vol. 8, p. 114, 2020. DOI: https://doi.org/10.3390/jmse8020114.

[116] H. Cheng, X. Long, B. Ji, X. Peng, and M. Farhat, "A new euler-lagrangian cavitation model for tip-vortex cavitation with the effect of non-condensable gas", *Int. J. Multiph. Flow*, vol. 134, p. 103 441, 2021. DOI: https://doi.org/10.1016/j.ijmultiphaseflow.2020.103441.

[117] B. Ji, X. Luo, R. Arndt, X. Peng, and Y. Wu, "Large eddy simulation and theoretical investigations of the transient cavitating vortical flow structure around a naca66 hydrofoil", *Int. J. Multiph. Flow*, vol. 68, 121–134, 2015. DOI: https://doi.org/10.1016/j.ijmultiphaseflow.2014.10.008.

[118] Z. Z. Wang, H. H. Cheng, and B. J. J., "Euler–lagrange study of cavitating turbulent flow around a hydrofoil", *Physics of Fluids*, vol. 33, p. 112 108, 2021. DOI: https://doi.org/10.1063/5.0070312.

[119] B. Yoon and Y. Semenov, "Cavity detachment on a hydrofoil with the inclusion of surface tension effects", *Eur. J. Mech. B Fluids*, vol. 30, 17–25, 2011. DOI: https://doi.org/10.1016/j.euromechflu.2010.10.002.

[120] C. Pellone and T. Maitre, "Partially cavitating hydrofoils: Experimental and numerical analysis", *J. Ship Res.*, vol. 44, 40–58, 2000. DOI: https://doi.org/10.5957/jsr.2000.44.1.40.

[121] S. Bal, S. Kinnas, and H. Lee, "Numerical analysis of 2-d and 3-d cavitating hydrofoils under a free surface", *J. Ship Res*, vol. 45, 34–49, 2001. DOI: https://doi.org/10.5957/jsr.2001.45.1.34.

[122] F. Celik, Y. Ozden, and S. Bal, "Numerical simulation of the flow around two-dimensional partially cavitating hydrofoil", *J. Mar. Sci. Appl.*, vol. 13, 245–254, 2014. DOI: https://doi.org/10.1007/s11804-014-1254-x.

[123] Y. Lee, C. Yang, and Y. Chow, "Evaluations of the outcome variability of rans simulations for marine propellers due to tunable parameters of cavitation models", *Ocean Eng.*, vol. 226, p. 108 805, 2021. DOI: https://doi.org/10.1016/j.oceaneng.2021.108805.

[124] S. Alavi, H. Haddadpour, and R. Firouz-Abadi, "Hydroelastic analysis of two degree of freedom hydrofoil using a reduced-order hydrodynamic model considering unsteady partial sheet cavity flows", *J. Fluids Struct.*, vol. 81, 116–130, 2018. DOI: https://doi.org/10.1016/j.jfluidstructs.2018.04.023.

[125] E. D'Amato, I. Notaro, V. Piscopo, and A. Scamardella, "Hydrodynamic design of fixed hydrofoils for planing craft", *Journal of Marine Science and Engineering*, vol. 11, no. 2, 2023. DOI: https://doi.org/10.3390/jmse11020246.

[126] D. Ntouras, G. Papadakis, and K. Belibassakis, "Ship bow wings with application to trim and resistance control in calm water and in waves", *Ocean Engineering*, vol. 10, p. 492, 4 2022. DOI: https://doi.org/10.3390/jmse10040492.

[127] J. H. Duncan, "The breaking and non-breaking wave resistance of a two-dimensional", *Journal of Fluid Mechanics*, vol. 126, no. 01, 507–520, 1983. DOI: https://doi.org/10.1017/S0022112083000294.

[128] O. Barannyk, B. J. Buckham, and P. Oshkai, "On performance of an oscillating plate underwater propulsion system with variable chordwise flexibility at different depths of submergence", *Journal of Fluids and Structures*, vol. 28, pp. 152–166, 2012. DOI: https://doi.org/10.1016/j.jfluidstructs.2011.10.005.

[129] E. Filippas and K. Belibassakis, "Hydrodynamic analysis of flapping-foil thrusters operating beneath the free surface and in waves", *Engineering Analysis with Boundary Elements*, vol. 41, pp. 47–59, 2014. DOI: https://doi.org/10.1016/j.enganabound.2014.01.008.

[130] Z.-M. Chen, "A vortex based panel method for potential flow simulation around a hydrofoil", *Journal of Fluids and Structures*, vol. 28, pp. 378–391, 2012. DOI: https://doi.org/10.1016/j.jfluidstructs.2011.10.003.

[131] L. Pernod, M. Sacher, J. Wackers, B. Augier, and P. Bot, "Free-surface effects on two-dimensional hydrofoils by rans-vof simulations", *Journal of Sailing Technology*, vol. 8, no. 01, pp. 24–38, 2023. DOI: https://doi.org/10.5957/jst/2023.8.2.24.

[132] N. Petikidis and G. Papadakis, "Investigation of submergence depth and wave-induced effects on the performance of a fully passive energy harvesting flapping foil operating beneath the free surface", *Journal of Marine Science and Engineering*, vol. 11, no. 8, 2023. DOI: https://doi.org/10.3390/jmse11081559.

[133] M. Jin, C. Ha, and W. Park, "Numerical study of ventilated cavitating flows with free surface effects", *J. Mech. Sci. Technol.*, vol. 27, 3683–3691, 2013. DOI: https://doi.org/10.1007/s12206-013-0914-0.

[134] P. Wu and J. Chen, "Numerical study on cavitating flow due to a hydrofoil near a free surface", *J. Ocean Eng. Sci.*, vol. 1, 238–245, 2016. DOI: https://doi.org/10.1016/j.joes.2016.02.002.

[135] T. Sun, Q. Xie, X. Li, and L. Zou, "Numerical investigation of the effects of free surface on tip-leakage vortex cavitation behaviors over a naca0009 hydrofoil", *Int. J. Multiph. Flow*, vol. 141, p. 103 671, 2021. DOI: https://doi.org/10.1016/j.ijmultiphaseflow.2021.103671.

[136] O. Faltinsen and Y. Semenov, "The effect of gravity and cavitation on a hydrofoil near the free surface", *Journal of Fluid Mechanics*, vol. 597, 371–394, 2008. DOI: https://doi.org/10.1017/S0022112007009822.

[137] C. de Boor, *A Practical Guide to Splines*. Springer, New York, 1978, ISBN: 978-0-387-95366-3.

[138] D. Thévenin and G. Janiga, *Optimization and Computational Fluid Dynamics*. Springer Berlin, Heidelberg, 2008. DOI: https://doi.org/10.1007/978-3-540-72153-6.

[139] A. Joodaki and A. Ashrafizadeh, "Surface shape design in fluid flow problems via hybrid optimization algorithms", *Aerospace Science and Technology*, vol. 39, pp. 639–651, 2014. DOI: https://doi.org/10.1016/j.ast.2014.06.012.

[140] H. Lim and H. Kim, "Multi-objective airfoil shape optimization using an adaptive hybrid evolutionary algorithm", *Aerospace Science and Technology*, vol. 87, pp. 141–153, 2019. DOI: https://doi.org/10.1016/j.ast.2019.02.016.

[141] A. Papanikolaou, "Holistic ship design optimization", *Computer-Aided Design*, vol. 42, no. 11, pp. 1028–1044, 2010, Computer aided ship design: Some recent results and steps ahead in theory, methodology and practice. DOI: https://doi.org/10.1016/j.cad.2009.07.002.

[142] L. Nikolopoulos and E. Boulougouris, "A novel method for the holistic, simulation driven ship design optimization under uncertainty in the big data era", *Ocean Engineering*, vol. 218, p. 107 634, 2020. DOI: https://doi.org/10.1016/j.oceaneng.2020.107634.

[143] A. Papanikolaou, *Ship Design - Methodologies of Preliminary Design*. Sep. 2014, ISBN: 978-94-017-8750-5. DOI: https://doi.org/10.1007/978-94-017-8751-2.

[144] K. Mizzi, Y. K. Demirel, C. Banks, O. Turan, P. Kaklis, and M. Atlar, "Design optimisation of propeller boss cap fins for enhanced propeller performance", *Applied Ocean Research*, vol. 62, pp. 210–222, 2017. DOI: https://doi.org/10.1016/j.apor.2016.12.006.

[145] K. Kostas, A. Ginnis, C. Politis, and P. Kaklis, "Shape-optimization of 2d hydrofoils using an isogeometric bem solver", *Computer-Aided Design*, vol. 82, pp. 79–87, 2017. DOI: https://doi.org/10.1016/j.cad.2016.07.002.

[146] Z. Masood, K. V. Kostas, S. Khan, and P. D. Kaklis, "Shape-informed dimensional reduction in airfoil/hydrofoil modeling", *Journal of Marine Science and Engineering*, vol. 11, no. 10, 2023. DOI: https://doi.org/10.3390/jmse11101851.

[147] O. Pironneau, *Optimal Shape Design For Elliptic Systems*. Springer-Verlag, 1984, ISBN: 978-3-642-87724-7. DOI: https://doi.org/10.1007/978-3-642-87722-3.

[148] E. Papoutsis-Kiachagias, S. Kyriacou, and K. Giannakoglou, "The continuous adjoint method for the design of hydraulic turbomachines", *Comput. Methods Appl. Mech. Eng.*, vol. 278, 621–639, 2014. DOI: https://doi.org/10.1016/j.cma.2014.05.018.

[149] A. N. Sloss and S. Gustafson, "Genetic programming theory and practice xvii: 2019 evolutionary algorithms review", in Springer International Publishing, 2020, pp. 307–344, ISBN: 978-3-030-39958-0. DOI: https://doi.org/10.1007/978-3-030-39958-0_16.

[150] K. Giannakoglou, "Design of optimal aerodynamic shapes using stochastic optimization methods and computational intelligence", *Progress in Aerospace Sciences*, vol. 38, no. 1, pp. 43–76, 2002. DOI: https://doi.org/10.1016/S0376-0421(01)00019-7.

[151] V. Asouti, M. Kontou, and K. Giannakoglou, "Radial basis function surrogates for uncertainty quantification and aerodynamic shape optimization under uncertainties", *Fluids*, vol. 8, no. 11, 2023. DOI: https://doi.org/10.3390/fluids8110292.

[152] I. Kampolis, A. Zymaris, V. G. Asouti, and K. Giannakoglou, "Multilevel optimization strategies based on metamodel-assisted evolutionary algorithms, for computationally expensive problems", in *2007 IEEE Congress on Evolutionary Computation*, 2007, pp. 4116–4123. DOI: https://doi.org/10.1109/CEC.2007.4425008.

[153] V. G. A. Stylianos A. Kyriacou and K. C. Giannakoglou, "Efficient pca-driven eas and metamodel-assisted eas, with applications in turbomachinery", *Engineering Optimization*, vol. 46, no. 7, pp. 895–911, 2014. DOI: https://doi.org/10.1080/0305215X.2013.812726.

[154] M. Sacher, M. Durand, Élisa Berrini, *et al.*, "Flexible hydrofoil optimization for the 35th america's cup with constrained ego method", *Ocean Engineering*, vol. 157, pp. 62–72, 2018. DOI: https://doi.org/10.1016/j.oceaneng.2018.03.047.

[155] D. Anevlavi, S. Zafiris, G. Papadakis, and K. Belibassakis, "Efficiency enhancement of marine propellers via reformation of blade tip-rake distribution", *Journal of Marine Science and Engineering*, vol. 11, no. 11, 2023. DOI: https://doi.org/10.3390/jmse11112179.

[156] D. Ntouras and G. Papadakis, "A coupled artificial compressibility method for free surface flows", *Journal of Marine Science and Engineering*, vol. 8, no. 8, 2020. DOI: https://doi.org/10.3390/jmse8080590.

[157] A. Karperaki, *Hydroelastic interaction between ocean waves and large floating structures in the inhomogeneous ocean environment*. National Technical University of Athens, 2021. DOI: http://dx.doi.org/10.26240/heal.ntua.20888. [Online]. Available: https://dspace.lib.ntua.gr/xmlui/handle/123456789/53190.

[158] D. Anevlavi and K. Belibassakis, "Analysis of partially cavitating hydrofoils under the free surface using bem-based adjoint optimization", *Applied Mathematical Modelling*, vol. 112, pp. 415–435, 2022. DOI: https://doi.org/10.1016/j.apm.2022.07.033.

[159] S. Barbarino, O. Bilgen, R. M. Ajaj, M. I. Friswell, and D. J. Inman, "A review of morphing aircraft", *Journal of Intelligent Material Systems*, vol. 22, no. 9, 823–877, 2011. DOI: https://doi.org/10.1177/1045389X11414084.

[160] D. Li, S. Zhao, A. Da Ronch, *et al.*, "A review of modelling and analysis of morphing wings", *Progress in Aerospace Sciences*, vol. 100, pp. 46–62, 2018. DOI: https://doi.org/10.1016/j.paerosci.2018.06.002.

[161] T. Kumar, S. Venugopal, B. Ramakrishnananda, and S. Vijay, "Aerodynamic performance estimation of camber morphing airfoils for small unmanned aerial vehicle", *J. Aerosp. Technol. Manag.*, vol. 12, e1420, 12 2020. DOI: https://doi.org/10.5028/jatm.v12.1094.

[162] F. Hao, T. Tang, Y. Gao, Y. Li, S. Yi, and J. Lu, "Continuous morphing trailing-edge wing concept based on multi-stable nanomaterial", *Chinese Journal of Aeronautics*, vol. 34, pp. 219–231, 7 2021. DOI: https://doi.org/10.1016/j.cja.2020.03.041.

[163] J. Zhang, A. Shaw, C. Wang, *et al.*, "Aeroelastic model and analysis of an active camber morphing wing", *Aerospace Science and Technology*, vol. 111, p. 106 534, 2021. DOI: https://doi.org/10.1016/j.ast.2021.106534.

[164] S. Vasista, A. D. Gaspari, S. Ricci, J. Riemenschneider, H. P. Monner, and B. van de Kamp, "Compliant structures-based wing and wingtip morphing devices", *Aircraft Engineering and Aerospace Technology*, vol. 88, 311–330, 2 2016. DOI: https://doi.org/10.1108/AEAT-02-2015-0067.

[165] SKF, *Retractable fin stabilizers type s. compact and proven design for roll reduction*, https://www.skf.com/group/industries/marine/stabilizing-systems-and-steering-gear/retractable-fin-stabilizers-type-s, Online; accessed 3 March 2014, 2016.

[166] Mitsubishi, *Fin stabilizers from mhi-mme are reliable, durable, and provide an excellent handling performance under all conditions.* https://www.mhi.com/products/ship/finstabilizer.html, Online; accessed 3 March 2014, 2023.

[167] N. Parolini and A. Quarteroni, "Mathematical models and numerical simulations for the america's cup", *Comput. Methods Appl. Mech. Engrg*, vol. 194, pp. 1001–1026, 2005. DOI: https://doi.org/10.1016/j.cma.2004.06.020.

[168] C. Amoroso, A. Liverani, D. Francia, and A. Ceruti, "Dynamics augmentation for high speed flying yacht hulls through pid control of foiling appendages", *Ocean Engineering*, vol. 221, p. 108 115, 2021. DOI: https://doi.org/10.1016/j.oceaneng.2020.108115.

[169] N. S. S. Prabahar, A. Persson, and L. Larsson, "Split-flaps – a way to improve the heel stability of t-foil supported craft", *Journal of Sailing Technology*, vol. 7, no. 01, pp. 1–30, 2022. DOI: https://doi.org/10.5957/jst/2022.7.1.1.

[170] B. K. Stanford and P. S. Beran, "Analytical sensitivity analysis of an unsteady vortex-lattice method for flapping-wing optimization", *Journal of Aircraft*, vol. 47, pp. 647–662, 2 2010. DOI: https://doi.org/10.2514/1.46259.

[171] Y. Li, Z. Pan, and N. Zhang, "Propulsive properties of a flexible oscillating wing with time-varying camber deformation", *Ocean Engineering*, vol. 235, p. 109 332, 2011. DOI: https://doi.org/10.1016/j.oceaneng.2021.109332.

[172] "A gpu-accelerated 3dbem supporting the optimization of actively morphing flapping-foil thrusters with application to auv propulsion",

[173] M. F. Neef and D. Hummel, "Euler and navier-stokes solutions for flapping wing propulsion", *E. Krause et al. (eds.), High Performance Computing in Science and Engineering '01*, 386–395, 2002. DOI: https://doi.org/10.1007/978-3-642-56034-7_37.

[174] G. Papadakis, E. Filippas, D. Ntouras, and K. Belibassakis, "Effects of viscosity and nonlinearity on 3d flapping-foil thruster for marine applications", *OCEANS 2019, Marseille*, pp. 1–10, DOI: https://doi.org/10.1109/OCEANSE.2019.8867084.

[175] E. Filippas, G. Papadakis, and K. Belibassakis, "Free-surface effects on the performance of flapping-foil thruster for augmenting ship propulsion in waves", *Journal of Marine Science and Engineering*, vol. 8, no. 5, p. 357, 2020. DOI: https://doi.org/10.3390/jmse8050357.

[176] M. Ghommem, M. R. Hajj, D. T. Mook, *et al.*, "Global optimization of actively morphing flapping wings", *Journal of Fluids and Structures*, vol. 33, 210–228, 2012. DOI: https://doi.org/10.1016/j.jfluidstructs.2012.04.013.

[177] D. Anevlavi, E. Filippas, A. Karperaki, and K. Belibassakis, "A non-linear bem–fem coupled scheme for the performance of flexible flapping-foil thrusters", *Journal of Marine Science and Engineering*, vol. 8, no. 1, p. 56, 2020. DOI: https://doi.org/10.3390/jmse8010056.

[178] I. Fejtek and J. Nehera, "Technical note: Experimental study of flapping wing lift and propulsion.", *The Aeronautical Journal*, vol. 84, no. 829, pp. 28–33, 1980. DOI: https://doi.org/10.1017/S0001924000030463.

[179] T. Lin, W. Xia, R. Pecora, K. Wang, and S. Hu, "Performance improvement of flapping propulsions from spanwise bending on a low-aspect-ratio foil", *Ocean Engineering*, vol. 284, p. 115 305, 2023. DOI: https://doi.org/10.1016/j.oceaneng.2023.115305.

[180] S. Heathcote, Z. Wang, and I. Gursul, "Effect of spanwise flexibility on flapping wing propulsion", *Journal of Fluids and Structures*, vol. 24, no. 2, pp. 183–199, 2008. DOI: https://doi.org/10.1016/j.jfluidstructs.2007.08.003.

[181] M. S. Vest and J. Katz, "Unsteady aerodynamic model of flapping wings", *AIAA*, vol. 34, no. 7, pp. 1435–1440, 1996. DOI: https://doi.org/10.2514/3.13250.

[182] J. Neira, C. Sequeiros, R. Huamani, E. Machaca, P. Fonseca, and W. Nina, "Review on unmanned underwater robotics, structure designs, materials, sensors, actuators, and navigation control", *Journal of Robotics*, vol. 2021, 2021. DOI: https://doi.org/10.1155/2021/5542920.

[183] A. Priovolos, E. Filippas, and K. Belibassakis, "A vortex-based method for improved flexible flapping-foil thruster performance", *Engineering Analysis with Boundary Elements*, vol. 95, pp. 69–84, 2018. DOI: https://doi.org/10.1016/j.enganabound.2018.06.016.

[184] Y. Liao, J. R. Martins, and Y. L. Young, "3-d high-fidelity hydrostructural optimization of cavitation-free composite lifting surfaces", *Composite Structures*, vol. 268, p. 113 937, 2021. DOI: https://doi.org/10.1016/j.compstruct.2021.113937.

[185] V. A. Riziotis and S. G. Voutsinas, "Dynamic stall modelling on airfoils based on strong viscous–inviscid interaction coupling", *International Journal for Numerical Methods in Fluids*, vol. 56, no. 2, pp. 185–208, 2008. DOI: https://doi.org/10.1002/fld.1525.

[186] G. Tortora, A. Concilio, and R. Pecora, "Airfoil shape morphing through a novel parameterization and fitting optimization method based on uniform non-rational b-spline functions", *Designs*, vol. 7, no. 1, 2023. DOI: 10.3390/designs7010028.

[187] C. Wang, J. Reddy, and K. Lee, *Shear Deformable Beams and Plates. Relationships with Practical Solutions*. Elsevier, 2000, ISBN: 9780080437842.

[188] S. Timoshenko and S. Woinowsky-Krieger, *Theory of Plates and Shells*. McGraw-Hill, 1959, ISBN: 0-07-064779-8.

[189] J. Reddy, *Theory and Analysis of Elastic Plates and Shells*. CRC Press, 2007, ISBN: 0-8493-8415-X.

[190] J.-L. Batoz and P. Lardeur, "A discrete shear triangular nine d.o.f. element for the analysis of thick to very thin plates", *International Journal for Numerical Methods in Engineering*, vol. 28, pp. 533–560, 3 1989. DOI: https://doi.org/10.1002/nme.1620280305.

[191] J. N. Reddy, *Mechanics of Laminated Composite Plates and Shells. Theory and Analysis*. CRC Press, 2004, ISBN: 0-8493-1592-1.

[192] O. Zienkiewicz and R. Taylor, *The Finite Element Method for Solid and Structural Mechanics*. Elsevier, 2014, ISBN: 978-1-85617-634-7. DOI: https://doi.org/10.1016/C2009-0-26332-X.

[193] T. J. R. Hughes, *The Finite Element Method. Linear Static and Dynamic Finite Element Analysis*. Prentice-Hall Inc., 1987, ISBN: 0-13-317025-X.

[194] Y. Fung and P. Tong, *Classical and Computational Solid Mechanics*. World Scientific, 2001, ISBN: 981-02-3912-2.

[195] J.-L. Batoz, K. Bathe, and L. Ho, "A study of three-node triangular plate bending elements", *International Journal for Numerical Methods in Engineering*, vol. 15, pp. 1771–1812, 1980. DOI: https://doi.org/10.1002/nme.1620151205.

[196] R. Sydenstricker, A. Coutinho, and L. Landau, "Pseudoconsistent load vector and mass matrix for the discrete kirchhoff triangle and the discrete shear triangle elements", *Communications in numerical methods in engineering*, vol. 11, pp. 317–330, 4 1995. DOI: https://doi.org/10.1002/cnm.1640110405.

[197] K. Kalita and S. Haldar, "Natural frequencies of rectangular plate with- and without-rotary inertia", *J. Inst. Eng. India Ser. C*, vol. 99, 539–555, 2018. DOI: https://doi.org/10.1007/s40032-016-0327-9.

[198] K.-J. Bathe, *Finite Element Procedures*. Prentice Hall, 1996, ISBN: 0-13-301458-4.

[199] D. Shepard, "A two-dimensional interpolation function for irregularly-spaced data", *ACM '68: Proceedings of the 1968 23rd ACM national conference*, pp. 517–524, 1968. DOI: https://doi.org/10.1145/800186.810616.

[200] I. Chowdhury and S. Dasgupta, "Computation of rayleigh damping coefficients for structures with large degrees of freedom", *Electronic Journal of Geotechnical Engineering*, vol. Volume 8, Apr. 2003.

[201] A. W. Leissa, "The free vibration of rectangular plates", *Journal of Sound and Vibration*, vol. 31, pp. 257–293, 3 1973. DOI: https://doi.org/10.1016/S0022-460X(73)80371-2.

[202] J. T. Katsikadelis and E. J. Sapountzakis, "A bem solution to dynamic analysis of plates with variable thickness", *Computational Mechanics*, vol. 7, pp. 369–379, 1991. DOI: https://doi.org/10.1007/BF00350166.

[203] J. R. Kuttler and V. G. Sigillito, "Vibrational frequencies of clamped plates of variable thickness", *Journal of Sound and Vibration*, vol. 86, pp. 181–189, 2 1983. DOI: https://doi.org/10.1016/0022-460X(83)90747-2.

[204] I. Shufrin and M. Eisenberger, "Vibration of shear deformable plates with variable thickness — first-order and higher-order analyses", *Journal of Sound and Vibration*, vol. 290, pp. 465–489, 2006. DOI: https://doi.org/10.1016/j.jsv.2005.04.003.

[205] J.-L. Batoz and I. Katili, "On a simple triangular reissner/mindlin plate element based on incompatible modes and discrete constraints", *International Journal for Numerical Methods in Engineering*, vol. 35, pp. 1603–1632, 8 1992. DOI: https://doi.org/10.1002/nme.1620350805.

[206] N. Garg, G. Kenway, J. R. Martins, and Y. Young, "High-fidelity multipoint hydrostructural optimization of a 3-d hydrofoil", *Journal of Fluids and Structures*, vol. 71, pp. 15–39, 2017. DOI: https://doi.org/10.1016/j.jfluidstructs.2017.02.001.

[207] G. A. Zarruk, P. A. Brandner, B. W. Pearce, and A. W. Phillips, "Experimental study of the steady fluid–structure interaction of flexible hydrofoils", *Journal of Fluids and Structures*, vol. 51, pp. 326–343, 2014. DOI: https://doi.org/10.1016/j.jfluidstructs.2014.09.009.

[208] P. Brandner and B. Pearce, "Experimental modelling of steady hydrofoil fluid-structure interaction", in *18th Australasian Fluid Mechanics Conference*, Australian Maritime College, 2012. DOI: https://hdl.handle.net/102.100.100/525420.

[209] P. Vecchia, E. Daniele, and E. D'Amato, "An airfoil shape optimization technique coupling parsec parameterization and evolutionary algorithm", *Aerospace Science and Technology*, vol. 32, no. 1, pp. 103–110, 2012. DOI: https://doi.org/10.1016/j.ast.2013.11.006.

[210] T. Spenke, N. Hosters, and M. Behr, "A multi-vector interface quasi-newton method with linear complexity for partitioned fluid–structure interaction", *Computer Methods in Applied Mechanics and Engineering*, vol. 361, p. 112 810, 2020, ISSN: 0045-7825. DOI: https://doi.org/10.1016/j.cma.2019.112810.

[211] M. Lauber, G. D. Weymouth, and G. Limbert, "Immersed-boundary fluid-structure interaction of membranes and shells", *XII International Conference on Structural Dynamics (EuroDyn)*, 2023. DOI: https://doi.org/10.48550/arXiv.2308.06494.

[212] D. Anevlavi and K. Belibassakis, "An adjoint optimization prediction method for partially cavitating hydrofoils", *J. Mar. Sci. Eng.*, vol. 9, p. 976, 2021. DOI: https://doi.org/10.3390/jmse9090976.

[213] M. Behbahani-Nejad and M. Changizian, "A fast non-iterative numerical algorithm to predict unsteady partial cavitation on hydrofoils", *Appl. Math. Model.*, vol. 37, 6446–6457, 2013. DOI: https://doi.org/10.1016/j.apm.2013.01.034.

[214] J. Uhlman, "The surface singularity method applied to partially cavitating hydrofoils", *J. Ship Res.*, vol. 31, 107–124, 1987. DOI: https://doi.org/10.5957/jsr.1987.31.2.107.

[215] J. Choi, R. Penmetsa, and R. Grandhi, "Shape optimization of the cavitator for a super-cavitating torpedo", *Struct. Multidiscip. Optim.*, vol. 29, 159–167, 2005. DOI: https://doi.org/10.1007/s00158-004-0466-0.

[216] A. R. H. Lemonnier, "Another approach in modelling cavitating flows", *J. Fluid Mech.*, vol. 195, 557–580, 1988. DOI: https://doi.org/10.1017/S0022112088002526.

[217] R. Yeung, "Numerical methods in free-surface flows", *Annu. Rev. Fluid Mech.*, vol. 14, 395–442, 1982. DOI: https://doi.org/10.1146/annurev.fl.14.010182.002143.

[218] P. D. Sclavounos, "Panel methods for free surface flows", in *Boundary Integral Methods*, Berlin, Heidelberg: Springer Berlin Heidelberg, 1991, pp. 450–459, ISBN: 978-3-642-85463-7.

[219] W. Tsai, "Computation of nonlinear free-surface flows", *Annu. Rev. Fluid. Mech*, vol. 28, 249–278, 1996. DOI: https://doi.org/10.1146/annurev.fl.28.010196.001341.

[220] H. Yoon, P. Hung, J. Jung, and M. Kim, "Effect of wavy leading edge on hydrodynamic characteristics for flow around low aspect ratio wing", *Computers & Fluids*, vol. 494, pp. 276–289, 2011. DOI: https://doi.org/10.1016/j.compfluid.2011.06.010.

[221] D. Boger and E. Paterson, "A continuous adjoint approach to design optimization in cavitating flow using a barotropic model", *Comput. Fluids*, vol. 101, 155–169, 2014. DOI: https://doi.org/10.1016/j.compfluid.2014.06.014.

[222] P. Vrionis, K. Samouchos, and K. Giannakoglou, "The continuous adjoint cut-cell method for shape optimization in cavitating flows", *Comput. Fluids*, vol. 224, p. 104 974, 2021. DOI: https://doi.org/10.1016/j.compfluid.2021.104974.

[223] F. Morlando, "Adjoint-based sensitivity analysis by panel methods and cas", *Optim. Lett.*, vol. 11, 739–752, 2017. DOI: https://doi.org/10.1007/s11590-016-1042-4.

[224] D. Papadimitriou and K. Giannakolgou, "A continuous adjoint method with objective function derivatives based on boundary integrals", *Comput. Fluids*, vol. 36, 325–341, 2007. DOI: https://doi.org/10.1016/j.compfluid.2005.11.006.

[225] T. Hughes, J. Cottrell, and Y Bazilevs, "Isogeometric analysi: Cad, finite elements, nurbs, exact geometry and mesh refinement", *Comput. Methods Appl. Mech. Eng.*, vol. 194, 4135–4195, 2005. DOI: https://doi.org/10.1016/j.cma.2004.10.008.

[226] T. Melin, *Parametric Airfoil Cataloge, Part I-II An Aerodynamic and Geometric Comparison Between Parametrized and Point Cloud Airfoils*. Linköping University, 2013, ISBN: 978-91-7519-656-5.

[227] P. He, G. Filip, J. Martins, and K. Maki, "Design optimization for self-propulsion of a bulk carrier using a discrete adjoint method", *Comput. Fluids*, vol. 192, 104–259, 2019. DOI: https://doi.org/10.1016/j.compfluid.2019.104259.

[228] D. Dawson, "A practical computer method for solving ship-wave problems, in: Proceedings of the 2nd international conference on numerical ship hydrodynamics", 1977.

[229] N. Kuznetsov, V. Maz'ya, and B. Vainberg, *Linear Water Waves: A Mathematical Approach*. Cambridge University Press, United Kingdom, 2002, ISBN: 9780511546778.

[230] R. Yeung and Y. Bouger, "A hybrid integral-equation method for steady two-dimensional ship waves", *Int. J. Numer. Methods Eng.*, vol. 14, 317–336, 1979. DOI: https://doi.org/10.1002/nme.1620140303.

[231] J. Giesing and A. Smith, "Potential flow about two-dimensional hydrofoils", *J. Fluid Mech.*, vol. 28, 113–129, 1967. DOI: https://doi.org/10.1017/S0022112067001934.

Appendix A

Iso-parametric 4-node Quadrilateral Element

The generic bilinear quadrilateral element is defined in the local coordinate system (ξ, η), bounded in $[-1, 1] \times [-1, 1]$, as shown in Figure **??**. Using an isoparametric transformation, the edges of the element are transformed to the 3D surface element with $\mathbf{x} \in E$,

$$\mathbf{x}(\xi, \eta) = \sum_{n=1}^{4} \mathbf{x}_n N_n(\xi, \eta), \tag{A.1}$$

where $\mathbf{x} = (x, y, z)$ denotes the Cartesian coordinates in the global coordinate system of a point with local coordinates (ξ, η) and $\mathbf{x}_n$ are the global coordinates of the element's corner nodes, see also the numbering scheme in Figure A.1.

Each one of these functions is connected to a single node, describing a curved surface (or 'hyper-surface'), comprising of four straight-line edges defined along the $\xi-$ and $\eta-$directions. The shape functions are expressed compactly as,

$$N_n = \frac{1}{2}(1 + \xi_n \xi)\frac{1}{2}(1 + \eta_n \eta), \tag{A.2}$$

where (ξ_n, η_n) are the local coordinates of each corner node shown in Figure A.1. The shape functions are depicted in Figure A.2. The individual shape function for each node, with respect to the numbering is,

$$N_1 = \frac{1}{4}(1 - \xi)(1 - \eta), \tag{A.3}$$

$$N_2 = \frac{1}{4}(1 + \xi)(1 - \eta), \tag{A.4}$$

$$N_3 = \frac{1}{4}(1 + \xi)(1 + \eta), \tag{A.5}$$

$$N_4 = \frac{1}{4}(1 - \xi)(1 + \eta). \tag{A.6}$$

The centroid c_o and the tangent vectors along the ξ,η directions are evaluated respectively using the following expressions,

$$c_o = 0.25(x_1 + x_2 + x_3 + x_4), \tag{A.7}$$

$$\mathbf{e}_\xi = \frac{\partial x}{\partial \xi} = \sum_{n=1}^{4} \frac{\partial N_n(\xi,\eta)}{\partial \xi}\mathbf{x}_n, \tag{A.8}$$

$$\mathbf{e}_\eta = \frac{\partial x}{\partial \eta} = \sum_{n=1}^{4} \frac{\partial N_n(\xi,\eta)}{\partial \eta}\mathbf{x}_n. \tag{A.9}$$

Moreover, any function defined on the element, i.e., $f = f(\mathbf{x}(\xi,\eta))$, can be integrated as,

$$\int_E f\, dS = 4\int_{\eta=-1}^{\eta=1}\int_{\xi=-1}^{\xi=1} f(\mathbf{x}(\xi,\eta))\sqrt{\alpha(\xi,\eta)}\, d\xi d\eta, \tag{A.10}$$

with

$$\sqrt{\alpha(\xi,\eta)} = ||\mathbf{e}_\xi \times \mathbf{e}_\eta||, \tag{A.11}$$

where $\sqrt{\alpha(\xi,\eta)}$ denotes the Jacobian of the transformation. The Jacobian is defined as the square root of the determinant expression of the cross product and it represents the area of one sub-cell in the local coordinate system. The unit normal vector can then be defined as,

$$\mathbf{n} = \frac{(\mathbf{e}_\xi \times \mathbf{e}_\eta)}{||\mathbf{e}_\xi \times \mathbf{e}_\eta||}. \tag{A.12}$$

The expressions above are derived using the theory of curvilinear coondinate systems, tensor analysis and standard approaches for Structured Grids (or Meshes), see, e.g., for additional information.

It is important to note that integral calculation, associated with the DtN operator, in the present 3dBEM implementation on a quadrilateral element is performed using adaptive numerical integration. Particularly, in Filippas & Belibassakis [12] problem-specific CUDA-kernels for efficient adaptive simpson integration were developed for far field calculations. For self-induced coefficient calculation a semi-analytical approach is introduced.

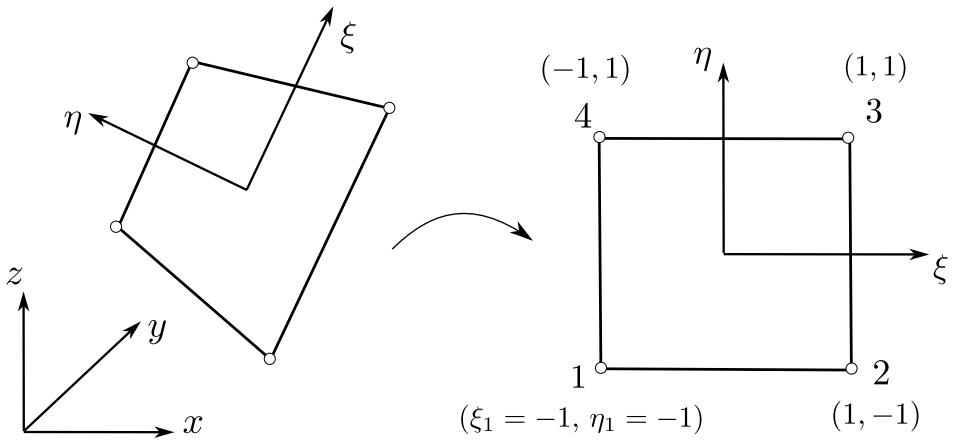

Figure A.1: Coordinate systems on a 4-node quadrilateral element in Global CS [left] and Local CS [right].

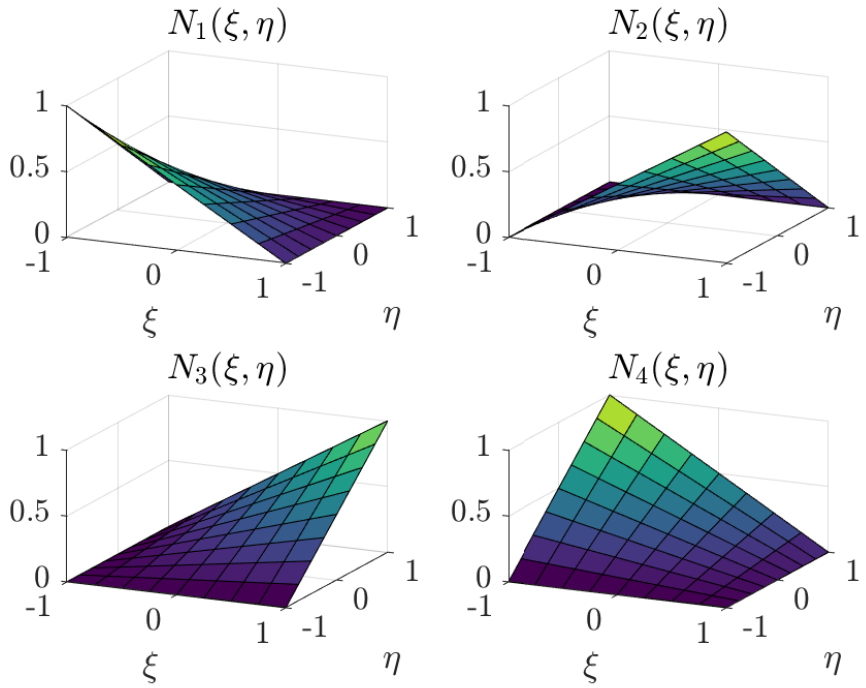

Figure A.2: Shape functions of the 4-node bilinear quadrilateral element.

Appendix B

Discrete Kirchhoff Triangle (DKT)

The shape functions below are defined in Batoz et al. 1980 [195] and in theory the DKT element is derived from the Discrete Shear Triangle (DST) formulation via a degeneration process. The DST element covers applications of thin to moderately thick plates and is based on First Order Shear Deformation Theory (FSDT), see also Batoz & Lardeur 1989 [190] and Batoz & Katili 1992 [205].

The quadratic shape functions $N_i(\xi, \eta)$ in Eq. (3.40) are defined over the element shown in Figure B as,

$$\begin{aligned} N_1 &= 2(1-\xi-\eta)(0.5-\xi-\eta), \quad N_2 = \xi(2\xi-1), \\ N_3 &= \eta(2\eta-1), \quad N_4 = 4\xi\eta, \\ N_5 &= 4\eta(1-\xi-\eta), \quad N_6 = 4\xi(1-\xi-\eta), \end{aligned} \tag{B.1}$$

with ξ and η denoting the local coordinates. Also, a schematic representation of the shape function is provided in Figure B.

Moreover, the functions $\mathbf{H}_x$ and $\mathbf{H}_y$ in Eqs. (3.48)-(3.49) are given compactly as,

$$\begin{aligned} H_{x_1} &= 1.5(a_6 N_6 - a_5 N_5), \quad H_{y_1} = 1.5(d_6 N_6 - d_5 N_5), \\ H_{x_2} &= b_5 N_5 + b_6 N_6, \quad H_{y_2} = -N_1 + e_5 N_5 + e_6 N_6, \\ H_{x_3} &= N_1 - c_5 N_5 - c_6 N_6, \quad H_{y_3} = -H_{x_2}. \end{aligned} \tag{B.2}$$

Functions H_{x_4}, H_{x_5}, H_{x_6}, H_{y_4}, H_{y_5} and H_{y_6} are obtained from the above by replacing N_1 by N_2, index 6 by 4 and index 5 by 6 respectively, whereas functions H_{x_7}, H_{x_8}, H_{x_9}, H_{y_7}, H_{y_8} and H_{y_9} are obtained by replacing N_1 by N_3, index 6 by

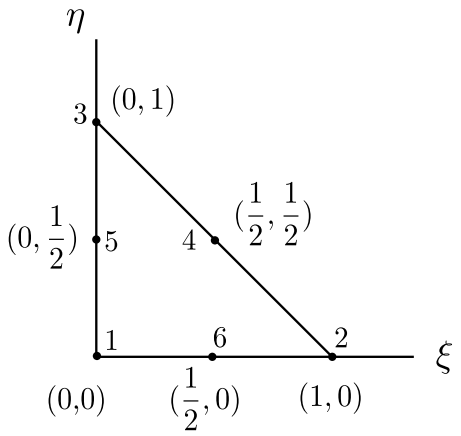

Figure B.1: Triangle element, adapted from [195].

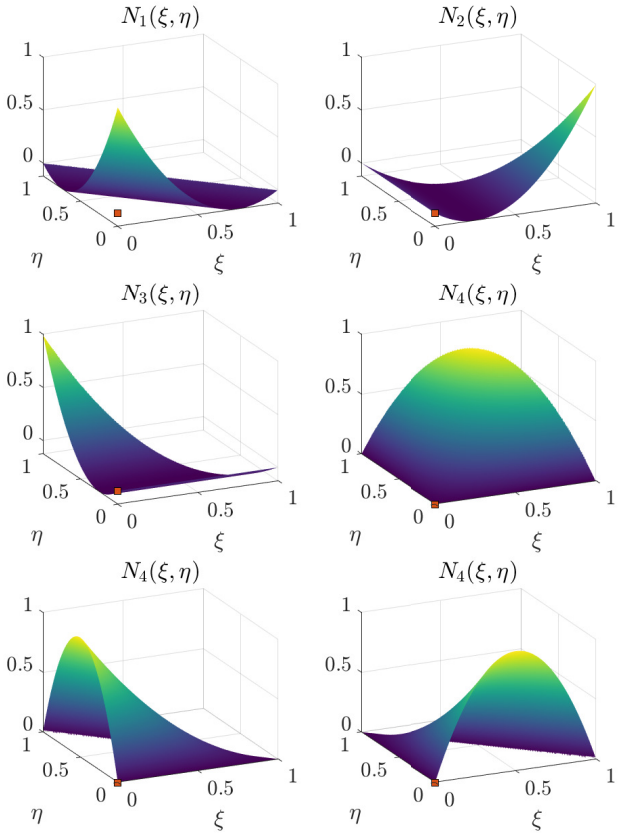

Figure B.2: Quadratic shape functions $N_i(\xi,\eta)$.

5 and index 5 by 4 respectively. Also,

$$
\begin{aligned}
a_k &= -x_{ij}/l_{ij}^2, \quad b_k = \frac{3}{4}x_{ij}y_{ij}/l_{ij}^2, \\
c_k &= (\frac{1}{4}x_{ij}^2 - \frac{1}{2}y_{ij}^2)/l_{ij}^2, \quad d_k = -y_{ij}/l_{ij}^2, \\
e_k &= (\frac{1}{4}y_{ij}^2 - \frac{1}{2}x_{ij}^2)/l_{ij}^2, \quad l_{ij}^2 = (x_{ij}^2 + y_{ij}^2),
\end{aligned}
\tag{B.3}
$$

based on the element geometry shown in Figure B.

The derivatives of $\mathbf{H}_x(\xi,\eta)$ and $\mathbf{H}_y(\xi,\eta)$ are obtained by differentiating Eqs. (B.2) in conjunction with Eqs. (B.1). The following arrangement is proposed in Batoz (1980),

$$
\mathbf{H}_{x,\xi} = \begin{bmatrix}
P_6(1-2\xi) + (P_5 - P_6)\eta \\
q_6(1-2\xi) - (q_5 - q_6)\eta \\
-4 + 6(\xi+\eta) + r_6(1-2\xi) - \eta(r_5 + r_6) \\
-P_6(1-2\xi) + \eta(P_4 + P_6) \\
q_6(1-2\xi) - \eta(q_6 - q_4) \\
-2 + 6\xi + r_6(1-2\xi) + \eta(r_4 - r_6) \\
-\eta(P_5 + P_4) \\
\eta(q_4 - q_5) \\
-\eta(r_5 - r_4)
\end{bmatrix}, \tag{B.4}
$$

$$
\mathbf{H}_{x,\eta} = \begin{bmatrix}
-P_5(1-2\eta) - \xi(P_6 - P_5) \\
q_5(1-2\eta) - \xi(q_5 + q_6) \\
-46(\xi+\eta) + r_5(1-2\eta) - \xi(r_5 + r_6) \\
\xi(P_4 + P_6) \\
\xi(q_4 - q_6) \\
-\xi(r_6 - r_4) \\
P_5(1-2\eta) - \xi(P_4 + P_5) \\
q_5(1-2\eta) + \xi(q_4 - q_5) \\
-2 + 6\eta + r_5(1-2\eta) + \xi(r_4 - r_5)
\end{bmatrix}, \tag{B.5}
$$

$$\mathbf{H}_{y,\xi} = \begin{bmatrix} t_6(1-2\xi)+\eta(t_5-t_6) \\ 1+r_6(1-2\xi)-\eta(r_5+r_6) \\ -q_6(1-2\xi)+\eta(q_5+q_6) \\ t_6(1-2\xi)+\eta(t_4+t_6) \\ -1+r_6(1-2\xi)+\eta(r_4-r_6) \\ -q_6(1-2\xi)-\eta(q_4-q_6) \\ -\eta(t_4+t_5) \\ \eta(r_4-r_5) \\ -\eta(q_4-q_5) \end{bmatrix}, \mathbf{H}_{y,\eta} = \begin{bmatrix} -t_5(1-2\eta)-\xi(t_6-t_5) \\ 1+r_5(1-2\eta)-\xi(r_5+r_6) \\ -q_5(1-2\eta)+\xi(q_5+q_6) \\ \xi(t_4+t_6) \\ \xi(t_4-r_6) \\ -\xi(q_4-q_6) \\ t_5(1-2\eta)-\xi(t_4+t_5) \\ -1+r_5(1-2\eta)+\xi(r_4-r_5) \\ -q_5(1-2\eta)-\xi(q_4-q_5) \end{bmatrix}, \tag{B.6}$$

where $k = 4, 5, 6$ for $ij = 23, 31, 12$ respectively,

$$\begin{aligned} P_k &= -6x_{ij}/l_{ij}^2 = 6a_k, \quad t_k = -6y_{ij}/l_{ij}^2 = 6d_k, \\ q_k &= 3x_{ij}y_{ij}/l_{ij}^2 = 4b_k, \quad r_k = 3y_{ij}^2/l_{ij}^2. \end{aligned} \tag{B.7}$$

Shape functions are evaluated on Gauss integration points, which are located at selected position in the element's interior. Regarding the planar mesh, the *2dFEM* solver uses the Delaynay triangulator provided in the Matlab PDE Toolbox. An example is shown in Figure 3.3. The mesher provides all necessary information by returning three arrays by default, let us denote them as $\mathbf{p}_{mat}$, $\mathbf{t}_{mat}$ and $\mathbf{e}_{mat}$. Array $\mathbf{p}_{mat}$ contains the nodal coordinates, whereas array $\mathbf{t}_{mat}$ the nodal indices corresponding to each triangle following a local-to-global numbering that is equivalent to the IEN format. For example the triangle with global index 1 has nodes given by

$$\begin{aligned} x_1 &= \mathbf{p}_{mat}(1, IEN(1,1)), \quad y_1 = \mathbf{p}_{mat}(1, IEN(1,1)), \\ x_2 &= \mathbf{p}_{mat}(1, IEN(2,1)), \quad y_2 = \mathbf{p}_{mat}(2, IEN(2,1)), \\ x_3 &= \mathbf{p}_{mat}(1, IEN(3,1)), \quad y_3 = \mathbf{p}_{mat}(2, IEN(3,1)), \end{aligned} \tag{B.8}$$

Array $\mathbf{e}_{mat}$ contains information about the triangle edges and it is useful for post-processing, since surface and contour plots can be generated using the 'pdeplot()' function in Matlab that needs to take as an input all three arrays from the mesher. Apart from the post-processing, our source code *2dFEM* needs only the first two arrays to retrieve mesh connectivity information and perform the global matrix assembly. Moreover, retaining Matlab as the pre/prost processing tool gives access to useful functions contained within the PDE Toolbox, such as the 'pdegrad($\mathbf{p}_{mat}$,$\mathbf{t}_{mat}$,u)' that returns the gradient of 'u' evaluated at the center of each mesh triangle.

Finally, since the process involving (IEN, ID, LM) arrays depends on array indexing, it is important to make sure that each programming language is different

with respect to the index of th first element in an array. For instance, Matlab programming language starts from index 1 whereas in C access to the first element of an array corresponds to an index 0.

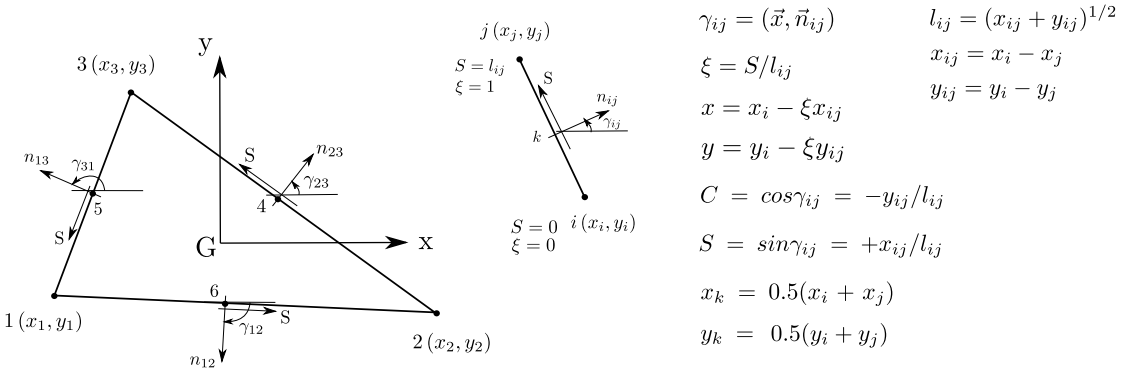

Figure B.3: Geometry of the triangular element, adapted from [195].

Appendix C

Coupling based on Crank-Nicolson

At each time step the solution is obtained using a Crank-Nicolson scheme for $\mathbf{w} = [\dot{\boldsymbol{q}}, \boldsymbol{q}]$[1] holds as,

$$\Big(\mathbf{A} - \frac{1}{2}dt\mathbf{B}\Big) \cdot \mathbf{w}_n = \Big(\mathbf{A} + \frac{1}{2}dt\mathbf{B}\Big) \cdot \mathbf{w}_{n-1} + \frac{1}{2}dt\Big(\mathbf{Q}_{n-1} + \mathbf{Q}_n\Big), \tag{C.1}$$

with the loading vector consisting of the interpolated pressure difference data at each triangle centroid of each DKT element $\mathbf{x}_i$ and fictitious forces terms.

Coupling scheme. The implicit nonlinearity is treated with an iterative scheme that considers the system of Eqs. (C.1) to be in fact nonlinear. Starting from an initial guess, typically $\mathbf{w}_n^\kappa = \mathbf{w}_{n-1}$, the residual equation is,

$$\mathbf{R}(\mathbf{w}_n^\kappa) = \Big(\mathbf{A} - \frac{1}{2}dt\mathbf{B}\Big) \cdot \mathbf{w}_n^\kappa - \Big(\mathbf{A} + \frac{1}{2}dt\mathbf{B}\Big) \cdot \mathbf{w}_{n-1} - \frac{1}{2}dt\Big(\mathbf{Q}_{n-1} + \mathbf{Q}_n^\kappa\Big), \tag{C.2}$$

with $\kappa = \{0, 1, ..., \kappa_{MAX}\}$ denoting the iteration index. Forcing term $\mathbf{Q}_n$ is implicitly dependent on the field of bending displacements and vice versa. The index n refers to the next time step $t + dt$ and thus $n - 1$ to the previous step whose information remains unaltered during the iterations of NR-scheme. Setting the residual expression to vanish,

$$\mathbf{R}(\mathbf{w}_n^\kappa) \to 0, \tag{C.3}$$

is pursued using the Newton-Raphson method and successively approximated via,

$$\mathbf{w}_n^{\kappa+1} = \mathbf{w}_n^\kappa - \omega_r \, \mathbf{J}^{-1}\Big(\mathbf{w}_n^\kappa\Big) \cdot \mathbf{R}\Big(\mathbf{w}_n^\kappa\Big), \quad \kappa = \{0, 1, ..., \kappa_{MAX}\}, \tag{C.4}$$

[1] This vector of unknowns stands as $\mathbf{w} = [\dot{\boldsymbol{q}}, \lambda_{\dot{\boldsymbol{q}}}, \boldsymbol{q}, \lambda_{\boldsymbol{q}}]$ where some places are reserved for the Lagrange multipliers $\lambda_{\dot{\boldsymbol{q}}}$, $\lambda_{\boldsymbol{q}}$ that are introduced to satisfy the boundary conditions.

where $\omega_r \leq 1.0$ denotes a relaxation factor and unless stated otherwise we assume $\omega_r = 0.98$. The matrix $\mathbf{J}$ is the Jacobian of function $\mathbf{R} : R^{2N} \rightarrow R^{2N}$ where $2N$ denotes the total number of unknowns for the structural problem,

$$J_{ij} = \frac{\partial R_i}{\partial w_j}, \quad \mathbf{R}(\mathbf{w}) = [R_1(\mathbf{w}_n^\kappa), R_1(\mathbf{w}_n^\kappa), ..., R_{2N}(\mathbf{w}_n^\kappa)]. \tag{C.5}$$

The calculation of Jacobian matrix requires knowledge of the partial derivatives of the scalar components $R_i(\mathbf{w})$ of the function $R(\mathbf{w})$. These components are numerically approximated via a central differences scheme,

$$\frac{\partial R_i}{\partial w_j^\kappa} \simeq \frac{R_i(w_j^\kappa + h_j) - R_i(w_j^\kappa - h_j)}{2h_j}, \tag{C.6}$$

assuming that the step-size h_j is sufficiently small. In practice it is selected as a small percentage of $|w_j|$, for instance $h_j = 0.001|w_j|$. Calculation of the Jacobian is indeed the most computationally expensive part of the simulation.

Although various criteria can be established to monitor the Newton-Raphson convergence at each time step, I found *heuristically* that the following criterion yields a good compromise between accuracy and iteration number,

$$max|\mathbf{R}(\mathbf{w}^\kappa)| < critEQ, \quad crtiEQ = \lambda\, max(\mathbf{T}),\ \lambda = 1e^{-3}, \tag{C.7}$$

where

$$\mathbf{T} = \Big[T_1, T_2, T_3, T_4\Big], \tag{C.8}$$

$$T_1 = \frac{1}{2N}\sum_{i=1}^{i=2N} abs\Big[\Big(\mathbf{A} - \frac{1}{2}dt\mathbf{B}\Big)\cdot \mathbf{w}_n^\kappa\Big]_{i-th},$$

$$T_2 = \frac{1}{2N}\sum_{i=1}^{i=2N} abs\Big[-\Big(\mathbf{A} + \frac{1}{2}dt\mathbf{B}\Big)\cdot \mathbf{w}_{n-1}^\kappa\Big]_{i-th},$$

$$T_3 = \frac{1}{2N}\sum_{i=1}^{i=2N} abs\Big[-\frac{1}{2}dt\mathbf{Q}_{n-1}\Big]_{i-th}, \quad T_4 = \frac{1}{2N}\sum_{i=1}^{i=2N} abs\Big[-\frac{1}{2}dt\mathbf{Q}_{n}\Big]_{i-th}.$$

It is important to note that the matrices in expressions above, whose size is slightly greater than $2N$, include components referring to the Lagrange multipliers - relating to how boundary conditions are satisfied in the present finite element scheme. The relevant components are excluded from the calculations involved in the derivation of $critEQ$. In any case, it is always possible to set $critEQ$ equal to the desired value for tolerance, such as $1e^{-9}$, and the scheme will work.

Variable κ_{MAX} is set by the user to limit the number of iterations that are allowed during each time step. Typically, convergence is achieved before this limit is reached however to avoid eternal while-loop this measure is also introduced for completeness.

Appendix D

On adjoint-BEM sensitivity derivation

This section provides additional information regarding the derivation and mathematical handling of certain terms related to the first variation of the augmented functional,

$$L = F + \int\int_{\Omega} \psi \nabla^2 \phi \, dV + \int_{\Gamma} \psi \delta(s - s_0) \Big[(\nabla\phi + \mathbf{U}_\infty) \cdot \hat{\boldsymbol{\tau}}|_{t_0} + (\nabla\phi + \mathbf{U}_\infty) \cdot \hat{\boldsymbol{\tau}}|_{t_1} \Big] \, ds \quad \text{(D.1)}$$

where $\delta(s - s_0)$ is the Dirac delta function.

The first term in Eq. (D.1) becomes

$$\frac{\delta F}{\delta b_n} = g(s_T) \frac{\delta s_T}{\delta b_n} - g(s_D) \frac{\delta s_D}{\delta b_n} + \int_{s_D}^{s_T} \frac{\delta g}{\delta b_n} \, ds + \int_{s_D}^{s_T} g \frac{\delta}{\delta b_n} (ds), \quad \text{(D.2)}$$

with the first two terms in the above expression appearing after the implementation of Leibniz rule for integration. Our goal here is to introduce terms including the field variable ϕ, the quantity $\delta\phi/\delta b_n$ and other known geometric quantities, see also [224] and [223]. Moreover the forth term,

$$\int_{s_D}^{s_T} g \frac{\delta}{\delta b_n} (ds) = \int_{t_D}^{t_T} g \frac{\delta ||\dot{\mathbf{r}}||}{\delta b_n} \, dt. \quad \text{(D.3)}$$

Also the third term,

$$\int_{s_D}^{s_T} \frac{\delta g}{\delta b_n} \, ds = \int_{s_D}^{s_T} (p - p_v) \frac{\delta p}{\delta b_n} \, ds - \int_{s_D}^{s_T} (p - p_v) \frac{\delta p_v}{\delta b_n} \, ds. \quad \text{(D.4)}$$

From Bernoulli's theorem for steady flows, i.e. $C_p = 1 - V_t^2/U_\infty^2$, it holds that $p = 0.5\rho U_\infty^2 - 0.5\rho V_t^2$ where V_t is the tangential velocity on the body boundary

$\partial\Omega$. Thus,

$$\frac{\delta p}{\delta b_n} = -\rho V_t \frac{\delta V_t}{\delta b_n} = -\rho V_t \Big[\frac{\delta}{\delta b_n}(\nabla\phi \cdot \hat{\boldsymbol{\tau}}) + (\nabla\phi + \mathbf{U}_\infty) \cdot \frac{\delta \hat{\boldsymbol{\tau}}}{\delta b_n} \Big] \tag{D.5}$$

where $V_t = (\nabla\phi + \mathbf{U}_\infty) \cdot \hat{\boldsymbol{\tau}}$. Assuming that we can exchange the operators,

$$\frac{\delta}{\delta b_n}(\nabla\phi \cdot \hat{\boldsymbol{\tau}}) = \nabla_s \Big(\frac{\delta\phi}{\delta b_n} \Big). \tag{D.6}$$

Taking all the above into consideration,

$$\begin{aligned} \frac{\delta F}{\delta b_n} &= g(s_T)\frac{\delta s_T}{\delta b_n} - g(s_D)\frac{\delta s_D}{\delta b_n} + \int_{t_D}^{t_T} g \frac{\delta ||\dot{\mathbf{r}}||}{\delta b_n}\, dt - \int_{s_D}^{s_T} (p - p_v)\frac{\delta p_v}{\delta b_n}\, ds \\ &- \int_{s_D}^{s_T} \rho V_t (p - p_v) \nabla_s \Big(\frac{\delta\phi}{\delta b_n} \Big)\, ds - \int_{s_D}^{s_T} \rho V_t (p - p_v)(\nabla\phi + \mathbf{U}_\infty) \cdot \frac{\delta \hat{\boldsymbol{\tau}}}{\delta b_n}\, ds. \end{aligned} \tag{D.7}$$

Moving on to the following term using Eq. (5.12),

$$\begin{aligned} \frac{\delta}{\delta b_n}\Big(\int\int_\Omega \psi \nabla^2\phi\, dV \Big) &= \int\int_\Omega \frac{\delta\psi}{\delta b_n} \cancel{\nabla^2\phi}\, dV + \int\int_\Omega \psi \frac{\delta}{\delta b_n}\Big(\nabla^2\phi \Big)\, dV \\ &+ \int\int_\Omega \psi \nabla^2\phi \cancel{\frac{\delta}{\delta b_n}\Big(dV \Big)}, \end{aligned} \tag{D.8}$$

assuming, for the last term in the above, that the variation of a differential volume dV with respect to the design variables is negligible. Then using Green's second identity[1] and exchanging operators $\delta(.)/\delta b_n$ and $\nabla^2(.)$, we can express the above term as follows,

$$\int\int_\Omega \psi \nabla^2 \Big(\frac{\delta\phi}{\delta b_n} \Big)\, dV = \int\int_\Omega \frac{\delta\phi}{\delta b_n} \nabla^2\psi\, dV + \int_{\partial\Omega} \psi \frac{\partial}{\partial \mathbf{n}} \Big(\frac{\delta\phi}{\delta b_n} \Big)\, ds - \int_{\partial\Omega} \frac{\delta\phi}{\delta b_n} \frac{\partial\psi}{\partial \mathbf{n}}\, ds. \tag{D.9}$$

Variation of Eq. (5.14), which holds on $\Gamma_c \cup \Gamma_w$, by parts with respect to the design variables yields,

$$\frac{\delta}{\delta b_n}\Big[(\nabla\phi + \mathbf{U}_\infty) \cdot \hat{\boldsymbol{n}} \Big] = \frac{\delta}{\delta b_n}(\nabla\phi) \cdot \hat{\boldsymbol{n}} + (\nabla\phi + \mathbf{U}_\infty) \cdot \frac{\delta \hat{\boldsymbol{n}}}{\delta b_n} = 0. \tag{D.10}$$

Using Eq. (D.10) the third term in (D.9) becomes,

$$\int_{\partial\Omega} \psi \frac{\partial}{\partial \mathbf{n}} \Big(\frac{\delta\phi}{\delta b_n} \Big)\, ds = -\int_{\Gamma_c} \psi (\nabla\phi + \mathbf{U}_\infty) \cdot \frac{\delta \hat{\boldsymbol{n}}}{\delta b_n}\, ds \tag{D.11}$$

$$- \int_{\Gamma_w} \psi (\nabla\phi + \mathbf{U}_\infty) \cdot \cancel{\frac{\delta \hat{\boldsymbol{n}}}{\delta b_n}}\, ds + \int_{\Gamma_{fs}} \psi \frac{\partial}{\partial \mathbf{n}} \Big(\frac{\delta\phi}{\delta b_n} \Big)\, ds, \tag{D.12}$$

[1] $\int_U (\psi\nabla^2\phi - \phi\nabla^2\psi) dV = \oint_{\partial U} \Big(\psi \frac{\partial\phi}{\partial \mathbf{n}} - \phi \frac{\partial\psi}{\partial \mathbf{n}} \Big)\, dS$

where the term $\delta\hat{\boldsymbol{n}}/\delta b_n$ is zero on the wetted portion of the boundary Γ_w, since only the attached cavity shape is affected by a variation in the design variable vector. Now the term that refer to the linearized free surface boundary Γ_{fs} need some attention. Using the Eq. (5.15) and integration by parts,

$$\int_{\Gamma_{fs}} \psi \frac{\partial}{\partial \mathbf{n}} (\frac{\delta\phi}{\delta b_n})\, ds = \Big[-\frac{1}{k_o}\psi \frac{\partial}{\partial x}\Big(\frac{\delta\phi}{\delta b_n}\Big) + \frac{1}{k_o}\frac{\partial\psi}{\partial x}\frac{\delta\phi}{\delta b_n}\Big]_{x_a^{fs}}^{x_b^{fs}} - \frac{1}{k_o}\int_{\Gamma_{fs}} \frac{\delta\phi}{\delta b_n}\frac{\partial^2\psi}{\partial x^2}\, dx \tag{D.13}$$

$$\simeq -\frac{1}{k_o}\int_{\Gamma_{fs}} \frac{\delta\phi}{\delta b_n}\frac{\partial^2\psi}{\partial x^2}\, dx, \quad \frac{\delta\phi}{\delta b_n}|_{\Gamma_{fs}} \to 0.$$

The last term in (D.9) becomes,

$$\begin{aligned}\int_{\partial\Omega} \frac{\delta\phi}{\delta b_n}\frac{\partial\psi}{\partial\mathbf{n}}\, ds &= \int_{\Gamma_c\cup\Gamma_w} \frac{\delta\phi}{\delta b_n}\frac{\partial\psi}{\partial\mathbf{n}}\, ds + \int_{\Gamma_{fs}} \frac{\delta\phi}{\delta b_n}\frac{\partial\psi}{\partial\mathbf{n}}\, ds \\ &= \int_{\Gamma_c\cup\Gamma_w} \frac{\delta\phi}{\delta b_n}\frac{\partial\psi}{\partial\mathbf{n}}\, ds + \int_{\Gamma_{fs}} \frac{\delta\phi}{\delta b_n}\frac{\partial\psi}{\partial z}\, dx\end{aligned} \tag{D.14}$$

since $(x, z = 0) \in \Gamma_{fs}$. To sum up,

$$\int\int_{\Omega} \psi\nabla^2\Big(\frac{\delta\phi}{\delta b_n}\Big)\, dV = \int\int_{\Omega} \frac{\delta\phi}{\delta b_n}\nabla^2\psi\, dV \tag{D.15}$$

$$-\int_{\Gamma_c} \psi(\nabla\phi + \mathbf{U}_\infty)\cdot\frac{\delta\hat{\boldsymbol{n}}}{\delta b_n} - \frac{1}{k_o}\int_{\Gamma_{fs}} \frac{\delta\phi}{\delta b_n}\frac{\partial^2\psi}{\partial x^2}\, dx \tag{D.16}$$

$$-\int_{\Gamma_c\cup\Gamma_w} \frac{\delta\phi}{\delta b_n}\frac{\partial\psi}{\partial\mathbf{n}}\, ds - \int_{\Gamma_{fs}} \frac{\delta\phi}{\delta b_n}\frac{\partial\psi}{\partial z}\, dx. \tag{D.17}$$

Variation of term two in Eq. (5.16) written compactly holds as,

$$\begin{aligned}\int\int_{\Omega} \psi\nabla^2\Big(\frac{\delta\phi}{\delta b_n}\Big)\, dV &= \int\int_{\Omega} \frac{\delta\phi}{\delta b_n}\Delta\psi\, dV - \int_{\Gamma_{fs}} \frac{\delta\phi}{\delta b_n}\Big[\frac{\partial\psi}{\partial z} + \frac{1}{k_o}\frac{\partial^2\psi}{\partial x^2}\Big]\, dx \\ &\quad -\int_{\Gamma_c} \psi(\nabla\phi + \mathbf{U}_\infty)\cdot\frac{\delta\hat{\boldsymbol{n}}}{\delta b_n} - \int_{\Gamma_c\cup\Gamma_w} \frac{\delta\phi}{\delta b_n}(\nabla\psi\cdot\hat{\mathbf{n}})\, ds.\end{aligned} \tag{D.18}$$

Finally, Eqs. (D.7) and (D.18) are used to derive the formula for sensitivities introduced previously in Eqs. (5.17)-(5.18).

Appendix E

Asymptotic behavior of a point singularity moving steadily beneath a free surface

An analytic solution for the case of point singularities with constant strength in uniform motion beneath the free surface is derived in [229] via the complex-variable method. Assuming that a combined source of strength Q and a point vortex of intensity Γ are located at $z_o = x_o + iy_o$, $y_o < 0$, the complex velocity potential at every point of the domain $z - x + iy$ can be calculated using,

$$f(z) = \frac{\Gamma + iQ}{2\pi i} log(z - z_o) - \frac{\Gamma - iQ}{2\pi i} log(z - z_o^*) \\ - \frac{\Gamma - iQ}{\pi i} PV \int_0^\infty \frac{e^{-ik(z-z_o^*)}}{k - \nu}\, dk - (\Gamma - iQ) e^{-i\nu(z-z_o^*)}, \tag{E.1}$$

where $\nu = g/U^2$ and U denotes the inflow velocity. The integral term is defined in sense of principal values (PV). An asymptotic form of this expression, i.e. $x \to \infty$ is given by doubling the last term based on [229] and is written as follows,

$$f(z) = \frac{\Gamma + iQ}{2\pi i} log(z - z_o) - \frac{\Gamma - iQ}{2\pi i} log(z - z_o^*) - 2(\Gamma - iQ) H e^{-i\nu(z-z_o^*)}. \tag{E.2}$$

where H denotes a smoothed Heaviside function $H(x) = 0.5 + 0.5 tanh(ax)$, $a = \nu/2$ which is used to satisfy the physical condition that no upstream waves occur. In addition it is important to note that based on the sign convention wave propagation occurs toward the negative of $x-$axis.

By introducing the following expression for the natural logarithm,

$$log(z) = log(|z|) + i arg(z), \quad -\pi + 2\kappa\pi < arg(z) < \pi + 2\kappa\pi,\ \kappa \in N \tag{E.3}$$

and obtaining the real part of Eq. (E.2) an expression for the velocity potential is derived

$$Re\Big[f(z)\Big] = \frac{Q}{2\pi}log(|z-z_o|) + \frac{Q}{2\pi}log(|z-z_o^*|) \tag{E.4}$$

$$+ \frac{\Gamma}{2\pi}arg(z-z_o) - \frac{\Gamma}{2\pi}argz(z-z_o^*) \tag{E.5}$$

$$+ 2H\Big[-\Gamma cos\big(\nu(x-x_o)\big) + Qsin\big(\nu(x-x_o)\big)\Big]e^{\nu(y_o+y)}$$

In that sense, for a translating point vortex the velocity potential can be obtained using the above for $Q=0$,

$$Re\Big[f(z), Q=0\Big] = \frac{\Gamma}{2\pi}arg(z-z_o) - \frac{\Gamma}{2\pi}argz(z-z_o^*) \tag{E.6}$$

$$+ 2H\Big[-\Gamma cos\big(\nu(x-x_o)\big)\Big]e^{\nu(y_o+y)}.$$

The velocity field is obtained via direct differentiation. The above asymptotic result offers an inexpensive, very good approximation of the wave potential and the free-surface elevation at a horizontal distance in the order of one wavelength away from the singularity and will be used in the present work for verification.